Nanomaterials for Biosensing and Cancer Therapy

Coline Jumeaux

IMPERIAL COLLEGE LONDON

Departments of Materials & Bioengineering

and the Institute of Biomedical Engineering

submitted in accordance with the requirements for the degree of

DOCTOR OF PHILOSOPHY

September 2016

Abstract

The unique features exhibited by nanomaterials endow them with great potential for applications interfacing with biological systems, and self-assembly enables to gain control over their architecture for fine-tuning of their properties and performances to achieve a highly specific response. High specificity is a key requirement for both biosensing and cancer therapy. This thesis explores the use of self-assembled nanomaterials for the development of new biosensing mechanisms and the design of stimuli-responsive drug delivery platforms for cancer therapy. MicroRNAs (miRNAs) present unique detection challenges, arising from their low abundance in clinical samples, short size, and high sequence homology. Here, DNA-mediated liposome fusion is used for highly specific detection of a clinically-relevant miRNA, initially using a standard laboratory microplate reader. Further, 2-color nanoparticle tracking microscopy is employed to directly follow fusion events occurring in liquid suspension, and a new analytical approach is developed to convert these observations into dose-response curves for increasing the sensitivity of the detection. In parallel, another strategy for increasing the assay sensitivity is explored, involving covalent binding of FRET pair dyes inside lipid bilayers. Further, cancer treatment at the nanoscale allows circumventing the limitations associated with conventional chemotherapy, by providing ways to enhance the treatment's specificity, increasing the aqueous solubility of anticancer molecules, improving their biodistribution, reversing multidrug resistance, and offering the possibility for personalized therapy. The nanovector employed in this project is the quantum rattle (QR), and is made of a mesoporous silica shell encapsulating gold nanoparticles and gold nanoclusters. In order to address QR towards a systemically administered multifunctional system for cancer therapy, it is engineered into a triggered release drug delivery system. A layer-by-layer type construct is designed using a thermoresponsive polymer, which provides a coating for QR, only allowing drug release after application of a trigger, here laser-induced gold-mediated hyperthermia.

Declaration

This is to certify that:

(i) The thesis comprises only my original work towards the PhD, at the exception of where it has been attributed to a collaborator who performed experiments or conducted data analysis.

(ii) Where portions of a chapter have been published in peer-reviewed journals, this is stated at the beginning of each chapter.

(iii) Due acknowledgement has been made in the text to all other material used.

(iv) This thesis is a record of the work performed at Imperial College London (London, UK), and at Chalmers University of Technology (Gothenburg, Sweden).

Coline Jumeaux

Publications

The following publications have been produced during the course of this PhD candidature:

[1] M. Hembury, C. Chiappini, S. Bertazzo, T. L. Kalber, G. L. Drisko, O. Ogunlade, S. Walker-Samuel, K. S. Krishna, C. Jumeaux, P. Beard, C. S. Kumar, A. E. Porter, M. F. Lythgoe, C. Boissière, C. Sanchez, M. M. Stevens. Gold-Silica Quantum Rattles for Multimodal Imaging and Therapy. *Proc Natl Acad Sci USA,* 2015, 112 (7), 1959-1964.

[2] C. Jumeaux, R. Chapman, R. Chandrawati, M. M. Stevens. Synthesis and self-assembly of temperature-responsive copolymers based on *N*-vinylpyrrolidone and triethylene glycol methacrylate. *Polym. Chem.,* 2015, 6, 4116-4122.

[3] A. J. Gormley, R. Chandrawati, A. J. Christofferson, C. Loynachan, C. Jumeaux, A. Artzy-Schnirman, D. Aili, I. Yarovsky, M. M. Stevens. Layer-by-Layer Self-Assembly of Polymer Films and Capsules through Coiled-Coil Peptides. *Chem. Mater*., 2015, 27, 5820−5824.

Selected presentations

The following presentations were delivered during the course of this PhD candidature:

[1] C. Jumeaux, R. Chandrawati, C. Chiappini, M. Hembury, G. Drisko, C. Boissière, C. Sanchez, M. M. Stevens. Stimuli-Responsive Hybrid Gold-Silica Nanoparticles for Controlled Drug Delivery in Cancer Therapy. 2014, poster presentation, Department of Materials Postgraduate research day, London, UK.

[2] C. Jumeaux, R. Chandrawati, C. Chiappini, M. Hembury, G. Drisko, C. Boissière, C. Sanchez, M. M. Stevens. Gold-silica hybrid nanovectors for combined cancer therapy and imaging. 2014, oral presentation (plenary speaker), INTERREG IV A 2Seas Training School: UoG - AAPS Chapter Conference, Chatham, UK.

[3] C. Jumeaux, C. Chiappini, R. Chandrawati, M. Hembury, G. L. Drisko, C. Boissière, C. Sanchez, A. Porter, M. M. Stevens. Systemically Injected Gold-Silica Hybrid Nanovectors for Combined Cancer Therapy and Imaging. 2014, oral presentation, 26th Annual Conference European Society for Biomaterials, Liverpool, UK.

[4] C. Jumeaux, R. Chandrawati, R. Chapman, C. Chiappini, A. Porter, M. M. Stevens. Stimuli-responsive Gold-Silica Hybrid Vectors for Controlled Drug Delivery in Cancer Therapy. 2015, oral presentation, Department of Materials Postgraduate research day, London, UK.

[5] C. Jumeaux, R. Chandrawati, R. Chapman, C. Chiappini, A. Porter, M. M. Stevens. Stimuli-responsive Gold-Silica Hybrid Vectors for Controlled Drug Delivery in Cancer Therapy. 2015, oral presentation, European Polymer Federation Congress 2015, Dresden, Germany.

[6] C. Jumeaux, P. D. Howes, E. Kim, R. Chandrawati, M. M. Stevens. Engineering nature-inspired diagnostic tests for rapid detection of flu. 2016, poster presentation, finalist at the SET for Britain poster competition, House of Commons, London UK.

[7] C. Jumeaux, P. D. Howes, E. Kim, O. Wahlsten, S. Block, R. Chandrawati, F. Höök, M. M. Stevens. Detection of influenza biomarker via DNA-mediated liposome fusion assays. 2016, poster presentation, 26th Anniversary World Congress on Biosensors, Gothenburg, Sweden.

Acknowledgements

The work reported in this thesis was supported financially by the Rosetrees Trust, and would not have been possible without the help and support of many people, to whom I am very grateful. In particular, I would like to acknowledge the contributions of the following:

First, I thank my supervisor, Prof. Molly Stevens, for giving me the opportunity to do my PhD in such an amazing group and stimulating environment. Her support and encouragements helped me navigate through my PhD, and I really appreciated that Molly trusted me with the freedom to pursue and work on my own ideas.

I have been extremely lucky to collaborate with and learn from many talented people. I would like to acknowledge the postdoctoral researchers I have worked with for being great teachers, and for becoming amazing friends. First and foremost, Dr Rona Chandrawati, a superstar researcher, the best mentor I could have asked for, and a close friend through good and bad times. Dr Mathew Hembury and Dr Ciro Chiappini for all their help, advice, and great discussions on the quantum rattle project. Dr Rob Chapman for helping me with the polymer chemistry, with his relentless energy and inspirational organisation skills. Dr Phil Howes and Dr Eunjung Kim taught me everything I know about DNA biosensing, and Dr Chris Spicer guided me through the synthesis of cyanine dyes.

I would also like to thank my collaborators: Dr Glenna Drisko and Dr Cédric Boissiere (Collège de France, Paris, France), for supplying the hollow mesoporous silica nanoparticles, and for all the discussions on the quantum rattle project. Prof. Fredrik Höök at Chalmers University of Technology (Gothenburg, Sweden) for welcoming me in his lab, Olov Wahlsten and Dr Stephan Block for a great collaboration and stimulating discussions. Prof. Irene Yarovsky and members of her group, Patrick Charchar and Dr Harun Rashid, at RMIT University (Melbourne, Australia), for their input with modelling, both on the quantum rattle and functional dyes projects.

A special thanks must go to the friends who have supported me since the beginning. To name a few: Dr Géraldine Durand, Prof. Lesley Chow, Dr Eugene “Tommy” Pashcock III, Dr Jason Chang, Dr Hélène Autefage, Dr Jean-Philippe St-Pierre, Dr Géraldine Guex, Markéta Kubánková, Astrid Armgarth, Dr Pauline Neirynck.

None of this would have been possible without the support of my family: my sister and brother, and most of all, my parents. I am so grateful for all the unconditional love you have given me, for being there for me at all times; your incredible support allowed me to be where I am today, and with it I can do anything.

Table of contents

List of Schemes, Tables, and Figures

List of Schemes

Chapter 3

Chapter 4

Chapter 5

List of Tables

Chapter 1

Chapter 2

Chapter 3

Chapter 5

List of Figures

Chapter 1

Chapter 2

Chapter 3

Chapter 4

Chapter 5

Appendix 1

Nomenclature

AIBN	Azobisisobutyronitrile
APTES	(3-aminopropyl)triethoxysilane
ARGET-ATRP	Activator ReGenerated by Electron Transfer
ATRP	Atom Transfer Radical Polymerisation
Au	Gold
cDNA	Complementary DNA
$CDCl_3$	Deuterated chloroform
CMOS	Complementary metal–oxide–semiconductor
CTA	Chain transfer agent
CTAB	Cetyl trimethylammonium bromide
DEPC	Diethylpyrocarbonate
DiL	1,1-dioctadecyl-3,3,3',3'-tetramethylindocarbocyanine perchlorate, DiIC18(3)
DiD	1,1'-Dioctadecyl-3,3,3',3'-tetramethylindodicarbocyanine perchlorate, DiIC18(5)
DLS	Dynamic light scattering
DNA	Deoxyribonucleic acid
dsDNA	Double stranded DNA
DOPC	1,2-Dioleoyl-*sn*-glycero-3-phosphocholine
DOPE	1,2-Dioleoyl-*sn*-glycero-3-phosphoethanolamine
DPA	Dipicolinic acid
DP_n	Degree of polymerization
DSN	Duplex-specific nuclease
EDTA	Ethylenediaminetetraacetic acid
ELISA	Enzyme-linked immunosorbent assay
EtOH	Ethanol
FTIR	Fourier transform infrared spectroscopy
FRET	Förster resonance energy transfer
FOV	Field of view
GO	Graphene oxide
HCl	Hydrochloric acid

HPLC	High Performance Liquid Chromatography
HS	Hollow silica
IUPAC	International Union of Pure and Applied Chemistry
LAMP	Loop-mediated isothermal amplification
LbL	Layer-by-layer
LCST	Lower critical solution temperature
LNA	Locked nucleic acid
LOD	Limit of detection
LSPR	Localized surface plasmon resonance
MALDI	Matrix-assisted laser desorption/ionization
MDR	Multidrug resistance
MES	2-(*N*-morpholino)ethanesulfonic acid
MeOH	Methanol
mRNA	Messenger RNA
miRNA	MicroRNA
MOPS	3-(*N*-morpholino)propanesulfonic acid
MPS	Mononuclear phagocyte system
MPTS	(3-mercaptopropyl)trimethoxysilane
MRI	Magnetic Resonance Imaging
MSN	Mesoporous Silica Nanoparticle
MWCO	Molecular Weight Cut Off
NaCl	Sodium chloride
NaOAc	Sodium acetate
NBD	*N*-(7-nitrobenz-2-oxa-1,3-diazol-4-yl)
NGS	Next-generation sequencing
NIR	Near infrared
NMR	Nuclear magnetic resonance
NP	Nanoparticle
NVP	*N*-vinylpyrrolidone
PAGE	Polyacrylamide gel electrophoresis

PBS	Phosphate Buffer Saline
PCR	Polymerase chain reaction
PEG	Poly(ethylene glycol)
PEI	Polyethylenimine
PL	Photoluminescence
PMA	Poly(methacrylic acid)
PNIPAM	Poly(*N*-isopropylacrylamide)
POEGMA	Poly[oligo(ethylene glycol) methacrylate]
pTEGMA	Poly[tri(ethylene glycol) methacrylate]
PTT	Photothermal therapy
PVP	Poly(*N*-vinylpyrrolidone)
QCM-D	Quartz crystal microbalance with dissipation monitoring
QD	Quantum dot
QE	Quantum efficiency
QR	Quantum rattle
qRT-PCR	Reverse transcription-quantitative polymerase chain reaction
RAFT	Reversible Addition-Fragmentation chain Transfer
RCA	Rolling circle amplification
rGO	Reduced graphene oxide
RNA	Ribonucleic acid
rpm	Round per minute
SiNP	Silica nanoparticle
SLB	Supported lipid bilayer
SNARE	Soluble *N*-ethylmaleimide-sensitive factor attachment protein receptors
SPIO	Superparamagnetic iron oxide
ssDNA	Single stranded DNA
TA	Tannic acid
TAM	Tumour associated macrophage
T_{cp}	Cloud point temperature
TEGMA	Tri(ethylene glycol) methacrylate

TEM	Transmission electron microscopy
TEOS	Tetraethyl orthosilicate
TGA	Thermogravimetric analysis
THF	Tetrahydrofuran
T_m	Melting temperature
TOF	Time of flight
Tris	2-Amino-2-hydroxymethyl-propane-1,3-diol

Scope of the thesis

Nanostructured materials, *i.e.* organized materials measuring less than 100 nm in size, have recently generated a high interest in the scientific community. Nanomaterials display unique physico-chemical properties, distinct from those of single molecules or bulk matter of the same composition. They have inspired the development of new tools and devices capable of interacting with biological systems at the nanoscale, essentially building a bridge at the interface of materials science and biology.[1,2] The ability to assemble nanomaterials into well-organized structures is crucial for the control of their properties and function.[3] Self-assembly encompasses reversible processes resulting in the association of distinct building blocks, made possible by the proper design of each component.[4] Using self-assembly, nanomaterials can be designed with a hierarchical order and high complexity resembling those observed in biological systems.[5] Therefore, self-assembly of nanomaterials holds great potential for a range of applications, as it combines emergent properties arising from scaling objects to nano-dimensions with complex designs that can respond to stimuli in a programmable way. This thesis explores the use of self-assembled nanomaterials as well as materials requiring self-assembly events to perform their function, first for the development of novel mechanisms for biosensing, then for the design of stimuli-responsive drug delivery platforms for cancer therapy.

This thesis will cover the following aspects of the use of nanostructured materials applied to biosensing and cancer therapy:

Chapter 1 opens on a comment on the emerging role of microRNAs (miRNAs) in disease diagnostics, and introduces the current state of the art methods for miRNA detection. As the challenges in miRNA detection are highlighted, the need for new sensing mechanisms emerges. Nanotechnology provides many exciting opportunities for miRNA biosensing, which are reviewed. The key advantages of bio-inspired sensor design are summarized, and model systems that mimic cell membrane fusion are presented, culminating with detailing the great potential of DNA self-assembly and liposomes for biosensing. Transitioning from biosensing to cancer therapy, this next section highlights the exciting opportunities that nanotechnology offers to meet the challenges hurdling conventional cancer chemotherapy. The benefits of cancer treatment on the nanoscale are described, concluding on the key features a therapeutic system should present to be an efficient anticancer agent.

In Chapter 2, the detection of miRNA via DNA-mediated liposome fusion is presented. First, the choice of a suitable assay for efficiently monitoring liposome fusion is discussed, and a Förster resonance energy transfer (FRET) based assay is selected. Then, a first detection mechanism is

introduced, where the presence of target miRNA inhibits liposome fusion. The influence of several factors on the kinetics of liposome fusion is determined, followed by a final evaluation of the sensitivity and specificity of this detection mechanism. In a second part, another detection mechanism is presented, where the presence of target miRNA promotes liposome fusion. The *in silico* rational design of DNA self-assembled constructs is illustrated, and the performances of these constructs are evaluated. The sensitivity and specificity of the assay for miRNA detection are determined, and the sensitivity of the assay is improved by using an advanced imaging setup.

In order to further improve the sensitivity of liposome fusion assays for miRNA biosensing developed in Chapter 2, Chapter 3 explores the synthesis of functional dyes for reporting lipid mixing. Herein, new dyes with 'clickable' chemical groups are synthesized, in the view of making them to react in the lipid bilayer as liposome-liposome fusion is proceeding. 'Clicked' dyes were hypothesized to increase FRET efficiency and therefore provide higher detection sensitivity. Several dyes are synthesized and fully characterized; the influence of their structure on their stability in the lipid bilayer is examined, and their performance in a liposome fusion assay is evaluated.

Chapter 4 introduces the quantum rattle (QR), a novel multifunctional platform for cancer therapy, based on gold-silica hybrid nanoparticles. In this Chapter, liposomes and polymers are assembled on QR, with the aim of developing smart drug delivery systems. As Chapter 1 outlined the challenges in cancer chemotherapy and introduced the ideal features for cancer treatment at the nanoscale, the summary of key properties of QR demonstrates the great potential for QR for this application. To further the aim of addressing QR towards a systemic delivery nanocarrier, this Chapter describes the development of QR as a stimuli-responsive drug delivery system allowing triggered drug delivery. As QR mediates hyperthermia when irradiated by a near-infrared laser, an increase of temperature is chosen as a stimulus. To do so, and building on knowledge and observations emerging from Chapter 3, liposomes are fused with QR to form a self-assembled, supported lipid bilayer on QR. By controlling the lipid composition, the properties of the new construct can be tuned: thermoresponsive lipids are used to impart stimuli-responsive features to QR. As this approach had shortcomings, another strategy is implemented: QR is coated with layers of a thermoresponsive polymer, which self-assembles above a critical temperature. The multilayer assembly is constructed using the layer-by-layer (LbL) technique. The assembly of polymer is optimized on planar substrates using Quartz Crystal Microbalance (QCM), and the optimized conditions are translated to QR. Drug delivery and further QCM studies led to infer the hypothesis that the thermoresponsive properties of the

cross-linked assembly of polymer were not retained, preventing the triggered drug delivery of therapeutic.

Chapter 5 is an extension of the work carried out on Chapter 4. To overcome the need for cross-linking to stabilize the LbL polymer assembly, here, new block copolymers are designed, containing an anchoring block used for the build-up of the multilayer assembly, and a thermoresponsive block. In this chapter, the synthesis of well-defined block copolymers by advanced polymerization techniques is demonstrated. The thermoresponsive properties of these polymers are characterised and the self-assembly properties of the block copolymers are investigated. A cross-linking strategy is exploited to stabilise the self-assembled structures below their assembly temperature. These novel block copolymers are applied for building a multilayer polymer film on QR as well as creating hybrid graphene oxide/polymer capsules.

Finally, Chapter 6 summarises the major findings and results of the thesis, and discusses future work.

References

1. P. K. Jain; X. Huang; I. H. El-Sayed; M. A. El-Sayed. *Acc. Chem. Res.* 2008, **41**, 1578–1586.
2. J. Cui; Y. Yan; Y. Wang; F. Caruso. *Adv. Funct. Mater.* 2012, **22**, 4718–4723.
3. K. Baek; I. Hwang; I. Roy; D. Shetty; K. Kim. *Acc. Chem. Res.* 2015, **48**, 2221–2229.
4. G. M. Whitesides; B. Grzybowski. *Science* 2002, **295**, 2418–2421.
5. G. M. Whitesides; M. Boncheva. *Proc. Natl. Acad. Sci. U. S. A.* 2002, **99**, 4769–4774.

Chapter 1

Literature review

1.1 Nanostructured materials for biosensing

Detection of target molecules in a specific and sensitive manner is of critical importance for the production of effective disease diagnostic tests. Biomarkers are biological components, which are used to identify specific physiological states; they encompass a range of molecules, from proteins and peptides, to nucleic acids. Their expression level can be linked to the presence of a pathogen in the organism, a disease state, or a response to pharmacological treatment. Analytical techniques such as polymerase chain reaction (PCR), and enzyme-linked immunosorbent assay (ELISA) are well-established procedures for biomarker detection. However, these procedures require extensive sample preparation, skilled technicians, and require taking place in laboratory settings. There is a growing trend for the development of miniaturized, easy-to-read assays, and with short time-to-results, which will enable portable, point-of-care diagnostics, for the fast detection of disease biomarkers. The unique features of nanomaterials open up new opportunities for developing sensing mechanisms and devices answering those challenges.

This thesis explores the use of liposome fusion driven by DNA self-assembly as a signal transducer and amplifier for biosensing. Recently, microRNAs (miRNA) have attracted a huge interest from the scientific community, due to their newly discovered potential to serve as biomarkers for a range of diseases. Their detection is particularly challenging, requiring the need for new mechanisms for biosensing. Hence, they were chosen as the target molecule to detect in this thesis.

1.1.1 MicroRNA biosensing

MicroRNAs (miRNAs) are small (~ 22 nucleotides), single-stranded, non-coding RNA molecules, which are involved in post-transcriptional regulation of gene expression via pairing with specific messenger RNA (mRNA) inducing translational repression or degradation.[1–3] They were discovered in 1993 in *C. elegans*.[4,5] Since then, studies have uncovered their role in the control of several key biological processes, such as immune response, cell differentiation, as well as cell proliferation and death.[6,7] The deregulation of the miRNA machinery can lead to aberrant processes, and diseases.[8] Therefore, efforts have focussed on identifying expression profiles of miRNAs to understand how their changes can lead to diseases, and miRNAs have emerged as promising biomarkers for diagnostics.[9] Initially, studies have demonstrated that the signature of miRNAs in blood, and most notably their relative concentration, can be an accurate diagnostic tool for several tumour types.[10–13] Since then, profiling of expression patterns have revealed their potential for the diagnosis of a range of diseases, although further research including

larger sample sizes still requires to be performed in order to confirm these findings.[14–17] Advantageously, the analysis of miRNAs is not limited to tissues, they can also be detected in several body fluids, including blood, serum, and saliva, providing minimally-invasive diagnostics tools.[9]

As the clinical and biological importance of miRNAs have been uncovered, there is a need for establishing robust methods for the analysis of miRNAs. Several challenges hurdle the detection of miRNAs, including their small size, low abundance, and high sequence homology.

MiRNAs are typically around 22 nucleotides long; the short size of their sequences implies low melting temperatures (T_m) for the corresponding duplex. As most detection methods rely on a hybridisation step between the target miRNA and a capture probe or primer, the low T_m of the duplex decreases the stringency of hybridization and therefore the specificity of the detection. In addition, as the T_m is highly dependent on GC content, the range of T_m observed for miRNAs is quite variable, which can lead to biases.[18] Moreover, the sequence size is similar to the size of a traditional polymerase chain reaction (PCR) primer, rendering the use of this technique difficult. Alternative PCR primers have been developed to solve this issue, which are detailed in a following paragraph describing the use of PCR for miRNA detection.

MiRNAs represent only a small fraction of the total extracted RNA (~ 0.01 %).[19] This low abundance requires detection methods with high sensitivity. Purifying and isolating miRNAs is difficult: unlike mRNAs, miRNAs lack the poly(A) tail which is used for sample pre-enrichment.[6] The number of miRNA copies per cell is also very variable: from a few copies to more than 50000 copies in a single cell, requiring detection techniques with a wide dynamic range.[6]

Another hurdle for miRNA detection is the sequence similarity between miRNAs: in families of miRNAs the sequences can differ from one to a few nucleotides only, whereas the homologous miRNA members of the family often perform different functions.[9] Therefore, detection systems need to be highly specific towards the target sequence and be able to distinguish between sequences with one nucleotide mismatch.

In summary, miRNA detection presents unique challenges, requiring detection techniques with high sensitivity, high specificity, and a large dynamic range. Furthermore, miRNAs often regulate multiple mRNAs, or one mRNA can be regulated by a variety of miRNAs, therefore the ability to detect several miRNAs at once, *i.e.* multiplexing, would be highly beneficial.

1.1.1.1 Conventional methods for miRNA detection

Conventional methods for miRNA detection include reverse transcription-quantitative polymerase chain reaction (qRT-PCR), hybridization-based microarrays, and next generation high-throughput RNA sequencing.

The current gold standard for miRNA analysis is qRT-PCR.[6,20] In this technique, miRNA is first reverse-transcripted to complementary DNA (cDNA), which is followed by amplification via qPCR and monitoring of product accumulation (Figure 1). This analytical technique provides a large dynamic range, a high sensitivity through selective amplification of the target of interest, and the ability to measure multiple miRNAs by running reactions in multiwell plates.[6] Furthermore, throughput can be increased by combining the instrument with microfluidic array platforms.[21] The short size of miRNAs, equivalent to the length of traditional PCR primers, presents a challenge for the design of qRT-PCR primers.[22] Two strategies are commonly used for solving this challenge. Stem-loop primers are long oligos that contain a region complementary with the sequence of the miRNA of interest, as well as a reverse primer complementary region.[23] The cDNA generated is amplified and quantified using TaqMan PCR (Figure 1). Another approach involves functionalizing the extremity of miRNA with a poly(A) tail via enzymatic addition, followed by SYBR Green based qPCR detection.[24]

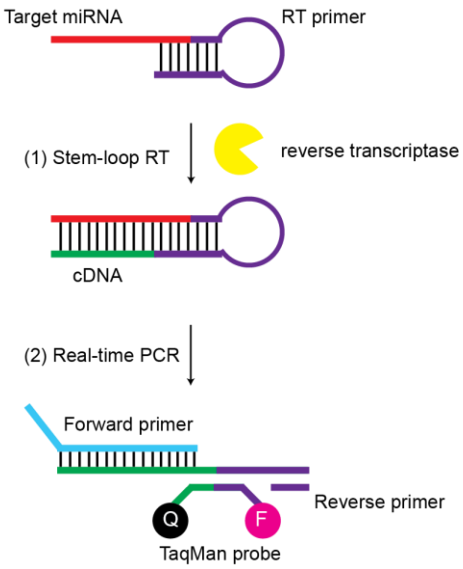

Figure 1. Schematic description of qRT-PCR for miRNA amplification and detection.

The main drawbacks of qRT-PCR lie in the complex primer design, and the inability to detect multiple targets in a single experimental volume.[25] Variability in PCR amplification efficiency results in run-to-run inconsistencies,[26] and requires the careful design of internal controls (*e.g.*

global mean averaging, using common housekeeping genes, spiking with non-natural RNA probes).[25] Additionally, results are often technology-dependent.[27]

Another widely used technique for miRNA detection is microarrays. Here, miRNAs are first labelled with a fluorescent probe by dephosphorylating the 5' end of the miRNA, followed by ligation with a fluorescently-tagged oligonucleotide using T4 ligase enzyme.[28] Then, the fluorescently labelled miRNAs are added to the array surface, which is functionalized with DNA capture probes; the surface is then scanned and the fluorescence is quantified. Using this technique, large numbers of miRNAs can be analysed in parallel. This method is only semi-quantitative, and is usually implemented to compare relative expression levels between different states (*e.g.* healthy *vs* disease).[6,28] As with qRT-PCR, the range of T_m is an issue which has been partially addressed by incorporating locked nucleic acid (LNA) into the DNA sequences of the probes. LNA is a modified nucleic acid, in which the 2' oxygen of the ribose is connected to the 4' carbon. These modified probes allow the use of a uniform T_m for a range of miRNAs.[29,30] Compared to qRT-PCR, microarrays have a smaller dynamic range. They also require additional validation (often achieved by PCR) to ensure specificity.[6]

Next-generation sequencing (NGS) represents an emerging technology for miRNA profiling. The process starts with reverse-transcribing miRNAs into a cDNA library. Adaptors are ligated to both 3' and 5' extremities of the cDNAs, which allows surface immobilization of the library. The immobilized cDNAs are amplified by PCR, and the products are analysed using bioinformatics. Alignment of the sequences against a miRNA sequence database enables the identification of the miRNAs present in the sample. Unlike qRT-PCR and microarrays, NGS can detect and identify new miRNA sequences.

Although these conventional methods represent great tools for miRNA profiling, several hurdles impede their widespread adoption in the clinical milieu. These methods require costly, specialized laboratory equipment and skilled researchers to perform miRNA detection. The time-to-result is also long, from hours to days.[6] There is a need for simple, low-cost, rapid assays for the detection of multiple miRNAs of interest with high sensitivity as well as high specificity. These technologies will have utility for basic and clinical research, as well as point-of-care diagnostics.

1.1.1.2 Biosensors-based methods for miRNA detection

A biosensor is a self-contained device, which provides quantitative analytical information, and integrates a chemical or molecular recognition system, a physico-chemical signal transduction element, and a reader interface to output results.[18,31] The selective biorecognition element in

miRNA biosensors is usually a DNA probe, which sequence is complementary to the miRNA sequence of interest. Advances in the field of nanotechnology have been a key factor for the development of biosensors meeting the aforementioned challenges in miRNA detection.[32–34] Unique properties displayed by nanomaterials, which are typically different from the corresponding bulk materials, such as quantum confinement of excitons resulting in bright tunable fluorescence from semiconductor nanoparticles (quantum dots) and localized surface plasmon resonance (LSPR) in metallic nanoparticles, have enabled the development of novel transduction mechanisms, increasing the sensitivity of the biosensor via signal amplification.[33–36] Indeed, owing to the size of nanomaterials, their interaction with target biomolecules greatly influences their properties, which makes them a highly sensitive detection system. Nanomaterials can also be used for signal amplification, towards the development of ultrasensitive biosensors: not only nanoparticles can provide signal amplification, nanomaterials can also serve as a host loading multiple signal-generating molecules.[36]

Promising electrochemical and optical technologies have been developed for the detection of miRNA. While early research aimed at demonstrating the proof-of-concept for these new methods, during the past few years the focus has been shifted to proving their use for clinical applications.

Electrochemical detection of miRNA is based on hybridization of miRNA at the surface of a solid electrode, and change in capacitance, impedance, as well as redox reactions are typically detected, often via an electrochemically-active reporter species.[18] Such sensors can detect miRNA with good sensitivity but require extensive sample preparation and normalization steps, and lack portability, which impedes their development towards point-of-care sensors.[18]

Several optical detection methods have been implemented successfully for miRNA detection, mainly, fluorescence or Förster resonance energy transfer (FRET) based approaches, and plasmonic approaches.

(i) Fluorescence-based approaches

FRET is a mechanism of energy transfer between two molecules, a fluorophore donor (D) and a chromophore acceptor (A), where the emission spectrum of D overlaps the absorption spectrum of A. In this mechanism, D is in an excited electronic state, and may transfer its excitation energy to A in a non-radiative process, through intermolecular long-range dipole-dipole interactions, as long as they are at a certain distance to each other (typically less than 10 nm) (Figure 2).[37] The transferred energy is dissipated by A via heat (A is a chromophore, quencher) or fluorescence (A is a fluorophore), a process called sensitized emission.[38]

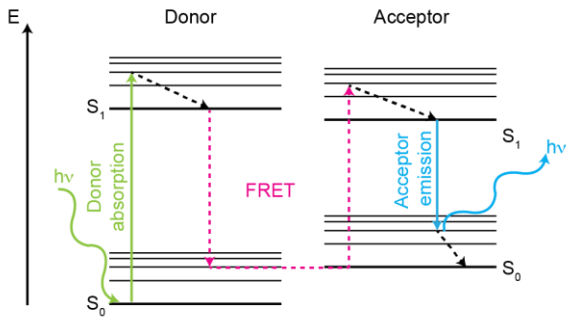

Figure 2. Jablonski diagrams illustrating FRET between a donor and an acceptor molecule. Absorption of a photon by the donor raises an electron to an excited energy state. The energy released by the relaxation of the donor is transferred to the acceptor in a non-radiative process, and leads to the excitation of one of its electron, which relaxes by dissipating energy in form of fluorescence (as illustrated, emission of a photon by the acceptor) or heat. Adapted from Hochreiter *et al*.[39]

FRET is a distance-dependant physical process: the efficiency of energy transfer varies to the inverse sixth power of the distance separating D and A, and the rate of energy transfer is given by Equation 1:[40]

$$k_T = \left(\frac{1}{\tau_D}\right) \times \left(\frac{R_0}{r}\right)^6 \quad (1)$$

where τ_D is the fluorescence lifetime of D, r is the distance between D and A, and R_0 is the Förster distance which defines the distance at which the energy transfer is 50 % efficient, and has a characteristic value for each FRET (D-A) pair.

The FRET efficiency E can be related to the donor-acceptor distance via Equation 2:[40]

$$E = \frac{1}{1+(r/R_0)^6} \quad (2)$$

The distance-dependence of FRET efficiency has led to numerous applications for probing the structure and conformation of biological systems.[40]

Fluorescence and FRET based biosensors improve from microarrays by using fluorescent reporter probes instead of labelling the miRNAs with a fluorescent dye. One of the simplest mechanisms is based on DNA strand displacement. A fluorescently-tagged DNA capture probe is hybridized with a short complementary DNA strand conjugated with a quencher dye. The target miRNA is able to displace the DNA-quencher strand by hybridising with the capture probe, which results in regeneration of fluorescence (Figure 3).[41] Wu *et al* demonstrated the multiplexed detection of three different miRNAs using this mechanism, reaching a limit of detection in the femtomolar range for the uniplexed assay.[41]

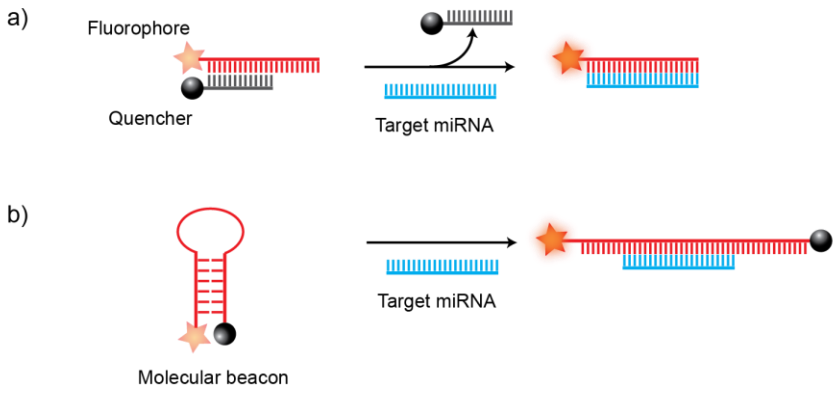

Figure 3. Schematics of a) strand displacement assay for miRNA detection and b) molecular beacon-based miRNA detection.

One of the main drawback of this mechanism is its poor specificity: miRNA sequences with one or a few mismatches are still able to displace the quencher strand, resulting in false positives.[41,42] Improved specificity can be obtained by using molecular beacons. Molecular beacons are stem-loop DNA strands functionalized at each extremity with a dye (Figure 3b). The dye pair can either generate FRET or fluorescence quenching. In absence of miRNA, the molecular beacon is in a "closed" form, adopting the most thermodynamically stable hairpin structure; the dyes are then in close proximity, and energy transfer can occur. The miRNA sequence is complementary to part of the hairpin, and when the miRNA is present, it hybridises to the molecular beacon and transforms it to an "open" form, where the dyes are spatially separated and the energy transfer efficiency dramatically decreases, either turning "ON" the fluorescence, or decreasing the FRET signal. Molecular beacons increase specificity by increasing the stringency of the hybridization.[43] Similarly to the strategy employed for RT-PCR, the incorporation of modified nucleic acids (locked nucleic acid, LNA) increase specificity: LNAs entail a much higher affinity for the perfectly complementary target compared to a mismatched miRNA, enabling specific detection of miRNA.[42]

Quantum dots (QDs) are fluorescent metallic semiconductor nanoparticles. Compared to organic fluorescent dyes, their fluorescence is very bright, and they are more photostable. Additionally, their fluorescence emission is very narrow and highly tunable, while their absorbance spectrum is very large, bestowing them a great potential for multiplexing: several QDs emitting at different wavelengths can be excited using a single light source.[33] QDs have been used in several miRNA biosensors, however, to reach lower limits of detections, additional enzymatic amplification steps were necessary.[44–46] Qui *et al* developed a simple, one-step assay for miRNA detection based on Terbium-to-QD FRET, and demonstrated the multiplexed detection of three different

miRNAs with sub-nanomolar detection limits, however, measurements in serum were not as efficient.[47]

(ii) Plasmonic and photonic approaches

One of the main issue with fluorescence-based detection is that multiplexing is achieved spectrally, which constrains the number of sequences that can be detected simultaneously. Unlike fluorescence-based approaches, plasmonic approaches have the advantage of being label-free, which simplifies the procedure as well as offers more possibilities for multiplexing, as they are not limited by the number of labels that can be independently read.[6]

Colloidal gold nanoparticles (AuNPs) have attracted a huge interest for biosensing applications, due to their unique optical properties. At a particular wavelength, concerted oscillation of the electrons on the surface of the AuNPs generate a phenomenon called localized surface plasmon resonance (LSPR), resulting in strong extinction of light.[48] Their interaction with light is strongly correlated with their size, shape, surface chemistry, aggregation state and environment. For instance, small AuNPs appear red in solution, due to their optical absorption centred around 520 nm, while the SPR wavelength of larger AuNPs shifts to the red part of the spectrum, yielding solutions with purple to pale blue colour.[48] The aggregation of AuNPs also results in a red shift of the SPR wavelength, due to interparticle plasmon coupling, and this colourimetric shift by aggregation has proven a valuable tool for probing DNA and other biomolecules,[49,50] and has been translated to miRNA detection.[51,52] AuNPs aggregation-based assays present the advantage of being simple, one-step, and rapid, with the possibility of naked eye detection. A limitation of using AuNPs aggregation is that the colourimetric shift occurs in a region of high absorbance by the native proteins in physiological samples, resulting in low sensitivity of such assays.[48] Alternatively, AuNPs can be used as a tag for signal amplification, due to their ease of surface functionalization with oligonucleotides.[53,54]

The SPR phenomenon can also be used to detect surface-hybridization through changes in the refractive index surrounding the nanostructures. Here, multiplexing can be achieved spatially, in a similar fashion to microarrays. However, in conventional label-free SPR experiments, the small size of captured miRNA does not result in a significant enough change in refractive index, resulting in low sensitivity.[55] To improve upon this, signal amplification via labelling and sandwich assays were implemented.[56] Another strategy to improve sensitivity explored the use of gold nanoprisms functionalized with complementary DNA as LSPR sensor.[57,58] Using these highly sensitive structures, attomolar limit of detection for miR-10b using clinical samples was demonstrated.[58] On a side note, surface tethering-based analytical techniques are limited by the diffusion of the species to the surface.

(iii) Amplification methods

The low abundance of miRNAs in analytical samples requires detection methods with high sensitivity. Nanoparticles inherently generate signal amplification; however, it does not usually enable to reach clinically-relevant concentration ranges. The aforementioned nanotechnology-assisted biosensing mechanisms were mostly based on stoichiometric miRNA detection, where one target triggered one signal transduction event. In order to improve the limit of detection of the assays, amplicons of the target miRNA can be generated using enzymatic reactions, before signal transduction.

In order to circumvent the problems intrinsic to PCR target amplification, more advanced miRNA amplification methods have been designed, among which isothermal amplification and rolling circle amplification are the most prominent. Isothermal amplification uses the activity of polymerase and nicking enzymes.[44,59,60] In this reaction, a cycle of polymerization (using RNA polymerase) and nucleotide release (using site-specific nicking enzyme) enables to rapidly synthesize short oligonucleotides (amplicons) specified by the sequence of an amplification template (Figure 4a). The reaction can be rendered exponential by further using the amplicons as initiators for a parallel amplification cycle, using an amplification template specific to their sequence. Using this method, Jia *et al* demonstrated the detection of miRNAs amount as low as 0.1 zmol.[60] This method requires the use of two enzymes, adding cost, complexity, and possibly errors. A further simplification of this system was developed, named loop-mediated isothermal amplification (LAMP), which takes advantage of the RNA polymerase and strand displacement activities of one single enzyme, *Bst* DNA polymerase.[61] However, the primer design for this reaction is extremely complex, and is only specific for a single miRNA sequence. Another commonly used isothermal amplification is rolling circle amplification (RCA).[62] A template is circularized by ligation with a short DNA or RNA strand, using a ligase enzyme (Figure 4b). Then, the procedure takes advantage of Phi 29 DNA polymerase's strong strand displacement and 3' to 5' exoribonuclolytic activities for the production of long DNA sequences.

An alternative option to the amplification of the target is the recycling/regeneration of the target by biocatalytic reactions. Duplex specific nuclease (DSN) is an enzyme that selectively cleaves double stranded DNA and DNA in DNA-RNA heteroduplexes. As the DNA capture sequence is cleaved, the target miRNA is released and recycled for another hybridization.[51,63]

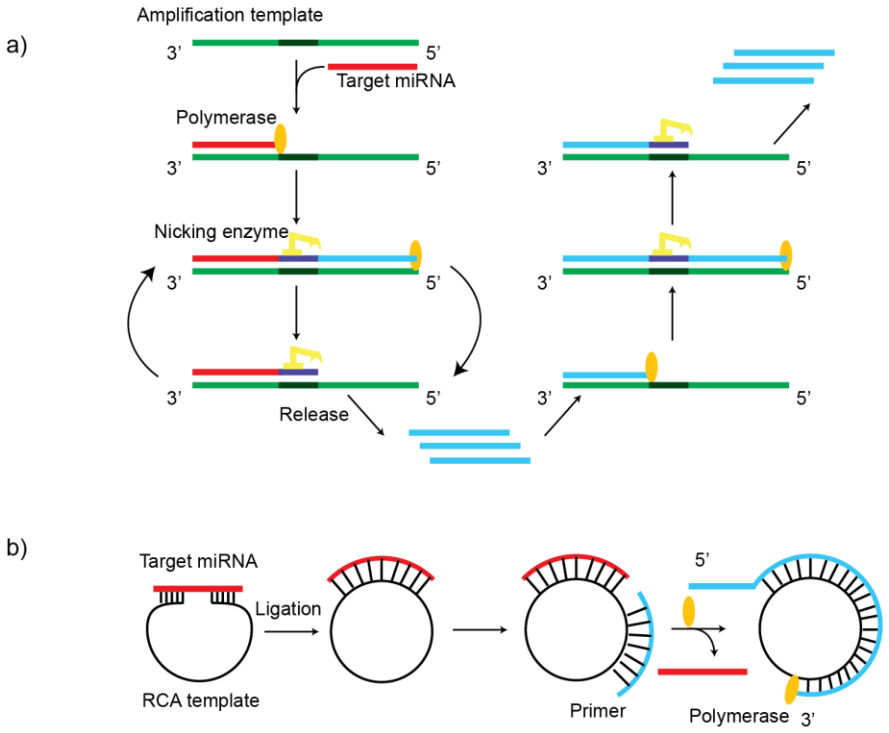

Figure 4. Amplification strategies of target miRNA. a) Isothermal exponential amplification. The target miRNA hybridizes on the amplification template, which contains two copies of the amplicons sequence surrounding the nicking enzyme recognition site. b) Rolling circle amplification.

Enzymatic approaches for target amplification enabled to improve the sensitivity of miRNA detection, however, this additional step increases the complexity of the biosensor. Extra caution needs to be taken in the design of the templates, in order to prevent non-specific amplification.[8] Furthermore, a lot of these enzymes also have secondary activities, towards other targets than the one intended in the assay, requiring fine tuning of the reaction conditions, such as temperature, ionic strength, metallic ions content. Enzymes are also expensive, and require particular storage conditions, which hurdles the development of enzymatic amplification based biosensors towards point-of-care diagnostics. This problem is starting to be addressed, and one very exciting advance towards the point-of-care development of miRNA sensor using RCA was achieved by Liu *et al.* who printed all the RCA components on a nitrocellulose membrane, and used pullulan, a polysaccharide, to stabilize and store them at room temperature.[64]

Therefore, despite the rapid advances in the field of miRNA biosensing, developing simple, sensitive, direct, and non-target-amplification methods for multiple miRNA analysis is still a challenge. On a side note, a remaining hurdle to overcome is the development of robust procedures for sample collection, preparation and storage for uniformed, reproducible results.[9,25]

1.1.2 Biomimetic sensor design: DNA-mediated liposome fusion

The increased understanding of biological processes and of the design principles underlying recognition events enables the progression of the field of biomimetic design of materials, which harnesses the power and simplicity of natural processes combined with biological building blocks (*e.g.* DNA, RNA, peptides, proteins) to create hierarchically organized materials, and the development of a new generation of sensors.[65]

This thesis explores the use of liposomes as a signal amplification tool for biosensing. Liposomes are spherical vesicles, composed of at least one bilayer of self-assembled phospholipids. Since their discovery in 1965,[66] they have been widely used as a model for membrane systems,[67] as well as drug delivery systems due to their ability to encapsulate a large payload of both hydrophilic and hydrophobic cargos.[66] More recently, this feature has been applied for biosensing, where a variety of signal transducer molecules has been encapsulated in liposomes for signal amplification.[68] By encapsulating and/or binding multiple signalling molecules, liposomes transform a stoichiometric one-to-one binding event to signal generation into a one-to-many, providing amplification of the signal by orders of magnitude. Furthermore, liposomes are cost-effective, easy to functionalize, and stable in complex physiological fluids, making them very attractive for biosensing. Here, in addition with signal amplification, the ability of liposomes to mimic membrane fusion is exploited as a signal transducer: the fusion of two liposomes indicates the presence or absence of target miRNA.

Nature is a great source of inspiration for the design of efficient sensors; high degree of sophistication and miniaturization are found in natural materials and processes.[65,69] Over the course of evolution, stringent selection processes have enabled the emergence of highly sensitive and specific sensing or signalling processes, using refined components made of few simple building blocks.[65] With the aid of molecular self-assembly, complex biological systems can be mimicked, with a high control over the function of each component.[32]

1.1.2.1 Mechanism of membrane fusion

Membrane fusion is an ubiquitous phenomenon occurring in eukaryotic organisms, and is an essential event in a variety of cellular processes. It allows the delivery of molecules across lipid bilayers, which are usually impervious to hydrophilic molecules.[70] Intracellular membrane fusion enables the trafficking of building blocks, such as proteins and chemicals, between cell compartments, maintaining the organelles' integrity and functionality.[71] Additionally, intracellular membrane fusion mediates intercellular communication by sending signalling molecules to the plasma membrane. Furthermore, extracellular membrane fusion allows the

merger between virus and host membrane during infection, as well as enables reproduction when a sperm fuses with an oocyte.[71,72]

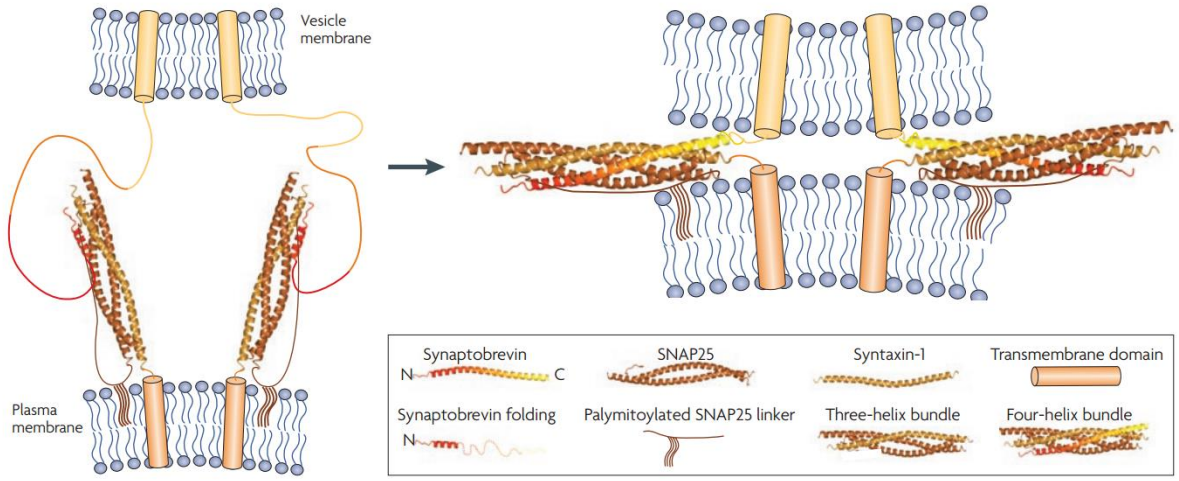

Figure 5. Neuronal membrane fusion is mediated by SNARE proteins. Vesicular synaptobrevin and plasma-membrane SNAP25 and synthaxin-1 form the SNARE complex. The formation of the four-helix bundle brings the membrane in close proximity. Reprinted by permission from Macmillan Publishers Ltd: Nature Reviews Molecular Cell Biology (S. Martens, H. T. McMahon. Nat. Rev. Mol. Cell Biol., 2008, 9, 543–556), copyright 2008.

The membrane fusion process, which merges two previously separate compartments, is regulated by a complex molecular machinery allowing to overcome several high-energy barriers, such as electrostatic repulsion of the membranes and the hydrophobic/hydrophilic organization of the bilayers.[73] In the case of viral fusion, the virus itself provides the fusogenic machinery, whereas for intracellular fusion, the fusion machinery is split in two halves, each bore by the fusing compartments. It has been hypothesized that proteins belonging to the SNARE family (soluble *N*-ethylmaleimide-sensitive factor attachment protein receptors) consist the minimal fusion machinery in almost all intracellular fusion events.[74,75] SNAREs are characterized by their highly conserved sequences called SNARE motifs, which have a high susceptibility to form coiled-coil.[76] They can be classified in two functional groups: *v*-SNAREs, which are associated with the fusing vesicle, and *t*-SNAREs, associated with the target membrane.[77] *v*-SNARE interact with *t*-SNARE to form a four-helix bundle via association of their SNARE motifs (Figure 5).[71,78] In general, the distance between biological membranes is no smaller than 10-20 nm, due to electrostatic repulsion and steric hindrance caused by membrane bound proteins.[67] After the initial tethering step, further protein folding brings the membranes in close proximity (a few nanometers),[79] causing a local disruption of the bilayer structure, and leading to the formation of a stalk-like structure where only the lipids from the outer leaflets have merged. Further disruption of the membranes leads to the formation of the fusion pore, which opens and dilates,

finally merging both lipid bilayers. The transition states between the initial lipid mixing and the full fusion are mostly unknown, hence research has focussed on developing model systems to understand the mechanisms of *in vivo* membrane fusion.[67]

1.1.2.2 Model systems for membrane fusion

One of the most characterized fusion machinery is the one facilitating synaptic communication, where a vesicle containing neurotransmitters fuses with the neural axon.[76,80] This machinery has been extensively studied using model systems such as proteoliposomes, in which the native fusogenic proteins are exposed on the surface of artificial lipid vesicles.[79,81–85] Another approach involves the design of biologically-inspired constructs to trigger artificial lipid vesicle docking and membrane fusion.

Reconstituted SNAREs proteins in liposomes for membrane fusion assays often yield contradictory results; the cumbersome reconstitution process, which employs detergents for solubilizing proteins, creates liposomes with size and protein density variability.[67] The biological relevance of using such systems is questionable, as *in vitro* assays do not reproduce the characteristics of *in vivo* membrane fusion.

A simpler experimental approach uses biomimicry and synthetic analogues of fusogenic proteins to engineer constructs enabling membrane fusion. Simplified synthetic analogues are an excellent tool to increase understanding of the fusion process at the atomistic level, and each segment of the synthetic construct can be varied to study its role.[67] Synthetic analogues enabling specific molecular recognition used to trigger membrane fusion include coiled-coil forming peptides,[70,86] and DNA.[87–90] In particular, Höök *et al* designed cholesterol-terminated double-stranded DNA (dsDNA) that self-insert into lipid vesicles, and demonstrated that their hybridization in a zipper-like fashion induced vesicle-vesicle fusion (Figure 6).

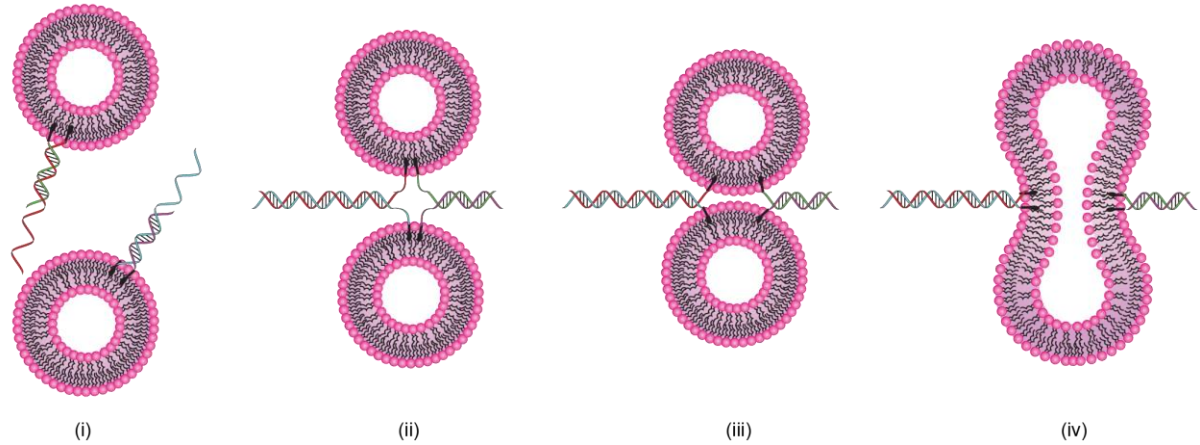

Figure 6. Mechanism for DNA-mediated liposome fusion. (i) Two separate populations of liposomes are functionalized with complementary DNA strands; (ii) and (iii) DNA hybridization in a zipper-like fashion brings two liposomes in close contact, eventually leading to mixing of outer leaflet lipids, and in some cases, (iv) opening of the fusion pore. Adapted from Stengel *et al.*[90]

This mechanism has great potential for addressing it towards biosensing. DNA self-assembly is highly specific, programmable, and fast.[32] The DNA sequences can be modified to be complementary to the target miRNA of interest, representing the biorecognition element, while the transduction and signal amplification element will be liposome fusion. As mentioned previously, liposomes can amplify signal by encapsulating a multitude of reporting molecules, and this alternative strategy to enzymatic target amplification was examined in this thesis.

1.1.2.3 Reporter assays for membrane fusion

Several assays for reporting membrane fusion have been developed, and can be subdivided into two categories, as they can assess different events occurring during membrane fusion: lipid mixing assays and content mixing assays.

(i) Lipid mixing assays

One of the most widely used assay across the literature for determining the kinetics and extent of lipid mixing is based on FRET between *N*-(7-nitrobenz-2-oxa-1,3-diazol-4-yl) (NBD) and rhodamine (Figure 7). In the NBD-rhodamine FRET dilution assay, both donor and acceptor dye are included in the same liposomes. Liposomes are functionalized with lipid-conjugated fluorophore pairs present at quenching concentration (*i.e.* high FRET efficiency). Upon fusion with unlabelled liposomes, the lipids functionalized with the fluorophores are diluted in the lateral plane, resulting in fluorescence dequenching, and decreased efficiency in the energy transfer (Figure 7a).[91] Instead of NBD and rhodamine, other molecules have been examined, such as self-quenching of octadecyl rhodamine B, and pyrene eximer formation.[92]

In another configuration, called probe mixing, a population of liposome is labelled with the donor and another population with the acceptor. Upon lipid, the FRET signal increases as the dyes come in close proximity (Figure 7b).

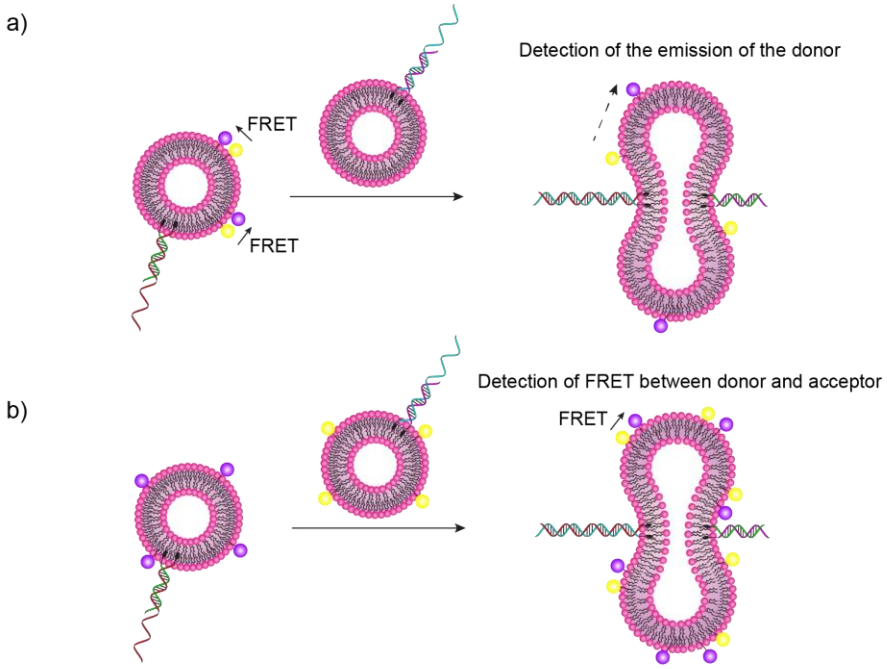

Figure 7. Lipid mixing assay. a) Probe dilution assay: two populations of liposomes are prepared, one labelled with dyes forming a FRET pair, the other unlabelled. Upon liposome fusion, the distance separating the FRET pair increases, leading to a decrease in FRET efficiency. b) Probe mixing assay: two populations of liposomes are prepared, each labelled with one dye from a FRET pair. Upon liposome fusion, the dyes mix, resulting in FRET signal.

This assay is very sensitive to liposome aggregation, to lipid transfer, and to the direct environment surrounding the fluorescent dyes, such as the ionic strength, hydration, presence of divalent cations and chemically-active compounds.[88,93]

Further modification of this protocol allows distinguishing inner lipid leaflet mixing from outer lipid mixing. Treatment of the media surrounding the liposomes with sodium dithionite selectively eliminates the fluorescence of the lipids from the outer leaflet, as sodium dithionite does not penetrate lipid bilayers. Hence, the resulting changes in FRET signals will only be caused by the lipids present in the inner leaflet.

(ii) Content mixing assays

The most frequently used assay is based on the formation of a fluorescent terbium-dipicolinic acid complex (Tb-DPA). Both species are encapsulated in the hydrophilic cavities of separate liposomes. Upon formation of a fusion pore, a Tb^{3+}/DPA complex is formed, which is by order of magnitudes more fluorescent than free Tb^{3+}. Leakage during fusion can be assessed by adding EDTA as a quencher to the media surrounding the liposomes: the fluorescence of leaked Tb^{3+}/DPA complexes is quenched due to ligand exchange.

1.1.3 Summary and outlook

MicroRNAs (miRNAs) are a class of small, non-coding RNAs, and since their discovery, they have been recognized as key regulators of important biological mechanisms. More recently, they have emerged as new biomarkers for a range of diseases, as their expression profile has been linked with disease states, and they can be assayed with minimally invasive medical procedures. Therefore, the accurate analysis of their expression profile in biological fluids is of great importance. Conventional methods for miRNA detection include RT-qPCR, microarrays and next generation sequencing. However, extensive and cumbersome sample preparation, the need for internal controls and complicated data analysis lead to increased costs, errors, and time-to-results, which hurdles their deployment for routine clinical diagnostics. Biosensors have risen as an alternative method for miRNA detection, and nanotechnology has enabled the development of novel transduction mechanisms with increased sensitivity. This thesis explores the use of liposome fusion as signal transducer in a novel biosensing mechanism for the detection of miRNA. Liposome fusion can be triggered using DNA self-assembly, which has great potential for biosensing, as it is predictable, fast, and specific. As miRNAs are present in low quantities in analytical samples, sensitive assays are required; currently amplifications are performed using catalytic reactions mediated by enzymes to lower the biosensors' limit of detection. However, enzymes add cost, and increase the probability of non-specific detection. Here, liposomes will serve as signal amplifier as they can encapsulate a large quantity of reporter molecules.

1.2 Nanotechnology for cancer therapy: challenges and opportunities

1.2.1 Challenges in cancer chemotherapy

Chemotherapy is a conventional treatment for cancer, where cytotoxic drugs are injected systemically and kill cells that divide rapidly, which is one of the characteristics of cancer cells. The rapid progresses in pharmacological sciences have enabled a good understanding of the physicochemical properties of drug molecules as well as their interactions with cells, leading to numerous successful therapeutic strategies.[94] However, several shortcomings limit the efficacy of conventional chemotherapy for cancer treatment.

The majority of chemotherapeutic agents are hydrophobic and therefore suffer from poor solubility in aqueous media.[95] For systemic injection, such drugs must be formulated with additional solvents that improve their solubility. However, the residual solvents carry a non-specific cytotoxic effect causing undesired side effects to healthy tissues.

Following systemic administration, the drug needs to be transported across several compartments (distribution phase) before it reaches the target and delivers the therapeutic effect. During this complex journey from the administration site to the target, several events can affect the fate of the drug, decreasing its efficacy. In order to reach the tumour, the drug should follow this ideal transport route: distribution via the vascular compartment, transport across the microvascular wall, and transport through the interstitial compartment, reaching the tumour.[96,97] However, during this journey the drug is subject to unfavourable interactions that affect its ultimate performance: the transport of the drug to the tumour after systemic injection is regulated by an ensemble of obstacles collectively called biological barriers. A biological barrier designates the element of separation between the different compartments where the drug is distributed.[98] They include defined biological surfaces (epithelia, endothelia, various membranes), as well as the monocytes and macrophages of the mononuclear phagocyte system (MPS).[98] In the particular case of tumour-targeted treatments, biological barriers include, from the point of systemic injection: enzymatic degradation, non-specific binding of the drug to healthy tissues, uptake by the MPS, adverse osmotic pressure originating from the tumour, the tumour interstitium, and efflux pumps that will expel the drug from the tumour cells.[98] Successful negotiation of these barriers is a prerequisite for achieving efficient drug delivery at the tumour.

Drugs undergo enzymatic degradation, and are subsequently excreted via the main excretion sites, the kidney and the liver, yielding a reduced circulation time and limited bioavailability that decreases the total amount of drug reaching the tumour.[98] The drug can bind non-specifically to healthy tissues and serum proteins.[99,100] It is extremely difficult to engineer drugs that discriminate between healthy and cancerous cells, thus drugs will also target non-cancerous cells that divide rapidly (e.g. bone marrow cells and cells of the gastrointestinal tract).[100–102] In addition to unwanted side-effects, this lack of specificity of the drug also reduces the amount of drug reaching the tumour, reducing therapeutic efficacy. Moreover, sequestration by the activated monocytes and macrophages of the MPS affects a drug performance by decreasing the quantity of circulating drug and acting as a competitor to the intended target site.[98] Macrophages, called tumour associated macrophages (TAMs),[103] are also present in the tumour environment and can prevent the progression of the drug into the tumour by sequestrating it. There is a lack of a lymphatic drainage network at the centre of the tumour, creating an osmotic pressure coming from the tumour towards its exterior, which can slow down the diffusion of the drug within the tumour.[94,101,104–106]

The therapeutic index of a drug is the ratio of the amount of drug that causes toxicity to the amount of drug that induces the therapeutic effect. Evaluation of the therapeutic index allows a realistic representation of the margin between anticancer efficacy and toxicity to normal cells.[104] A higher therapeutic index is preferable to a lower one, since it indicates a high margin of safety for the drug dose that can be injected before it causes toxicity (Figure 8). Due to the systemic toxicity of anticancer drugs caused by their lack of specificity, their maximal dose that can be injected without causing deleterious side effects is in majority very low. As a consequence, the therapeutic index of anticancer drugs is also very close to 1.[104] Excessive drug levels cause toxicity, while insufficient dose causes suboptimal therapeutic effects. The therapeutic dose enables treating the disease with efficacy while remaining within the safety range.

The poor specificity of cytotoxic drugs in terms of both drug biodistribution and interaction with healthy cells, the limited dose that can be used in cancer treatment in order to reduce their systemic toxicity, as well as the uptake of the drug by macrophages, result in a decrease of the amount of drug reaching the tumour, reducing the therapeutic efficacy of the anticancer treatment.

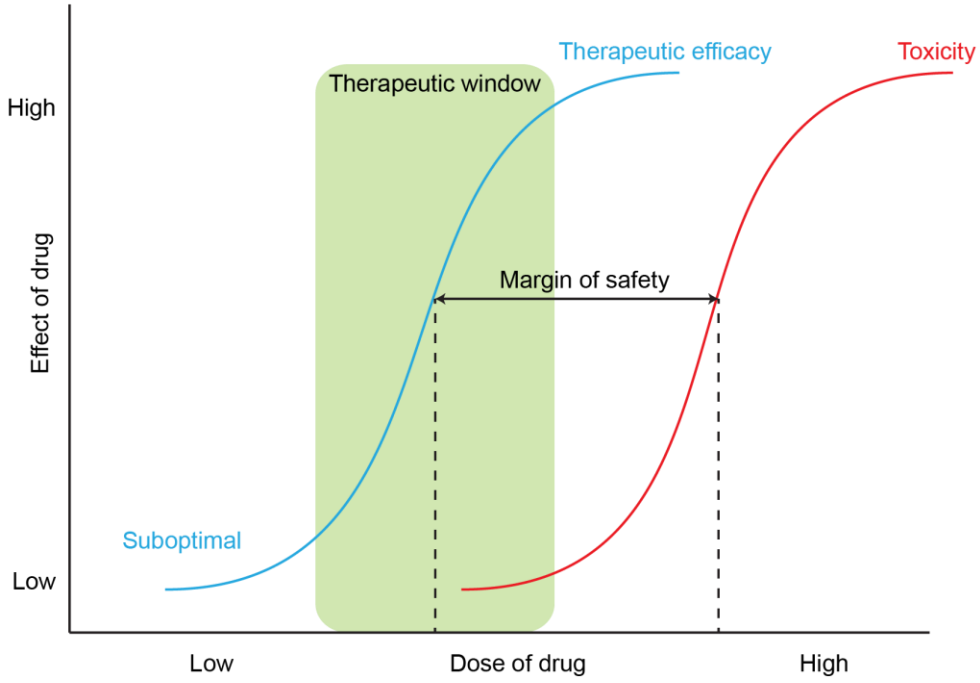

Figure 8. Illustration of the concepts of margin of safety, which delimits the zone between anticancer agent efficacy and toxicity, therapeutic window, and suboptimal dose.

Limited exposure of the tumour to the drug also induces multidrug resistance (MDR).[105,107] In order to counteract the effects of anticancer drugs, cancer cells implement an ensemble of mechanisms at the cellular level. MDR in tumours is mostly due to increased efflux pumps such as P-glycoprotein in the cell membrane,[95,108] responsible for the transport of the drug out of the cell. The exposure of cancer cells to the drug triggers the activation of the efflux pumps, making the cells resistant to the drug; if the cells are exposed to a suboptimal dose of drug, they will not all be killed and will develop drug resistance; such cells will then survive and multiply. This very often leads to a compromised clinical outcome for the patient.[100]

Finally, there is a need for individualized cancer chemotherapy.[109] The biological barriers presented above vary from patients to patients, also depending of the type and stage of cancer and evolving during the course of the therapy.[98] If the therapeutic course is not optimized towards negotiating each individual biological barriers, this exposes a risk related to non-optimal use of the therapeutic, and appearance of deleterious side effects or development of MDR. The margin of safety of chemotherapeutics is small, and requires careful monitoring of the therapy course. Current techniques involve the measurement of the chemotherapeutic concentration in the biological fluids; however, they are of limited usefulness as therapeutic indexes for individual patients are unknown. There is a need for strategies that can provide an understanding of therapeutic efficacy for each given patient and tumour, enabling personalized therapy.

1.2.2 Cancer treatment at the nanoscale

Nanotechnology is a rapidly progressing field which is contributing to solve several limitations of conventional drugs by developing advanced delivery systems. Nanotechnology can provide solutions to improve drug solubility, negotiate biological barriers to increase drug bioavailability, provide opportunities for targeting therapeutics and mediating controlled drug release, and enable personalized therapy.

This thesis focuses on addressing a novel multifunctional platform for cancer therapy, called quantum rattle (QR), towards a systemically injected anticancer agent. QR is composed of a mesoporous silica shell, encapsulating gold nanoparticles and gold nanoclusters. The structure and properties of QR were first published in 2015 in a study by Hembury *et al*.[110]

1.2.2.1 Nanocarriers improve drug solubility

Most anticancer drugs show poor aqueous solubility, decreasing their bioavailability and leading to suboptimal therapeutic dose at the tumour level.[95] Commercial formulations using adjuvant solvents that increase drug solubility carry elevated toxicity.

Several nano drug encapsulation systems have been designed for transporting hydrophobic drugs *in vivo*. Nanovectors typically present two surfaces, one in contact with the outer environment, the other one in contact with the drug, protecting it from the exterior. The outer surface is either naturally hydrophilic or rendered hydrophilic by functionalization, enabling solubilisation in physiological fluids.

Paclitaxel is an anticancer drug, which is poorly soluble in water.[101] It has been successfully encapsulated in various nanostructures, such as albumin (Abraxane) and liposomes.[111] Compared to the free administration form of the same drug, Taxol, Abraxane showed reduced acute toxicity and longer circulation time.[95] Abraxane has been approved by the US Food and Drug Administration (FDA) and is currently benefiting cancer patients.[101]

1.2.2.2 Nanocarriers increase specificity by targeting

Drug specificity can be enhanced using nanoparticle carriers either by passive targeting, which exploits the enhanced permeability and retention (EPR) effect or by active targeting by functionalization with recognition moieties such as antibodies, peptides, small molecules or aptamers.

Tumour blood vessels are functionally and structurally abnormal.[102,112–114] They present an increased permeability, which manifests through the formation of fenestrations.[101,115]

Fenestrations are small pores in endothelial cells lining the interior surface of blood vessels.[102] In general for tumour fenestrations, the pore cut-off size lies between 400 nm and 600 μm,[116,117] whereas for normal blood vessels the pores are just 2 to 6 nm in size.[101] This variability provides an opportunity for tumour-specific delivery of therapeutic agent, that nanotechnology can exploit.

Indeed, nanoparticles of 10 nm to a few hundreds of nm are able to extravasate through the fenestrations of the blood vessels supplying tumours while they are unable to penetrate within healthy tissues, since typically the small dimensions of the fenestrations of the endothelial cells (up to 6 nm) do not allow it.[101,118] This selective accumulation of systemically injected nanoparticles in tumour tissue over time constitutes the enhanced permeability and retention (EPR) effect, which allows nanoparticles to accumulate preferentially at the tumour site and improves the therapeutic index through their biodistribution. Compared to the administration of free drug, nanoparticles selectively accumulate in tumours via the EPR effect (Figure 9). Unlike nanoparticles, "small" chemotherapeutic agents are not retained in tumours because of their rapid excretion to the bloodstream.[119] Moreover, small molecules do not exhibit the same biodistribution as nanoparticles, since their size allows them to extravasate from large or small fenestrations alike, so they do not specifically accumulate in tumours via the EPR effect. A long circulation time is a prerequisite for nanoparticles' accumulation in tumours via the EPR effect, and strategies implemented in nanotechnology to allow this will be discussed later in this Chapter.[120]

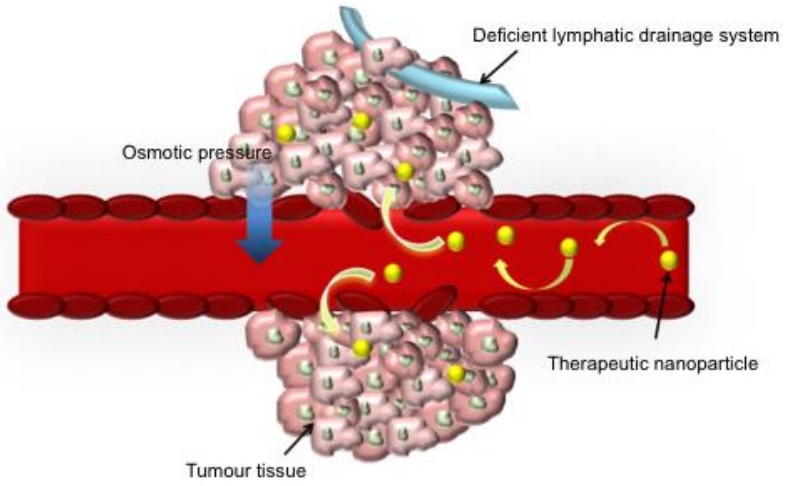

Figure 9. Nanoparticles selectively accumulate in tumours via the EPR effect. The tumour's leaky vasculature enables the nanoparticles to diffuse through the vascular endothelium to the tumour. The diffusion of the nanoparticles is slowed down by the osmotic pressure created by a lack of lymphatic drainage at the centre of the tumour. Adapted from Dreaden *et al*.[121]

The EPR effect has clearly been demonstrated in many tumours in animal models.[96,116,122] Amongst many nanoformulations of chemotherapeutic agents, the encapsulation of paclitaxel in micelles was shown to accumulate in tumours much better than its commercial formulation Taxol, resulting in a 25-fold improved drug accumulation in tumour and decrease in the side effects.[123,124]

However, the EPR effect is not universal: the porosity of the vasculature varies depending on the tumour type, the stage of the tumour, and microenvironment, as well as between different patients,[125] therefore prompting the need for alternative targeting strategies.[126] The accumulation of the nanoparticles in tumour tissue will also depend on osmotic pressure created in the tumour centre due to the lack of lymphatic drainage,[94,101,115,127] potentially slowing the diffusion of the nanoparticles in the tumour, but also allowing the retention of the nanoparticles inside the tumour.[101,115,128] Moreover, resident immune cells populate the microenvironment of the tumours (tumour associated macrophages, TAMs), which can potentially capture the nanoparticles while they are diffusing in the tumour interstitium.

Active targeting strategies involve ligands that will specifically bind to receptors expressed on the cell surface of interest, sometimes inducing receptor-mediated endocytosis and drug release inside the cell.[125] These strategies require significant overexpression of the target receptor in cancerous cells relative to healthy cells (10^4–10^5-fold copies per cell), so that the recognition event is specific to cancer cells.[107,125] Moieties used for active targeting include antibodies, peptides, small molecules, aptamers. Anti-tumour antibodies can be used as carriers for the chemotherapeutic drug (immunovectorized drugs), however, this strategy was not extremely successful in cancer therapy, with only one injected molecule in 1,000-100,000 reaching its target, inducing undesirable side effects.[98,129]

Targeting of nanovectors by functionalization with recognition molecules provides advantages over immunovectorized drugs. By their nature, nanovectors allow for multiple functionalizations, owing to the extensive surface areas and orthogonal conjugation strategies.[130] Therefore several recognizing moieties can be added to the nanovector, improving the targeting efficiency by multiplying the type of recognition events, in turn increasing the probability of recognition, or by increasing the amount of recognition molecules, increasing the number of recognition complexes formed hence the binding to the target. Moreover, typically a nanovector encapsulates large amounts of drug, compared to immunotargeted drugs, since it allows to convey a higher dose of drug to the tumour.[130] This is important for the delivery of the optimal therapeutic dose to the tumour, in order to reduce the risk of developing MDR.

However, the increased specificity is obtained at the expense of added complexity to the synthesis of the conjugated nanoparticles and increased risk of biological adverse reaction to the targeting agent, especially in the case of antibody-based targeting.[130] Furthermore, for solid tumours, strong binding of the targeting agent can prevent the penetration of the nanocarrier into the tissue.[118] Since many chemotherapeutic agents need to be released in the cytoplasm of the cancer cells to attain a therapeutic effect, lack of internalisation reduces the therapeutic effect.[118,131] Therefore, when designing a nanovector with targeting abilities, a balance must be found between high affinity for the target, which could prevent internalization, and low affinity, which would affect specificity. Without increasing affinity, specificity can be increased through multivalent binding effects, for which nanoparticles are at an advantage since they allow multiple functionalizations.[118]

1.2.2.3 Nanocarriers provide drug stabilization and increase circulation time

In order to deliver drugs to the target, the drug must circulate in the bloodstream long enough to reach it, without being removed by active phagocytosis of the mononuclear phagocyte system (MPS) and renal clearance.[120,132] After injection, the capture of molecules or particles by the MPS depends notably on their size and surface characteristics.[120,133]

Nanoparticles, differently from molecules, have a tailorable size and shape, which can be controlled over a wide range, and optimized for biodistribution. The size of nanoparticles should be large enough to exploit the selectivity offered by the EPR effect, but small enough to escape capture from the circulating and resident macrophages of the MPS, such as in the liver and the spleen.[120] Kupffer cells are specialized resident macrophages of the liver. They are located in the liver sinusoids, which are a typical blood vessel structure of the liver, optimized for filtering and lined with sinusoidal endothelial cells.[134] Kupffer cells participate in the response of the liver to the presence of toxic compounds, such as anticancer agents, and act as a filter, removing toxic agents from the blood.[134] Adsorption of opsonins (plasma proteins) on particles or molecules takes place in the blood circulation and causes their recognition by the macrophages, followed by phagocytosis and elimination. If the particle is non-degradable, then it is immobilized and accumulated in the organs of the MPS (liver and spleen), potentially inducing toxicity and associated side effects.[135] Without the presence of opsonins on the surface of the nanoparticles, the macrophages would not be able to bind to or recognize the nanoparticles.[135] Figure 10 illustrates the process of opsonization. The size of particles has been shown to have a strong influence on their opsonization.[136] Smaller particles are less subject to phagocytosis, and it has been suggested that it could be due to the increased curvature of the surface, preventing the interaction with the phagocytosis system components.[137]

Additionally, the surface characteristics of the nanoparticles such as charge and lipophilicity control their uptake and circulation time.[120] Surface charge of the particles has been shown to influence their rate of phagocytosis. It has been reported that negatively charged particles showed a lower uptake by the phagocytes than positively charged particles, due to a reduced interaction with negatively charged cell membranes.[136,138] Other studies in appearance contradictory suggested that negatively charged particles were in fact more prone to bind to the cationic sites on the macrophages' cell membranes therefore resulted in a higher capture rate than neutral particles or particles presenting a low positive charge on their surface.[136] In fact, the absolute value of the zeta potential of the particles may be the most important factor for phagocytosis of nanoparticles, with an increase of zeta potential inducing an increased phagocytosis of the particles.[136] The surface's hydrophobicity is a key parameter influencing the uptake of the nanoparticles by the macrophages of the MPS. Hydrophobic particles are preferentially tagged by the plasma proteins, inducing their uptake by the macrophages.[135,136]

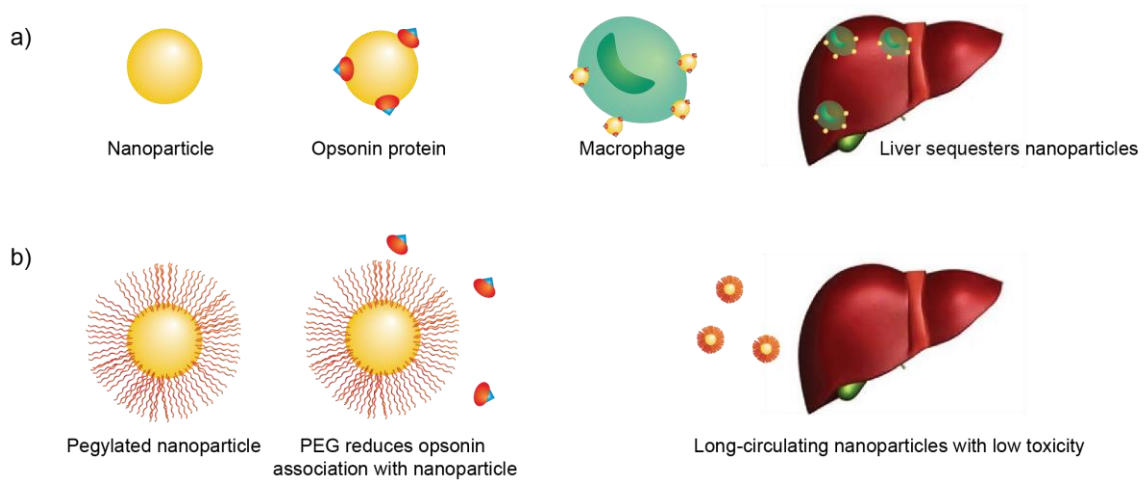

Figure 10. Poly(ethylene glycol) coating reduces opsonization events and therefore decreases the capture of PEG-coated nanoparticles by the macrophages of the MPS. a) Non-pegylated nanoparticles are conjugated with opsonins, which are plasma proteins. This triggers the recruitment of macrophages from the MPS, followed by phagocytosis and elimination of the nanoparticles. Kupffer cells, resident macrophages in the liver, can also immobilize opsonins-tagged nanoparticles. b) Pegylated nanoparticles present a neutral, hydrophilic and sterically bulky surface, making the opsonization process less frequent. Therefore the PEGylated particles are not sequestered by the macrophages and their circulation time is increased compared to non-PEGylated particles. Adapted from Jokerst *et al*.[139]

Surface functionalization strategies have been implemented in order to confer longer circulating time to the nanoparticles. In particular, many nanoparticles have been coated with poly(ethylene glycol) (PEG) and its derivatives.[132,139] PEG is a neutral, hydrophilic polymer of various chain lengths. The PEG coating acts as a protective layer that reduces the amount of opsonization via

steric hindrance, as well as neutralises the surface charge and confers hydrophilic character to the particles (Figure 10).

However, there is a fine line between providing surface functionalization imparting escape from the MPS, and interaction with the target cell surface. Poly(ethylene glycol), while granting MPS escape, could also reduce interaction with cell surface,[125] leading to fewer internalisation of the particles in the tumour, hence reducing the dose diffusing into the tumour. This would reduce therapeutic efficacy and increase the risk of multidrug drug resistance, as previously described.

1.2.2.4 Nanocarriers increase specificity via triggered release of the therapeutic

Stimulus-triggered drug delivery for the treatment of cancer at the nanoscale addresses the need for higher specificity of therapy, which is of foremost importance when using highly toxic drug like anti-cancer agents [140]. When an external stimulus is applied, both the time and location of the drug delivery are controlled; therefore this event only occurs at a determined place and time, providing greater specificity.

Furthermore, a therapeutic needs to overcome the tumour interstitium biological barrier. Indeed, diffusion of particles depends on their size, charge and configuration,[141] and the small chemotherapeutic agents diffuse more easily and uniformly within the tumour than the more hindered nanoparticles carriers.[101,141] Indeed, even if 100-nm liposomes can extravasate from the blood vessels to reach the tumour, their distribution pattern can be extremely heterogeneous.[106] The size of nanoparticles also limits their diffusion in the tumour to one or two cell layers.[106] Triggering the release of the anticancer agent from the particles, once they reached the site of action will facilitate its uniform diffusion throughout the tumour interstitium. Therefore, as summarized in Table 1, a variety of 'smart' nanoparticles have been designed to release their drug payload after receiving a stimulus to facilitate drug diffusion into the tumour.[101,115] Either environmental triggers (self-triggers) or external triggers can stimulate drug release.

Self-triggered release requires a change of the microenvironment at the site of action (pH, redox conditions, temperature, presence of a specific enzyme)[142] to induce changes of the nanocarrier, which in turn triggers the release of the cargo. For instance, since the microenvironment of a tumour is more acidic than normal tissues,[143,144] a variety of pH-responsive systems have been developed to increase the drug delivery at the tumour, such as pH-sensitive liposomes, designed to be stable at a physiological pH of 7.4 but degrading and releasing the drug when the pH is less than the physiological value, like in tumour cells.[144]

Wong *et al* developed a dual-stage therapeutic delivery system that takes advantage of the high concentrations of matrix metalloproteinases (MMPs) in tumours.[145] The 100 nm nanoparticles were composed of a gelatine core, and the surface was covered with 10 nm quantum dots. The gelatine nanoparticles passively targeted the tumours via the EPR effect due to their size and were efficiently degraded at the site of action by MMP-2 and MMP-9, releasing the small quantum dots. The shrinkage of the particles from 100 nm to 10 nm was designed to reduce their risk of steric hindrance when the particles diffuse in the tumour interstitium. Ultimately, the quantum dots, here used for the proof-of-principle due to their inherent imaging capacities, will need to be replaced by therapeutic agents encapsulated in similarly sized vectors. Variations in the level of MMPs can occur in different tumour types and individual, and this could lead to inconsistent behaviour of such a treatment. However, this system has the potential for personalized therapy, since it can be customized to account for the various levels of MMPs measured in individual patients (*e.g.* by increasing or decreasing the crosslinking of the gelatine network, making it more or less sensitive to protease degradation).

Triggers can also originate from external sources such as light, magnetic field and ultrasounds.[142] Externally-triggered drug release provides great control over the time and localisation of the desired effect, since the drug is only released after application of the trigger, which can be controlled both spatially and temporally. This increases the specificity of the therapy and reduces unwanted side effects for healthy tissues, also enhancing diffusion of the small drug in the tumour compared to the more hindered nanoparticle.

Ultrasound can trigger the release of doxorubicin, an anticancer drug, from micelles.[146] Rapoport *et al* showed that drug uptake by cells was enhanced through ultrasound-triggered delivery.[146] The application of ultrasounds created an increased permeability of the targeted cells, and destabilized the micelles at the site of action, causing a burst release of their cargo.[147] Drug resistance induced by a sub-therapeutic dose delivered to the tumour could be overcome by this approach. Ultrasounds are also non-invasive, and can penetrate deep into the tissues.[148]

Several systems use light as a stimulus (Table 1), but not all wavelengths are ideal for *in vivo* applications: UV light causes tissue damages, and visible light has a very low penetration depth due to the high absorption of tissues in these wavelengths range. A more useful wavelength range is the NIR light in the “bio-window” (650-900 nm), which is less absorbed by tissues (Figure 11).[121] A major system using NIR light for triggering its therapeutic effect is gold nanoshells.[149] The irradiation of the gold nanoshells by NIR light causes a local hyperthermia in their vicinity, and ultimately the death of the tumour cells.

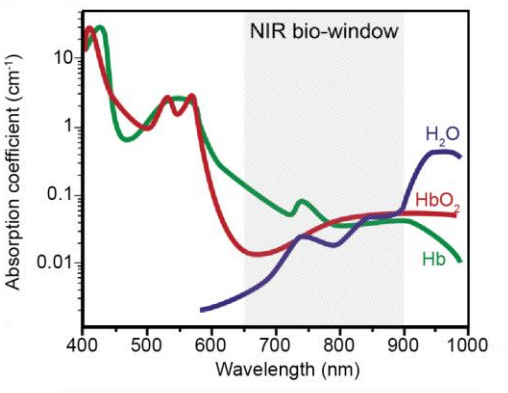

Figure 11. In the NIR bio-window (650-900 nm), the absorption of light from physiological fluids such as oxy/deoxyhemoglobin and water is minimal allowing maximal penetration depths. Modified from Dreaden *et al*.[121]

Variation of temperature has also been used as a stimulus for triggered drug-delivery. Notably, poly(N-isopropylacrylamide) (pNIPAM) is a temperature-responsive polymer that has attracted great interest over the past years.[150–152] This polymer can undergo a reversible structural transition characterized by a lower critical solution temperature (LCST). Below the LCST, the structure of the polymer is solvated random coils, and above the LCST, the polymer becomes insoluble in aqueous media and forms tightly packed globular particles.[152] Effectively, the LCST switch can modulate polymer hydrophobicity/lipophilicity.[153] This switch has been exploited for triggered drug delivery: You *et al* reported the synthesis of pNIPAM-modified mesoporous silica nanospheres, with a drug release profile controlled by thermal packing modification of the polymer.[154]

Table 1. Various systems used for triggered drug delivery. MSN = mesoporous silica nanoparticles; NP = nanoparticles.

System	Stimulus	Trigger	Gating mechanism	Ref	Advantages / Drawbacks
MSN	Light	UV light (λ=350 nm)	Cyclodextrin-azobenzene derivative (photocleavable linker)	155	Irreversible
MSN	Light	UV light (λ=350 nm)	Azobenzene derivative	156	Reversible
MSN	Light	UV light (λ=250 nm)	Coumarin dimers	157	Reversible
Metallic NP	Light	Gold Nanocapsules	N/A	158	Sustained therapeutic effect
MSN	Redox	S-S bond	CdS capping molecule	159	Irreversible
MSN	Redox	S-S bond	Gold nanoparticles capping agent	160	Irreversible
MSN	Redox	Oxidation of a chemical moiety	Switchable rotaxane molecules	161	Synthetic complexity of rotaxane
Liposomes	pH	Destabilisation of the bilayer	N/A	162	Irreversible
Micelles	Ultrasound	Destabilisation of micelles	N/A	148	Enhanced drug intake/ Irreversible
MSN	Temperature	Change in polymer packing (coil to globule)	Thermoresponsive polymer (PNIPAM) grafted to the silica surface	154	Simple and reversible

1.2.2.5 Nanocarriers address multidrug resistance through combination therapy

Tumour multidrug resistance is a major issue in chemotherapy.[118,163] Multidrug resistance phenotype results in the efflux of toxic compounds out of the cell by molecular or ionic pumps. When the tumour is exposed to a suboptimal therapeutic dose, some cancer cells may survive, expressing the MDR phenotype, and as the tumour redevelops it becomes resistant to chemotherapeutic treatment. Therefore in order to avoid the development of multidrug resistance, the therapeutic dose should be delivered to every cell within the tumour.

Drug delivery nanosystems typically encapsulate large quantities of drug and deliver it to the tumour, exposing the tumour to a high dose of therapeutic in a short time frame. This delivery strategy induces a higher mortality in the tumour and is aimed at reducing the risk of MDR.

Combination therapy contributes to mitigate multidrug resistance by the synergistic action of the combined therapies.[164] Drugs with different mechanism of action can be combined, allowing additive and synergistic therapeutic effects on the tumour, while remaining within the safe therapeutic dose range for each agent.[165]

Currently combination of various chemotherapeutic drugs is a clinical standard.[165] However, very often in the case of combination therapy, the synergistic therapeutic results obtained *in vitro* do not translate *in vivo* to an enhancement of cancer cells killing, and sometimes even induce higher toxicity.[164] Different drugs have different pharmacokinetics: after injection, drugs undergo different fates and heterogeneous biodistribution. Therefore there is a need for more control on the delivery of multiple agents to the tumour. Nanocarriers can achieve multifunctionality by incorporating different individual therapeutic agents. By encapsulating multiple agents in the same structure, they allow the synchronized delivery of the anticancer agents to the tumour.

Combinations of anticancer drugs have been successfully encapsulated in various types of nanoparticles.[164] Cytarabine and daunorubicin is a standard drug combination used in the treatment of leukaemia. However, when co-delivered, these drugs need to be delivered to the tumour at an ideal ratio. Non-ideal ratios between these drugs can lead to antagonist effects with a loss of therapeutic activity.[166] Even if injected at their ideal ratio, when distributing in the systemic circulation unpredictable biological events can cause circulating drug ratios to change. Their encapsulation in a liposome-based nanocarrier (CPX-351) allowed their co-delivery to tumour cells at the optimal

therapeutic ratio, providing a dramatic increase in the therapeutic index compared to the free-drug co-administration.[166] Based on these promising results, CPX-351 is currently in phase II of clinical trial.[164]

Photothermal therapy using gold nanoshells/nanoparticles induces local hyperthermia that kills cancerous cells selectively due to laser irradiation at the tumour site triggering gold-mediated hyperthermia.[121] Moreover, the elevated temperature increases membrane permeability and induces blood vessel dilation,[167] enhancing the efficacy of cytotoxic agents.[168] Therefore, combining PTT with chemotherapy should provide synergistic therapeutic effect.[163,167,169] Liu *et al* developed a system composed of gold nanoshells seeded on mesoporous silica nanoparticles loaded with doxorubicin.[163] Very interestingly, they demonstrated a synergistic therapeutic effect of doxorubicin and PTT *in vitro*. In all these systems, the efficient co-delivery of PTT and chemotherapy remains a challenge. For Liu *et al,* the release of doxorubicin was not controlled and relied on its passive diffusion through the defects in the gold nanoshell surrounding the mesoporous silica rattles.[163] They observed a burst release of 30 % of the loaded drug in the first hour in phosphate buffer saline (PBS) at pH 7.4; therefore the drug would be released as soon as the carrier is injected in the systemic circulation, which is undesirable for maintaining low toxicity levels. Park *et al* used biodegradable polymer–metal multilayer half-shell nanoparticles; they showed that drug release was enhanced when the particles were irradiated by a laser emitting in the NIR.[167] However, the drug diffused passively from the particle, without any control over its release.

1.2.3 Nanoparticles for cancer diagnostics and imaging

In cancer diagnostics, there is a need for non-invasive techniques to image the presence of a tumour in the patient, giving information about its size, geometry, and its localisation. This requires a technique with high sensitivity and resolution, that would ideally be cost-effective, and comfortable for the patients.[170] The current imaging techniques include nuclear imaging (positron emission tomography (PET) and single photon emission computed tomography (SPECT)), X-ray computed tomography (CT), magnetic resonance imaging (MRI), optical imaging, and ultrasound imaging (US imaging).[171] Nanotechnology can provide useful agents to supplement and enhance these imaging techniques.

Contrast agents

Contrast agents enhance image contrast and improve the visibility of features that would have been otherwise difficult to detect. Nanoparticles as contrast agents are currently receiving a lot of attention, since they provide greater bioavailability and reduced toxicity compared to conventional chemical contrast agents.[172] The range of nanoparticles designed for use as contrast agents is detailed in Table 2.

For CT imaging, conventional contrast agents include barium sulphate suspension, and iodine-based compounds. These compounds have a very low retention rate and lack tissue specificity.[171] Using poly(ethylene glycol) (PEG)-coated gold nanoparticles, Kim *et al* demonstrated that they could provide longer circulation time, together with a high contrast between tumour and normal tissues.[173]

The current contrast agents used for MRI are mostly gadolinium-based, and they present a short half-life in circulation. Super-paramagnetic iron oxide nanoparticles (SPIONs) offer enhanced relaxation properties and increased biocompatibility.[171]

Table 2. Examples of nanoparticles that can be used as contrast agents for medical imaging.

Imaging mode	Contrast agent	Example
CT	Gold nanorod	[174]
	Gold NP	[173]
	Fullerenes and carbon nanotubes	[175]
MRI	Iron Oxide	[176]
	Alloyed NP ($CoFe_2O_4$, $MnFeO_4$, $NiFe_2O_4$)	[177]
	Hollow MnO	[178]
Ultrasound	Nanosized bubble	[171]
	Liposomes	[179]
	Polylactic nanobubbles	[180]
	Silica	[181]
	Iron oxide	[182]
Photoacoustic	Gold or Silver NP	[171]
	Carbon nanotubes	[171]

Optical imaging

Nanotechnology has enabled great breakthrough in particular in the field of optical imaging.[171] The visible light-range has a low tissue penetration depth, and in addition, light scattering and tissue autofluorescence arise in the visible light-range.[183] As seen previously, these effects are minimized when using light in the NIR range instead. Therefore fluorescent probes tuned for imaging in the NIR window are necessary. Luminescent quantum dots (QDs) and metal nanoparticles/nanoclusters are a promising alternative to conventional organic dyes for fluorescence-based applications. They improve detection limits and pave the way for early diagnosis of tumours.

Fluorescent quantum dots (QDs) are semiconductor crystals with intense and stable fluorescence. In a semiconductor nanocrystal, absorption of a photon whose energy is higher than the energy bandgap leads to the formation of a bound electron-hole pair: the exciton. Strong quantum-size confinement arises when particle sizes are smaller than the exciton Bohr radius. Due to quantum confinement, the band gap increases as the size of the nanocrystal decreases, therefore the optical properties of the quantum dots, such as their absorption spectrum and their fluorescence emission is strongly dependent on their size.

The optical and electronic properties of quantum dots are superior to that of organic fluorophores for live cell imaging. While organic fluorophores have a narrow excitation spectrum, QDs can be excited at any wavelength from UV to NIR, allowing a great flexibility in imaging conditions.[184] Organic fluorophores also have broad emission spectra, which limits the number of fluorescent probes that can be detected simultaneously, since their emission signals overlap. On the contrary, QDs emission spectra are narrow and size- and composition-tunable, allowing emission from visible to infrared wavelengths; they are therefore well-suited for multiplexing. QDs are very bright when excited, with a high quantum yield.[185] Moreover, QDs have a higher photobleaching threshold and are more stable than organic fluorophores, allowing more reliable monitoring of biological systems for extended periods of time.[186,187] QDs can be conjugated with biomolecules, such as peptides and antibodies, for *in vivo* detection and imaging of specific targets.[185] Their higher brightness compared to organic dyes allows the detection of analytes in small concentrations, such as detection of low copy-number cancer markers.[187]

However, the use of QDs for biological imaging is not without challenges; the heavy metals contained in QDs are toxic and severely limit their *in vivo* applications.[188]

Colloidal gold nanoparticles exhibit very intense extinction peak due to Surface Plasmon Resonance (SPR),[189] resulting from the collective oscillation of the conduction electrons in response to optical excitation.[190,191] The position of this peak is tunable, depending on the size, shape, structure (solid or hollow) of the particles and interparticle distance, as well as the dielectric properties of surrounding media.[189,192,193] For gold nanospheres of about 50 nm diameter the surface Plasmon resonance peak is located at 520 nm.[192] The position of the peak for particles of simple morphology can be predicted by using Mie's theory to solve Maxwell's electromagnetic field equations.[192] Unlike dyes, gold nanoparticles are photostable and allow prolonged imaging.[190] They exhibit a very intense extinction, making them more sensitive than dyes.[190,194]

Gold nanoshells are spherical particles composed of a dielectric core covered by a thin gold shell. They present very interesting properties for use in cancer imaging and treatment based on gold-mediated photothermal therapy. The gold nanoshells absorption to scattering ratio can be tuned by varying the dimensions of the core and the shell.[158] It is therefore possible to design gold nanoshells for imaging and photothermal therapy-based applications, where scattering provides features for imaging and absorption facilitate photothermal therapy. Moreover, the location of the extinction peak within the spectrum is dependent upon the ratio of the core radius to the shell thickness. It can be red-shifted to the NIR bio-window where the penetration depth for the light in the tissues is much higher and where there is less background autofluorescence.[121,195]

Gold nanoparticles and nanoshells can exploit the EPR effect to selectively accumulate in tumours.[121] A variety of sizes can be synthesized to maximize the tumour uptake.[192] The ease of conjugation of the gold nanoparticles' surface enables the multifunctionality of these particles; additional functionalities such as targeting and antifouling can be added via simple surface functionalization chemistry.[121]

A cut-off in the optical properties of gold metal nanoparticles is reached when their size falls below 2 nm.[196] These ultrasmall gold nanoparticles, often called gold nanoclusters and containing a few tens to a few hundreds of atoms,[197] exhibit multiple absorption peaks instead of the single broad Surface-Plasmon peak.[196,198,199] They display molecule-like properties, such as HOMO-LUMO transitions.[196,198,199] Their strong photoluminescence, combined with good photostability, large Stokes shift and high emission rate make them good candidates for optical imaging.[200,201] Both their emission and absorption can belong to the NIR region of the spectra. Wu *et al* reported the use of

ultrasmall gold nanoclusters for NIR tumour imaging *in vivo*, proving the great potential of nanoclusters for fluorescent imaging.[194]

Despite the great advances in the synthetic strategies for gold-thiolated nanoclusters (Au(SR)), many challenges remain, such as the unambiguous determination of the stoichiometry of the cluster and its geometric structure.[196,202] A critical challenge to meet is to obtain monodispersed crystals, in order to attribute meaningful properties to them.[196] Some of the most stable stoichiometries of gold-thiolate nanoclusters (denoted as Au_nSR_m) have been characterized.[196–198,203] Notably, Zhu *et al* determined the crystal structure of a $Au_{25}(SR)_{18}$ cluster, which is based on a centred icosahedral Au_{13} core, capped by an exterior shell composed of the remaining twelve Au atoms, and the whole cluster is encapsulated by eighteen thiolate ligands.[202]

The available crystal structure of the $Au_{25}(SR)_{18}$ cluster enabled a full analysis of its electronic structure and its absorption spectrum by density function theory (DFT) (Figure 12).[196,198]

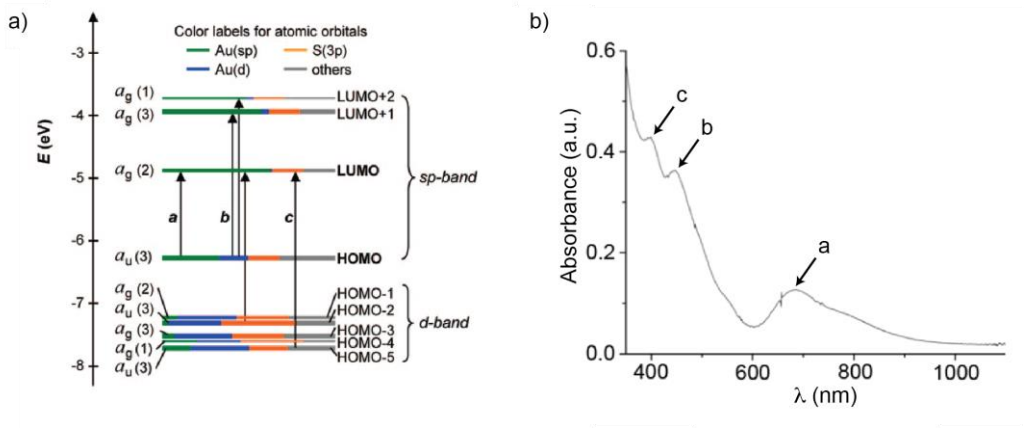

Figure 12. a) Kohn-Sham orbital level diagram for $Au_{25}(SH)_{18}^-$. b) Peak assignment for the UV-Vis absorption spectrum of $Au_{25}(SR)_{18}$ gold nanoclusters in toluene. Adapted with permission from M. Zhu; C. M. Aikens; F. J. Hollander; G. C. Schatz; R. Jin. *J. Am. Chem. Soc.* 2008, **130**, 5883–5885. Copyright 2008 American Chemical Society.

A better understanding of the origin of photoluminescence from the clusters could provide insights to optimize it for optical imaging applications.[194,198] In general, there are two main sources for the fluorescence of metal nanoclusters: the metal core (e.g., a manifestation of intrinsic quantization effects) and the particle surface, because of the interaction of the metal core and surface ligands (non-fluorescent ligands).[196,204] Wu *et al* showed that the fluorescence of $Au_{25}(SR)_{18}$ nanoclusters was greatly influenced by the nature of the surface ligand.[204] More specifically, the ligand enhanced the fluorescence by

direct charge transfer with the metal core through Au-S bonds or by direct donation of delocalized electrons from electron rich atom or groups (e.g. NH_2, OH, COOH). This observation enables new strategies to maximize the fluorescence of gold nanoclusters, through specially designed gold-coating ligands with electron donating capacities. Maximizing the fluorescence ultimately results in better imaging properties.

The inherent instability, chemical reactivity and tendency for agglomeration of gold nanoclusters is impeding their widespread use.[201] In general, the reduction of gold in aqueous solutions results in the formation of nanoparticles instead of nanoclusters due to the tendency of the hydrophobic nanoclusters to aggregate in aqueous media.[200] Moreover, the choice of the capping ligand is crucial since it can affect the nanoclusters emission properties.[204] Thiol-containing molecules, such as glutathione have been commonly used to stabilize nanoclusters due to the strong interaction between the thiols and the gold. These nanoclusters can fluoresce in the blue to NIR regions of the spectrum; however, their quantum yield is in general low (0.001 % - 0.1 %).[200] Recently Xie *et al* developed a synthesis method for the production of red-emitting gold nanoclusters with a quantum yield of 6 % using bovine serum albumin (BSA) as a template for the formation of the clusters.[205] Upon the addition of Au(III) ions to an aqueous BSA solution, the protein molecules entrapped the ions. The sequestered ions underwent *in situ* reduction by the BSA when the pH of the media was adjusted to 12. BSA served as a template for the formation on Au_{25} gold nanoclusters. BSA-stabilized gold nanoclusters were recently used for *in vivo* fluorescence imaging.[194] This study showed that the fluorescence of the gold nanoclusters was well-distinguishable from the background, with a maximum of emission at 710 nm. Encapsulating the clusters in silica has also granted enhanced stability and functionality. The silica surface can be further functionalised without affecting the emission properties of the gold nanoclusters, and gives a hydrophilic surface for aqueous solubilisation.[201]

Multi-modal imaging

Each imaging technique has advantages and limitations, in terms of sensitivity, resolution, data acquisition time and complexity, making it difficult to obtain accurate and reliable information at the disease site.[171,206] To compensate for this problem, the combination of contrast agents for multiple imaging modalities into a single vector has received great attention. Multi-modal imaging has potential for improving the treatment of cancer patients, by providing more accurate and reliable detection of cancer lesions.[206] Bifunctional nanoparticles combining an MRI contrast agent (SPIONs) and

fluorescent optical imaging agents allowed to combine the high spatial resolution of MRI with the elevated sensitivity of fluorescent optical imaging.[171,207]

Designing these bifunctional nanoparticles requires bestowing them good magnetic and fluorescent properties.[142] Indeed, the combination of magnetism and fluorescence often results in a strong fluorescence quenching.[208,209] The addition of protective layers that space the magnetic and fluorescent agents avoided fluorescence quenching.[210] Embedding both imaging agent in protective silica shells has also been studied; and this ensured that both agents retained their optimal imaging properties.[142]

1.2.4 Combining imaging and therapy: theranostics

Nanosystems with a single functionality have limited utility; multiple systems are required to treat, detect, and monitor cancer.[211] The systemic injection of multiple systems often results in variable individual biodistribution, and therefore poor control on the coordinated actions of each modality. When all the components are integrated into the same carrier, they are expected to behave similarly towards the various biological barriers. Therefore theranostics systems, integrating multiple components into the same device to provide diagnostic and therapeutic functions, carry a great potential for cancer therapy.[167,207,212–216] Theranostics systems allow simultaneous, real-time and non-invasive monitoring of biological responses to the therapy (Figure 13).[215]

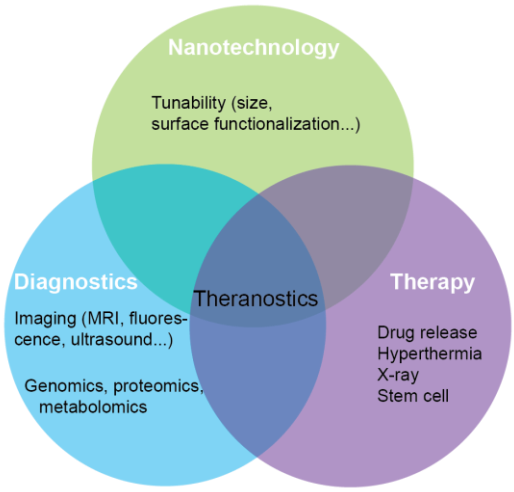

Figure 13. Theranostics systems combine diagnostic and therapeutic modalities at the nanoscale.

The combination of imaging and therapy allows the labelling of targeted sites, monitoring the *in vivo* biodistribution of therapeutic agents, and evaluating the results of the therapy, therefore paving the way for personalized cancer therapy. Based on this

method, the characteristics of nanocarriers can be adapted for each patient according to the individual response to the treatment. For instance, targeting modalities can be incorporated on the nanocarriers for more efficient targeting of the tumour, or the size of the carrier can be tuned, in order to take into account the variability in the fenestration size between lesions and patients.

When both drug and imaging modality are incorporated in the same structure, it is expected that they will share the same fate during their *in vivo* distribution. This theory is at the basis of the indirect validation of drug targeting to tumours. This technique was demonstrated *in vivo* by de Smet *et al* using temperature sensitive liposomes encapsulating doxorubicin and gadolinium-based MRI contrast agent.[217] They showed that the *in vivo* release of doxorubicin could be monitored in real time by MRI imaging.

Imaging can also guide for photothermal therapy or externally triggered drug release. When the localisation of the nanocarriers is precisely determined by imaging techniques, the external trigger can be applied in a precise local dimension, therefore reducing the side effects of drug toxicity or hyperthermia-induced damage of healthy tissues.[211]

1.2.5 Summary and outlook

The ideal system for cancer treatment at the nanoscale should ideally be biocompatible, negotiate the biological barriers, and have targeting capacities to increase the specificity of the treatment. Furthermore, controlled and triggered drug release is required to maximize the on-site delivery of the therapeutic. Imaging moieties associated with the nanovector endow diagnostics capacities, and combining several modes of imaging enables to circumvent the limitations of each mode. A nanocarrier possessing all these characteristics would provide enormous improvements to therapeutic efficacy of cancer treatments, enable personalized medicine, and open up a new area in cancer treatment.

References

1. D. P. Bartel. *Cell* 2004, **116**, 281–297.
2. J. Winter; S. Jung; S. Keller; R. I. Gregory; S. Diederichs. *Nat. Cell Biol.* 2009, **11**, 228–234.
3. V. Ambros. *Nature* 2004, **431**, 350–355.
4. R. C. Lee; R. L. Feinbaum; V. Ambros. *Cell* 1993, **75**, 843–854.
5. B. Wightman; I. Ha; G. Ruvkun. *Cell* 1993, **75**, 855–862.
6. R. M. Graybill; R. C. Bailey. *Anal. Chem.* 2016, **88**, 431–450.
7. C. Zhang. *Curr. Opin. Mol. Ther.* 2009, **11**, 641–651.
8. T. Tian; J. Wang; X. Zhou. *Org. Biomol. Chem.* 2015, **13**, 2226–2238.
9. R. Tavallaie; S. R. M. De Almeida; J. J. Gooding. *Nanomedicine and nanobiotechnology* 2015, **7**, 580–592.
10. F. Causa; A. Aliberti; A. M. Cusano; E. Battista; P. A. Netti. *J. Am. Chem. Soc.* 2015, **137**, 1758–1761.
11. P. Zhang; Z. He; C. Wang; J. Chen; J. Zhao; X. Zhu; C. Z. Li; Q. Min; J. J. Zhu. *ACS Nano* 2015, **9**, 789–798.
12. A. Esquela-Kerscher; F. J. Slack. *Nat. Rev. Cancer* 2006, **6**, 259–269.
13. S. Sandhu; R. Garzon. *Semin. Oncol.* 2011, **38**, 781–787.
14. Z. Zhu; Y. Qi; A. Ge; Y. Zhu; K. Xu; H. Ji; Z. Shi; L. Cui; M. Zhou. *Viruses* 2014, **6**, 1525–1539.
15. Y. Qi; L. Cui; Y. Ge; Z. Shi; K. Zhao; X. Guo; D. Yang; H. Yu; L. Cui; Y. Shan; M. Zhou; H. Wang; Z. Lu. *BMC Infect. Dis.* 2012, **12**, 384–393.
16. B. Jin; Y. Zhang; W. Jin; X. Sun; G. Qiao; Y. Wei; L. Sun; W. Zhang; N. Li. *Sci. Rep.* 2015, **5**, 15026–15038.
17. S. Mi; J. Zhang; W. Zhang; R. S. Huang. *Microrna* 2013, **2**, 63–71.
18. B. N. Johnson; R. Mutharasan. *Analyst* 2014, **139**, 1576–1588.
19. H. Dong; J. Lei; L. Ding; Y. Wen; H. Ju; X. Zhang. *Chem. Rev.* 2013, **113**, 6207–6233.
20. T. D. Schmittgen; E. J. Lee; J. Jiang; A. Sarkar; L. Yang; T. S. Elton; C. Chen. *Methods* 2008, **44**, 31–38.
21. P. Chugh; D. P. Dittmer. *Wiley Interdiscip. Rev. RNA* 2013, **3**, 17–36.
22. C. K. Raymond; B. S. Roberts; P. Garrett-Engele; L. P. Lim; J. M. Johnson. *RNA* 2005, **11**, 1737–1744.
23. C. Chen; D. A. Ridzon; A. J. Broomer; Z. Zhou; D. H. Lee; J. T. Nguyen; M. Barbisin; N. L. Xu; V. R. Mahuvakar; M. R. Andersen; K. Q. Lao; K. J. Livak; K. J. Guegler. *Nucleic Acids Res.* 2005, **33**, 1–9.
24. R. Shi; V. L. Chiang. *Biotechniques* 2005, **39**, 519–524.
25. M. Nagarkatti; S. Rieder; V. Hegde. *Trends Pharmacol. Sci.* 2011, **717**, 85–90.
26. D. Leshkowitz; S. Horn-Saban; Y. Parmet; E. Feldmesser. *RNA* 2013, **19**, 527–538.
27. G. W. Tan; A. S. B. Khoo; L. P. Tan. *Sci. Rep.* 2015, **5**, 9430.
28. C. C. Pritchard; H. H. Cheng; M. Tewari. *Nat. Rev. Genet.* 2012, **13**, 358–369.
29. K. N. Ballantyne; R. A. H. van Oorschot; R. J. Mitchell. *Genomics* 2008, **91**, 301–305.
30. M. Castoldi; S. Schmidt; V. Benes; M. Noerholm; A. E. Kulozik; M. W. Hentze; M. U. Muckenthaler. *RNA* 2006, **12**, 913–920.
31. D. R. Thevenot; K. Toth; R. A. Durst; G. S. Wilson. *Biosens. Bioelectron.* 2001, **16**, 121–131.
32. E. Busseron; Y. Ruff; E. Moulin; N. Giuseppone. *Nanoscale* 2013, **5**, 7098–7140.
33. P. D. Howes; R. Chandrawati; M. M. Stevens. *Science* 2014, **346**, 1247390–1247400.
34. C. Jianrong; M. Yuqing; H. Nongyue; W. Xiaohua; L. Sijiao. *Biotechnol. Adv.* 2004, **22**, 505–518.
35. J. Wang; X. Qu. *Nanoscale* 2013, **5**, 3589–3600.
36. J. Wang. *Small* 2005, **1**, 1036–1043.

37. J. R. Lakowicz. *Principles of Fluorescence Spectroscopy*; Springer US: Boston, MA, 2006.
38. V. V. Didenko. *Biotechniques* 2001, **31**, 1106–1121.
39. B. Hochreiter; A. P. Garcia; J. A. Schmid. *Sensors* 2015, **15**, 26281–26314.
40. R. M. Clegg. *Curr. Opin. Biotechnol.* 1995, **6**, 103–110.
41. P. Wu; Y. Tu; Y. Qian; H. Zhang; C. Cai. *Chem. Commun.* 2014, **50**, 1012–1014.
42. J. Lee; G. Park; D.-H. Min. *Chem. Commun.* 2015, **51**, 5–8.
43. G. Bonnet; S. Tyagi; A. Libchaber; F. R. Kramer. *Proc. Natl. Acad. Sci. U. S. A.* 1999, **96**, 6171–6176.
44. Y. Zhang; C. Y. Zhang. *Anal. Chem.* 2012, **84**, 224–231.
45. Y. Zeng; G. Zhu; X. Yang; J. Cao; Z. Jing; C. Zhang. *Chem. Commun.* 2014, **50**, 7160–7162.
46. A. F. Jou; C.-H. Lu; Y.-C. Ou; S.-S. Wang; S.-L. Hsu; I. Willner; J. A. Ho. *Chem. Sci.* 2015, **6**, 659–665.
47. X. Qiu; N. Hildebrandt. *ACS Nano* 2015, **9**, 8449–8457.
48. P. D. Howes; S. Rana; M. M. Stevens. *Chem. Soc. Rev.* 2014, **43**, 3835–1853.
49. C. A. Mirkin; R. L. Letsinger; R. C. Mucic; J. J. Storhoff. *Nature* 1996, **382**, 607–609.
50. J. S. Lee; P. A. Ulmann; M. S. Han; C. A. Mirkin. *Nano Lett.* 2008, **8**, 529–533.
51. Q. Wang; R.-D. Li; B.-C. Yin; B.-C. Ye. *Analyst* 2015, **140**, 6306–6312.
52. Y. Wang; E. MacLachlan; B. K. Nguyen; G. Fu; C. Peng; J. I. L. Chen. *Analyst* 2015, **140**, 1140–1148.
53. H. Lee; J.-E. Park; J.-M. Nam. *Nat. Commun.* 2014, **5**, 3367.
54. K. J. Jang; H. Lee; Hua-Lan Jin; Y. Park; J. M. Nam. *Small* 2009, **5**, 2665–2668.
55. H. Šípová; S. Zhang; A. M. Dudley; D. Galas; K. Wang; J. Homola. *Anal. Chem.* 2010, **82**, 10110–10115.
56. D. Zhang; Y. Yan; W. Cheng; W. Zhang; Y. Li; H. Ju; S. Ding. *Microchim. Acta* 2013, **180**, 397–403.
57. G. K. Joshi; S. Deitz-Mcelyea; M. Johnson; S. Mali; M. Korc; R. Sardar. *Nano Lett.* 2014, **14**, 6955–6963.
58. G. K. Joshi; S. Deitz-McElyea; T. Liyanage; K. Lawrence; S. Mali; R. Sardar; M. Korc. *ACS Nano* 2015, **9**, 11075–11089.
59. J. Van Ness; L. K. Van Ness; D. J. Galas. *Proc. Natl. Acad. Sci. U. S. A.* 2003, **100**, 4504–4509.
60. H. Jia; Z. Li; C. Liu; Y. Cheng. *Angew. Chemie - Int. Ed.* 2010, **49**, 5498–5501.
61. C. Li; Z. Li; H. Jia; J. Yan. *Chem. Commun.* 2011, **47**, 2595–2597.
62. B. Yao; J. Li; H. Huang; C. Sun; Z. Wang; Y. Fan; Q. Chang; S. Li; J. Xi. *RNA* 2009, **15**, 1787–1794.
63. B. C. Yin; Y. Q. Liu; B. C. Ye. *J. Am. Chem. Soc.* 2012, **134**, 5064–5067.
64. M. Liu; C. Y. Hui; Q. Zhang; J. Gu; B. Kannan; S. Jahanshahi-Anbuhi; C. D. M. Filipe; J. D. Brennan; Y. Li. *Angew. Chemie - Int. Ed.* 2016, **55**, 2709–2713.
65. J. H. Lee; H.-E. Jin; M. Desai; S. Ren; S. Kim; S.-W. Lee. *Nanoscale* 2015, 18379–18391.
66. P. R. C. Theresa M. Allena. *Adv. Drug Deliv. Rev.* 2013, **65**, 36–48.
67. H. Robson Marsden; I. Tomatsu; A. Kros. *Chem. Soc. Rev.* 2011, **40**, 1572–1585.
68. Q. Liu; B. J. Boyd. *Analyst* 2013, **138**, 391–409.
69. C. Sanchez; H. Arribart; M. M. G. Guille. *Nat. Mater.* 2005, **4**, 277–288.
70. H. Robson Marsden; A. V. Korobko; T. Zheng; J. Voskuhl; A. Kros. *Biomater. Sci.* 2013, **1**, 1046.
71. T. H. Söllner. *Curr. Opin. Cell Biol.* 2004, **16**, 429–435.
72. L. Simonsson; P. Jönsson; G. Stengel; F. Höök. *ChemPhysChem* 2010, **11**, 1011–1017.
73. R. Jahn; T. Lang; T. C. Südhof. *Cell* 2003, **112**, 519–533.
74. T. Weber; B. V. Zemelman; J. A. McNew; B. Westermann; M. Gmachl; F. Parlati; T. H. Söllner; J. E. Rothman. *Cell* 1998, **92**, 759–772.

75. W. Antonin; D. Fasshauer; S. Becker; R. Jahn; T. R. Schneider. *Nat. Struct. Biol.* 2002, **9**, 107–111.
76. J. Rizo; C. Rosenmund. *Nat. Struct. Mol. Biol.* 2008, **15**, 665–674.
77. J. E. Rothman. *Nature* 1994, **372**, 55–63.
78. W. Wickner; R. Schekman. *Nat. Struct. Mol. Biol.* 2008, **15**, 658–664.
79. X. Chen; D. Araç; T.-M. Wang; C. J. Gilpin; J. Zimmerberg; J. Rizo. *Biophys. J.* 2006, **90**, 2062–2074.
80. A. T. Brunger; K. Weninger; M. Bowen; S. Chu. *Annu. Rev. Biochem.* 2009, **78**, 903–928.
81. W. Xu; J. Wang; J. E. Rothman; F. Pincet. *Angew. Chemie Int. Ed.* 2015, **54**, 14388 – 14392.
82. J. Diao; Y. Ishitsuka; H. Lee; C. Joo; Z. Su; S. Syed; Y.-K. Shin; T.-Y. Yoon; T. Ha. *Nat. Protoc.* 2012, **7**, 921–934.
83. B. Gong; B.-K. Choi; J.-Y. Kim; D. Shetty; Y. H. Ko; N. Selvapalam; N. K. Lee; K. Kim. *J. Am. Chem. Soc.* 2015, **137**, 8908–8911.
84. T.-Y. Yoon; B. Okumus; F. Zhang; Y.-K. Shin; T. Ha. *Proc. Natl. Acad. Sci. U. S. A.* 2006, **103**, 19731–19736.
85. S. M. Christensen; M. W. Mortensen; D. G. Stamou. *Biophys. J.* 2011, **100**, 957–967.
86. H. Robson Marsden; N. A. Elbers; P. H. H. Bomans; N. A. J. M. Sommerdijk; A. Kros. *Angew. Chemie Int. Ed.* 2009, **48**, 2330–2333.
87. Y. M. Chan; B. van Lengerich; S. G. Boxer. *Biointerphases* 2008, **3**, 17–21.
88. Y. M. Chan; B. van Lengerich; S. G. Boxer. *Proc. Natl. Acad. Sci. U. S. A.* 2009, **106**, 979–984.
89. G. Stengel; R. Zahn; F. Höök. *J. Am. Chem. Soc.* 2007, **129**, 9584–9585.
90. G. Stengel; L. Simonsson; R. A. Campbell; F. Höök. *J. Phys. Chem. B* 2008, **112**, 8264–8274.
91. D. K. Struck; D. Hoekstra; R. E. Pagano. *Biochemistry* 1981, **20**, 4093–4099.
92. T. Stegmann; P. Schoen; R. Bron; J. Wey; I. Bartoldus; A. Ortiz; J. L. Nieva; J. Wilschut. *Biochemistry* 1993, **32**, 11330–11337.
93. V. S. Malinin; E. Haque; B. R. Lentz. *Biochemistry* 2001, **40**, 8292–8299.
94. Y. H. Bae; K. Park. *J. Control. release* 2011, **153**, 198–205.
95. C. Moorthi; R. Manavalan; K. Kathiresan. *J. Pharm. Pharm. Sci.* 2011, **14**, 67–77.
96. R. K. Jain. *Annu. Rev. Biomed. Eng.* 1999, **1**, 241–263.
97. J. L. Au; S. H. Jang; J. Zheng; C. T. Chen; S. Song; L. Hu; M. G. Wientjes. *J. Control. Release* 2001, **74**, 31–46.
98. M. Ferrari. *Trends Biotechnol.* 2010, **28**, 181–188.
99. J. Dobson. *Drug Dev. Res.* 2006, **67**, 55–60.
100. H. L. Wong; R. Bendayan; A. M. Rauth; Y. Li; X. Y. Wu. *Adv. Drug Deliv. Rev.* 2007, **59**, 491–504.
101. J. H. Grossman; S. E. McNeil. *Phys. Today* 2012, **65**, 38.
102. K. Greish. Grobmyer, S. R., Moudgil, B. M., Eds.; Methods in Molecular Biology; Humana Press: Totowa, NJ, 2010; Vol. 624, pp 25–37.
103. A. Mantovani; S. Sozzani; M. Locati; P. Allavena; A. Sica. *Trends Immunol.* 2002, **23**, 549–555.
104. J. Double; M. Bibby. *J. Natl. Cancer Inst.* 1989, **81**, 988–994.
105. R. Krishna; L. D. Mayer. *Eur. J. Pharm. Sci.* 2000, **11**, 265–283.
106. A. A. Manzoor; L. H. Lindner; C. D. Landon; J.-Y. Park; A. J. Simnick; M. R. Dreher; S. Das; G. Hanna; W. Park; A. Chilkoti; G. A. Koning; T. L. M. ten Hagen; D. Needham; M. W. Dewhirst. *Cancer Res.* 2012, **72**, 5566–5575.
107. C. E. Ashley; E. C. Carnes; G. K. Phillips; D. Padilla; P. N. Durfee; P. A. Brown; T. N. Hanna; J. Liu; B. Phillips; M. B. Carter; N. J. Carroll; X. Jiang; D. R. Dunphy; C. L. Willman; D. N. Petsev; D. G. Evans; A. N. Parikh; B. Chackerian; W. Wharton; D. S. Peabody; C. J. Brinker. *Nat. Mater.* 2011, **10**, 389–397.
108. F. Tang; L. Li; D. Chen. *Adv. Mater.* 2012, **24**, 1504–1534.

109. M. E. De Jonge; A. Huitema; J. H. M. Schellens; S. Rodenhuis; J. H. Beijnen. *Clin. Pharmacokinet.* 2005, **44**, 147–173.
110. M. Hembury; C. Chiappini; S. Bertazzo; T. L. Kalber; G. L. Drisko; O. Ogunlade; S. Walker-Samuel; K. S. Krishna; C. Jumeaux; P. Beard; C. S. S. R. Kumar; A. E. Porter; M. F. Lythgoe; C. Boissière; C. Sanchez; M. M. Stevens. *Proc. Natl. Acad. Sci. U. S. A.* 2015, **112**, 1959–1964.
111. J. A. Zhang; G. Anyarambhatla; L. Ma; S. Ugwu; T. Xuan; T. Sardone; I. Ahmad. *Eur. J. Pharm. Biopharm.* 2005, **59**, 177–187.
112. P. Carmeliet; R. K. Jain. *Nature* 2000, **407**, 249–257.
113. H. Hashizume; P. Baluk; S. Morikawa; J. W. McLean; G. Thurston; S. Roberge; R. K. Jain; D. M. McDonald. *Am. J. Pathol.* 2000, **156**, 1363–1380.
114. E. Ruoslahti; S. N. Bhatia; M. J. Sailor. *J. Cell Biol.* 2010, **188**, 759–768.
115. R. K. Jain; T. Stylianopoulos. *Nat. Rev. Clin. Oncol.* 2010, **7**, 653–664.
116. S. K. Hobbs; W. L. Monsky; F. Yuan; W. G. Roberts; L. Griffith; V. P. Torchilin; R. K. Jain. *Proc. Natl. Acad. Sci. U. S. A.* 1998, **95**, 4607–4612.
117. F. Yuan; M. Dellian; D. Fukumura; M. Leunig. *Cancer Res.* 1995, **55**, 3752–3756.
118. D. Peer; J. M. Karp; S. Hong; O. C. Farokhzad; R. Margalit; R. Langer. *Nat. Nanotechnol.* 2007, **2**, 751–760.
119. H. Maeda; T. Sawa; T. Konno. *J. Control. Release* 2001, **74**, 47–61.
120. K. Cho; X. Wang; S. Nie; Z. G. Chen; D. M. Shin. *Clin. Cancer Res.* 2008, **14**, 1310–1316.
121. E. C. Dreaden; M. A. Mackey; X. Huang; B. Kang; M. a El-Sayed. *Chem. Soc. Rev.* 2011, **40**, 3391–3404.
122. H. Maeda; J. Wu; T. Sawa; Y. Matsumura; K. Hori. *J. Control. Release* 2000, **65**, 271–284.
123. V. Torchilin. *Adv. Drug Deliv. Rev.* 2011, **63**, 131–135.
124. T. Hamaguchi; Y. Matsumura; M. Suzuki; K. Shimizu; R. Goda; I. Nakamura; I. Nakatomi; M. Yokoyama; K. Kataoka; T. Kakizoe. *Br. J. Cancer* 2005, **92**, 1240–1246.
125. M. K. Yu; J. Park; S. Jon. *Theranostics* 2012, **2**, 3–44.
126. S. Wilhelm; A. J. Tavares; Q. Dai; S. Ohta; J. Audet; H. F. Dvorak; W. C. W. Chan. *Nat. Rev. Mater.* 2016, **1**, 16014.
127. M. A. Swartz; A. W. Lund. *Nat. Rev. Cancer* 2012, **12**, 210–219.
128. A. Potineni; D. M. Lynn; R. Langer; M. M. Amiji. *J. Control. Release* 2003, **86**, 223–234.
129. A. Epenetos; D. Snook; H. Durbin. *Cancer Res.* 1986, **46**, 3183–3191.
130. M. Ferrari. *Nat. Rev. Cancer* 2005, **5**, 161–171.
131. J. L. Vivero-Escoto; I. I. Slowing; B. G. Trewyn; V. S.-Y. Lin. *Small* 2010, **6**, 1952–1967.
132. L. Li; F. Tang; H. Liu; T. Liu; N. Hao; D. Chen; X. Teng; J. He. *ACS Nano* 2010, **4**, 6874–6882.
133. S. M. Moghimi; A. C. Hunter; J. C. Murray. *Pharmacol. Rev.* 2001, **53**, 283–318.
134. R. A. Roberts; P. E. Ganey; C. Ju; L. M. Kamendulis; I. Rusyn; J. E. Klaunig. *Toxicol. Sci.* 2007, **96**, 2–15.
135. D. E. Owens; N. A. Peppas. *Int. J. Pharm.* 2006, **307**, 93–102.
136. X. Duan; Y. Li. *Small* 2013, **9**, 1521–1532.
137. A. Vonarbourg; C. Passirani; P. Saulnier; J.-P. Benoit. *Biomaterials* 2006, **27**, 4356–4373.
138. Y. Yamamoto; Y. Nagasaki; Y. Kato; Y. Sugiyama; K. Kataoka. *J. Control. Release* 2001, **77**, 27–38.
139. J. Jokerst; T. Lobovkina; R. Zare; S. Gambhir. *Nanomedicine* 2011, **6**, 715–728.
140. I. I. Slowing; J. L. Vivero-Escoto; C.-W. Wu; V. S.-Y. Lin. *Adv. Drug Deliv. Rev.* 2008, **60**, 1278–1288.
141. R. K. Jain. *Adv. Drug Deliv. Rev.* 2001, **46**, 149–168.

142. C.-S. Lee; H. H. Chang; P.-K. Bae; J. Jung; B. H. Chung. *Macromol. Biosci.* 2013, **13**, 321–331.
143. H. Mok; J. W. Park; T. G. Park. *Bioconjug. Chem.* 2008, **19**, 797–801.
144. K. H. Min; J.-H. Kim; S. M. Bae; H. Shin; M. S. Kim; S. Park; H. Lee; R.-W. Park; I.-S. Kim; K. Kim; I. C. Kwon; S. Y. Jeong; D. S. Lee. *J. Control. Release* 2010, **144**, 259–266.
145. C. Wong; T. Stylianopoulos; J. Cui; J. Martin; V. P. Chauhan; W. Jiang; Z. Popovic; R. K. Jain; M. G. Bawendi; D. Fukumura. *Proc. Natl. Acad. Sci. U. S. A.* 2011, **108**, 2426–2431.
146. N. Rapoport. *Int. J. Pharm.* 2004, **277**, 155–162.
147. S. Mitragotri. *Nat. Rev. Drug Discov.* 2005, **4**, 255–260.
148. G. A. Husseini; G. D. Myrup; W. G. Pitt; D. A. Christensen; N. Y. Rapoport. *J. Control. Release* 2000, **69**, 43–52.
149. L. R. Hirsch; R. J. Stafford; J. A. Bankson; S. R. Sershen; B. Rivera; R. E. Price; J. D. Hazle; N. J. Halas; J. L. West. *Proc. Natl. Acad. Sci. U. S. A.* 2003, **100**, 13549–13554.
150. J.-F. Lutz. *J. Polym. Sci. Part A Polym. Chem.* 2008, **46**, 3459–3470.
151. Y. Wang; X. Li; C. Hong; C. Pan. *J. Polym. Sci. Part A Polym. Chem.* 2011, **49**, 3280–3290.
152. Z. Li; Y.-H. Kim; H. S. Min; C.-K. Han; K. M. Huh. *Macromol. Res.* 2010, **18**, 618–621.
153. D. J. Phillips; M. I. Gibson. *Chem. Commun.* 2012, **48**, 1054–1056.
154. Y. You; K. Kalebaila; S. Brock; D. Oupicky. *Chem. Mater.* 2008, **20**, 3354–3359.
155. C. Park; K. Lee; C. Kim. *Angew. Chem. Int. Ed. Engl.* 2009, **48**, 1275–1278.
156. M. Alvaro; M. Benitez; D. Das; H. Garcia; E. Peris. 2005, 4958–4964.
157. N. K. Mal; M. Fujiwara; Y. Tanaka. 2003, **421**, 350–353.
158. J. Morton; E. Day; N. Halas; J. West. In *Methods in Molecular Biology*; Grobmyer, S. R., Moudgil, B. M., Eds.; 2010; pp 101–117.
159. C.-Y. Lai; B. G. Trewyn; D. M. Jeftinija; K. Jeftinija; S. Xu; S. Jeftinija; V. S.-Y. Lin. *J. Am. Chem. Soc.* 2003, **125**, 4451–4459.
160. F. Torney; B. G. Trewyn; V. S.-Y. Lin; K. Wang. *Nat. Nanotechnol.* 2007, **2**, 295–300.
161. T. D. Nguyen; H.-R. Tseng; P. C. Celestre; A. H. Flood; Y. Liu; J. F. Stoddart; J. I. Zink. *Proc. Natl. Acad. Sci. U. S. A.* 2005, **102**, 10029–10034.
162. O. Gerasimov; J. Boomer; M. Qualls; D. Thompson. *Adv. Drug Deliv. Rev.* 1999, **38**, 317–338.
163. H. Liu; D. Chen; L. Li; T. Liu; L. Tan; X. Wu; F. Tang. *Angew. Chemie* 2011, **123**, 921–925.
164. C.-M. J. Hu; L. Zhang. *Biochem. Pharmacol.* 2012, **83**, 1104–1111.
165. V. Malhotra; M. Perry. *Cancer Biol. Ther.* 2003, **2**, 4–6.
166. P. Tardi; S. Johnstone; N. Harasym; S. Xie; T. Harasym; N. Zisman; P. Harvie; D. Bermudes; L. Mayer. *Leuk. Res.* 2009, **33**, 129–139.
167. H. Park; J. Yang; S. Seo; K. Kim; J. Suh; D. Kim; S. Haam; K.-H. Yoo. *Small* 2008, **4**, 192–196.
168. K. Komatsu; R. C. Miller; E. J. Hall. *Br. J. Cancer* 1988, **57**, 59–63.
169. J. You; G. Zhang; C. Li. *ACS Nano* 2010, **4**, 1033–1041.
170. R. G. Aswathy; Y. Yoshida; T. Maekawa; D. S. Kumar. *Anal. Bioanal. Chem.* 2010, **397**, 1417–1435.
171. Y. Huang; S. He; W. Cao; K. Cai; X.-J. Liang. *Nanoscale* 2012, **4**, 6135–6149.
172. L. Smith; Z. Kuncic; K. Ostrikov; S. Kumar. *J. Nanomater.* 2012, **2012**, 1–7.
173. D. Kim; S. Park; J. H. Lee; Y. Y. Jeong; S. Jon. *J. Am. Chem. Soc.* 2007, **129**, 7661–7665.
174. R. Popovtzer; A. Agrawal; N. A. Kotov; A. Popovtzer; T. E. Carey; R. Kopelman. *Nano Lett.* 2008, **8**, 4593–4596.
175. A. Miyamoto; H. Okimoto; H. Shinohara; Y. Shibamoto. *Eur. Radiol.* 2006, **16**, 1050–1053.
176. H.-T. Song; J. Choi; Y.-M. Huh; S. Kim; Y. Jun; J.-S. Suh; J. Cheon. *J. Am. Chem. Soc.*

2005, **127**, 9992–9993.
177. Y. Jun; J.-H. Lee; J. Cheon. *Angew. Chem. Int. Ed. Engl.* 2008, **47**, 5122–5135.
178. K. An; S. G. Kwon; M. Park; H. Bin Na; S.-I. Baik; J. H. Yu; D. Kim; J. S. Son; Y. W. Kim; I. C. Song; W. K. Moon; H. M. Park; T. Hyeon. *Nano Lett.* 2008, **8**, 4252–4258.
179. A. Yudina; M. de Smet; M. Lepetit-Coiffé; S. Langereis; L. Van Ruijssevelt; P. Smirnov; V. Bouchaud; P. Voisin; H. Grüll; C. T. W. Moonen. *J. Control. Release* 2011, **155**, 442–448.
180. C. W. Burke; Y.-H. J. Hsiang; E. Alexander; A. L. Kilbanov; R. J. Price. *Small* 2011, **7**, 1227–1235.
181. Y.-L. Liu; Y.-H. Wu; W.-B. Tsai; C.-C. Tsai; W.-S. Chen; C.-S. Wu. *Carbohydr. Polym.* 2011, **84**, 770–774.
182. X. Cai; F. Yang; N. Gu. *Theranostics* 2012, **2**, 103–112.
183. S. A. Hilderbrand; R. Weissleder. *Curr. Opin. Chem. Biol.* 2010, **14**, 71–79.
184. X. Gao; Y. Cui; R. M. Levenson; L. W. K. Chung; S. Nie. *Nat. Biotechnol.* 2004, **22**, 969–976.
185. H. Zhang; D. Yee; C. Wang. *Nanomedicine* 2008, **3**, 83–91.
186. J. K. Jaiswal; H. Mattoussi; J. M. Mauro; S. M. Simon. *Nat. Biotechnol.* 2003, **21**, 47–51.
187. A. M. Smith; S. Dave; S. Nie; L. True; X. Gao. *Expert Rev. Mol. Diagn.* 2006, **6**, 231–244.
188. R. Hardman. *Environ. Health Perspect.* 2006, **114**, 165–172.
189. Y. Sun; Y. Xia. *Analyst* 2003, **128**, 686.
190. P. K. Jain; X. Huang; I. H. El-Sayed; M. A. El-Sayed. *Acc. Chem. Res.* 2008, **41**, 1578–1586.
191. M. Alvarez; J. Khoury; T. G. Schaaff; M. N. Shafigullin; I. Vezmar; R. L. Whetten. *J. Phys. Chem. B* 1997, 3706–3712.
192. M. Hu; J. Chen; Z.-Y. Li; L. Au; G. V Hartland; X. Li; M. Marquez; Y. Xia. *Chem. Soc. Rev.* 2006, **35**, 1084–1094.
193. X. Li; L. Jiang; Q. Zhan; J. Qian; S. He. *Colloids Surfaces A Physicochem. Eng. Asp.* 2009, **332**, 172–179.
194. X. Wu; X. He; K. Wang; C. Xie; B. Zhou; Z. Qing. *Nanoscale* 2010, **2**, 2244–2249.
195. R. D. Averitt; S. L. Westcott; N. J. Halas. *J. Opt. Soc. Am. B* 1999, **16**, 1824.
196. H. Qian; M. Zhu; Z. Wu; R. Jin. *Acc. Chem. Res.* 2012, **45**, 1470–1479.
197. S. Link; A. Beeby; S. FitzGerald; M. A. El-Sayed; T. G. Schaaff; R. L. Whetten. *J. Phys. Chem. B* 2002, **106**, 3410–3415.
198. C. Aikens. *J. Phys. Chem. Lett.* 2010, **2**, 99–104.
199. S. Park; D. Lee. *Langmuir* 2012, **28**, 7049–7054.
200. L. Shang; S. Dong; G. U. Nienhaus. *Nano Today* 2011, **6**, 401–418.
201. A. Samanta; B. B. Dhar; R. N. Devi. *J. Phys. Chem. C* 2012, **116**, 1748–1754.
202. M. Zhu; C. M. Aikens; F. J. Hollander; G. C. Schatz; R. Jin. *J. Am. Chem. Soc.* 2008, **130**, 5883–5885.
203. T. Huang; R. Murray. *J. Phys. Chem. B* 2001, **3290**, 12498–12502.
204. Z. Wu; R. Jin. *Nano Lett.* 2010, **10**, 2568–2573.
205. J. Xie; Y. Zheng; J. Y. Ying. *J. Am. Chem. Soc.* 2009, **131**, 888–889.
206. D.-E. Lee; H. Koo; I.-C. Sun; J. H. Ryu; K. Kim; I. C. Kwon. *Chem. Soc. Rev.* 2012, **41**, 2656–2672.
207. F. Zhang; G. B. Braun; A. Pallaoro; Y. Zhang; Y. Shi; D. Cui; M. Moskovits; D. Zhao; G. D. Stucky. *Nano Lett.* 2012, **12**, 61–67.
208. E. Dulkeith; A. Morteani; T. Niedereichholz; T. Klar; J. Feldmann; S. Levi; F. van Veggel; D. Reinhoudt; M. Möller; D. Gittins. *Phys. Rev. Lett.* 2002, **89**, 203002.
209. T. Pons; I. L. Medintz; K. E. Sapsford; S. Higashiya; A. F. Grimes; D. S. English; H. Mattoussi. *Nano Lett.* 2007, **7**, 3157–3164.
210. Y. Jin; X. Gao. *Nat. Nanotechnol.* 2009, **4**, 571–576.
211. M. J. Sailor; J.-H. Park. *Adv. Mater.* 2012, **24**, 3779–3802.

212. T.-T. Wang; F. Chai; C.-G. Wang; L. Li; H.-Y. Liu; L.-Y. Zhang; Z.-M. Su; Y. Liao. *J. Colloid Interface Sci.* 2011, **358**, 109–115.
213. Y. Chen; H. Chen; D. Zeng; Y. Tian; F. Chen; J. Feng; J. Shi. *ACS Nano* 2010, **4**, 6001–6013.
214. W. Fan; B. Shen; W. Bu; F. Chen; K. Zhao; S. Zhang; L. Zhou; W. Peng; Q. Xiao; H. Xing; J. Liu; D. Ni; Q. He; J. Shi. *J. Am. Chem. Soc.* 2013, **135**, 6494–6503.
215. J. E. Lee; N. Lee; T. Kim; J. Kim; T. Hyeon. *Acc. Chem. Res.* 2011, **44**, 893–902.
216. M. P. Melancon; M. Zhou; C. Li. *Acc. Chem. Res.* 2011, **44**, 947–956.
217. M. de Smet; E. Heijman; S. Langereis; N. M. Hijnen; H. Grüll. *J. Control. Release* 2011, **150**, 102–110.

Chapter 2

Detection of microRNA via DNA-mediated liposome fusion

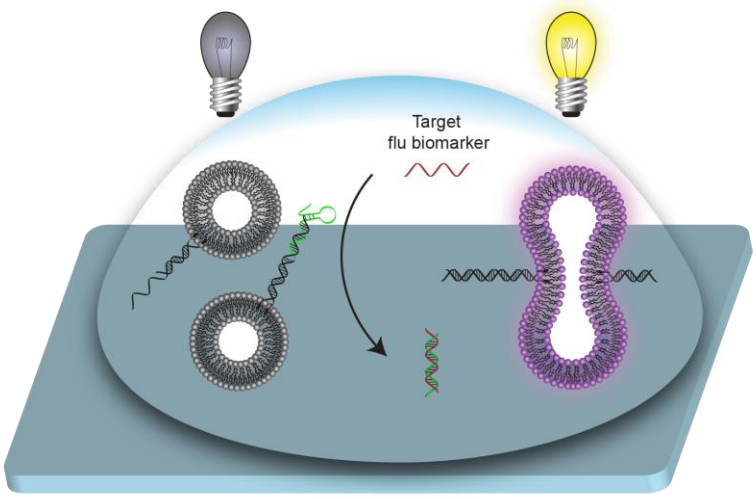

2.1 Introduction

Efficient diagnostic of diseases requires sensors that are able to detect target molecules of interest with high sensitivity as well as high specificity. Advances in the field of nanotechnology have been a key factor for the development of biosensors meeting these challenges.[1–3]

MicroRNAs (miRNAs) are small (~ 22 nucleotides), single-stranded, non-coding RNA molecules, which are involved in post-transcriptional regulation of gene expression via pairing with specific messenger RNA (mRNA), inducing translational repression or degradation.[4,5] Recently, they have emerged as promising biomarkers for a range of diseases.[4,6] For instance, studies have demonstrated that the signature of miRNAs in blood, and most notably their relative concentration, can be an accurate diagnostics tool for several tumour types.[7–9] Sensing miRNAs in body fluids remains a challenge, due to their short sequences, and high levels of sequence homology, requiring ultra-specific detection mechanisms. Additionally, miRNAs are typically present at low concentration in clinical samples; hence a target amplification step is often coupled to the biosensor, adding complexity to the design.

This Chapter reports the design of new mechanisms for miRNA detection, which were created by following a biomimetic approach. Nature is a great source of inspiration for the design of efficient sensors, as over the course of evolution highly sensitive and specific sensing or signalling processes have emerged, using refined components made of few simple building blocks.[10] Membrane fusion is an ubiquitous process that has been extensively studied using model systems such as DNA-mediated liposome fusion (Figure 1).[11,12] The self-assembly properties of DNA and DNA hybrids have been thoroughly studied, allowing to predict with high efficiency the structures formed upon strand hybridization, which has great potential for biosensing. Here, the development of diagnostics assays for the detection of miRNA based on DNA-mediated liposome fusion is reported, which performances directly arise from the self-assembly properties of DNA as well as the capacity of liposomes to encapsulate a large payload of reporter dyes, acting as signal transducer and amplifier.

The sequences of the DNA strands illustrated on Figure 1 were specially designed to render their self-assembly subjective to the presence of a specific miRNA, microRNA-29a (miR-29a). This RNA molecule is involved in host response to influenza virus infection and has been recognized as a suitable biomarker.[13] Constant mutation of influenza virus strains makes their direct detection challenging.[14] Alternatively to direct pathogen detection, monitoring the host response to infection has emerged as a new indirect diagnostics method,[15] and miRNAs have recently been recognized as a promising host marker.

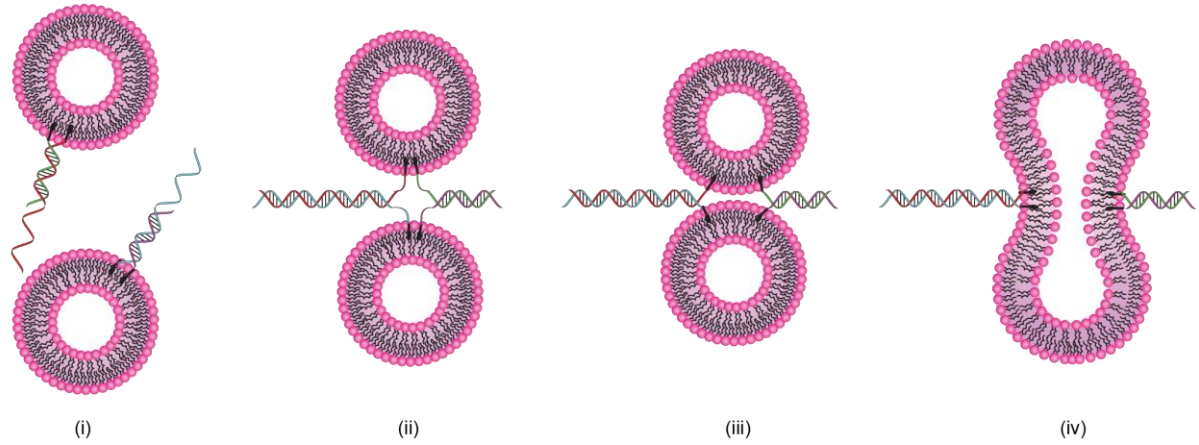

Figure 1. Mechanism for DNA-mediated liposome fusion. (i) Two separate populations of liposomes are functionalized with complementary DNA strands; (ii) and (iii) DNA hybridization in a zipper-like fashion brings two liposomes in close contact, eventually leading to mixing of outer leaflet lipids, and in some cases, (iv) opening of the fusion pore. Adapted from Stengel et al.[12]

In the engineered mechanisms, miR-29a regulates the self-assembly of the double-stranded DNA (dsDNA) functionalizing the liposomes, which in turn control liposome fusion. Therefore, the amount of liposome fusion events can be used to derive the presence of miR-29a in a sample (Figure 2).

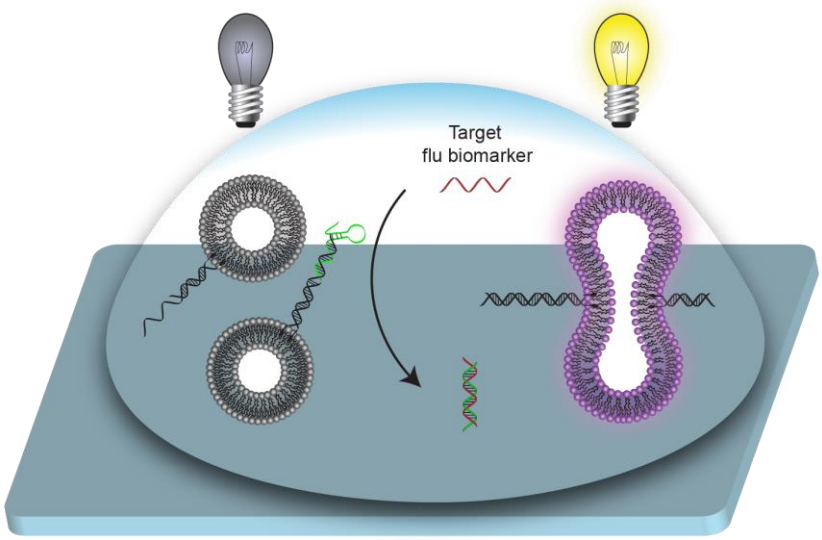

Figure 2. Schematic of proposed DNA-mediated liposome fusion assay for miRNA detection. It is hypothesized that the target miRNA (red strand) can regulate the self-assembly of dsDNA functionalizing liposomes, controlling liposome fusion. This figure illustrates the proposed liposome fusion promotion mechanism, in which target miRNA promotes liposome fusion ('ON' state).

In this Chapter, first, the choice of transduction signal for reporting liposome fusion is examined. Then, two different mechanisms for miRNA detection are presented: one where miR-29a inhibits liposome fusion, and a second one where miR-29a promotes liposome fusion (Figure 3).

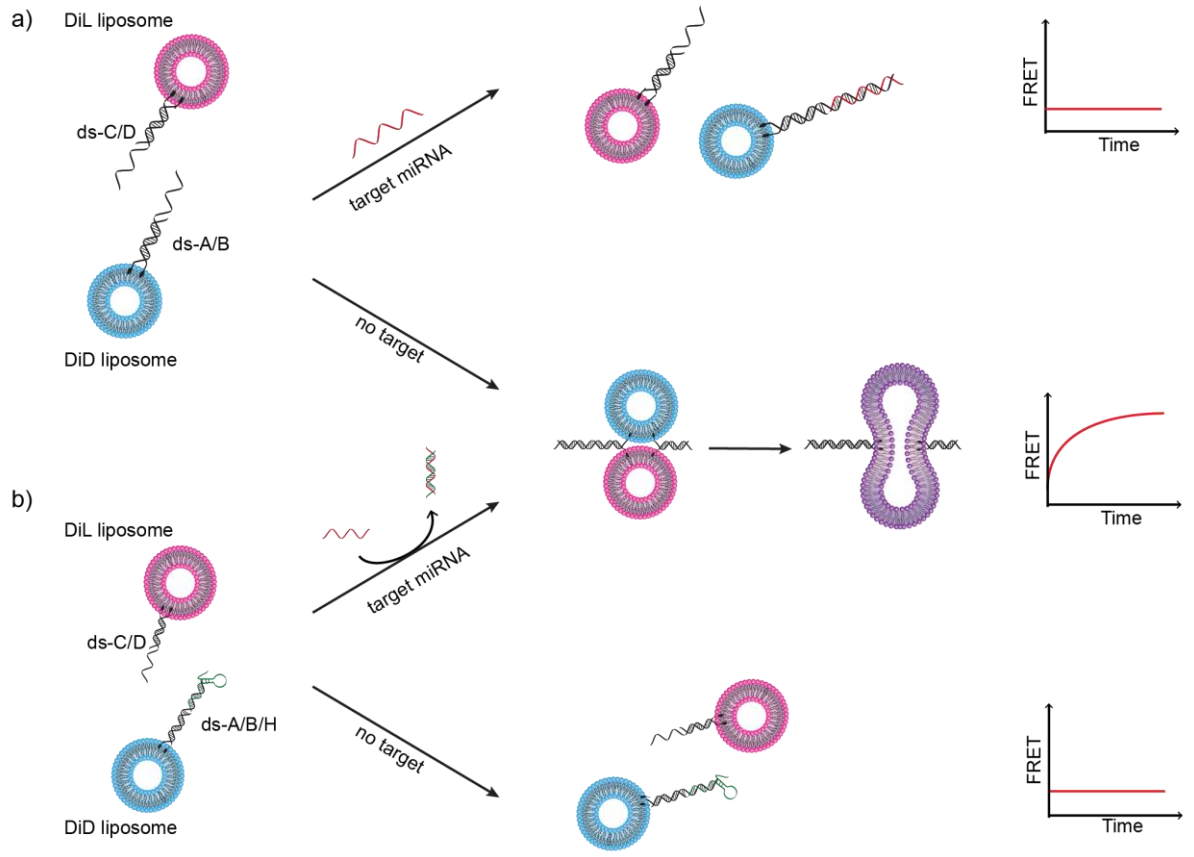

Figure 3. Schematics of the novel miRNA detection mechanisms using DNA-mediated liposome fusion. a) Liposome fusion inhibition mechanism. b) Liposome fusion promotion mechanism.

2.2 Materials and methods

2.2.1 Materials

All chemical reagents were purchased from Sigma-Aldrich and used as supplied unless otherwise indicated. 1,2-Dioleoyl-*sn*-glycero-3-phosphocholine (DOPC) and 1,2-dioleoyl-*sn*-glycero-3-phosphoethanolamine (DOPE) lipids were purchased from Avanti Polar Lipids, Inc. 1,1'-Dioctadecyl-3,3,3',3'-tetramethylindodicarbocyanine perchlorate, DiIC18(5) (DiD), 1,1-dioctadecyl-3,3,3',3'-tetramethylindocarbocyanine perchlorate, DiIC18(3) (DiL), Tris/boric acid/EDTA (TBE) buffer, 10 bp DNA ladder, BlueJuice gel loading buffer, and SYBR gold nucleic acid gel stain were purchased from Invitrogen Life Technologies. 30 % Acrylamide/bis solution (29:1) was obtained from Bio-Rad (USA). HPLC-purified oligonucleotides were purchased from IBA GmbH (Germany) and Integrated DNA Technologies (Belgium). Nuclease-free water (non DEPC-treated) was purchased from Thermo Fisher Scientific (Ambion™).

2.2.2 Liposome fusion inhibition

Nucleic acid sequences

The nucleic acid sequences and their modifications are listed on Table 1.

Table 1. Nucleic acid sequences used in this study.

Name	Sequence (5' – 3')	Modification
A	TCCGTCGTGCCTACTGATTTCTTTTGGTGTTCAG	5'-Cholesterol
B	AGGCACGACGGA	3'Cholesterol
C	CTGAACACCAAAAGAAATCAGTAGGCACGACGGA	3'Cholesterol
D	TCCGTCGTGCCT	5'-Cholesterol
miR-29a	ACUGAUUUCUUUUGGUGUUCAG	-
miR-29b-1	GCUGGUUUCAUAUGGUGGUUUAGA	-
miR-29b-2	CUGGUUUCACAUGGUGGCUUAG	-
miR-29c	UGACCGAUUUCUCCUGGUGUUC	-
miR-29a-1MM	ACUGAUUUCUUCUGGUGUUCAG	-
miR-29a-2MM	ACUGAGUUCUUCUGGUGUUCAG	-
miR-29a-3MM	ACUGAGUUCUUCUGGUGCUCAG	-

Liposome preparation and functionalization

Liposomes were composed of DOPC/DOPE/Cholesterol (50:25:25 mass ratio) and contained 2 mol % of DiL or DiD. Dry lipid films were hydrated in buffer (30 min, 5 $mg.mL^{-1}$, 37 °C, TE buffer containing 150 mM NaCl; buffer composition: 10 mM Tris, 150 mM NaCl, 1 mM EDTA, pH adjusted to 8.0 using HCl). Liposomes were extruded using an Avanti Lipid Mini-Extruder with

100 nm polycarbonate membranes (Whatman). DNA strands A/B and C/D were mixed at a 1:1 molar ratio, annealed at 80 °C for 5 min, then allowed to hybridize by slowly cooling down the solution to 25 °C. DiL liposomes were functionalized with DNA A/B and DiD liposomes were functionalized with DNA C/D by allowing the cholesterol modified dsDNA to self-incorporate in the lipid vesicles for 60 min. Unbound DNA was removed using Nanosep® Centrifugal Device with Omega Membrane (MWCO 30 kDa, 5 min × 5000 g, Pall).

Measurement of fusion kinetics

Liposomes were diluted to the required concentration in the fusion buffer (TE buffer containing 150 mM NaCl, pH 7.4). Target miRNA was added to solutions of DiD liposomes, and allowed to hybridize for 1 h at room temperature. Then, 1:1 volume ratio of DiL and DiD liposomes were mixed. Kinetics of fusion of DiL and DiD liposomes were measured in 96-well plates, and fluorescence emission of the dyes was recorded with a SpectraMax M5 microplate reader (Molecular Devices, USA) at room temperature or 37 °C, using λ_{ex} = 530 nm, $\lambda_{em,DiL}$ = 570 nm, $\lambda_{em,DiD}$ = 670 nm.

Measurement of fusion kinetics for sensitivity and specificity of the assay

DiL and DiD liposomes were functionalized with 10 dsDNA copies per liposomes. Unbound DNA was removed using Nanosep® Centrifugal Device with Omega Membrane (MWCO 30 kDa, 5 min × 5000 g, Pall). Liposomes were diluted in TE buffer containing 150 mM NaCl (pH 7.4) to 100 μM lipid concentration. Various concentrations of target miR-29a (for evaluation of the sensitivity of the assay; 1 molar equivalent of target corresponds to a concentration of miR-29a equal to 7.6×10^{-9} M) or various other miRNAs (for evaluation of the specificity of the assay, see Table 1 for the detailed nucleic acids sequences) were added to solutions of DiD liposomes, and allowed to hybridize for 1 h at room temperature. For evaluation of the specificity, the concentration of miRNA was set to 7.6×10^{-9} M (1 molar equivalent). Then, equal volumes of DiL and DiD liposomes were mixed. Kinetics of fusion of DiL and DiD liposomes were measured in 96-well plates, and fluorescence emission of the dyes was recorded with a SpectraMax M5 microplate reader (Molecular Devices, USA) at the specified temperature, 25 °C or 37 °C, using λ_{ex} = 530 nm, $\lambda_{em,DiL}$ = 570 nm, $\lambda_{em,DiD}$ = 670 nm. Results were obtained in triplicates.

2.2.3 Liposome fusion promotion

Nucleic acid sequences

The nucleic acid sequences and their modifications are listed on Table 2.

Table 2. Nucleic acid sequences used in this study.

Name	Sequence (5' – 3')	Modification
A	TCCGTCGTGCCTCGCGCACTGATT	5'-Cholesterol
A'	TCCGTCGTGCCTATTGGGTGAATTATTGAGAG	5'Cholesterol
B	AGGCACGACGGA	3'Cholesterol
C	AATCAGTGCGCGAGGCACGACGGA	3'-Cholesterol
C'	CTCTCAATAATTCACCCAATAGGCACGACGGA	3'-Cholesterol
D	TCCGTCGTGCCT	5'-Cholesterol
H_6	*CTCTCAATAA***CACTGA**ACACCAAAAGAAA**TCAGTG***CACCCAAT*	-
H_{13}	*CTCTCAATAA***CTGAACACCAAAA**GAAATCAG**TTTTGGTGTTC AG***CACCCAAT*	-
H_7	AAA**TCTTTTG**CTGAACAC**CAAAAGA***AATCAGTGCGCG*	-
miR-29a	ACUGAUUUCUUUUGGUGUUCAG	-
miR-29b-1	GCUGGUUUCAUAUGGUGGUUUAGA	-
miR-29b-2	CUGGUUUCACAUGGUGGCUUAG	-
miR-29c	UGACCGAUUUCUCCUGGUGUUC	-
miR-29a-1MM	ACUGAUUUCUUCUGGUGUUCAG	-
miR-29a-2MM	ACUGAGUUCUUCUGGUGUUCAG	-
miR-29a-3MM	ACUGAGUUCUUCUGGUGCUCAG	-

Mismatches compared with the sequence of miR-29a are indicated in red.
Stem sequences are indicated in bold.
Nucleobases binding to the sticky end of A or A' are indicated in italic.

Analysis of hairpin structures

Secondary structure analysis of hairpin DNA hybridized with dsDNA was performed by means of NUPACK analysis algorithms[16] using the internet-based tool NUPACK nucleic acid package.[17]

Native polyacrylamide gel electrophoresis (PAGE) assay

To analyse hairpin hybridization with dsDNA and hairpin displacement by target miR-29a in solution, all the duplexes were formed in TE buffer containing 50 mM NaCl (pH 8.0) or TE buffer containing 150 mM NaCl (pH 7.4) for hairpin displacement, and resolved in 15 % native PAGE in 1× TBE buffer. For PAGE, 3 pmol of each mixture, combined with gel loading buffer, were loaded into each lane and the gels were run in 1× TBE buffer at 50 V for 10 min and 110 V for 65 min. The gels were post-stained with 1× SYBR gold for 30 min at room temperature and imaged using the BioSpectrum Imaging System (Ultra-Violet Products, Cambridge, UK).

Liposome preparation and functionalization

Liposomes were composed of DOPC/DOPE/Cholesterol (50:25:25 mass ratio) and contained 2 mol % of DiL or DiD. Dry lipid films (5 $mg.mL^{-1}$) were hydrated in TE buffer (10 mM Tris, 1 mM EDTA, pH 8.0) containing 150 mM NaCl at 37 °C for 30 min. Liposomes were extruded using the Avanti Lipids Mini-Extruder with 100 nm polycarbonate membranes (Whatman). Each DNA strand (A and B, C and D) was mixed at a 1:1 molar ratio. To form ds-A/B, ds-C/D and H, the mixtures were annealed at 80 °C for 5 min, then allowed to hybridize by slowly cooling down the solution to 25 °C. Then ds-A/B and H were mixed at 1:1 molar ratio and left to hybridize at 25 °C for 1 h. DiD liposomes were functionalized with ds-A/B/H and DiL liposomes were functionalized with ds-C/D, both at a ratio of 100 dsDNA copies per liposome, by allowing the cholesterol modified dsDNA to self-incorporate into the lipid vesicles for 60 min. Unbound DNAs were removed using Nanosep® Centrifugal Device with Omega Membrane (MWCO 30 kDa, 5 min x 5000 g, Pall).

Measurement of fusion kinetics in bulk assay

Liposomes were diluted to 1.7 nM in TE buffer containing 150 mM NaCl (pH 7.4). Various concentrations of target miR-29a (for evaluation of the sensitivity of the assay) or various other miRNAs (for evaluation of the specificity of the assay, see Table 2 for the detailed nucleic acids sequences) were added to solutions of DiD liposomes, and allowed to hybridize for 1 h at room temperature. For evaluation of the specificity, the concentration of miRNA was set to 2.1×10^{-7} M (1:1 mole equivalent). Then, equal volumes of DiL and DiD liposomes was mixed. Kinetics of fusion of DiL and DiD liposomes were measured in 96-well plates, and fluorescence emission of the dyes was recorded with a SpectraMax M5 microplate reader (Molecular Devices, USA) at 25 °C, using λ_{ex} = 530 nm, $\lambda_{em,DiL}$ = 570 nm, $\lambda_{em,DiD}$ = 670 nm.

Measurement of the assay sensitivity using 2-color fluorescence microscopy setup

These experiments were performed at Chalmers University of Technology (Gothenburg, Sweden), in the laboratory of Prof. Fredrik Höök, in collaboration with Olov Wahlsten.

2-color fluorescence correlation microscopy analysis measurements were performed on an upright Olympus BX61 microscope equipped with a Hamamatsu ORCA-Flash4.0 V2 Digital CMOS camera. The sample containing the liposomes was introduced in a narrow sample channel, constructed by two thin glass slides distanced a couple of mm by several layers of double-sided tape yielding a channel volume of ~100 µl. The sample was exposed to monochromatic light (488 nm) via a laser (max power: 150 mW, Cobolt) coupled to a single mode polarization maintaining optical fibre (P460-HP, Thorlabs), which was carefully inserted

into the sample channel using a manual micrometer translational stage. The emitted light from the liposomes in solution was collected with an Olympus 20×, NA = 0.5, water immersion objective (UMPlanFL) and then passed through a dual emission image splitter (OptoSplit II, Cairn Research). The image splitter was equipped with a filter cube containing a dichroic mirror (transmission > 650 nm, Cairn Research) and two fluorescence filters (590/50 nm and 700/75 nm, Chroma Technology Corporation). Additionally, a 10× objective (Olympus) was placed between the image splitter and the CMOS camera. Images were acquired at 33 frames per second (2×2 binning) at 30 ms exposure time with a laser power of 50 mW.

Liposomes were diluted to 10 pM in TE buffer containing 150 mM NaCl (pH 7.4). DiL and DiD liposomes were mixed at a 1:1 volume ratio, and various concentrations of target miR-29a were added to the liposomes. These solutions were left to react for 1 h at room temperature, and then the liposomes were further diluted to 2 pM before measuring the amount of FRET in the 2-color fluorescence microscopy setup.

2.3 Results and discussion

2.3.1 Choice of reporter assay

The signal transduction element of the miRNA sensing mechanism relies on liposome fusion. A majority of methods for detecting membrane fusion are based on fluorescence generation or Förster resonance energy transfer (FRET), and careful method selection allows selective discrimination between lipid mixing (inner or outer lipid leaflet) and content mixing.[18] These assays have been discussed in Chapter 1, section 1.1.2.3.

Studies have shown that a high level of lipid mixing can occur with a limited degree of content mixing,[12,19,20] therefore it is expected that an enhanced signal can be generated when the reporter fluorophores are present in the lipid bilayer rather than in the hydrophilic cavity of liposomes. Therefore, for this purpose, lipid mixing assays were deemed more suitable reporters. Initial tests were carried using the NBD-rhodamine FRET pairs dilution assay, where both lipid-conjugated dyes are initially on one population of liposomes, generating a high FRET signal. Upon fusion of these labelled liposomes with unlabelled liposomes, the FRET signal decreases as the dyes are transported further apart. The results obtained using the NBD-rhodamine assay were noisy, and not easily reproducible. As the dyes are conjugated to the lipid head, in this setup they are exposed outside of the liposomes, rendering the assay more sensitive to liposome aggregation, as well as environmental factors (*i.e.* ionic strength, hydration, chemically-active molecules).[21] This assay has also been shown to cause non-specific lipid mixing.[20]

In order to circumvent these issues, an assay where the dyes are encapsulated within the lipid bilayer was selected. DiL and DiD FRET pairs are based respectively on Cy3 and Cy5 cyanine dyes (Figure 4), and contain long alkane chains rendering them very lipophilic; therefore they will be included in the lipid bilayer of liposomes upon encapsulation. In this assay, two populations of liposomes containing either DiL or DiD are mixed; upon membrane fusion and lipid mixing, these fluorescent dyes come in close proximity, resulting in FRET signal generation (Figure 5).[22]

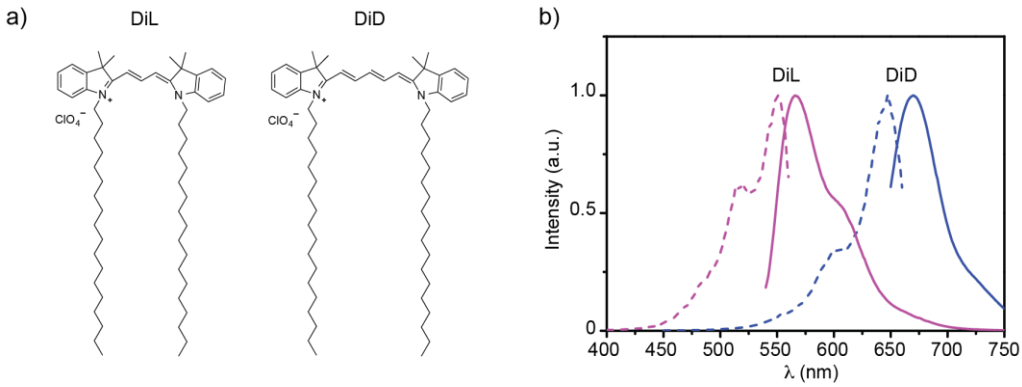

Figure 4. a) Chemical structures of DiL and DiD FRET pairs. b) Absorbance (dashed lines) and fluorescence emission (full lines) spectra of DiL (λ_{ex} = 530 nm) and DiD (λ_{ex} = 647 nm).

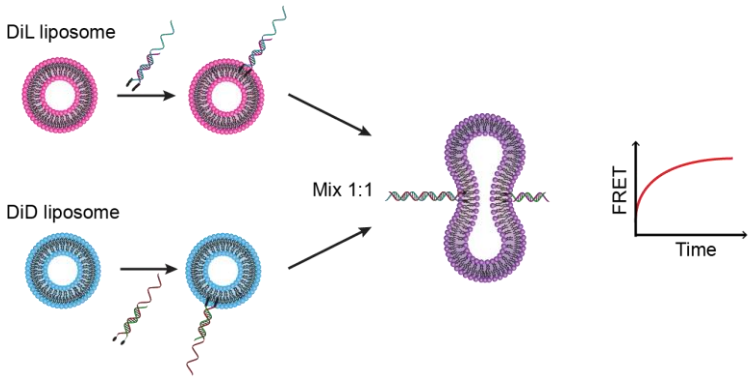

Figure 5. DiL/DiD FRET assay for reporting liposome fusion. The dyes are encapsulated in separate populations of liposomes, which are functionalized with complementary dsDNA. Liposomes are mixed at equal volume and dsDNA hybridization triggers lipid mixing. The dyes come in close contact in the fused lipid bilayers, which increases the efficiency of energy transfer between donor (DiL) and acceptor (DiD).

2.3.2 Liposome fusion inhibition

In the liposome fusion inhibition mechanism, the presence of target miRNA specifically inhibits liposome fusion. Two populations of liposomes, one containing DiL and the other one DiD, are functionalized with complementary double stranded DNA (dsDNA) strands, dsDNA A/B and C/D (nucleic acid sequences are detailed in Table 1), designed to hybridize in a zipper-like fashion.[11,12] The toehold region of DNA C is specifically designed to be complementary to the target miRNA. In absence of target, dsDNA A/B and C/D hybridize, bringing the liposomes in close contact, driving lipid mixing and allowing diffusion of DiL and DiD dyes to close proximity, resulting in an increase of FRET signal (Figure 6). When the target is present, its hybridization to the toehold prevents dsDNA A/B and C/D to hybridize and subsequent fusion between DiL and DiD liposomes.

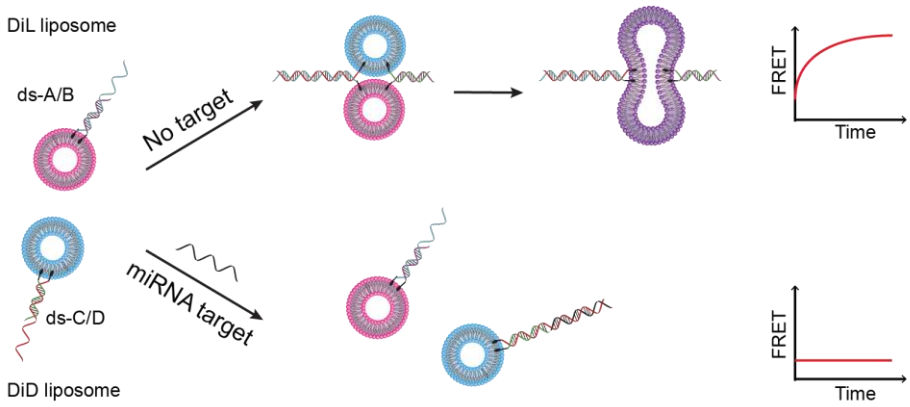

Figure 6. Schematics for miRNA detection assay based on inhibition of DNA-mediated liposome fusion. Target miRNA (black strand) is complementary to the toehold (red strand) and hybridizes to it, blocking liposome fusion. In the absence of target, liposome fusion is promoted by dsDNA A/B and C/D hybridizing in a zipper-like manner.

2.3.2.1 Optimization of the assay conditions

Influence of DNA functionalization and temperature of the assay:

The effect of dsDNA functionalization on the kinetics of fusion and on the efficiency of fusion inhibition after addition of target miRNA was investigated (Figure 7). Liposomes were functionalized with 100, 50, 25 or 10 dsDNA copies, then equal volumes of DiL and DiD liposomes were mixed and the FRET signal generated over time was measured. As previously reported, a higher degree of dsDNA coverage resulted in higher lipid mixing efficiency (Figure 7).[12] When DiD liposomes functionalized with dsDNA C/D were first incubated with 1 molar equivalent of miR-29a before mixing with DiL liposomes, a decreased amount of lipid mixing was observed (Figure 7, open symbols), confirming that the presence of target was able to inhibit liposome fusion. The percentage of fusion inhibition, defined here as the ratio of FRET signal in absence of target over the FRET signal in presence of target was similar across the range of dsDNA copy numbers. Reducing the number of copies, thus the moles, of dsDNA per liposome also decreased the amount of target required to inhibit liposome fusion, which is advantageous for lowering the limit of detection of the assay.

Then, the influence of assay temperature on the fusion and inhibition efficiency was also studied (Figure 7). Increasing the temperature to 37 °C resulted in increasing lipid mixing efficiency, as previously reported in the literature.[12] Similarly, when DiD liposomes were pre-incubated with miR-29a, the amount of lipid mixing was reduced, although not to the same level as when the liposomes were mixed at room temperature. The percentage of fusion inhibition slightly decreased, but was also conserved across the range of dsDNA copies per liposomes. However

the dynamic margin, defined here as the difference between the FRET signal in absence of target and the FRET signal in presence of target, notably increased when the assay was measured at 37 °C.

These results demonstrated the high flexibility of this assay: by varying the amount of dsDNA functionalizing the liposomes and by changing the assay temperature, a wide range of miR-29a concentrations could be detected with different dynamic margins, and the minimum detectable amount of miRNA could be decreased. For this study, the optimal conditions for the detection of miRNA towards a low limit of detection and high dynamic margin were defined to be using liposomes functionalized with 10 dsDNA copies and incubating the liposomes at 37 °C during the assay.

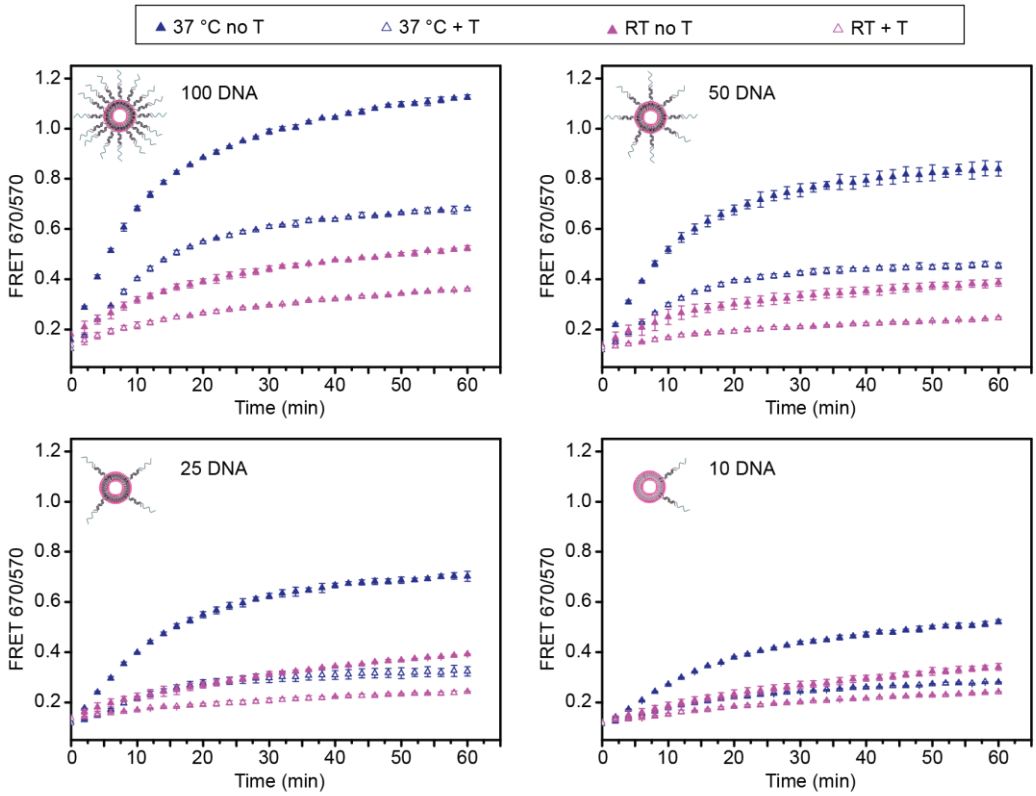

Figure 7. Influence of DNA functionalization and temperature on the kinetics of fusion. Kinetics of lipid mixing in the absence of target (closed symbols) or in the presence of target miRNA (T) (open symbols) for 100, 50, 25 or 10 dsDNA copies per liposome at room temperature (pink traces) or at 37 °C (blue traces).

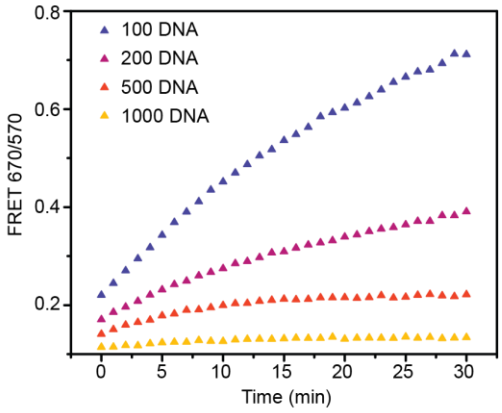

Figure 8. Influence of DNA functionalization on the kinetics of fusion. Kinetics of lipid mixing in the absence of target for 100, 200, 500, or 1000 dsDNA per liposome at room temperature.

The upper range of DNA functionalization was also investigated (Figure 8). The amount of lipid mixing was highest for 100 dsDNA per liposome, and decreased as the number of dsDNA per liposome increased; for 1000 dsDNA, lipid mixing was inhibited. This observation was attributed to the increased steric hindrance and electrostatic repulsion provided by the DNA strands. For lipid mixing to occur, docked liposomes must come in close contact; the negatively-charged dsDNA functionalizing the liposomes can prevent this step to occur, above a threshold of dsDNA copy number.

Influence of liposome concentration:

Diluting the liposomes results in lower abundance of dsDNA copies present in the solution, which would require fewer target molecules to inhibit the fusion, therefore lowering the limit of detection for miR-29a. DiL and DiD liposomes functionalized with 100 dsDNA copies were diluted to several concentrations between 500 μM and 10 μM (corresponding to lipid concentration) and mixed in equal volumes. Diluting the liposomes up to 10 μM did not affect the fusion rate and dynamic margins significantly (Figure 9). However, as the liposomes were diluted, the fluorescence signal readout decreased as well, reaching the detection limit of the laboratory equipment. Therefore, the optimal lipid concentration used in the following assays was set at 100 μM.

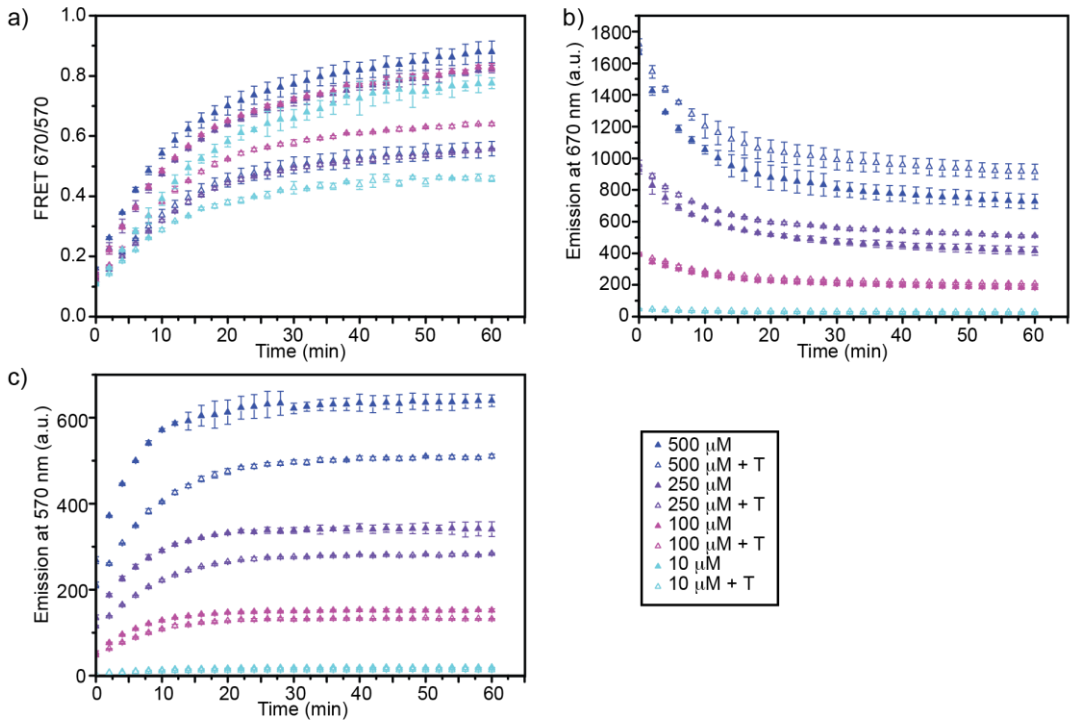

Figure 9. Study of the influence of liposome concentration on the assay. Kinetics of fusion at 37 °C of lipid vesicles diluted to 10 µM (cyan), 100 µM (pink), 250 µM (purple) or 500 µM (blue), in absence (closed symbols) or in presence (open symbols) of target miR-29a, introduced at 1:1 molar equivalents. a) FRET ratio, b) fluorescence emission at 670 nm, and c) fluorescence emission at 570 nm. λ_{ex} = 530 nm.

2.3.2.2 Determination of the sensitivity of the assay

Having defined the optimal assay conditions, the sensitivity of this assay was then determined. DiL and DiD liposomes were functionalized with 10 dsDNA copies, and diluted to a lipid concentration of 100 µM. DiD liposomes were incubated with various concentrations of miR-29a for 1 hour at room temperature, then equal volumes of DiL and DiD liposomes were mixed and the FRET ratio was recorded over time at 37 °C (Figure 10a). The values of FRET ratio after 30 minutes of incubation at 37 °C were plotted against miR-29a concentration to obtain the dose-response curve (Figure 10b). The limit of detection (LOD) was determined, by first calculating the z-value (z = blank + 3σ, where σ is the standard deviation of the blank), which was converted into miR-29a concentration using the fitted curve. A LOD of 5.1×10^{-10} M was obtained. This result shows the strength of this assay: it enabled the detection of sub-nanomolar concentrations of miR-29a with enzyme-free signal amplification. Additionally, it did not require specialized equipment and temperature cycling, which are needed for other RNA detection methods such as polymerase chain reaction (PCR), therefore this approach has great potential for point-of-care diagnostics.

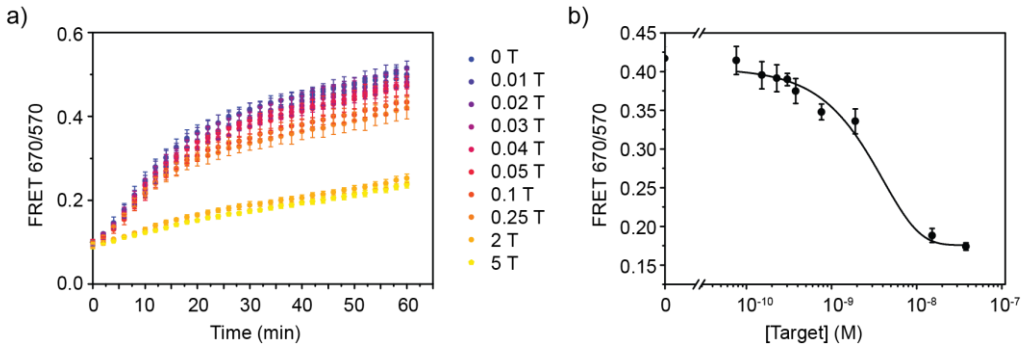

Figure 10. Evaluation of the sensitivity of the miRNA detection assay. a) FRET signal traces evolution over time corresponding to various molar equivalent of target (1 molar equivalent of target corresponds to a concentration of miR-29a equal to 7.6×10^{-9} M). b) Corresponding dose-response curve measured after 30 min of incubating DiL and DiD liposomes together at 37 °C. n=3.

2.3.2.3 Determination of the specificity of the assay

Finally, the specificity of the miRNA detection assay was studied. The miR-29 family members are important regulators of human diseases,[23] and include miR-29a, miR-29b-1, miR-29b-2, and miR-29c. In a microarray assay, the expression levels of both miR-29a and miR-29b were significantly different between critically ill patients with H1N1 infection and healthy controls.[13] In this study, the ability of the assay to discriminate between the fully complementary target, miR-29a, and its miR-29 family counterparts, miR-29b and miR-29c was evaluated. Additionally, as the sequences of miR-29b and miR-29c possess several nucleotides additions and mismatches compared to miR-29a, artificially designed miRNAs were also included in the study, similar in sequence to miR-29a but containing respectively 1, 2 and 3 nucleotides mismatches: miR-29a-1MM, miR-29a-2MM, and miR-29a-3MM (Table 1). DiD liposomes were incubated with the different miRNAs at a final concentration of 7.6×10^{-9} M. Then, an equal volume of DiL liposomes was added and the kinetics of lipid mixing were measured at 37 °C (Figure 11a). The values of the FRET ratio for each miRNA relative to the FRET ratio of the negative control (liposomes mixed in absence of target) after 30 min of incubation are reported in the graph in Figure 11b. MiR-29a showed the highest degree of fusion inhibition, followed by miR-29a-1MM and miR-29a-2MM. The rest of the miRNAs tested did not significantly differ from the negative control at the concentration tested. As miR-29a-1MM only differs by one nucleotides from miR-29a, it was expected to be able to hybridize to the toehold and to partially inhibit liposome fusion, as was observed during this experiment. However, the inhibition of fusion by miR-29a-1MM was significantly lower than for miR-29a. Thus, the liposome fusion assay was selective for fully complementary RNA.

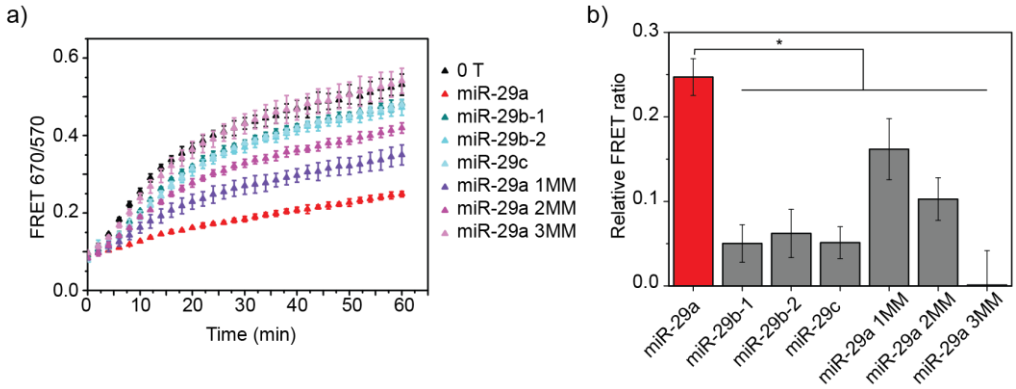

Figure 11. Evaluation of the specificity of the miRNA detection assay. a) FRET signal traces over time corresponding to various miRNA sequences added to DiD liposomes at a concentration of 7.6×10^{-9} M. b) Corresponding bar chart representing the FRET ratio value for each miRNA sequence after 30 min of mixing DiL and DiD liposomes. n=3, *p < 0.05 (ANOVA followed by Tukey *post-hoc* test).

2.3.3 Liposome fusion promotion

In the liposome fusion promotion mechanism, the presence of target miRNA specifically promotes liposome fusion. In this assay, liposomes containing either DiL or DiD FRET pairs in the bilayer are functionalized with self-inserting, cholesterol-terminated dsDNA (Figure 12). A hairpin DNA (H, green strand in Figure 12) is designed to block the toehold of dsDNA A/B (ds-A/B), preventing their hybridization with dsDNA C/D (ds-C/D) and inhibiting liposome docking and fusion. The hairpin DNA is also specially designed to include a region containing a complementary sequence with miR-29a. Hence, in the presence of target miRNA, hybridization with hairpin DNA reveals the toehold of ds-A/B, which in turn hybridizes with ds-C/D, initializing lipid vesicle docking and membrane fusion. This is then detected by an increase of FRET signal.

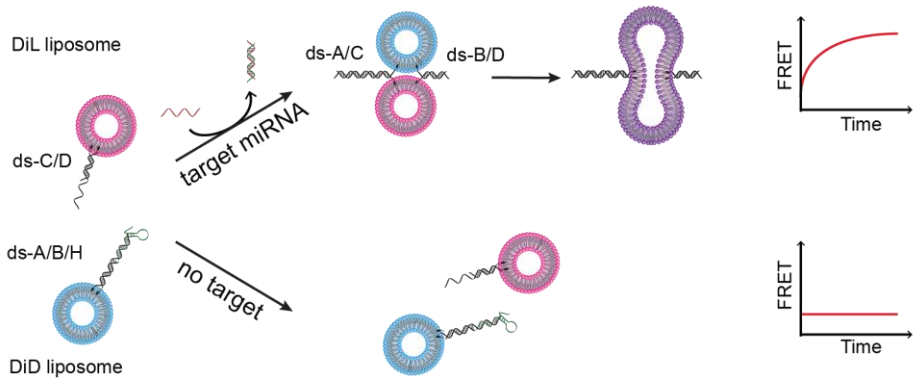

Figure 12. Schematic for miRNA detection based on promotion of DNA-mediated liposome fusion. Target miRNA (red strand) is complementary to the hairpin (green strand) and hybridizes to it; this displacement reveals the toehold in ds-A/B. In the presence of target, liposome fusion is promoted by ds-A/B and ds-C/D hybridizing in a zipper-like manner, resulting in an increase in FRET signal. In the absence of target, liposome fusion is inhibited, as hairpin DNA stays hybridized on ds-A/B, and no FRET increase is observed.

The fusion inhibition mechanism presented in the previous section was an inverse assay, where the presence of the target resulted in a decrease of signal measured. Here, target addition results in an increase of FRET signal, which is a more intuitive output. In addition, the experimental complexity is reduced in this assay: DiL and DiD liposomes are maintained in a stable suspension as the hairpin blocks the toehold on ds-A/B; therefore this assay only requires a one-step target addition.

2.3.3.1 Optimization of the hairpin sequence

In this assay, the hairpin DNA strand (H) is designed to hybridize on the toehold of a duplex and to be displaced in the presence of target miRNA. This novel mechanism of dual-function hairpin DNA is an advantageous strategy as it offers a unique site for target hybridization and its design can be tailored to adapt to a broad spectrum of target biomarkers. It is crucial to optimize the design of H, to meet the following two requirements: (i) H must be strongly hybridized to ds-A/B in absence of target, preventing the hybridization of A with C and further unzipping of the dsDNAs, and (ii) H must be displaced specifically only by target miRNA, revealing the toehold of ds-A/B, which will initiate liposome docking by hybridizing with ds-C/D.

Three different hairpins were designed: H_6, H_7, and H_{13}, and the influence of the length of the stem and the position of the hairpin stem on the toehold of ds-A/B on the hybridization and displacement of the hairpin were studied. H_6 and H_{13} have 6 and 13 base pairs in their stem, respectively, and are hybridized in a central position on the toehold of dsDNA, while H_7 has 7

base pairs in its stem and is hybridized in a terminal position on the toehold of dsDNA (sequences in Table 2). The sequence of the long single stranded DNA (ssDNA) in ds-A/B was identical in the case of H_6 and H_{13} and is referred as A'. For H_7 the toehold of dsDNA was shortened to 12 bases in order to favour the displacement of the hairpin by miR-29a and the long ssDNA strand is referred as A.

The predicted secondary structures formed by A or A' (long ssDNA), B (short ssDNA) and H (hairpin) were visualized using algorithms provided in the NUPACK software (Figure 13).[16] Out of the 3 predicted constructs, ds-A/B/H_7 had the highest probability of formation followed by ds-A'/B/H_6 then ds-A'/B/H_{13} (Figure 13, Table 3); the base-paring probability at the base of the stem was lower when the hairpin hybridized in the centre of the dsDNA toehold.

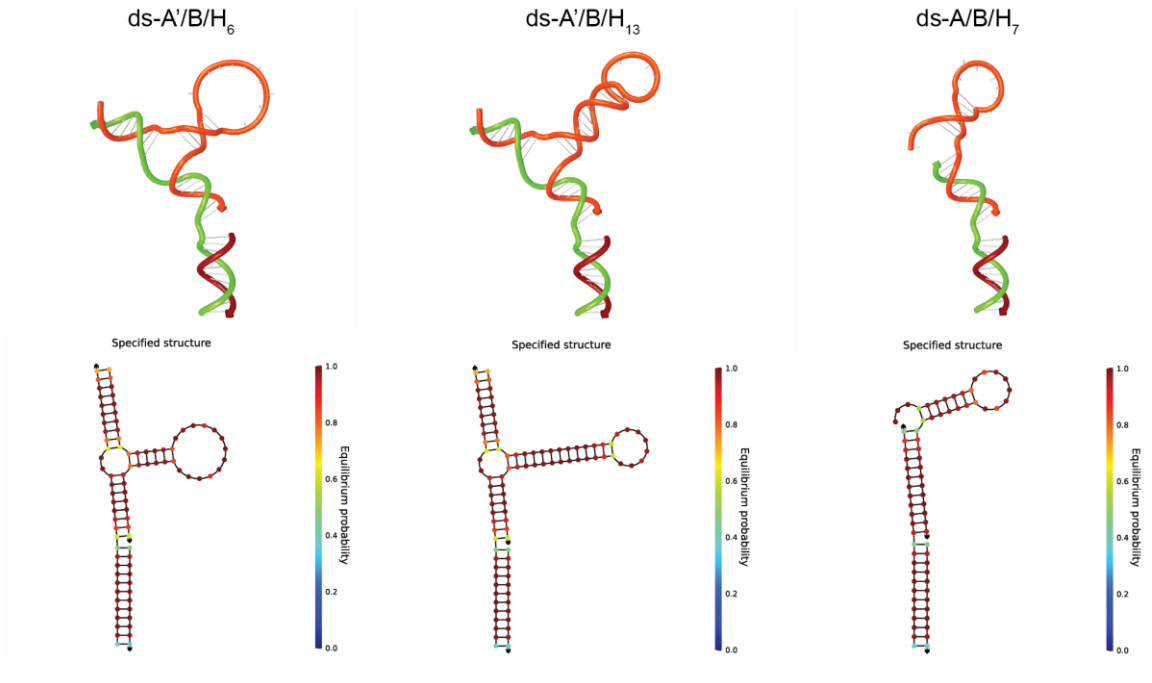

Figure 13. Predicted secondary structures formed by A or A' (long strand), B (short strand) and H (hairpin) using NUPACK analysis algorithms, with associated depiction of equilibrium base-pairing probabilities.

Table 3. Properties of the hairpins' structure and sequence, calculated using NUPACK analysis algorithms.

	Free energy[a] (kcal/mol)	Probability[b]	Ensemble defect[c] (nt)	Normalized ensemble defect[d] (%)	Length (nt)
H_6	-35.1	0.007	8.1	9.3	87
H_{13}	-43.3	0.005	8.7	9.1	96
H_7	-38.2	0.015	6.5	8.8	73

[a]Free energy of the specified secondary structure.
[b]The probability for the formation of this structure.
[c]The average number of nucleotides that are incorrectly paired at equilibrium relative to the specified secondary structure, evaluated over the Boltzmann-weighted ensemble of secondary structures (0 is best, N is worst, for a strand with N bases).
[d]The average percentage of nucleotides that are incorrectly of paired at equilibrium relative to the specified secondary structure (0 % is best, 100 % is worst).

Subsequently, the hybridization and displacement of the hairpins were studied in solution, with DNA strands not tethered on liposomes. The formation and disruption of DNA duplexes was characterized using native PAGE analysis (Figure 14). When using dsDNA functionalized with a terminal cholesterol group, it was observed that there was no retardation of dsDNA on the gel image (data not shown). This was attributed to the formation of micelles, preventing the migration of dsDNA into the pores of the gel due to their relatively large size.[24] Therefore, the following experiments were performed with DNA without cholesterol functionalization. Equal molar ratio of A (or A') and B were mixed and hybridized by first annealing them at 85 °C then cooling the solution slowly to 25 °C. The hairpin was also individually formed following the same process. Then, equal molar ratio of ds-A/B and H_7, and ds-A'/B and H_6 or H_{13} were mixed and hybridized for 1 h at room temperature. Finally, the resulting DNA solutions were diluted to 1.2 μM, 5 moles excess of target miR-29a were added to the constructs and left to react for 1 h at room temperature. Each stage was characterized using PAGE (Figure 14). In the first step, it was confirmed that ds-A/B and ds-A'/B were formed successfully (lanes 4 and 5). H_6 was not well hybridized with ds-A'/B (lane 9), but formed a duplex with the target (T) (lane 13). A fraction of H_{13} was hybridized with ds-A'/B (lane 10), but the displacement by T did not occur (lane 14). Only H_7 showed both complete hybridization with ds-A/B (lane 11) and displacement by T (lane 15), as further evidenced by the regeneration of the band corresponding to ds-A/B. Therefore, the hairpin sequence H_7 was chosen for the liposome fusion assay.

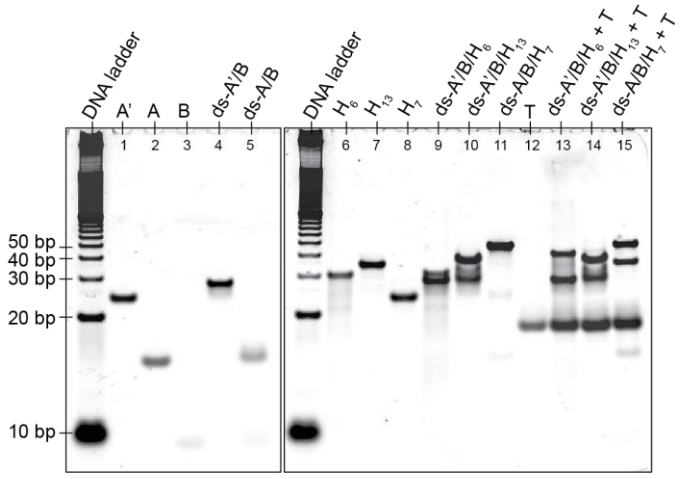

Figure 14. 15 % native PAGE analysis of hairpin hybridization with dsDNA and displacement by target miR-29a (T) of 3 hairpin designs: H_6, H_{13} and H_7.

2.3.3.2 Determination of the sensitivity of the assay

Following selection of H_7, the hairpin strand displacement mechanism was translated into a liposome fusion assay in the presence of target miR-29a. As in the previous section, DiL/DiD FRET assay was used to signal lipid mixing.

DiD and DiL liposomes were functionalized with ds-A/B/H_7 and ds-C/D respectively, and the ability of miR-29a to displace H_7 and trigger liposome fusion was studied (Figure 15). DiD liposomes functionalized with ds-A/B/H_7 were incubated with various quantities of miR-29a for 1 h. Then, equal volumes of DiL and DiD liposomes were mixed and the evolution of the FRET ratio was measured over time (Figure 15a). In absence of miR-29a, the FRET ratio did not increase significantly over time, showing that H_7 was successfully hybridized on ds-A/B and was able to prevent liposome fusion. As the quantity of miR-29a increased, the FRET ratio increased, demonstrating that miR-29a was able to displace H_7 and trigger liposome fusion. In order to study the sensitivity of the bulk assay, the dose-response curve obtained after 30 minutes of incubating DiL and DiD liposomes was plotted (Figure 15b). The limit of detection was calculated by first determining the z-value ($z = \text{blank} + 3\sigma$) where σ is the standard deviation of the blank. The limit of detection was obtained by reporting the z-value in the equation of the model curve, and was determined to be 18 nM. This LOD value was 2 orders of magnitude higher than the LOD calculated for the liposome fusion inhibition assay. This can partly be explained by the increased amount of dsDNA copies functionalizing the liposomes used in this assay compared with the liposome fusion inhibition assay (100 vs. 10 dsDNA copies), as well as the reduced assay temperature (25 °C vs. 37 °C), which implies that more moles of target are needed to observe a FRET response in the case of the liposome fusion promotion assay.

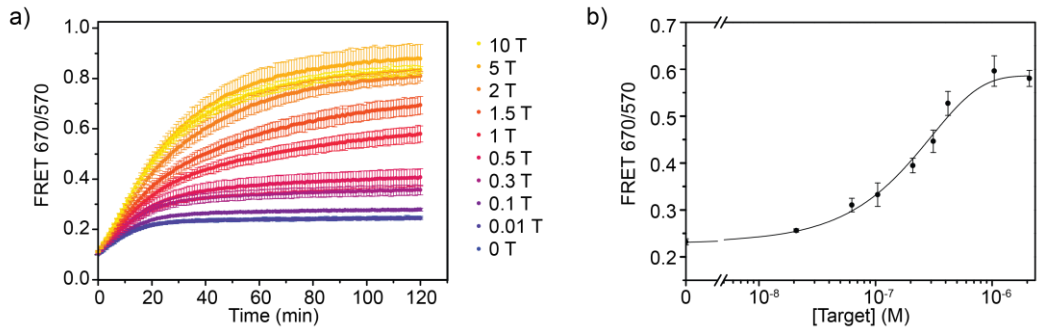

Figure 15. Evaluation of the sensitivity of DNA-mediated liposome fusion assay for miR-29a detection: a) evolution of FRET signals over time showing the kinetics of DNA-mediated liposome fusion in the presence of different concentrations of target miR-29a (where 1 T corresponds to 2.1×10^{-7} M) and b) corresponding dose-response curve obtained after 30 min of mixing DiL- and DiD-labelled DNA-functionalized liposomes (n=3).

2.3.3.3 Determination of the specificity of the assay

Next the specificity of the assay was determined (Figure 16). Similarly to the liposome fusion inhibition mechanism, the ability of the assay to discriminate between the perfectly complementary sequence miR-29a, and its miR-29 family counterparts miR-29b and miR-29c, as well as artificially-designed miRNA sequences comprising respectively 1, 2 or 3 nucleotide mismatches: miR-29a-1MM, miR-29a-2MM and miR-29a-3MM (Table 2) was tested. DiD liposomes functionalized with ds-A/B/H_7 were incubated with 1 molar equivalent of different miRNAs. Subsequently, equal volumes of DiL and DiD liposomes were mixed, and the evolution of the FRET signal was measured over time (Figure 16a). Only the fully complementary target, miR-29a, was able to trigger liposome fusion, while all the other sequences did not show a significant increase in the FRET ratio compared to the signal measured in absence of target. Figure 16b summarizes the relative values of the FRET ratios at 30 minutes of incubation obtained with each miRNA compared to the control, and showed that this assay has a high specificity, as it enabled discriminating between sequences with one nucleotide mismatch. This high specificity is attributed to the fact that displacing the hairpin requires high stringency.[25]

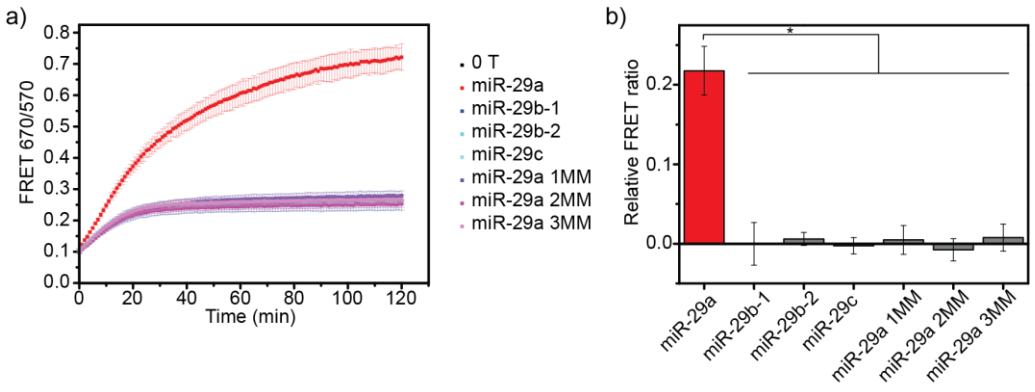

Figure 16. Evaluation of the specificity of DNA-mediated liposome fusion assay for miR-29a detection: a) evolution of FRET signals over time showing the kinetics of DNA-mediated liposome fusion in the presence of various miRNA sequences at a concentration of 2.1×10^{-7} M. b) Corresponding bar chart representing the FRET ratio values for each miRNA sequence after 30 min of mixing DiL- and DiD-labelled DNA-functionalized liposomes. n=3, *p < 0.05 (ANOVA followed by Tukey *post-hoc* test).

2.3.3.4 2-color fluorescence correlation microscopy analysis

The experiments for 2-color fluorescence correlation microscopy analysis were carried in the laboratory of Prof. Fredrik Höök at Chalmers University of Technology (Gothenburg, Sweden). I prepared all materials and acquired the data with Olov Wahlsten. Dataa was analysed using MATLAB scripts written by Dr Stephan Block (currently at Freie Universität Berlin, Berlin, Germany); data analysis was performed by Dr Stephan Block with active discussion between Olov Wahlsten, Dr Stephan Block, and I.

To further improve the understanding of the assay for miRNA detection, a suspension-based 2-color fluorescence correlation microscopy method was created allowing extracting FRET signals from imaging a small amount of liposomes (< 50).[26] The setup is a suspension-based 2-color fluorescence microscope, which relies on the direct excitation of DiL-labelled liposomes by a laser source (488 nm) via an optical fibre inserted in the sample chamber (Figure 17a). As the target miRNA displaces hairpin DNA, FRETing fusion complexes are formed. Using an image splitter and a suitable fluorescence filter set (Figure 17a), it is possible to separate the emitted light originating from DiL liposomes (centred around 570 nm; denoted as “green channel” in the following) and fused DiL and DiD liposome complexes (centred around 670 nm; “red channel”). The separated channels are then projected onto different parts of the camera sensor, allowing to simultaneously image the same field of view (FOV) using the different emission filters, such that fused liposome complexes exhibiting FRET appear in the red channel, whereas non-fused DiL liposomes only appear in the green channel (Figure 17b, as indicated by the coloured boxes).

The increased sensitivity of the 2-color fluorescence microscopy setup was exploited and liposomes solutions were mixed at 10 pM concentration for the target incubation step, and then diluted to 2 pM before performing the measurements (compared to 1.7 nM liposomes concentration used for the microplate reader setup). Various miR-29a concentrations were added to solutions containing 10 pM DiL and DiD liposomes and left to equilibrate for 1 h at 25 °C. The liposomes were then diluted to 2 pM before being measured in the 2-color fluorescence microscopy setup. The FOV was placed approximately 200 µm away from the optical fibre facet. Duplicates of 5 measurements of 3000 frames each were performed and compiled, yielding a total measurement time of about 1000 seconds for each miRNA concentration.

A direct attempt to assess the FRET ratio of single liposomes (*i.e.*, single particle tracking of liposomes in both channels followed by determination of their fluorescence intensity in each channel and calculation of the FRET ratio for each tracked liposome) gave only broad distributions of the extracted FRET ratio and did not permit to resolve any dose-response curve as in Figure 15b. This behaviour was attributed to the random movement of the liposomes through the illumination profile, which leads to ill-defined illumination intensities. In particular, liposomes that are not close to the focal plane may be visible in one channel but drop below the detection limit in the other, thereby causing large errors in the determination of the FRET ratio and broadening of the extracted distributions. Hence, the random movement, which is used to co-localize liposomes in both channels, also impedes reliable intensity extraction.

This motivated to rather use intensities integrated over the entire channels (yielding intensity traces $I_g(t)$ and $I_r(t)$ for the green and red channel, respectively), which is similar to the microplate reader assay but has lower background noise since the illumination and readout areas are much smaller. A visual inspection of $I_g(t)$ and $I_r(t)$ (Figure 17c) showed pronounced fluctuations caused by liposomes entering and leaving the FOV. Most of the time, these fluctuations occurred simultaneously in both channels (Figure 17c, black arrows). These correlated fluctuations were attributed to DiL-labelled liposomes, showing pronounced emission into the green channel but also small bleed-through into the red one. However, uncorrelated fluctuations were observed as well (Figure 17c, red arrow), which showed large intensity increases in the red channel, while no increase or even a decrease in intensity was found in the green channel. Those fluctuations were attributed to fused FRETing liposomes entering and leaving the field of view, since they are expected to cause strong emission in the red but no emission in the green channel.

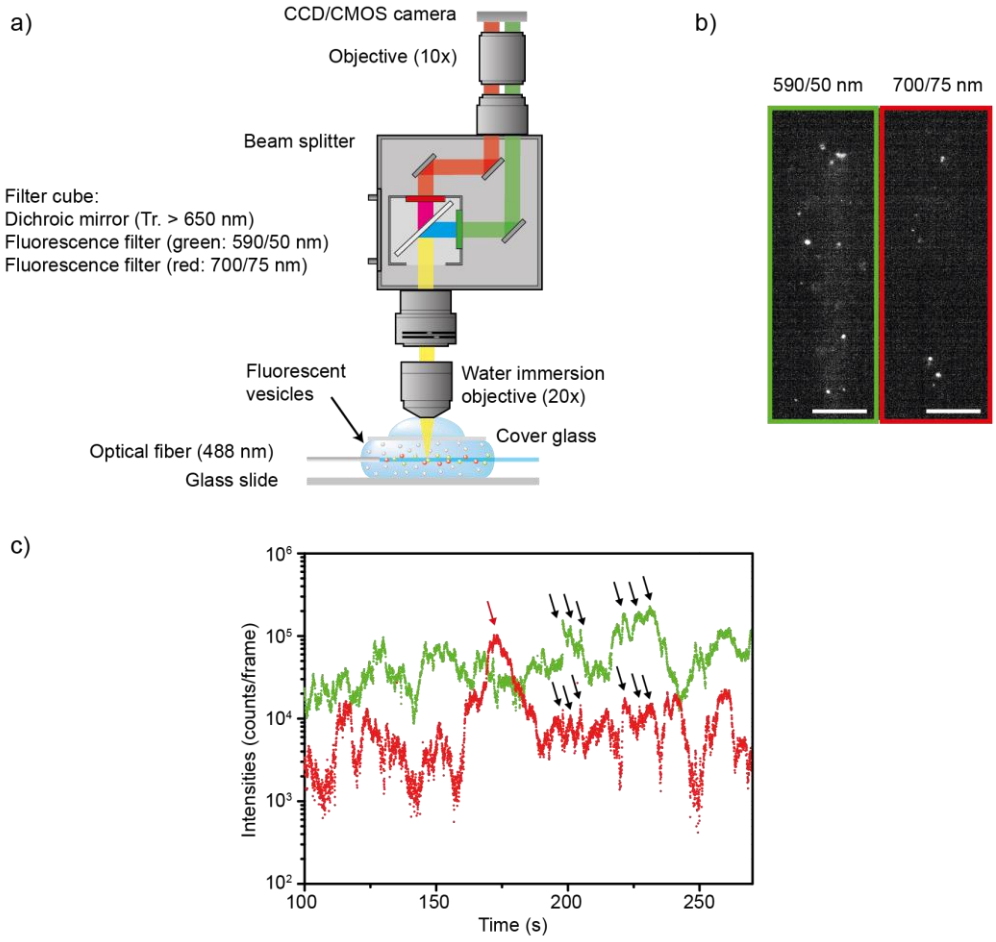

Figure 17. a) Schematic (not to scale) of the 2-color fluorescence microscopy setup. Liposomes in suspension in the sample chamber are excited using a laser source at 488 nm via an optical fiber. A filter cube and beam splitter setup allows the separation of the emitted light into two distinct channels. b) Micrograph snapshot illustrating how the field of view of the camera is split in two. The left side is referred to as the green channel (590/50 nm) and the right as the red channel (700/75 nm) (Scale bars: 25 µm). c) Fluctuations in the intensities $I_g(t)$ and $I_r(t)$ (integrated over the entire green and red channel, respectively) are caused by non-FRETing DiL (black arrow) and fused FRETing liposomes entering and leaving the field of view.

The feature of liposomes entering and exiting the FOV is conceptually similar to the method fluorescence correlation spectroscopy (FCS), in which single, dye-labelled objects enter and exit a defined optical readout volume (usually the diffraction-limited spot of a confocal microscope) causing fluctuations in the recorded fluorescence intensity $I(t)$, which are proportional to the temporal fluctuations in $N(t)$, the number of labelled objects within the readout volume.[27–29] If only one species is investigated using such a setup, it can be shown that the time average of $N(t)$,

$$N = < N(t) >, \quad (1)$$

can be extracted from the autocorrelation function $G(\tau)$ of $I(t)$

$$G(\tau) = \frac{< I(t) \cdot I(t+\tau) >}{< I(t) >^2} \tag{2}$$

based on the identification

$$G(\tau) = 1 + \frac{1}{N} \cdot \frac{1}{1+\tau/\tau_D} \cdot \frac{1}{\sqrt{1+z^2\tau/\tau_D}} \tag{3}$$

with τ denoting the lag time (used in the calculation of the autocorrelation function), τ_D the object's mean residence time within the confocal readout volume, and z the ratio of radial to axial dimensions of the confocal readout volume.[30] It is to be noted that Eq. 3 includes only fluctuations caused by temporal changes in $N(t)$, which is the only source of fluctuations that can be resolved using the 2-color fluorescence microscopy setup (acquisition rate ~ 30 Hz). FCS implementations achieve acquisition rates on the order of 10 MHz, making it necessary to include additional contributions in Eq. 3 like triplet dynamics. Nevertheless, the average number of objects within the observation volume, N, can be extracted from Eq. 2 and 3 in the limit of $\tau \to 0$:

$$N = 1/g(0) \text{ , with } g(\tau) = G(\tau) - 1 \tag{4}$$

Eq. 4 reflects the rare situation that a signal (here the magnitude of the autocorrelation function) becomes enhanced with a decreasing object concentration, which is a consequence of the fact that entering and exiting of a small number of objects in the readout volume creates larger fluctuations in $I(t)$ (with respect to the time average value) than a larger number. Hence, fluctuation-based approaches typically work best for small N, an advantage that has to be paid by increased observation times to arrive at feasible signal-to-noise ratios.

A direct application of this concept to the liposome fusion assay failed, however, since even in absence of any target DNA, liposomes were detectable in the red channel. Most of these liposomes showed weak intensity in the red and strong intensity in the green channel, suggesting a bleed-through mechanism to be responsible for this observation, either caused by non-specific (partial) fusion of DiD and DiL liposomes (inducing small FRETing) or lipid transfer between DiD and DiL liposomes. Indications for this bleed-through mechanism can be found in Figure 17c, showing correlated fluctuations (black arrows) in $I_g(t)$ and $I_r(t)$, i.e. the intensities of the green and red channel, respectively.

As the number concentration of DiL liposomes in the experiments was usually larger than the number concentration of fused FRETing liposomes, a direct application of Eqs 2 - 4 to $I_r(t)$ gives a N value that will be dominated by DiL liposomes. However, taking the bleed-through into account, it is possible to express $I_r(t)$ by

$$I_r(t) = \gamma \cdot I_g(t) + \Gamma \cdot N_{FRET}(t) \tag{5}$$

with γ denoting the average bleed-through factor between both channels, $N_{FRET}(t)$ and the number and brightness of FRETing liposomes in the FOV. This can be further transformed into:

$$\frac{I_r(t)}{I_g(t)} = \gamma + \Gamma \cdot \frac{N_{FRET}(t)}{I_g(t)} \tag{6}$$

Under the assumption that the number concentration of DiL liposomes is larger than the number concentration of fused FRETing liposomes, which is fulfilled in our experiments, the fluctuations in $I_g(t)$ (relative to its average value) will be smaller than the corresponding fluctuations in N_{FRET}, making the autocorrelation function of the ratio

$$R(t) = I_r(t) / I_g(t) - \gamma \tag{7}$$

strongly dependent on N_{FRET}:

$$\lim_{\tau \to 0} \frac{< R(t) \cdot R(t+\tau) >}{< R(t) >^2} \approx \frac{1}{N_{FRET}} \tag{8}$$

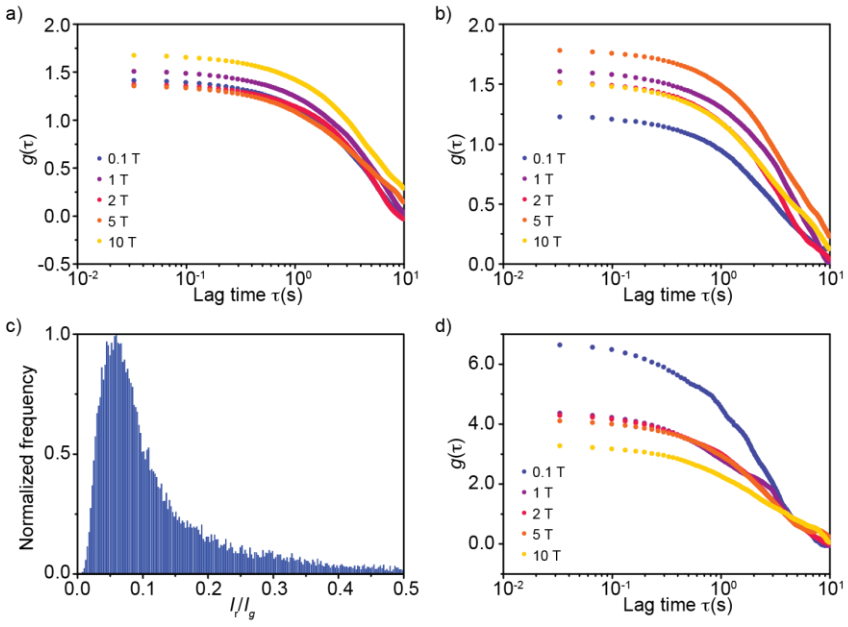

Figure 18. Autocorrelation functions of a) $I_g(t)$, b) $I_r(t)$, and d) $I_r(t)/I_g(t) - \gamma$, with γ = 0.065 as determined from the peak position in c) showing the distribution of the ratio $I_r(t)/I_g(t)$. The intensity traces were recorded from solutions containing 10 pM DiL and DiD liposomes mixed with the indicated amount of miR-29a (where 1 T corresponds to 7.2×10^{-10} M) followed by further dilution to a liposome concentration of 2 pM. Shown are autocorrelation functions averaged over 2 independent sample sets covering 5 measurements each.

This is illustrated in Figure 18 showing the autocorrelation functions of $I_g(t)$ and $I_r(t)$ for miR-29a concentrations as indicated. Due to bleed-through and the larger number concentration of DiL liposomes with respect to fused FRETing liposomes, the $g(0)$ values are mainly sensitive to the number of DiL liposomes within the field of view, indicated by non-systematic fluctuations of the plateau of the autocorrelation function observed at short lag times. Analysing instead the ratio of $I_r(t)$ and $I_g(t)$, as introduced by Eq. 7, solves this problem. The average bleed-through factor γ was determined from the distribution of the ratio $I_g(t)$ and $I_r(t)$, typically showing a pronounced peak at 0.065 followed by a broad tail distribution (Figure 18c), motivating to set γ = 0.065 for all measurements shown in Figure 18d. The corresponding autocorrelation function of the intensity ratio $R(t)$ clearly shows a strong dependence of miR-29a concentration on the $g(0)$ values (indicated by a systematic decrease of the autocorrelation function plateau at short lag times for increasing DNA concentration) (Figure 18d), allowing the estimation of the average number N_{FRET} of fused FRETing liposomes in the FOV using Eq. 8.

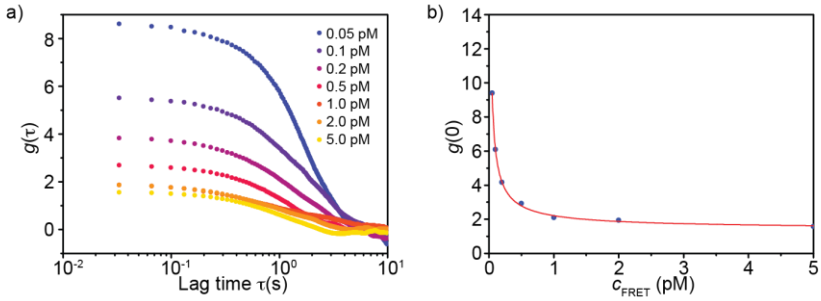

Figure 19. a) Autocorrelation functions of the intensity ratio $I_r(t)/I_g(t)$ for solutions containing only FRETing liposomes (with bulk concentrations c_{FRET} as indicated). This control clearly shows that the $g(0)$ value decreases with increasing concentration of FRETing liposomes, as expected by Eq. 8, although saturation effects are observed for c_{FRET} > 1 pM. b) Extracted $g(0)$ values (open circles) and fit (red line) using the relation $g(0)$ = 0.56 pM/c_{FRET} + 1.55, which was used to determine the bulk concentration of FRETing vesicles based on the measured $g(0)$ values.

In order to quantitatively extract c_{FRET} from $g(0)$, the same data analysis was performed on additional measurements involving solutions containing only FRETing liposomes of known concentration c_{FRET} (Figure 19). Based on Eq. 8, it is expected that the $g(0)$ value of the autocorrelation function decreases with increasing N_{FRET}, a trend which is qualitatively observed in Figure 19a. On a quantitative basis, however, deviations from Eq. 8 are observed (Figure 19b), which are attributed to saturation effects in the recorded fluctuations (for c_{FRET} > 1 pM), a feature that is frequently observed in FCS measurements performed at too high analyte concentrations. Nevertheless, these measurements allowed to calibrate the relationship between concentration of FRETing vesicle and $g(0)$ finally yielding:

$$c_{FRET} = \frac{0.56\text{pM}}{g(0) - 1.55} \qquad (9)$$

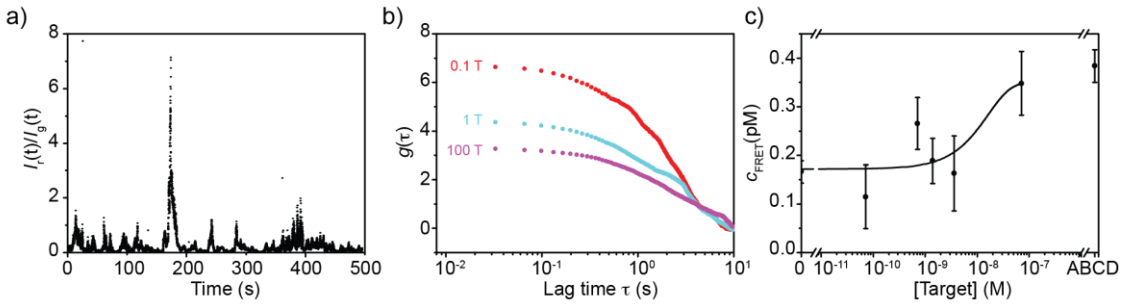

Figure 20. a) Ratio $I_r(t)/I_g(t)$ of the total intensity of the red channel over the green channel. b) Representative autocorrelation functions of $I_r(t)/I_g(t)$ - γ (with γ = 0.065 the average bleed-through factor), for miR-29a concentrations as indicated (where 1 T corresponds to 7.2×10^{-10} M). c) Dose-response curve obtained using the imaging fluorometer setup (averaged over 2 independent sample sets covering 5 measurements each). ABCD = DiD liposomes functionalized with ds-A/B (without H_7) mixed with DiL liposomes functionalized with ds-C/D, representing maximum fusion.

Figure 20 summarizes the approach taken to resolve the dose-response curve using the 2-color fluorescence microscopy setup. Figure 20a shows the normalized intensity traces obtained from the imaging fluorometer setup, $I_r(t)/I_g(t)$; as described above this normalization was necessary since fluctuations in $I_r(t)$ are caused by two processes, bleed-through of DiL liposomes and fused FRETing liposomes, making $g(0)$ more sensitive of the number of DiL liposomes than FRETing DiD liposomes. Since DiL liposomes cause correlated fluctuations in $I_g(t)$ and $I_r(t)$, using $I_r(t)/I_g(t)$ eliminates the sensitivity on DiL liposomes but boosts FRET-based fluctuations (Figure 20a), making $g(0)$ mainly sensitive to the number of FRETing DiD liposomes. Representative examples for the autocorrelation function of $I_r(t)/I_g(t)$ are shown in Figure 20b, clearly indicating a decrease in $g(0)$ with increasing miR-29a concentration, which is, due to $N\sim1/g(0)$, indicative for an increase in the number of FRETing DiD liposomes N_{FRET} in the field of view. Calibration of this approach using solutions containing only FRETing vesicles of known bulk concentration c_{FRET} allowed extracting a dose-response curve (Figure 20c) similar to the bulk assay but the inflexion point of the dose-response curve was shifted to approximately 2 orders of magnitude lower miR-29a concentration.

2.4 Conclusion

In this Chapter, the development of novel mechanisms for the detection of miR-29a, which is involved in host response to influenza virus infection and has been recognized as a suitable biomarker, was demonstrated. Following a biomimetic approach enabled harnessing the efficacy and simplicity of highly evolved natural processes. Here, the source of inspiration was membrane fusion, which presents a highly selective recognition mechanism that has been extensively studied using model systems such as DNA-mediated liposome fusion. In addition to being useful models for membrane fusion, liposomes and DNA constructs are also attractive tools for biosensing. Liposomes can encapsulate a large payload of various signal markers allowing signal amplification, and their surface can be easily functionalized. DNA is easily synthesized, and sequence-directed hybridization of nucleic acids provides a high level of control over the specific self-assembly of nanostructures. This study demonstrates the sensitive and specific detection of miR-29a using novel mechanisms based on DNA-mediated liposome fusion. As such, this study constitutes the first example of target-mediated control over liposome fusion. In these assays the presence of miRNA target either inhibited or promoted liposome fusion. Lipid mixing was used as the reporter signal, and was assessed using DiL and DiD fluorophores FRET pairs acting as lipophilic dyes in the liposomes' membrane.

In the case of liposome fusion inhibition mechanism, miR-29a was able to hybridize on the toehold of double-stranded DNA (dsDNA) functionalizing liposomes, blocking the further hybridization with complementary DNA and inhibiting liposome fusion. The influence of DNA functionalization was studied, and it was found was the amount of lipid mixing was the highest when liposomes were functionalized with 100 dsDNA copies. Increasing the temperature to 37 °C resulted in faster fusion kinetics and increased lipid mixing. When the liposomes were pre-incubated with miR-29a, the amount of lipid mixing was decreased, proving the successful hybridization of miR-29a on the dsDNA toehold. Changing the number of dsDNA functionalizing the surface allowed covering a variety of dynamic ranges. The influence of liposome concentration on the lipid mixing kinetics was studied, and it was found to not be a limiting factor. Fusion kinetics could be measured using liposomes diluted to 10 μM, however the signals generated were approaching the limit of detection for the laboratory instrumentation, therefore a liposome concentration of 100 μM was selected. In order to decrease the limit of detection of the assay, it is advantageous to have a small amount of dsDNA copies functionalizing the liposomes; for evaluation of the assay sensitivity, 10 dsDNA copies per liposomes were selected. Various quantities of miR-29a were added to a solution containing DiL and DiD liposomes functionalized with 10 dsDNA copies and the kinetics of fusion were measured at 37 °C. The

dose-response curve was constructed by plotting the FRET ratio against miR-29a concentration after 15 min of incubation, and allowed to extract a sub-nanomolar limit of detection (LOD) (0.5 nM). Furthermore, the specificity of the assay was assessed, by screening the perfectly complementary miR-29a sequence against miR-29 family members as well as artificially-designed miRNAs containing 1, 2 or 3 nucleotide mismatches. The assay was selective for miR-29a, however miRNA with one nucleotide mismatch was also able to inhibit liposome fusion, although to a lesser extent.

In the case of liposome fusion promotion mechanism, miR-29a sequence is complementary to a hairpin DNA, which is pre-hybridized on the toehold of dsDNA functionalizing liposomes. Upon hybridization with miR-29a, the hairpin reveals the toehold of dsDNA, allowing complementary dsDNA to hybridize and driving liposome fusion. First, the design of hairpin DNA was optimized *in silico* and tested in solution using PAGE analysis. The optimized hairpin sequence was then transferred in the liposome fusion assay, first visualizing the evolution of FRET signal generated by the liposome fusion assay using ensemble fluorescence measurements. It was demonstrated that miR-29a was able to promote liposome fusion, and the dose-response derived from the assay kinetics yielded a LOD in the nanomolar range (18 nM). Similarly with the liposome fusion inhibition assay, the specificity towards the fully complementary miR-29a sequence was tested. This assay was highly specific for miR-29a, and a sequence containing only one nucleotide mismatch did not cause significant fusion compared to control. This high specificity was attributed to the stringency enabled by the hairpin. To further improve both the understanding of the fusion mechanism, and to decrease the LOD, the assay was analysed using a 2-color fluorescence microscope. In this setup, liposomes in suspension are excited by a laser source, and the light emitted by the liposomes entering the field of view (FOV) is collected and spatially separated onto two channels, by using a beam splitter placed before the camera and distinct fluorescence filter sets for each channel. The imaging fluorometer setup was initially designed to offer the possibility of determining the fluorescence intensity of single liposomes simultaneously at two distinct wavelength intervals, thereby allowing to extract FRET ratios of single liposomes that are suspended in bulk solution using co-localization analysis. The extracted FRET ratio distributions were broader than expected and did not permit to extract dose-response curves similar to the bulk assay measurements. Instead of analysing single liposome intensity values, the intensity of the whole FOV was summed. Using an analytical approach similar to fluorescence correlation spectroscopy (FCS) enabled to derive the number of FRETing liposomes from autocorrelation functions, and to build-up a dose-response curve displaying increased sensitivity for the detection of miR-29a.

In summary, this work demonstrates the potential of using interactions with target molecules to mediate the liposome fusion process, and of achieving ultrasensitive detection using such approach. It can be anticipated that further tuning of liposome composition, surface-bound DNA fusion mechanisms, and fluorescent reporter molecules will lead to even greater sensitivity, and that this mechanism has potential for use in disease diagnostics targeting miRNA and other nucleic acids.

References

1. E. Busseron, Y. Ruff, E. Moulin, N. Giuseppone. *Nanoscale*, 2013, **5**, 7098–7140.
2. P. D. Howes, R. Chandrawati, M. M. Stevens. *Science*, 2014, **346**, 1247390–1247400.
3. C. Jianrong, M. Yuqing, H. Nongyue, W. Xiaohua, L. Sijiao. *Biotechnol. Adv.*, 2004, **22**, 505–518.
4. D. P. Bartel. *Cell*, 2004, **116**, 281–297.
5. J. Winter, S. Jung, S. Keller, R. I. Gregory, S. Diederichs. *Nat. Cell Biol.*, 2009, **11**, 228–234.
6. E. J. Carthew, Richard W. and Sontheimer. *Cell*, 2009, **136**, 642–655.
7. F. Causa, A. Aliberti, A. M. Cusano, E. Battista, P. A. Netti. *J. Am. Chem. Soc.*, 2015, **137**, 1758–1761.
8. P. Zhang, Z. He, C. Wang, J. Chen, J. Zhao, X. Zhu, C. Z. Li, Q. Min, J. J. Zhu. *ACS Nano*, 2015, **9**, 789–798.
9. A. Esquela-Kerscher, F. J. Slack. *Nat. Rev. Cancer*, 2006, **6**, 259–269.
10. J. H. Lee, H.-E. Jin, M. Desai, S. Ren, S. Kim, S.-W. Lee. *Nanoscale*, 2015, 18379–18391.
11. G. Stengel, R. Zahn, F. Höök. *J. Am. Chem. Soc.*, 2007, **129**, 9584–9585.
12. G. Stengel, L. Simonsson, R. A. Campbell, F. Höök. *J. Phys. Chem. B*, 2008, **112**, 8264–8274.
13. H. Song, Q. Wang, Y. Guo, S. Liu, R. Song, X. Gao, L. Dai, B. Li, D. Zhang, J. Cheng. *BMC Infect. Dis.*, 2013, **13**, 257–271.
14. J. F. C. Loo, S. S. Wang, F. Peng, J. A. He, L. He, Y. C. Guo, D. Y. Gu, H. C. Kwok, S. Y. Wu, H. P. Ho, W. D. Xie, Y. H. Shao, S. K. Kong. *Analyst*, 2015, **140**, 4566–4575.
15. M. Kaforou, V. J. Wright, T. Oni, N. French, S. T. Anderson, N. Bangani, C. M. Banwell, A. J. Brent, A. C. Crampin, H. M. Dockrell, B. Eley, R. S. Heyderman, M. L. Hibberd, F. Kern, P. R. Langford, L. Ling, M. Mendelson, T. H. Ottenhoff, F. Zgambo, R. J. Wilkinson, L. J. Coin, M. Levin. *PLoS Med.*, 2013, **10**, e1001538.
16. J. N. Zadeh, C. D. Steenberg, J. S. Bois, B. R. Wolfe, M. B. Pierce, A. R. Khan, R. M. Dirks, N. A. Pierce. *J. Comput. Chem.*, 2011, **32**, 170–173.
17. NUPACK Nucleic Acid Package http://www.nupack.org (accessed Jan 8, 2016).
18. G. van den Bogaart, M. G. Holt, G. Bunt, D. Riedel, F. S. Wouters, R. Jahn. *Nat. Struct. Mol. Biol.*, 2010, **17**, 358–364.
19. S. M. Christensen, M. W. Mortensen, D. G. Stamou. *Biophys. J.*, 2011, **100**, 957–967.
20. Y. M. Chan, B. van Lengerich, S. G. Boxer. *Proc. Natl. Acad. Sci. U. S. A.*, 2009, **106**, 979–984.
21. V. S. Malinin, E. Haque, B. R. Lentz. *Biochemistry*, 2001, **40**, 8292–8299.
22. J. Diao, Y. Ishitsuka, H. Lee, C. Joo, Z. Su, S. Syed, Y.-K. Shin, T.-Y. Yoon, T. Ha. *Nat. Protoc.*, 2012, **7**, 921–934.

23. F. Ma, S. Xu, X. Liu, Q. Zhang, X. Xu, M. Liu, M. Hua, N. Li, H. Yao, X. Cao. *Nat. Immunol.*, 2011, **12**, 861–869.

24. A. Johnson-Buck, S. Jiang, H. Yan, N. G. Walter. *ACS Nano*, 2014, **8**, 5641–5649.

25. G. Bonnet, S. Tyagi, A. Libchaber, F. R. Kramer. *Proc. Natl. Acad. Sci. U. S. A.*, 1999, **96**, 6171–6176.

26. A. Cypionka, A. Stein, J. M. Hernandez, H. Hippchen, R. Jahn, P. J. Walla. *Proc. Natl. Acad. Sci. U. S. A.*, 2009, **106**, 18575–18580.

27. E. L. Elson, D. Magde. *Biopolymers*, 1974, **13**, 1–27.

28. D. Magde, E. L. Elson, W. W. Webb. *Biopolymers*, 1974, **13**, 29–61.

29. R. Rigler, Ü. Mets, J. Widengren, P. Kask. *Eur. Biophys. J.*, 1993, **22**, 169–175.

30. J. Langowski. *Methods Cell Biol.*, 2008, **85**, 471–484.

Chapter 3

Synthesis of functional dyes for improved signal generation in biosensing assays

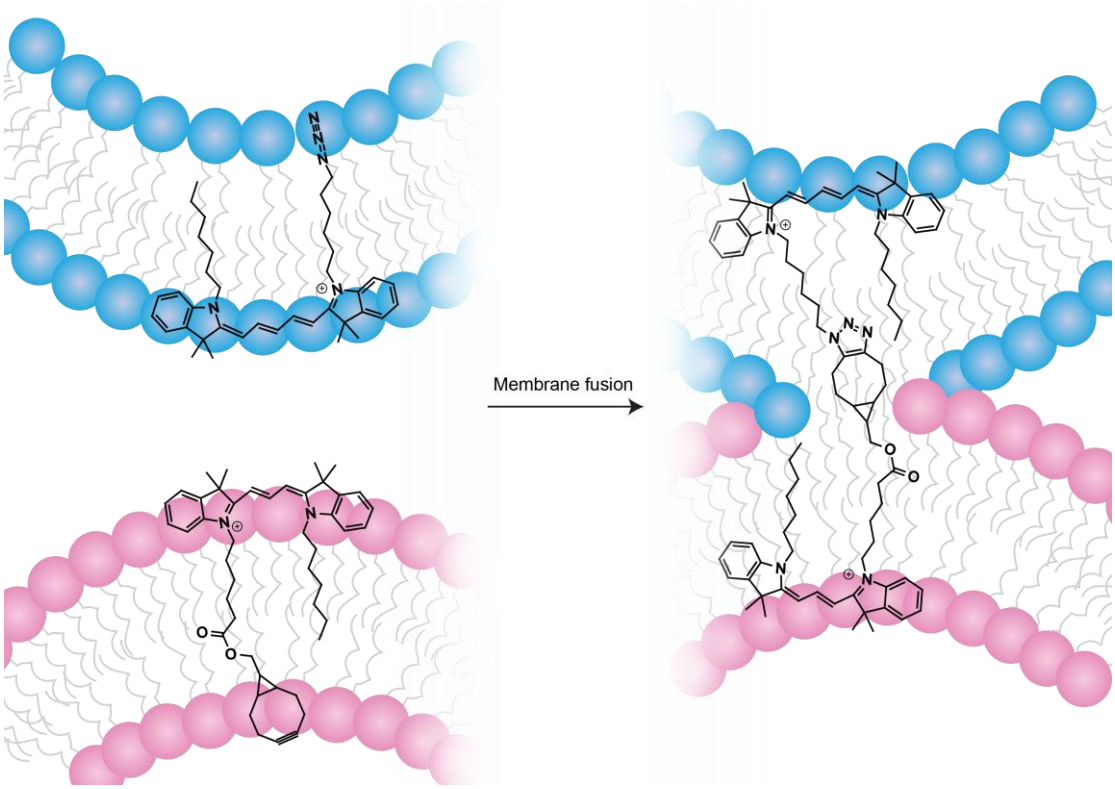

3.1 Introduction

Fluorescence and Förster resonance energy transfer-based lipid mixing assays, which are reviewed in Chapter 1 section 1.1.2.3, represent powerful tools for investigating the mechanisms of liposome fusion. In Chapter 2, liposome fusion was used as a signal transducer and amplifier for the detection of a flu biomarker, microRNA miR-29a. The lipid mixing assay used in this study was based on lipophilic FRET pairs DiL and DiD, inserted in the lipid bilayer. In order to increase the sensitivity of the assay, it is advantageous to maximize the FRET efficiency between the donor and acceptor dyes. An increased signal will enable the liposome concentration used in the assay to be decreased, and therefore lower the limit of detection for the target miRNA.

In this Chapter, covalent binding of FRET pair dyes inside lipid bilayers is investigated as a means to improve FRET efficiency. It was hypothesized that when the dyes are covalently bound, they are maintained in close proximity allowing efficient FRET to occur. In contrast, when the dyes are not covalently bound, they diffuse freely in the lipid bilayer resulting in a lower FRET efficiency based only on dye concentration.

In order to achieve covalent binding of the dyes in the lipid bilayer, there is a need for an uncatalysed, fast reaction, which can proceed in the unique environment that represents the lipid bilayer. Indeed, the lipid bilayer acts as a barrier to the permeation of polar molecules, due to the hydrophobicity of its interior.[1] Hydrophobicity of the bilayer is determined by the extent of water penetration and is dependent on bilayer composition: incorporation of unsaturated alkyl chains or cholesterol increases the hydrophobicity.[1] For saturated phosphatidylcholine (PC) membranes, the hydrophobicity at the centre of the bilayer can approach those of 2-propanol and 1-octanol.[1] Inclusion of cholesterol in the bilayer increases the hydrophobicity, bringing the dielectric constant closer to that of hexane.[1] Therefore an adequate reaction for the ligation of the dyes in lipid bilayers has to be able to proceed in an apolar and hydrophobic environment, be un-catalysed, and fast.

Within the organic chemistry toolbox, a limited set of reactions, which have been engineered to perform site-selective conjugation in living cells and organisms, fulfil these criteria. Bio-orthogonal chemistry has been developed to tag naturally occurring biomolecules in their native settings, using highly selective and biocompatible chemical reactions.[2,3] In particular, reactions involving azides have found great utility, due to the small size, stability under physiological conditions, and ease of synthetic accessibility of the azide group.[4] Such reactions include the Staudinger-Bertozzi ligation,[5,6] copper-catalysed azide-alkyne cycloaddition (CuAAC),[7] and strain-promoted azide-alkyne cycloaddition (SPAAC),[8] often referred to as “copper-free click”

chemistry. The SPAAC reaction between an azide and a cyclooctyne was first reported in 1953,[9] and subsequently introduced for applications in living systems by the group of Bertozzi.[8] In this reaction, the alkyne of a cyclooctyne is activated by ring strain, destabilizing the ground state *versus* the transition state of the reaction, enabling the [3+2] cycloaddition to occur readily under physiological conditions without the need for metal catalysts (Figure 1c).[8]

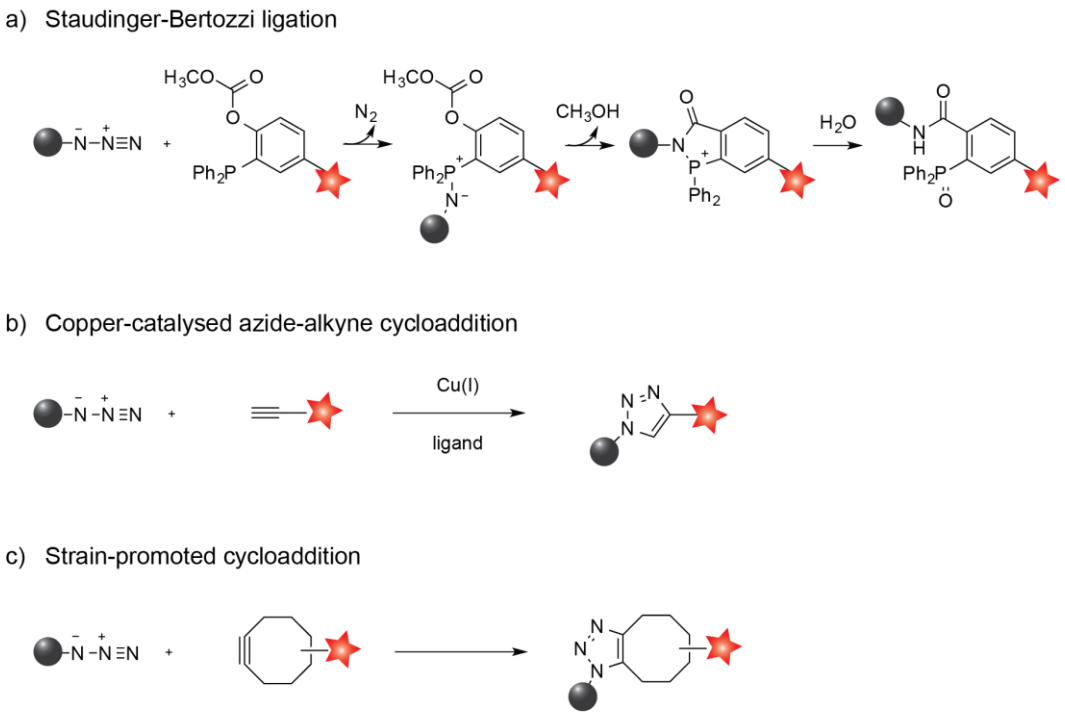

Figure 1. Example of bio-orthogonal reactions. a) Staudinger-Bertozzi ligation. b) Copper-catalysed azide-alkyne cycloaddition (CuAAC). c) Strain-promoted azide-alkyne cycloaddition (SPAAC). Adapted from Spicer *et al.*[3]

The reaction rate constants of unsubstituted cyclooctynes are not as high as those of the Staudinger-Bertozzi ligation.[10] Much work has therefore focussed on generating modified cyclooctyne derivatives with increased reactivity, due to steric or electronic effects, such as fluorine-substituted cyclooctyne or dibenzocyclooctyne derivatives.[10–13]

Most bio-orthogonal chemistry reactions have been optimized to proceed in water, however, the high hydrophobicity of cyclooctynes has also prompted the study of SPAAC reactions in hydrophobic environments, with dramatic rate enhancements up to 1000-fold being observed.[14,15] Therefore, this reaction has great potential for the purpose of ligating dyes within lipid bilayers (Figure 2).

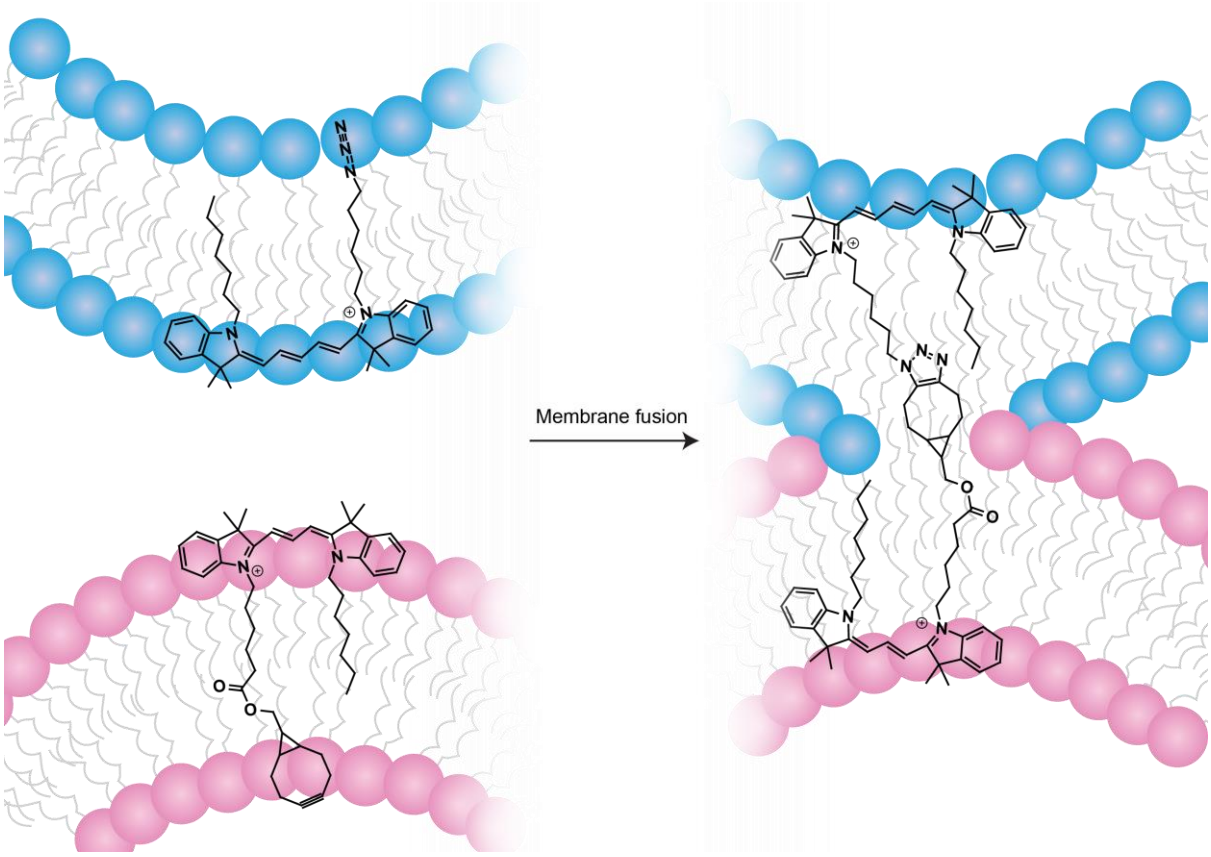

Figure 2. Upon lipid mixing, the functional dyes undergo cycloaddition to form the covalently bound product.

In this Chapter, the synthesis of functional lipophilic dyes, based on Cy3 and Cy5 cores, functionalized with a cyclooctyne and azide functionality respectively, is reported. These dyes, Lipo-Cy3-CO and Lipo-Cy5-N_3, present the same core structure as the DiL and DiD dyes used in Chapter 2. Then, the photonic properties of the dyes, as well as their ability to undergo SPAAC in solution are examined. The functional dyes are then integrated into liposomes, and the stability of the new formulation is tested. Finally, the formation of 'clicked' product during liposome fusion is assessed, and the proof-of-concept for using the functional dyes in a biosensing assay is demonstrated.

3.2 Materials and methods

3.2.1 Materials

All chemical reagents were purchased from Sigma-Aldrich and used as supplied unless otherwise indicated. Dichloromethane was purchased from AGTC Bioproducts. 1,1'-Dioctadecyl-3,3,3',3'-tetramethylindodicarbocyanine perchlorate, DiIC18(5) (DiD), 1,1-dioctadecyl-3,3,3',3'-tetramethylindocarbocyanine perchlorate, DiIC18(3) (DiL), were purchased from Invitrogen Life Technologies. 1,16-Hexadecanediol was obtained from Tokyo Chemical Industry UK Ltd. Illustra NAP-10 columns were obtained from GE Healthcare. Magnesium sulphate ($MgSO_4$) was obtained from VWR. Malonaldehyde bis(phenylimine) monohydrochloride was obtained from Alfa Aesar. Zeba™ spin desalting column, 40 KDa MWCO was purchased from Thermo Fisher Scientific. 1,2-Dioleoyl-*sn*-glycero-3-phosphocholine (DOPC) and 1,2-dioleoyl-*sn*-glycero-3-phosphoethanolamine (DOPE) lipids were purchased from Avanti Polar Lipids, Inc. HPLC-purified oligonucleotides were purchased from IBA GmbH (Germany) and Integrated DNA Technologies (Belgium). Nuclease-free water (non DEPC-treated) was purchased from Thermo Fisher Scientific (Ambion™).

3.2.2 Analytical techniques and purification methods

Thin layer chromatography (TLC) was carried out on aluminium sheets coated with 60 F254 silica gel (Merck). Visualization of the silica plates was achieved using UV irradiation (λ_{max} = 254 nm or 318 nm) and a suitable staining with ammonium molybdate (5 w/v % in 2M H_2SO_4), potassium permanganate (5 w/v % in 1M NaOH containing 5 w/v % K_2CO_3), triphenylphosphine (10 w/v % PPh_3 in DCM) and/or ninhydrin (0.2 w/v % in ethanol). Flash column chromatography was carried out using Geduran Si 60 (40-63 μm) silica gel (Merck). Mobile phases are reported as % volume of more polar solvent in less polar solvent.

Proton nuclear magnetic resonance (^{1}H NMR) spectra were recorded on a Bruker DPX-400 (400 MHz) spectrometer. Carbon nuclear magnetic resonance (^{13}C NMR) spectra were recorded on the same machine (100 MHz). All chemical shifts are quoted on the δ scale in ppm using residual solvent as the internal standard (^{1}H NMR: $CDCl_3$ = 7.26, and ^{13}C NMR: $CDCl_3$ = 77.16). The following abbreviation is used: Ar = aromatic. Coupling constants, *J*, are reported in Hz with the following splitting abbreviations: s = singlet, d = doublet, t = triplet, q = quartet, quin = quintet, m = multiplet, app = apparent, br = broad.

The numbering system used for indole-based compounds is presented in Figure 3.

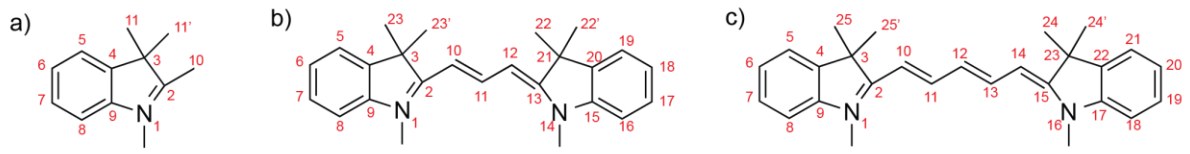

Figure 3. Numbering of the carbon backbone used for NMR identification.

Matrix-assisted laser desorption/ionisation (MALDI) time of flight (ToF) spectra were collected on a Waters Micromass MALDI-ToF in positive ion reflectron mode, calibrated using poly(ethylene glycol) standards, with the help of Dr Yiyang Lin. α-Cyano-4-hydroxycinnamic acid (CHCA) was used as the MALDI matrix substance.

3.2.3 Synthesis of functional cyanine dyes

Synthesis of Lipo-Cy3-CO

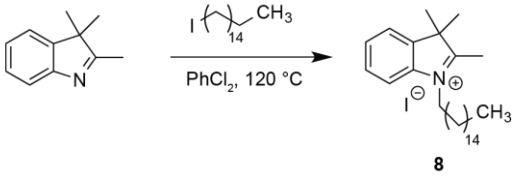

Scheme 1. Synthesis of **8**.

1-Iodohexadecane (2.66 g, 7.55 mmol) was weighed and placed under an inert atmosphere (N_2). Dry dichlorobenzene (10 mL) was added, followed by 2,3,3-trimethylindolenine (1 g, 6.29 mmol). The reaction vessel was heated to 120 °C, and stirred for 15 h. The reaction mixture was then cooled to room temperature, added drop-wise to diethyl ether (200 mL), and left to stir for 30 min. The precipitate formed was filtered, washed with diethyl ether (500 mL), and dried *in vacuo*, to afford **8** as a peach-coloured powder (2.133 g, 4.2 mmol, 88 %).

^{1}H-NMR (400 MHz, $CDCl_3$, δ, ppm): 0.86 (t, *J* = 6.4 Hz, 3H, C<u>H</u>$_3$-$(CH_2)_{13}$-CH_2-CH_2-N), 1.20-1.50 (br m, 26H, CH_3-(C<u>H</u>$_2$)$_{13}$-CH_2-CH_2-N), 1.65 (s, 6H, Ar(C<u>H</u>$_3$)$_2$, H11;11'), 1.92 (quin, *J* = 7.6 Hz, 2H, CH_3-$(CH_2)_{13}$-C<u>H</u>$_2$-CH_2-N), 3.12 (s, 3H, ArC<u>H</u>$_3$, H10), 4.67 (t, *J* = 7.6 Hz, 2H, CH_3-$(CH_2)_{13}$-CH_2-C<u>H</u>$_2$-N), 7.53-7.60 (m, 3H, <u>ArH</u>), 7.60-7.66 (m, 1H, <u>ArH</u>).

^{13}C-NMR (100 MHz, $CDCl_3$, δ, ppm): 14.23 (<u>C</u>H_3-CH_2-$(CH_2)_{11}$-CH_2-CH_2-CH_2-N), 17.25 (N=C-<u>C</u>H_3, C10), 22.79 (CH_3-<u>C</u>H_2-$(CH_2)_{11}$-CH_2-CH_2-CH_2-N), 23.34 (CH_3-CH_2-$(CH_2)_{11}$-<u>C</u>H_2-CH_2-CH_2-N), 26.96 ((<u>C</u>H_3)$_2$, C11;11'), 28.08 (CH_3-CH_2-$(CH_2)_{11}$-CH_2-<u>C</u>H_2-CH_2-N), 29.25-29.80 (CH_3-CH_2-(<u>C</u>H_2)$_{11}$-CH_2-CH_2-CH_2-N), 32.03 (<u>C</u>-$(CH_3)_2$, C3), 50.40 (CH_3-CH_2-$(CH_2)_{11}$-CH_2-CH_2-<u>C</u>H_2-N), 115.43 (Ar<u>C</u>),

123.47 (ArC), 129.64 (ArC), 130.25 (ArC), 141.13 (ArC, C4/C9), 141.80 (ArC, C4/C9), 195.67, (C=N, C2).

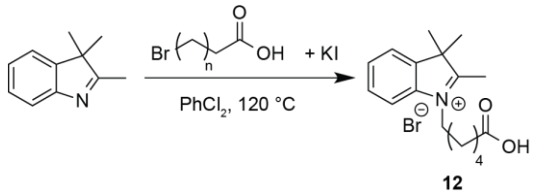

Scheme 2. Synthesis of **12**.

6-Bromohexanoic acid (292.2 mg, 1.5 mmol) and potassium iodide (249 mg, 1.5 mmol) were weighed in a flask, which was equipped with a septum and kept under inert atmosphere (N_2). Dry dichlorobenzene (4 mL) was added, then 2,3,3-trimethylindolenine (200 mg, 1.26 mmol). The reaction vessel was heated to 120 °C, and stirred for 15 h. The reaction mixture was then cooled to room temperature, added drop-wise to diethyl ether (200 mL), and left to stir for 30 min. The precipitate formed was filtered, and washed with diethyl ether. The solids were dissolved in dichloromethane (DCM), which was evaporated *in vacuo* to afford **12** as a black solid (97 mg, 0.2 mmol, 19 %).

^{1}H-NMR (400 MHz, $CDCl_3$, δ, ppm): 1.55-1.62 (m, 2H, COOH-CH_2-CH_2-CH_2-CH_2-CH_2-N), 1.64 (s, 6H, (CH_3)$_2$, H11;11'), 1.74 (quin, *J* = 7.2 Hz, 2H, COOH-CH_2-CH_2-CH_2-CH_2-CH_2-N), 2.03 (quin, *J* = 7.2 Hz, 2H, COOH-CH_2-CH_2-CH_2-CH_2-CH_2-N), 2.45 (t, *J* = 6.8 Hz, 2H, COOH-CH_2-CH_2-CH_2-CH_2-CH_2-N), 3.14 (s, 3H, ArCH_3, H10), 4.71 (t, *J* = 7.6 Hz, 2H, COOH-CH_2-CH_2-CH_2-CH_2-CH_2-N), 7.54-7.64 (m, 3H, ArH), 7.70-7.75 (m, 1H, ArH).

^{13}C-NMR (100 MHz, $CDCl_3$, δ, ppm): 16.47 (N=C-CH_3, C10), 23.23 ((CH_3)$_2$, C11;11'), 24.18 (CAlkyl), 25.93 (CAlkyl), 27.62 (CAlkyl), 33.78 (COOH-CH_2-(CH_2)$_3$-CH_2-N), 49.40 (C(CH_3)$_2$, C3), 54.68 (COOH-CH_2-(CH_2)$_3$-CH_2-N), 115.48 (ArC), 123.28 (ArC), 129.66 (ArC), 130.59, (ArC), 140.94 (ArC, C4/C9), 141.65 (ArC, C4/C9), 175.81 (COOH-CH_2-(CH_2)$_3$-CH_2-N), 196.20 (C=N, C2).

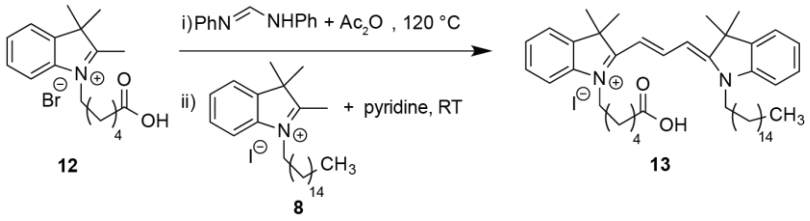

Scheme 3. Synthesis of **13**.

12 (90 mg, 0.33 mmol), acetic anhydride (1 mL), and *N*,*N*′-diphenylformamidine (78.4 mg, 0.40 mmol) were mixed. The mixture was stirred at 120 °C for 30 min, then cooled down to room temperature. **8** (235 mg, 0.46 mmol) and pyridine (1 mL) were then added to the reaction mixture, and this was stirred for 15 h at room temperature, protected from light. The mixture was then precipitated in hexane (50 mL) twice, the precipitate was dissolved in DCM (100 mL) and washed with H_2O (200 mL). The organic phase was dried ($MgSO_4$), filtered, and DCM was evaporated *in vacuo*. The residue was purified by flash column chromatography (eluent: 5-10 % v/v MeOH in DCM). The fractions of interest were collected, and the solvent was evaporated *in vacuo* to afford **13** as a pink solid (43 mg, 54 µmol, 16 %).

^{1}H-NMR (400 MHz, $CDCl_3$, δ, ppm): 0.86 (t, *J* = 6.8 Hz, 3H, C<u>H</u>$_3$-(CH$_2$)$_{13}$-CH$_2$-CH$_2$-N), 1.11-1.57 (m, 30H, CH$_3$-(C<u>H</u>$_2$)$_{13}$-CH$_2$-CH$_2$-N & COOH-CH$_2$-(C<u>H</u>$_2$)$_2$-CH$_2$-CH$_2$-N), 1.71 (s, 12H, (C<u>H</u>$_3$)$_2$ & (C<u>H</u>$_3$)$_2$, H22;22';23;23'), 1.81-1.94 (m, 4H, CH$_3$-(CH$_2$)$_{13}$-C<u>H</u>$_2$-CH$_2$-N & COOH-CH$_2$-(CH$_2$)$_2$-C<u>H</u>$_2$-CH$_2$-N), 2.46 (t, *J* = 6.8 Hz, 2H, COOH-C<u>H</u>$_2$-(CH$_2$)$_2$-CH$_2$-CH$_2$-N), 4.15-4.29 (m, 4H, CH$_3$-(CH$_2$)$_{13}$-CH$_2$-C<u>H</u>$_2$-N & COOH-CH$_2$-(CH$_2$)$_2$-CH$_2$-C<u>H</u>$_2$-N), 7.06-7.15 (m, 2H, <u>ArH</u>), 7.17-7.25 (m, 3H, <u>ArH</u>), 7.30-7.45 (m, 5H, <u>ArH</u> & C-C<u>H</u>=CH-C<u>H</u>=C, H10;12), 8.42 (t, *J* = 13.6 Hz, 1H, C-CH=C<u>H</u>-CH=C, H11).

^{13}C-NMR (100 MHz, $CDCl_3$, δ, ppm): 14.15 (<u>C</u>H$_3$-CH$_2$-CH$_2$-(CH$_2$)$_{12}$-CH$_2$-N), 22.70 (CH$_3$-<u>C</u>H$_2$-CH$_2$-(CH$_2$)$_{12}$-CH$_2$-N), 24.57 (<u>CAlkyl</u>), 26.23 (<u>CAlkyl</u>), 26.99 (<u>CAlkyl</u>), 27.01 (<u>CAlkyl</u>), 27.74 (<u>CAlkyl</u>), 28.18 ((<u>C</u>H$_3$)$_2$ & (<u>C</u>H$_3$)$_2$), 29.37 (<u>CAlkyl</u>), 29.51 (<u>CAlkyl</u>), 29.67 (<u>CAlkyl</u>), 29.71 (<u>CAlkyl</u>), 31.93 (<u>CAlkyl</u>), 34.38 (COOH-<u>C</u>H$_2$-(CH$_2$)$_3$-CH$_2$-N), 44.71 (CH$_3$-CH$_2$-CH$_2$-(CH$_2$)$_{12}$-<u>C</u>H$_2$-N), 45.09 (COOH-CH$_2$-(CH$_2$)$_3$-<u>C</u>H$_2$-N), 48.90 (<u>C</u>-(CH$_3$)$_2$, C3/21), 48.96 (<u>C</u>-(CH$_3$)$_2$, C3/21), 104.25 (N=C-<u>C</u>=C-C=C-N, C10), 110.95 (N=C-C=C-<u>C</u>=C-N, C12), 111.09 (Ar<u>C</u>), 122.12 (Ar<u>C</u>), 125.23 (Ar<u>C</u>), 128.82 (Ar<u>C</u>), 128.93 (Ar<u>C</u>), 142.09 (N=C-C=<u>C</u>-C=C-N, C11), 142.28 (Ar<u>C</u>), 150.75 (Ar<u>C</u>), 173.44 (N=<u>C</u>-C=C-C=<u>C</u>-N, C2/C13), 173.73 (N=<u>C</u>-C=C-C=<u>C</u>-N, C2/C13).

MS (MALDI-TOF, CHCA matrix) (*m/z*): $[M+H]^+$ calcd. for $C_{45}H_{68}N_2O_2$, 668.52; found, 668.5.

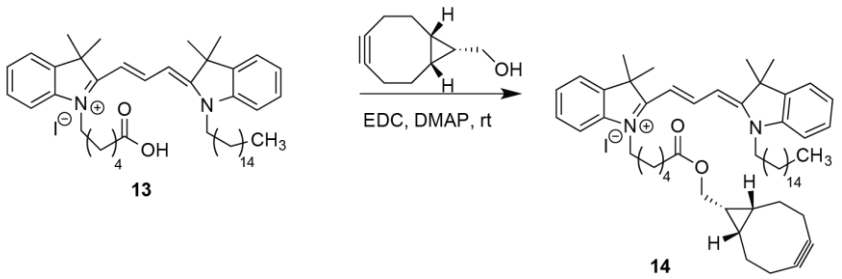

Scheme 4. Synthesis of **14**.

13 (20 mg, 0.025 mmol), (1*R*,8*S*,9*s*)-bicyclo[6.1.0]non-4-yn-9-ylmethanol (11.3 mg, 0.075 mmol), *N*-(3-Dimethylaminopropyl)-*N*′-ethylcarbodiimide (EDC, 9.6 mg, 0.050 mmol), and 4-(dimethylamino)pyridine (0.3 mg, 0.002 mmol) were solubilized in DCM (4 mL) and stirred at room temperature for 15 h. The reaction was then diluted in DCM (100 mL) and washed with H_2O. The organic phase was dried ($MgSO_4$), filtered, and DCM was evaporated *in vacuo*. The residue was purified by flash column chromatography (eluent: 5 % v/v MeOH in DCM). The fractions of interest were collected, and the solvent was evaporated *in vacuo* to afford **14** as a pink solid (17.5 mg, 19 µmol, 76 %).

^{1}H-NMR (400 MHz, $CDCl_3$, δ, ppm): 0.06 (m, 2H, cyclooctyneH), 0.87 (t, *J* = 6.8 Hz, 3H, CH_3-$(CH_2)_{13}$-CH_2-CH_2-N), 0.90-0.98 (m, 1H, cyclooctyneH), 1.19-1.65 (m, 34H, CH_3-$(CH_2)_{13}$-CH_2-CH_2-N & COOH-CH_2-$(CH_2)_2$-CH_2-CH_2-N & cyclooctyneH), 1.70 (s, 12H, $(CH_3)_2$ & $(CH_3)_2$, H22;22';23;23'), 1.82-1.94 (m, 4H, CH_3-$(CH_2)_{13}$-CH_2-CH_2-N & COOH-CH_2-$(CH_2)_2$-CH_2-CH_2-N), 2.16-2.34 (m, 4H, cyclooctyneH), 2.38 (t, *J* = 7.2 Hz, 2H, COOH-CH_2-$(CH_2)_2$-CH_2-CH_2-N), 4.12 (d, *J* = 8.4 Hz, 2H, cyclooctyne-CH_2-O-C=O), 4.27 (t, *J* = 7.4 Hz, 4H, CH_3-$(CH_2)_{13}$-CH_2-CH_2-N & COOH-CH_2-$(CH_2)_2$-CH_2-CH_2-N), 7.10 (dd, *J* = 8 Hz, *J* = 2.4 Hz, 2H, ArH), 7.20-7.25 (m, 2H, ArH), 7.32-7.41 (m, 4H, ArH), 7.47 (dd, *J* = 13.4 Hz, *J* = 1 Hz, 2H, C-CH=CH-CH=C, H10;12), 8.43 (t, *J* = 13.4 Hz, 1H, C-CH=CH-CH=C, H11).

^{13}C-NMR (100 MHz, $CDCl_3$, δ, ppm): 14.14 (CH_3-CH_2-CH_2-$(CH_2)_{12}$-CH_2-N), 17.45 (CAlkyl), 20.14 (Ccyclooctyne), 21.43 (Ccyclooctyne) 22.70 (CH_3-CH_2-CH_2-$(CH_2)_{12}$-CH_2-N), 24.78 (CAlkyl), 26.45 (CAlkyl), 26.98 (CAlkyl), 27.42 (CAlkyl), 27.79 (CAlkyl), 28.17 (C22, C22'), 29.08 (C23, C23'), 29.37 (CAlkyl), 29.49 (CAlkyl), 29.71 (CAlkyl), 31.93 (CAlkyl), 34.12 (COOR-CH_2-$(CH_2)_3$-CH_2-N), 44.85 (CH_3-CH_2-CH_2-$(CH_2)_{12}$-CH_2-N), 45.13 (COOH-CH_2-$(CH_2)_3$-CH_2-N), 48.75 (C3/C21), 48.83 (C3/C21), 62.16 (Ccyclooctyne), 98.04 (Ccylooctyne), 104.86 (C10), 105.081 (C12), 111.05 (ArC), 122.04 (ArC), 125.05 (ArC), 128.80 (ArC), 150.89 (ArC), 151.35 (ArC), 173.28 (C2/C13), 173.56 (C2/C13).

MS (MALDI-TOF, CHCA matrix) (*m/z*): $[M+H]^+$ calcd. for $C_{55}H_{80}N_2O_2$, 800.62; found, 800.6.

Synthesis of Lipo-Cy5-N_3

Synthesis of Lipo-Cy5-N_3 C_6

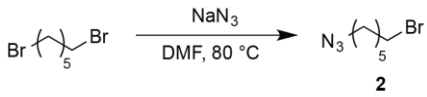

Scheme 5. Synthesis of **2**.

1,6-Dibromohexane (2 g, 8.2 mmol), sodium azide (NaN_3, 533 mg, 8.2 mmol) and dimethylformamide (DMF, 10 mL) were mixed. The reaction was heated to 80 °C and allowed to proceed for 17 h under inert atmosphere. The reaction mixture was diluted in DCM (50 mL) and washed 3 times with 1 M HCl (150 mL). The organic phase was dried ($MgSO_4$) and concentrated under vacuum. The residue was purified by flash column chromatography (eluent: 1 % v/v EtOAc in hexane, TLC stain 10 w/w % PPh_3 in DCM then ninhydrin). The fractions of interest were collected, and the solvent was evaporated *in vacuo* to afford **2** as a yellow liquid (1.031 g, 5.0 mmol, 61 %).

^{1}H-NMR (400 MHz, $CDCl_3$, δ, ppm): 1.31-1.51 (m, 4H, Br-CH_2-CH_2-C$\underline{H_2}$-C$\underline{H_2}$-CH_2-CH_2-N_3), 1.59 (quin, *J* = 7.1 Hz, 2H, Br-CH_2-CH_2-CH_2-CH_2-C$\underline{H_2}$-CH_2-N_3), 1.84 (quin, *J* = 7.0 Hz, 2H, Br-CH_2-C$\underline{H_2}$-CH_2-CH_2-CH_2-CH_2-N_3), 3.25 (t, *J* = 6.8 Hz, 2H, Br-CH_2-CH_2-CH_2-CH_2-CH_2-C$\underline{H_2}$-N_3), 3.38 (t, *J* = 6.8 Hz, 2H, Br-C$\underline{H_2}$-CH_2-CH_2-CH_2-CH_2-CH_2-N_3).

^{13}C-NMR (100 MHz, $CDCl_3$, δ, ppm): 25.88 (C$\underline{Alkyl}$), 26.28 (C$\underline{Alkyl}$), 27.66 (C$\underline{Alkyl}$), 28.54-28.86 (C$\underline{Alkyl}$), 30.89 (Br-CH_2-CH_2-CH_2-CH_2-C$\underline{H_2}$-CH_2-N_3), 32.53 (Br-CH_2-C$\underline{H_2}$-CH_2-CH_2-CH_2-CH_2-N_3), 33.64 (Br-C$\underline{H_2}$-CH_2-CH_2-CH_2-CH_2-CH_2-N_3), 51.28 (Br-CH_2-CH_2-CH_2-CH_2-CH_2-C$\underline{H_2}$-N_3).

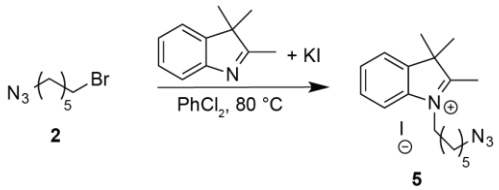

Scheme 6. Synthesis of **5**.

2 (500 mg, 2.43 mmol) and potassium iodide (KI) (403 mg, 2.43 mmol) were mixed and kept under inert atmosphere (N_2). Dry dichlorobenzene (5 mL) was added, then 2,3,3-trimethylindolenine (321.6 mg, 2.02 mmol). The reaction vessel was heated to 100 °C, and stirred for 15 h. The reaction mixture was then cooled to room temperature, added drop-wise to

diethyl ether (200 mL), and left to stir for 30 min. The precipitate formed was filtered, and washed with diethyl ether (500 mL). The solids were dissolved in dichloromethane (DCM), which was evaporated *in vacuo* to afford **5** as a brown viscous oil (345 mg, 0.8 mmol, 41 %).

^{1}H-NMR (400 MHz, $CDCl_3$, δ, ppm): 1.45-1.64 (m, 6H, N_3-CH_2-C$\underline{H_2}$-C$\underline{H_2}$-C$\underline{H_2}$-CH_2-CH_2-N), 1.66 (s, 6H, (C$\underline{H_3}$)$_2$, H11;11'), 1.99 (quin, *J* = 7.9 Hz, 2H, N_3-CH_2-CH_2-CH_2-CH_2-C$\underline{H_2}$-CH_2-N), 3.12 (s, 3H, C$\underline{H_3}$, H10), 3.30 (t, *J* = 6.6 Hz, 2H, N_3-C$\underline{H_2}$-CH_2-CH_2-CH_2-CH_2-CH_2-N), 4.72 (t, *J* = 7.8 Hz, 2H, N_3-CH_2-CH_2-CH_2-CH_2-CH_2-C$\underline{H_2}$-N), 7.54-7.64 (m, 3H, $\underline{ArH}$), 7.67-7.72 (m, 1H, $\underline{ArH}$).

^{13}C-NMR (100 MHz, $CDCl_3$, δ, ppm): 16.91 (Ar$\underline{C}H_3$, C10), 23.27 (($\underline{C}H_3$)$_2$, C11;11'), 26.37 ($\underline{CAlkyl}$), 26.42 ($\underline{CAlkyl}$), 28.09 ($\underline{CAlkyl}$), 28.57 ($\underline{CAlkyl}$), 49.94 ($\underline{C}(CH_3)_2$, C3), 51.24 (N_3-$\underline{C}H_2$-$(CH_2)_4$-CH_2-N), 54.73 (N_3-CH_2-$(CH_2)_4$-$\underline{C}H_2$-N), 115.48 (Ar$\underline{C}$), 123.43 (Ar$\underline{C}$), 129.70 (Ar$\underline{C}$), 130.33 (Ar$\underline{C}$), 140.87 (Ar$\underline{C}$, C4/C9), 141.60 (Ar$\underline{C}$, C4/C9), 195.69 ($\underline{C}$=N, C2).

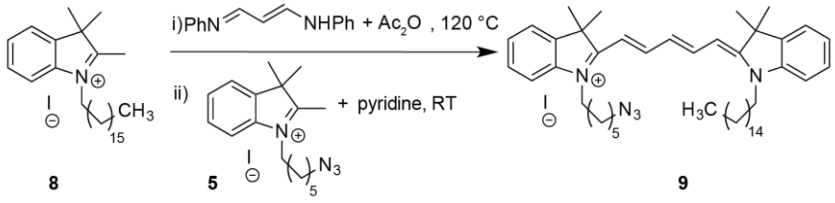

Scheme 7. Synthesis of **9**.

8 (87 mg, 0.17 mmol), acetic anhydride (1 mL), and malonaldehyde bis(phenylimine) monohydrochloride (54.3 mg, 0.21 mmol) were mixed. The mixture was stirred at 120 °C for 30 min, then cooled down to room temperature. **5** (100 mg, 0.24 mmol) and pyridine (1 mL) were then added to the reaction mixture, and this was stirred for 15 h at room temperature, protected from light. The mixture was then precipitated in hexane twice, the precipitate was diluted in DCM (100 mL) and washed with H_2O. The organic phase was dried ($MgSO_4$), filtered, and DCM was evaporated *in vacuo*. The residue was purified by flash column chromatography (eluent: 5 % v/v MeOH in DCM). The fractions of interest were collected, and the solvent was evaporated *in vacuo* to afford **9** as a blue viscous oil (113 mg, 0.14 mmol, 80 %).

^{1}H-NMR (400 MHz, $CDCl_3$, δ, ppm): 0.89 (t, *J* = 6.8 Hz, 3H, C$\underline{H_3}$-$(CH_2)_{13}$-CH_2-CH_2-N), 1.21-1.36 (s, 25H, $\underline{HAlkyl}$), 1.36-1.45 (m, 5H, $\underline{HAlkyl}$), 1.45-1.55 (m, 2H, $\underline{HAlkyl}$), 1.55-1.66 (m, 2H, $\underline{HAlkyl}$), 1.74 (s, 12H, (C$\underline{H_3}$)$_2$ & (C$\underline{H_3}$)$_2$, H24;24'25;25'), 1.79-1.87 (m, 4H, CH_3-$(CH_2)_{13}$-C$\underline{H_2}$-CH_2-N & N_3-CH_2-$(CH_2)_3$-C$\underline{H_2}$-CH_2-N), 3.29 (m, 2H, N_3-C$\underline{H_2}$-$(CH_2)_3$-CH_2-CH_2-N), 4.12 (t, *J* = 7.2 Hz, 4H, CH_3-$(CH_2)_{13}$-CH_2-C$\underline{H_2}$-N & N_3-CH_2-$(CH_2)_3$-CH_2-C$\underline{H_2}$-N), 6.30 (d, *J* = 13.6 Hz, 2H, N=C-C$\underline{H}$=CH-CH=CH-C$\underline{H}$=C-N, H10;14), 6.66 (t, *J* = 12.4 Hz, 1H, N=C-CH=CH-C$\underline{H}$=CH-CH=C-N, H12), 7.22-7.34 (m, 2H,

ArH), 7.37-7.46 (m, 2H, ArH), 7.47-7.57 (m, 4H, ArH), 8.27 (t, *J* = 13.0 Hz, 2H, N=C-CH=CH-CH=CH-CH=C-N, H11;13).

^{13}C-NMR (100 MHz, $CDCl_3$, δ, ppm): 13.06 (CH_3-CH_2-$(CH_2)_{13}$-CH_2-N), 22.41 (CH_3-CH_2-$(CH_2)_{13}$-CH_2-N), 25.20-29.95 (CAlkyl), 26.57 ((CH_3)$_2$ & (CH_3)$_2$, C24;24';25;25'), 31.67 (C-$(CH_3)_2$, C3/23), 49.21 (C-$(CH_3)_2$, C3/23), 50.95 (CH_3-CH_2-$(CH_2)_{13}$-CH_2-N), 53.42 (N_3-CH_2-$(CH_2)_4$-CH_2-N), 102.93 (N=C-C=C-C=C-C=C-N, C10), 103.13 (N=C-C=C-C=C-C=C-N, C14), 110.61, (ArC), 110.72 (ArC), 119.76 (ArC), 119.86 (ArC), 122.02 (ArC), 123.72 (ArC), 124.89 (ArC), 128.35 (N=C-C=C-C=C-C=C-N, C11/13), 141.29 (ArC), 142.07 (N=C-C=C-C=C-C=C-N, C11), 153.75 (ArC), 170.24 (N=C-C=C-C=C-C=C-N, C2/C15), 173.19 (N=C-C=C-C=C-C=C-N, C2/C15).

MS (MALDI-TOF, CHCA matrix) (*m/z*): $[M+H]^+$ calcd. for $C_{47}H_{71}N_5$, 705.57; found, 705.8.

Synthesis of Lipo-Cy5-N_3 C_{12}:

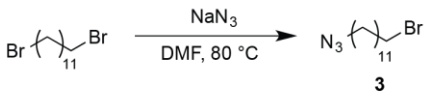

3

Scheme 8. Synthesis of **3**.

1,12-Dibromododecane (1 g, 3.05 mmol), sodium azide (NaN_3, 198 mg, 3.05 mmol) and dimethylformamide (DMF, 15 mL) were mixed. The reaction was heated to 80 °C and was allowed to proceed for 17 h under inert atmosphere. The reaction mixture was diluted in DCM (50 mL) and washed 3 times with 1 M HCl (150 mL). The organic phase was dried ($MgSO_4$) and concentrated under vacuum. The residue was purified by flash column chromatography (eluent: petroleum benzene, TLC stain 10 w/w % PPh_3 in DCM then ninhydrin). The fractions of interest were collected, and the solvent was evaporated *in vacuo* to afford **3** as a pale yellow viscous oil (325 mg, 1.12 mmol, 37 %).

^{1}H-NMR (400 MHz, $CDCl_3$, δ, ppm): 1.23-1.48 (m, 16H, Br-CH_2-CH_2-(CH_2)$_8$-CH_2-CH_2-N_3), 1.60 (quin, *J* = 7.2 Hz, 2H, Br-CH_2-CH_2-$(CH_2)_8$-CH_2-CH_2-N_3), 1.85 (quin, *J* = 7.2 Hz, 2H, Br-CH_2-CH_2-$(CH_2)_8$-CH_2-CH_2-N_3), 3.26 (t, *J* = 7.0 Hz, 2H, Br-CH_2-CH_2-$(CH_2)_8$-CH_2-CH_2-N_3), 3.41 (t, *J* = 6.8 Hz, 2H, Br-CH_2-CH_2-$(CH_2)_8$-CH_2-CH_2-N_3).

^{13}C-NMR (100 MHz, $CDCl_3$, δ, ppm): 26.71 (Br-CH_2-CH_2-CH_2-CH_2-$(CH_2)_4$-CH_2-CH_2-CH_2-CH_2-N_3), 28.17 (Br-CH_2-CH_2-CH_2-CH_2-$(CH_2)_4$-CH_2-CH_2-CH_2-CH_2-N_3), 28.75 (Br-CH_2-CH_2-CH_2-CH_2-$(CH_2)_4$-CH_2-CH_2-CH_2-CH_2-N_3), 28.84 (Br-CH_2-CH_2-CH_2-CH_2-$(CH_2)_4$-CH_2-CH_2-CH_2-CH_2-N_3), 29.14 (Br-CH_2-CH_2-CH_2-CH_2-$(CH_2)_4$-CH_2-CH_2-CH_2-CH_2-N_3), 29.40-29.48 (Br-CH_2-CH_2-CH_2-CH_2-(CH_2)$_4$-CH_2-CH_2-

CH_2-CH_2-N_3), 32.84 (Br-CH_2-$\underline{C}H_2$-CH_2-CH_2-$(CH_2)_4$-CH_2-CH_2-CH_2-CH_2-N_3), 34.04 (Br-$\underline{C}H_2$-CH_2-CH_2-CH_2-$(CH_2)_4$-CH_2-CH_2-CH_2-CH_2-N_3), 51.50 (Br-CH_2-CH_2-CH_2-CH_2-$(CH_2)_4$-CH_2-CH_2-CH_2-$\underline{C}H_2$-N_3).

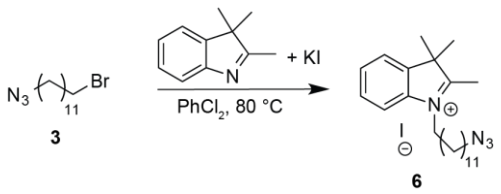

Scheme 9. Synthesis of **6**.

3 (250 mg, 0.86 mmol) and potassium iodide (KI, 143 mg, 0.86 mmol) were mixed and kept under inert atmosphere (N_2). Dry dichlorobenzene ($PhCl_2$, 4 mL) was added, then 2,3,3-trimethylindolenine (114.5 mg, 0.72 mmol). The reaction vessel was heated to 80 °C, and stirred for 15 h. The reaction mixture was then cooled to room temperature, added drop-wise to diethyl ether (200 mL), and left to stir for 30 min. The precipitate formed was filtered, and washed with diethyl ether. The solids were dissolved in dichloromethane (DCM), which was evaporated *in vacuo* to afford **6** as a brown viscous oil (47 mg, 95 µmol, 13 %).

^{1}H-NMR (400 MHz, $CDCl_3$, δ, ppm): 1.21-1.64 (m, 18H, N_3-CH_2-CH_2-$(C\underline{H}_2)_9$-CH_2-N), 1.68 (s, 6H, $(C\underline{H}_3)_2$, H11;11'), 1.96 (quin, *J* = 7.6 Hz, 2H, N_3-CH_2-$C\underline{H}_2$-$(CH_2)_9$-CH_2-N), 3.12 (s, 3H, Ar$C\underline{H}_3$, H10), 3.27 (t, *J* = 7.0 Hz, 2H, N_3-$C\underline{H}_2$-CH_2-$(CH_2)_9$-CH_2-N), 4.69 (t, *J* = 7.8 Hz, 2H, N_3-CH_2-CH_2-$(CH_2)_9$-$C\underline{H}_2$-N), 7.57-7.69 (m, 4H, Ar$\underline{H}$).

^{13}C-NMR (100 MHz, $CDCl_3$, δ, ppm): 17.03 ($\underline{C}H_3$, C10), 23.27 (($\underline{C}H_3)_2$, C11;11'), 26.69 ($\underline{C}$Alkyl), 26.86 ($\underline{C}$Alkyl), 28.04 ($\underline{C}$Alkyl), 28.82 ($\underline{C}$Alkyl), 29.10 ($\underline{C}$Alkyl), 29.14 ($\underline{C}$Alkyl), 29.31 ($\underline{C}$Alkyl), 29.40 ($\underline{C}$Alkyl), 50.27 ($\underline{C}(CH_3)_2$, C3), 51.48 (N_3-$\underline{C}H_2$-$(CH_2)_{10}$-CH_2-N), 54.70 (N_3-CH_2-$(CH_2)_{10}$-$\underline{C}H_2$-N), 115.39 (Ar$\underline{C}$), 123.40 (Ar$\underline{C}$), 129.61 (Ar$\underline{C}$), 130.25 (Ar$\underline{C}$), 140.96 (Ar$\underline{C}$, C4/C9), 141.65 (Ar$\underline{C}$, C4/C9), 188.13 ($\underline{C}$=N, C2).

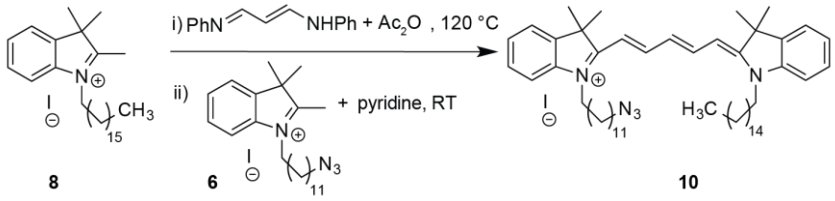

Scheme 10. Synthesis of **10**.

8 (33 mg, 0.065 mmol), acetic anhydride (1 mL), and malonaldehyde bis(phenylimine) monohydrochloride (20 mg, 0.078 mmol) were mixed. The mixture was stirred at 120 °C for 30 min, then cooled down to room temperature. **6** (45 mg, 0.091 mmol) and pyridine (1 mL) were

then added to the reaction mixture, and this was stirred for 15 h at room temperature, protected from light. The mixture was then precipitated in hexane twice, the precipitate was diluted in DCM (100 mL) and washed with H_2O. The organic phase was dried ($MgSO_4$), filtered, and DCM was evaporated *in vacuo*. The residue was purified by flash column chromatography (eluent: 5 % v/v MeOH in DCM). The fractions of interest were collected, and the solvent was evaporated *in vacuo* to afford **10** as a blue viscous oil (40.5 mg, 44 µmol, 68 %).

^{1}H-NMR (400 MHz, $CDCl_3$, δ, ppm): 0.86 (t, *J* = 6.8 Hz, 3H, C$\underline{H_3}$-$(CH_2)_{14}$-CH_2-N), 1.15-1.47 (s, 44H, CH_3-(C$\underline{H_2}$)$_{13}$-CH_2-CH_2-N & N_3-CH_2-(C$\underline{H_2}$)$_9$-CH_2- CH_2-N), 1.57 (quin, *J* = 7.3 Hz, 4H, CH_3-(C$\underline{H_2}$)$_{13}$-C$\underline{H_2}$-CH_2-N & N_3-CH_2-(C$\underline{H_2}$)$_9$-CH_2- C$\underline{H_2}$-N), 1.77 (s, 12H, (C$\underline{H_3}$)$_2$ & (C$\underline{H_3}$)$_2$, H24;24';25;25'), 3.23 (t, *J* = 7.0 Hz, 2H, N_3-C$\underline{H_2}$-$(CH_2)_{10}$-CH_2-N), 4.03 (t, *J* = 7.4 Hz, 4H, CH_3-$(CH_2)_{14}$-C$\underline{H_2}$-N & N_3-CH_2-$(CH_2)_{10}$-C$\underline{H_2}$-N), 6.25 (d, *J* = 13.6 Hz, 2H, N=C-C$\underline{H}$=CH-CH=CH-C$\underline{H}$=C-N, H10;14), 6.76 (t, *J* = 12.4 Hz, 1H, N=C-CH=CH-C$\underline{H}$=CH-CH=C-N, H12), 6.99-7.07 (m, 2H, $\underline{ArH}$), 7.17-7.25 (m, 2H, $\underline{ArH}$), 7.31-7.39 (m, 4H, $\underline{ArH}$), 8.21 (t, *J* = 13.2 Hz, 2H, N=C-CH=C$\underline{H}$-CH=C$\underline{H}$-CH=C-N, H11;13).

^{13}C-NMR (100 MHz, $CDCl_3$, δ, ppm): 14.13 ($\underline{C}H_3$-CH_2-$(CH_2)_{13}$-CH_2-N), 22.69 (CH_3-$\underline{C}H_2$-$(CH_2)_{13}$-CH_2-N), 26.69 ($\underline{CAlkyl}$), 27.00 ($\underline{CAlkyl}$), 27.44 ($\underline{CAlkyl}$), 28.16 (($\underline{C}H_3$)$_2$ & ($\underline{C}H_3$)$_2$, C24;24';25;25'), 28.82 ($\underline{CAlkyl}$), 29.11 ($\underline{CAlkyl}$), 29.22-29.85 ($\underline{CAlkyl}$), 31.92 (N_3-CH_2-$\underline{C}H_2$-$(CH_2)_9$-CH_2-N), 44.53 (CH_3-CH_2-$(CH_2)_{13}$-$\underline{C}H_2$-N), 49.52 (N_3-CH_2-CH_2-$(CH_2)_9$-$\underline{C}H_2$-N), 51.48 (N_3-$\underline{C}H_2$-CH_2-$(CH_2)_9$-CH_2-N), 103.59 (N=C-$\underline{C}$=C-C=C-$\underline{C}$=C-N; C10;14), 110.44 (Ar$\underline{C}$), 119.93 (Ar$\underline{C}$), 122.36 (Ar$\underline{C}$), 123.70 (Ar$\underline{C}$), 125.10 (Ar$\underline{C}$), 128.49 (N=C-C=C-$\underline{C}$=C-C=C-N, C12), 128.69 (N=C-C=C-C=$\underline{C}$-C=C-N, C13), 141.46 (Ar$\underline{C}$), 142.07 (N=C-C=$\underline{C}$-C=C-C=C-N, C11), 153.81 (Ar$\underline{C}$), 172.91-173.12 (N=$\underline{C}$-C=C-C=C-C=$\underline{C}$-N, C2;15).

MS (MALDI-TOF, CHCA matrix) (*m/z*): $[M+H]^+$ calcd. for $C_{53}H_{83}N_5$, 789.66; found, 789.6.

Synthesis of Lipo-Cy5-N_3 C_{16}:

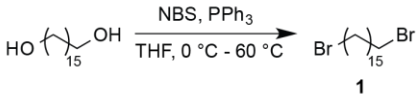

Scheme 11. Synthesis of **1**.

N-Bromosuccinimide (NBS, 2.67 g, 15 mmol) was weighed, and kept under inert atmosphere (N_2). Anhydrous THF (40 mL) was added, and the mixture was cooled to 0 °C using an ice/water bath. Triphenylphosphine (PPh_3, 3.93 g, 15 mmol) dissolved in 40 mL dry THF was added to the flask, and the mixture was stirred vigorously. 1,16-Hexadecanediol (1 g, 3.9 mmol) dissolved in 20 mL dry THF was slowly added to the mixture of NBS and PPh_3. The ice bath was removed,

and the reaction was allowed to warm to room temperature, then slowly heated to 60 °C. The reaction was allowed to proceed for 2 h then the THF was evaporated *in vacuo*. The product of interest was obtained by recrystallizing the residue from refluxing ethanol. Briefly, the solids were dissolved in 20 mL of EtOH by heating the mixture to reflux. As soon as full dissolution was observed, the stirring and heating were interrupted, and the flask was allowed to cool down slowly to room temperature over 15 h. The precipitate was filtered and washed with ice cold EtOH, and then dried under vacuum, to afford **1** as a white powder (954 mg, 2.5 mmol, 64 %).

^{1}H-NMR (400 MHz, $CDCl_3$, δ, ppm): 1.20-1.35 (m, 20H, Br-CH_2-CH_2-CH_2-($C\underline{H_2}$)$_{10}$-CH_2-CH_2-CH_2-Br), 1.35-1.47 (m, 4H, Br-CH_2-CH_2-$C\underline{H_2}$-$(CH_2)_{10}$-$C\underline{H_2}$-CH_2-CH_2-Br), 1.85 (quin, *J* = 7.2 Hz, 2H, Br-CH_2-$C\underline{H_2}$-CH_2-$(CH_2)_{10}$-CH_2-$C\underline{H_2}$-CH_2-Br), 3.41 (t, *J* = 6.8 Hz, 2H, Br-$C\underline{H_2}$-CH_2-CH_2-$(CH_2)_{10}$-CH_2-CH_2-$C\underline{H_2}$-Br).

^{13}C-NMR (100 MHz, $CDCl_3$, δ, ppm): 28.20 (CAlkyl), 28.79 (CAlkyl), 29.45 (CAlkyl), 29.55 (CAlkyl), 29.60-29.66 (CAlkyl), 32.86 (Br-CH_2-$\underline{C}H_2$-$(CH_2)_{12}$-$\underline{C}H_2$-CH_2-Br), 34.10 (Br-$\underline{C}H_2$-CH_2-$(CH_2)_{12}$-CH_2-$\underline{C}H_2$-Br).

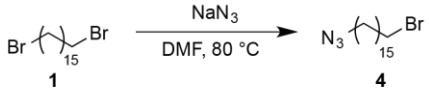

Scheme 12. Synthesis of **4**.

1 (920 mg, 2.4 mmol), sodium azide (NaN_3, 156 mg, 2.4 mmol) and dimethylformamide (DMF, 10 mL) were mixed. The reaction was heated to 80 °C and was allowed to proceed for 17 h under inert atmosphere. The reaction mixture was diluted in DCM (50 mL) and washed 3 times with 1 M HCl (150 mL). The organic phase was dried ($MgSO_4$) and concentrated under vacuum. The residue was purified by flash column chromatography (eluent: hexane, TLC stain 10 w/w % PPh_3 in DCM then ninhydrin). The fractions of interest were collected, and the solvent was evaporated *in vacuo* to afford **4** as a clear viscous oil (26 mg, 75 µmol, 3 %).

^{1}H-NMR (400 MHz, $CDCl_3$, δ, ppm): 1.23-1.48 (m, 24H, Br-CH_2-CH_2-($C\underline{H_2}$)$_{12}$-CH_2-CH_2-N_3), 1.52-1.66 (m, 2H, Br-CH_2-CH_2-$(CH_2)_{12}$-$C\underline{H_2}$-CH_2-N_3), 1.85 (quin, *J* = 7.2 Hz, 2H, Br-CH_2-$C\underline{H_2}$-$(CH_2)_{12}$-CH_2-CH_2-N_3), 3.25 (t, *J* = 7.0 Hz, 2H, Br-CH_2-CH_2-$(CH_2)_{12}$-CH_2-$C\underline{H_2}$-N_3), 3.41 (t, *J* = 7.0 Hz, 2H, Br-$C\underline{H_2}$-CH_2-$(CH_2)_{12}$-CH_2-CH_2-N_3).

^{13}C-NMR (100 MHz, $CDCl_3$, δ, ppm): 26.73 (CAlkyl), 28.19 (CAlkyl), 28.79 (CAlkyl), 28.85 (CAlkyl), 29.17 (CAlkyl), 29.40-29.70 (CAlkyl), 32.86 (Br-CH_2-$\underline{C}H_2$-$(CH_2)_{12}$-CH_2-CH_2-N_3), 34.09 (Br-$\underline{C}H_2$-CH_2-$(CH_2)_{12}$-CH_2-CH_2-N_3), 51.51 (Br-CH_2-CH_2-$(CH_2)_{12}$-CH_2-$\underline{C}H_2$-N_3).

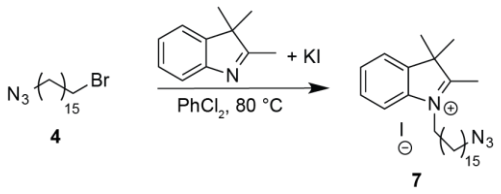

Scheme 13. Synthesis of **7**.

4 (200 mg, 0.58 mmol) and potassium iodide (96 mg, 0.58 mmol) were weighed in a 50 mL round bottom flask, which was equipped with a septum and kept under inert atmosphere (N_2). Dry dichlorobenzene (4 mL) was added, then 2,3,3-trimethylindolenine (76 mg, 0.48 mmol). The reaction vessel was heated to 100 °C, and stirred for 15 h. The reaction mixture was then cooled to room temperature, added drop-wise to hexane (200 mL), and left to stir for 30 min. The precipitate formed was filtered, and washed with hexane. The solids were dissolved in dichloromethane (DCM), which was evaporated *in vacuo* to afford **7** as a brown viscous oil (47 mg, 85 µmol, 18 %).

^{1}H-NMR (400 MHz, $CDCl_3$, δ, ppm): 1.20-1.34 (m, 26H, N_3-CH_2-CH_2-($C\underline{H}_2$)$_{13}$-CH_2-N), 1.67 (s, 6H, ($C\underline{H}_3$)$_2$, H11;11'), 1.93-2.00 (m, 2H, N_3-CH_2-$C\underline{H}_2$-$(CH_2)_{13}$-CH_2-N), 3.05 (s, 3H, Ar$C\underline{H}_3$, H10), 3.25 (t, *J* = 7.0 Hz, 2H, N_3-$C\underline{H}_2$-CH_2-$(CH_2)_{13}$-CH_2-N), 4.66 (t, *J* = 7.6 Hz, 2H, N_3-CH_2-CH_2-$(CH_2)_{13}$-$C\underline{H}_2$-N), 7.57-7.69 (m, 4H, Ar$\underline{H}$).

The product was utilised in the subsequent reaction step without further analysis.

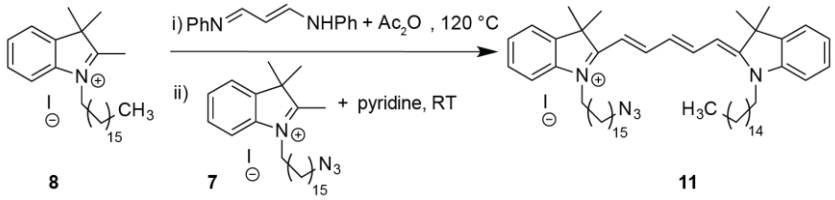

Scheme 14. Synthesis of **11**.

8 (17.4 mg, 0.034 mmol), acetic anhydride (1 mL), and malonaldehyde bis(phenylimine) monohydrochloride (10.3 mg, 0.040 mmol) were mixed. The mixture was stirred at 120 °C for 30 min, then cooled down to room temperature. **7** (26 mg, 0.047 mmol) and pyridine (1 mL) were then added to the reaction mixture, and this was stirred for 15 h at room temperature, protected from light. The mixture was then precipitated in hexane twice, the precipitate was diluted in DCM (100 mL) and washed with H_2O. The organic phase was dried ($MgSO_4$), filtered, and DCM was evaporated *in vacuo*. The residue was purified by flash column chromatography

(eluent: 5 % v/v MeOH in DCM). The fractions of interest were collected, and the solvent was evaporated *in vacuo* to afford **11** as a blue viscous oil (10.2 mg, 10 µmol, 31 %).

^{1}H-NMR (400 MHz, $CDCl_3$, δ, ppm): 0.87 (t, *J* = 6.8 Hz, 3H, C$\underline{H_3}$-$(CH_2)_{14}$-CH_2-N), 1.19-1.48 (s, 56H, CH_3-(C$\underline{H_2}$)$_{14}$-CH_2-N & N_3-CH_2-(C$\underline{H_2}$)$_{14}$-CH_2-N), 1.73 (s, 12H, (C$\underline{H_3}$)$_2$ & (C$\underline{H_3}$)$_2$, H24;24';25;25'), 3.25 (t, *J* = 6.8 Hz, 2H, N_3-C$\underline{H_2}$-$(CH_2)_{14}$-CH_2-N), 4.10 (t, *J* = 7.2 Hz, 4H, CH_3-$(CH_2)_{14}$-C$\underline{H_2}$-N & N_3-CH_2-$(CH_2)_{14}$-C$\underline{H_2}$-N), 6.28 (d, *J* = 13.6 Hz, 2H, N=C-C$\underline{H}$=CH-CH=CH-C$\underline{H}$=C-N, H10;14), 6.63 (t, *J* = 12.4 Hz, 1H, N=C-CH=CH-C$\underline{H}$=CH-CH=C-N, H12), 7.22-7.33 (m, 2H, $\underline{ArH}$), 7.36-7.45 (m, 2H, $\underline{ArH}$), 7.46-7.56 (m, 4H, $\underline{ArH}$), 8.26 (t, *J* = 13.0 Hz, 2H, N=C-CH=C$\underline{H}$-CH=C$\underline{H}$-CH=C-N, H11;13).

^{13}C-NMR (100 MHz, $CDCl_3$, δ, ppm): 13.07 ($\underline{C}H_3$-CH_2-$(CH_2)_{13}$-CH_2-N), 22.34 (CH_3-$\underline{C}H_2$-$(CH_2)_{13}$-CH_2-N), 26.07-26.82 ($\underline{C}$Alkyl), 26.57 (($\underline{C}H_3$)$_2$ & ($\underline{C}H_3$)$_2$, C24;24';25;25'), 28.52-29.75 ($\underline{C}$Alkyl), 31.67 (N_3-CH_2-$\underline{C}H_2$-$(CH_2)_{13}$-CH_2-N), 43.51 (CH_3-CH_2-$(CH_2)_{13}$-$\underline{C}H_2$-N), 49.18 (N_3-CH_2-CH_2-$(CH_2)_{13}$-$\underline{C}H_2$-N), 51.05 (N_3-$\underline{C}H_2$-CH_2-$(CH_2)_{13}$-CH_2-N), 103.01 (N=C-$\underline{C}$=C-C=C-$\underline{C}$=C-N, C10;14), 109.98 (Ar$\underline{C}$), 110.68 (Ar$\underline{C}$), 119.76 (Ar$\underline{C}$), 122.02 (Ar$\underline{C}$), 123.72 (Ar$\underline{C}$), 124.86 (Ar$\underline{C}$), 128.35 (N=C-C=C-$\underline{C}$=C-C=C-N, C12), 141.26 (Ar$\underline{C}$), 142.15 (N=C-C=$\underline{C}$-C=C-C=C-N, C11), 153.97 (Ar$\underline{C}$), 173.31 (N=$\underline{C}$-C=C-C=C-C=$\underline{C}$-N, C2;15).

MS (MALDI-TOF, CHCA matrix) (*m/z*): $[M+H]^+$ calcd. for $C_{57}H_{91}N_5$, 845.73; found, 845.3.

3.2.4 Characterization of the dyes in solution

Determination of the quantum yield

Stock solutions of the dyes (DiL, DiD, Lipo-Cy3-CO **14** and Lipo-Cy5-N_3 **9**, **10**, **11**) were prepared in methanol (MeOH). The absorbance of the stock solutions was adjusted to ~0.1 (a.u.). Series of dilutions of the stock solutions were performed in MeOH. The absorbance as well as the fluorescence of each solution (100 µL) were measured on a SpectraMax M5 microplate reader (Molecular Devices, USA), using λ_{abs} = 549 nm (DiL, Lipo-Cy3-CO), λ_{abs} = 644 nm (DiD, Lipo-Cy5-N_3), λ_{ex} = 549 nm and λ_{em} = 570 nm (DiL, Lipo-Cy3-CO), and λ_{ex} = 644 nm and λ_{em} = 670 nm (DiD, Lipo-Cy5-N_3).

SPAAC reaction in solution

Stock solutions of the dyes were prepared in DCM (10 µM). Samples were mixed at equal volume ratios (100 µL each), concentrated by evaporating DCM under a stream of N_2, then resuspended in 400 µL of DCM and stirred for 24 h. FRET spectra were then recorded on a fluorometer (FluoroLog spectrophotometer, Horiba, Stanmore, UK) using λ_{ex} = 530 nm, and slit = 5 nm.

3.2.5 Evaluation of the lipophilicity of Lipo-Cy5-N_3 dyes

SMILES strings were generated using an online translator (Table 1).[16] The lipophilicity (logP) for each structure was then predicted using ALOGPS 2.1 online program.[17]

Table 1. SMILES string equivalence for the different Lipo-Cy5-N_3 dye structures.

Name	SMILES string
Lipo-Cy5-N_3 C_6	CCCCCCCCCCCCCCCC[N+]4=C(C=CC=CC=C2N(CCCCCCN=N#N)c1ccccc1C2(C)C)C(C)(C)c3ccccc34
Lipo-Cy5-N_3 C_{12}	CCCCCCCCCCCCCCCC[N+]4=C(C=CC=CC=C2N(CCCCCCCCCCCCN=N#N)c1ccccc1C2(C)C)C(C)(C)c3ccccc34
Lipo-Cy5-N_3 C_{16}	CCCCCCCCCCCCCCCC[N+]4=C(C=CC=CC=C2N(CCCCCCCCCCCCCCCCN=N#N)c1ccccc1C2(C)C)C(C)(C)c3ccccc34

3.2.6 Liposome fusion assays

Liposome preparation and functionalization

Liposomes were composed of DOPC/DOPE/Cholesterol (50:25:25 mass ratio) and contained 2 mol % of either donor or acceptor dye. Lipids were dissolved in chloroform ($CHCl_3$) and mixed, and $CHCl_3$ was evaporated under inert atmosphere for 1 h, then *in vacuo* overnight. Dry lipid films were hydrated in buffer (30 min, 2.5 mg.mL^{-1}, 37 °C, TE buffer containing 150 mM NaCl; buffer composition: 10 mM Tris, 150 mM NaCl, 1 mM EDTA, pH adjusted to 8.0 using HCl). Liposomes were extruded using an Avanti Lipid Mini-Extruder with 100 nm polycarbonate membranes (Whatman). DNA strands A/B and C/D (see Chapter 2 section 2.3.2 for detail of DNA sequences) were mixed at a 1:1 molar ratio, annealed at 80 °C for 5 min, then allowed to hybridize by slowly cooling down the solution to 25 °C. Donor liposomes were functionalized with DNA A/B and acceptor liposomes were functionalized with DNA C/D by allowing the cholesterol modified dsDNA to self-insert into the lipid vesicles for 60 min.

Measurement of fusion kinetics

Liposomes were diluted to 100 μM (lipid concentration) in the fusion buffer (TE buffer containing 150 mM NaCl, pH 7.4). If required, target miRNA (10 molar excess) was added to solutions of acceptor liposomes, and allowed to hybridize for 1 h at room temperature. Then, 1:1 volume ratio of donor and acceptor liposomes were mixed. Kinetics of liposome fusion were measured in 96-well plates, and fluorescence emission of the dyes were recorded with a

SpectraMax M5 microplate reader (Molecular Devices, USA) at room temperature, using λ_{ex} = 530 nm, $\lambda_{em,DiL}$ = 570 nm, $\lambda_{em,DiD}$ = 670 nm.

Measurement of fusion kinetics in presence of excess DOPC liposomes

Liposomes composed of DOPC only were prepared by drying lipids in a round bottom flask, followed by rehydration in buffer (30 min, 5 mg.mL^{-1}, 37 °C, TE buffer containing 150 mM NaCl; buffer composition: 10 mM Tris, 150 mM NaCl, 1 mM EDTA, pH adjusted to 8.0 using HCl). Liposomes were extruded using an Avanti Lipid Mini-Extruder with 100 nm polycarbonate membranes (Whatman). These liposomes were added to a mixture of donor and acceptor liposomes (200 µM lipid concentration) at a 4.7× molar excess. The kinetics of fusion were measured as previously described.

Leakage assay

Liposomes were composed of DOPC/DOPE/Cholesterol (50:25:25 mass ratio) containing 2 mol % of DiD or Lipo-Cy5-N_3 C_{12} (**10**). A solution of carboxyfluorescein, prepared in 1× PBS buffer (50 mM, pH adjusted to ~7 using HCl) was used to rehydrate dry lipid films (30 min, 2.5 mg.mL^{-1}, 37 °C). Liposomes were extruded using the Avanti Lipid Mini-Extruder with 100 nm polycarbonate membranes (Whatman). Excess unencapsulated carboxyfluorescein was removed by purifying the liposomes on a size exclusion column (Illustra NAP-10, GE Healthcare Life Sciences, UK). The recovered liposomes were further diluted in 1× PBS, and the fluorescence of the liposome solutions was monitored with a SpectraMax M5 microplate reader (Molecular Devices, USA) at room temperature, using λ_{ex} = 495 nm, and λ_{em} = 520 nm. After 30 min, the liposomes were ruptured by addition of 1 v/v % Triton X-100, to assess the maximum fluorescence intensity of the solution.

Purification of liposomes by size exclusion chromatography

Liposomes containing Lipo-Cy5-N_3 C_{12} (**10**) or Lipo-Cy3-CO (**14**) were purified using Zeba™ spin desalting column, 40 KDa MWCO (2 mL), by following the instructions of the manufacturer. The recovered fraction was further purified using sephadex® G-100. The evolution of FRET signal over time for a mixture of 100 µM Lipo-Cy5-N_3 and Lipo-Cy3-CO liposomes was recorded with a SpectraMax M5 microplate reader (Molecular Devices, USA) at room temperature, using λ_{ex} = 530 nm, $\lambda_{em,DiL}$ = 570 nm, $\lambda_{em,DiD}$ = 670 nm.

Modelling the insertion of Lipo-Cy5-N_3 dyes in lipid bilayers

Molecular dynamics simulations were performed by Dr Harun Rashid and Prof. Irene Yarovsky, at RMIT University, Melbourne (Australia).

Lipid bilayer models were constructed with 200 DOPC lipids in each leaflet. A Cy5-azide residue was embedded in place of one lipid (considering DOPC head group has a similar width to Cy5), as there was no packing information available for Cy5. A ratio of 40 TIP3P water molecules to 1 lipid head group was used and 150 mM NaCl was also added in to the system, which was charge neutralized. The DOPC lipid molecules were modelled with the AMBER Lipid14 force field parameters.[18] Parameters for Cy5 dye were taken from general amber force field (GAFF),[19,20] and azide parameters for GAFF were taken from Pieffet *et al*.[21] Simulations were performed with the NAMD (version 2.10) program[22] in a NPT environment at 303 K and 1 atmospheric pressure.

Disruption of liposomes

Liposomes were composed of DOPC/DOPE/Cholesterol (50:25:25 mass ratio) and contained 1 mol % of donor or acceptor dye. Dry lipid films were hydrated in buffer (30 min, 2.5 $mg.mL^{-1}$, 37 °C, TE buffer containing 150 mM NaCl; buffer composition: 10 mM Tris, 150 mM NaCl, 1 mM EDTA, pH adjusted to 8.0 using HCl). Liposomes were extruded using an Avanti Lipid Mini-Extruder with 100 nm polycarbonate membranes (Whatman). Liposomes were diluted to 200 µM (lipid concentration) in the fusion buffer (TE buffer containing 150 mM NaCl, pH 7.4), and split in to 100 µL aliquots. Various quantities of disrupting agents were added to theses aliquots: triton X-100, ethanol, or chloroform. The fluorescence emission of the dyes were recorded with a SpectraMax M5 microplate reader (Molecular Devices, USA) at room temperature, using λ_{ex} = 530 nm, $\lambda_{em,DiL}$ = 570 nm, $\lambda_{em,DiD}$ = 670 nm.

Kinetics of SPAAC in liposomes

Liposomes encapsulating either Lipo-Cy3-CO or Lipo-Cy5-N_3 (C_6/C_{12}/C_{16}) were functionalised with 100 dsDNA copies per liposome. They were then diluted to 200 µM (lipid concentration) in the fusion buffer (TE buffer containing 150 mM NaCl, pH 7.4), and mixed at an equal volume ratio. For each time point, a 100 µL aliquot was sampled, and the FRET spectrum of the solution was measured with a SpectraMax M5 microplate reader (Molecular Devices, USA), using λ_{ex} = 530 nm. Then, immediately after, 100 molar excess of 11-Azido-3,6,9-trioxaundecan-1-amine (PEG-N_3) was added and the liposomes were disrupted by addition of ethanol (150 µL). The FRET spectrum was then re-measured to assess the formation of 'clicked' product.

3.3 Results and discussion

3.3.1 Synthesis of the functional dyes

The novel asymmetric functional cyanine dyes Lipo-Cy3-CO and Lipo-Cy5-N_3 were synthesized following modified literature procedures.[23] The quaternary ammonium indolenine compounds (**5**, **6**, and **7**) were obtained by functionalizing 2,3,3-trimethylindolenine with alkyl chains of varying lengths and functionalities: alkyl halide 1-iodohexadecane, carboxylic acid 6-bromohexanoic acid, or azide-functionalized alkyl halides (**2**, **3**, **4**) in dichlorobenzene. While 1-iodohexadecane and 6-bromohexanoic acid were commercially available, the azide-functionalized alkyl halide compounds were synthesized from the equivalent diol or dibromo precursors (Figure 4). For instance, 1,16-hexadecanediol was converted to 1,16-dibromohexadecane (**1**) by bromination using *N*-bromosuccinimide and triphenylphosphine.[24] Then, the azide derivative 1-azido-16-bromohexadecane (**4**) was obtained by reacting 1,16-dibromohexadecane with one equivalent of sodium azide.

Potassium iodide was added to the reaction mixture in order to form the alkyl iodo derivative *in situ*, by substituting the bromo substituent for iodine. Iodo derivatives are more reactive than bromo counterparts, as the C-I bond is weaker than C-Br, and it was necessary to enhance the reactivity of the alkyl halide to maximize the formation of the quaternary ammonium indolenine compounds, since the products could not be purified efficiently due to their instability to column chromatography. Quaternary ammonium indolenine compounds were isolated from the crude reaction mixture by precipitation. As a result of the hydrophobic nature of the alkyl chains, a number of the products did not readily precipitate in diethyl ether, requiring the use of *n*-hexane to induce precipitation of the crude products, which were found to be sufficiently pure for further manipulation. The reaction was carried out at 120 °C for the functionalization with 1-iodohexadecane and 6-bromohexanoic acid, however, for the azido alkyl halide derivatives, the reaction temperature was lowered to either 80 °C or 100 °C as the azide group is unstable at high temperature. Lowering the reaction temperature caused a decrease in the yield of the isolated products but allowed the generation of sufficient material for subsequent steps.

The asymmetric cyanine dyes were then obtained by condensation of two functionalized quaternary ammonium indolenine compounds with *N*,*N*′-diphenylformamidine or malonaldehyde bis(phenylimine), spacing the two indolenines by respectively three carbons in the case of Cy3, and five carbons in the case of Cy5. First, an activated intermediate was formed by reacting a quaternary ammonium indolenine with the imine linker in acetic anhydride (Ac_2O)

at 120 °C. This intermediate was then reacted with the other quaternary ammonium indolenine in the presence of pyridine at room temperature, in order to form the cyanine dye.

The Cy3 based dye (**13**) was functionalized with a cyclooctyne group by esterification of the carboxylic acid group with a commercially-available alcohol-functionalized cyclooctyne, using 1-ethyl-3-(3-dimethylaminopropyl)carbodiimide (EDC) as a coupling agent (Figure 5).

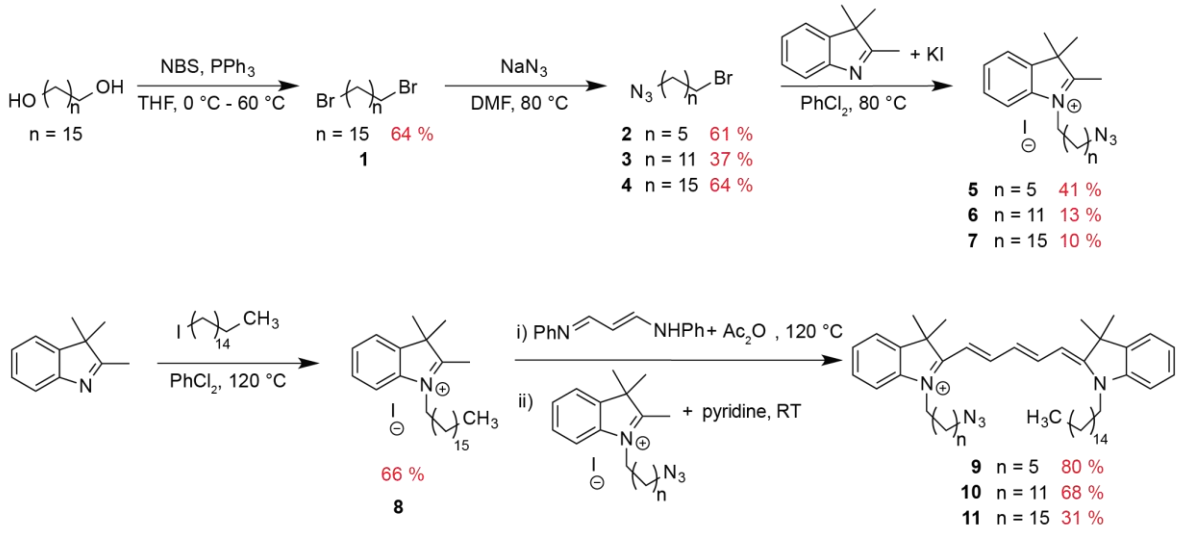

Figure 4. Synthesis of Lipo-Cy5-N_3 dyes, containing azide functional group. Lipo-Cy5-N_3 dyes were synthesized with 3 different alkyl chain lengths: C_6, C_{12}, and C_{16}.

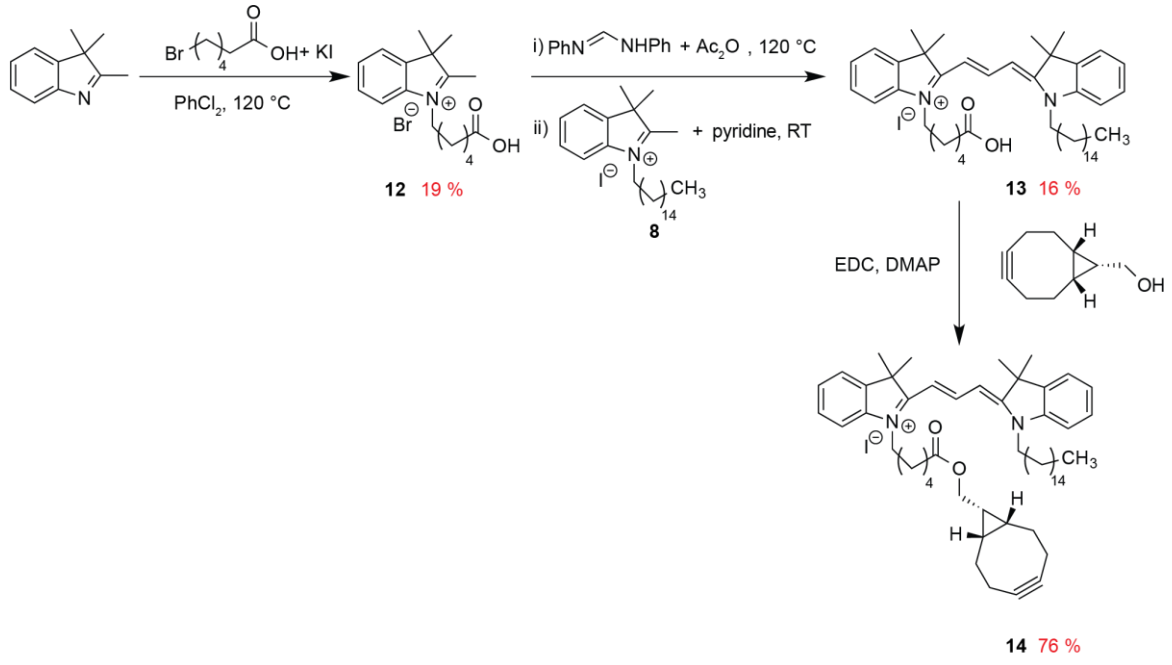

Figure 5. Synthesis of Lipo-Cy3-CO dye, containing cyclooctyne functional group.

Lipo-Cy5-N_3 was synthesized with three different alkyl chain lengths: 6-, 12-, and 16-carbons long, in order to study the influence of the lipophilicity of Lipo-Cy5-N_3 on its stability in lipid bilayers, as discussed later in this Chapter.

3.3.2 FRET in solution

The quantum yield of the synthesized functional dyes Lipo-Cy3-CO and Lipo-Cy5-N_3 was compared to their commercial counterparts DiL and DiD. To measure the quantum yield, several solutions of the dyes in methanol (MeOH) were prepared, in order to give an absorbance in the range of 0.02-0.1 (a.u.), and their fluorescence intensity measured (Figure 6). The quantum yield can be determined using the following equation:

$$Q_S = Q_r \times \frac{Grad_S}{Grad_r} \times \frac{n_S^2}{n_r^2}, \quad (1)$$

where Q_s is the quantum yield of the dye of interest, Q_r is the quantum yield of the reference dye, *Grad* is the slope obtained from the linear fitting of the plot of absorbance *vs* integrated fluorescence intensity, and n is the refractive index of the solvent in which the measurements are made. As all measurements were made in MeOH, the ratio of the refractive indexes is equal to 1.

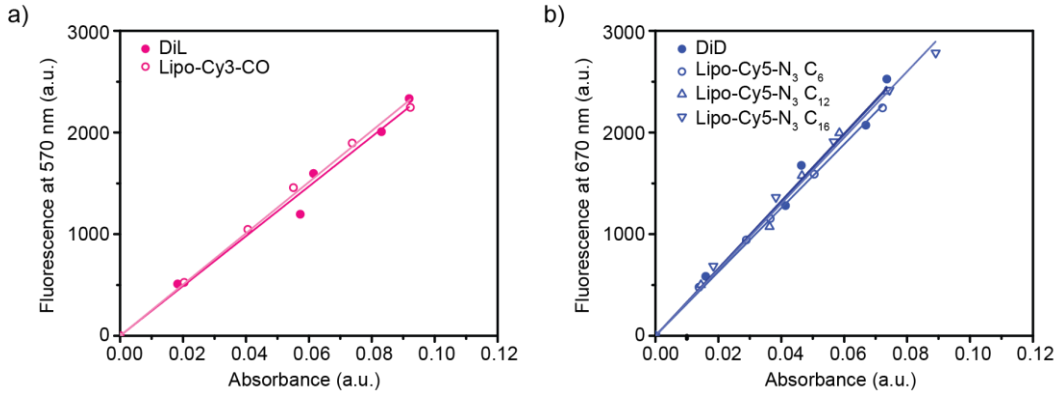

Figure 6. a) Fluorescence intensity of DiL and Lipo-Cy3-CO (1) solutions of various concentrations characterized by their absorbance at 549 nm (λ_{ex} = 549 nm, λ_{em} = 570 nm). b) Fluorescence intensity of DiD and Lipo-Cy5-N_3 (2-4) solutions of various concentrations characterized by their absorbance at 644 nm (λ_{ex} = 644 nm, λ_{em} = 670 nm).

Table 2 summarizes the quantum yields for the synthesized dyes and compares them to the commercial counterparts DiL and DiD. The quantum yields of the synthesized dyes closely matched those of DiL and DiD, demonstrating that the introduction of the azide and cyclooctyne groups did not significantly alter the spectroscopic properties of the dyes.

Table 2. Summary of the quantum yield (QY) of the synthesized dyes Lipo-Cy3-CO and Lipo-Cy5-N_3 and of the commercial dyes DiL and DiD (n=2).

Name	Slope (a.u.)	QY[a]
DiL	$2.42\times10^4 \pm 3.97\times10^2$	0.24
Lipo-Cy3-CO	$2.55\times10^4 \pm 3.57\times10^2$	0.26
DiD	$3.28\times10^4 \pm 4.70\times10^2$	0.33
Lipo-Cy5-N_3 C_6	$3.28\times10^4 \pm 3.25\times10^2$	0.33
Lipo-Cy5-N_3 C_{12}	$3.11\times10^4 \pm 5.04\times10^2$	0.31
Lipo-Cy5-N_3 C_{16}	$3.16\times10^4 \pm 1.19\times10^3$	0.32

[a]QY was calculated using DiD as a reference, using $QY_{dye} = QY_{DiD} \times (Slope_{dye}/Slope_{DiD})$.[25]

With the azide and cyclooctyne functionalised dyes in hand, their reaction was first studied in solution. Stock solutions of the dyes were prepared in dichloromethane (DCM, 10 µM). Lipo-Cy3-CO and Lipo-Cy5-N_3 dyes were mixed at equal volume ratio, and the FRET spectrum of the dye mixture was measured (Figure 7). Significantly higher FRET ratios were measured for mixtures of the functional dyes, compared to a mixture of Lipo-Cy3-CO and DiD. This supports the successful cycloaddition of Lipo-Cy3-CO and Lipo-Cy5-N_3, as the dyes were maintained in close enough proximity for FRET to occur. Lipo-Cy3-CO and DiD were found to be too far apart for significant FRET to occur.

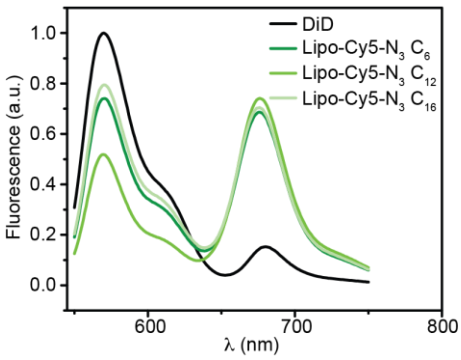

$E = I_{670} / (I_{670}+I_{570})$

Lipo-Cy3-CO-DiD	E = 0.10
Lipo-Cy3-CO-Lipo-Cy5-N_3 C_6	E = 0.46
Lipo-Cy3-CO-Lipo-Cy5-N_3 C_{12}	E = 0.57
Lipo-Cy3-CO-Lipo-Cy5-N_3 C_{16}	E = 0.45

Figure 7. Evaluation of the FRET efficiency of Lipo-Cy3-CO-Lipo-Cy5-N_3 (C_6, C_{12}, or C_{16}) pairs in dichloromethane. Significantly higher FRET efficiency (E) was observed for the functional dyes compared with Lipo-Cy3-CO-DiD (λ_{ex} = 530 nm).

3.3.3 FRET in liposomes

Having successfully demonstrated the chemical conjugation of Lipo-Cy3-CO and Lipo-Cy5-N_3 in solution, the dyes were incorporated into liposome bilayers and used as FRET pairs in the liposome fusion assay developed in Chapter 2. Figure 8 summarizes the principle of the assay. Briefly, two populations of liposomes are prepared, incorporating either DiL or Lipo-Cy3-CO, and DiD or Lipo-Cy5-N_3. The liposomes are functionalized with complementary double stranded DNA (dsDNA), designed to hybridize in a zipper-like manner, bringing the liposomes into close proximity. This initiates lipid mixing and eventually liposome fusion, which is detected by an increase of FRET. When liposomes are not functionalized with DNA, no increase in FRET signal is expected.

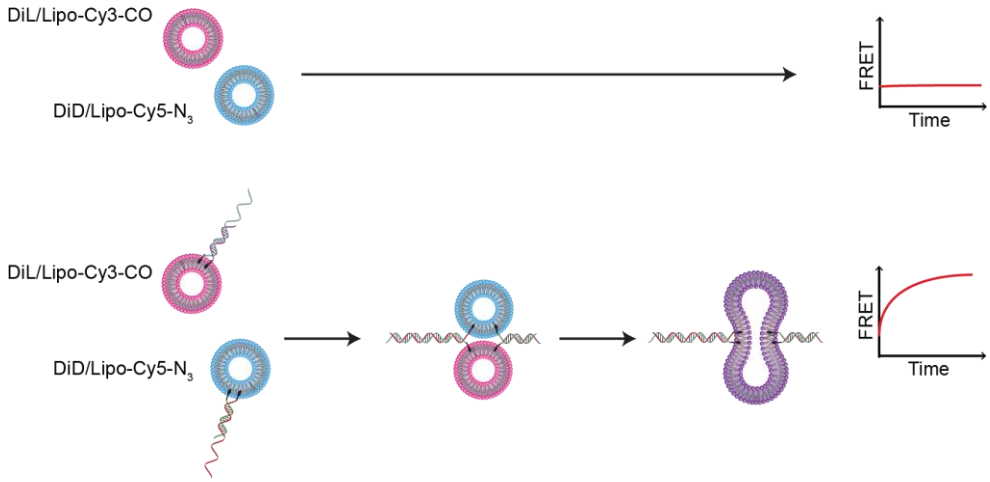

Figure 8. Schematic of the liposome fusion assay. Liposome fusion is detected by an increase of FRET signal, as the dyes come in close contact during lipid mixing.

First, the liposome formulation containing Lipo-Cy5-N_3 C_{12} was studied. Liposomes containing Lipo-Cy3-CO were mixed with liposomes containing Lipo-Cy5-N_3 C_{12}, and the FRET signal was measured over time. In initial experiments, the liposomes were not functionalized with dsDNA. As a control, liposomes containing DiL and DiD were also prepared. Figure 9a shows the evolution of FRET signal over time. When DiD and DiL liposomes were mixed, no increase in FRET was observed, as expected (Figure 8). A similar result was obtained for a mixture of Lipo-Cy3-CO and DiD liposomes. However, when Lipo-Cy3-CO and Lipo-Cy5-N_3 C_{12} liposomes were mixed, as well as liposomes containing DiL and Lipo-Cy5-N_3 C_{12}, the FRET signal increased over time.

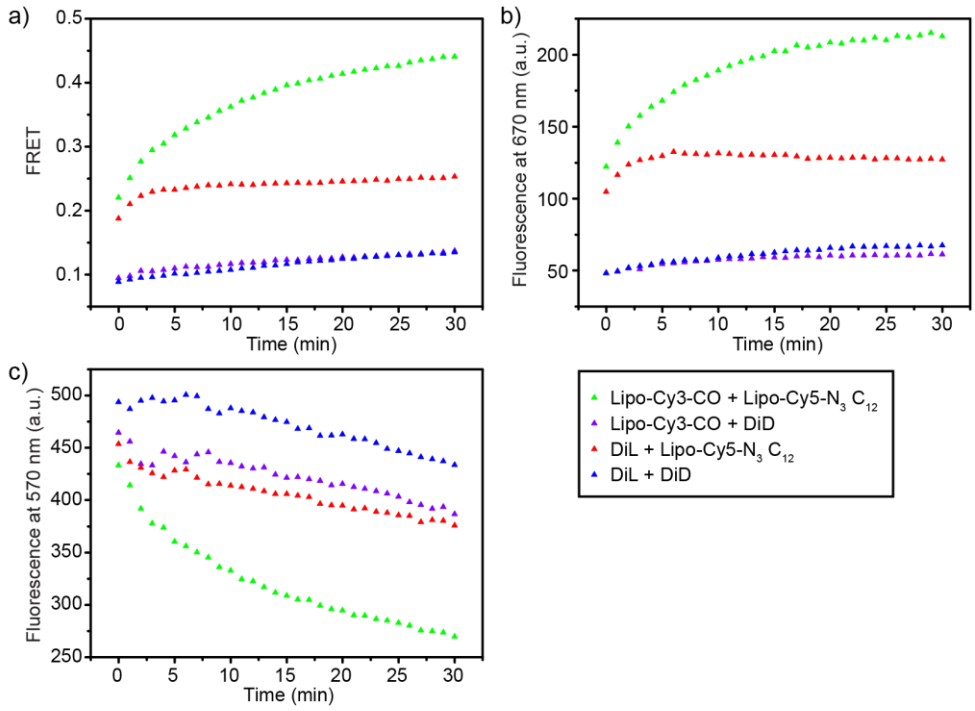

Figure 9. Evolution of a) FRET signal, b) Emission of the donor Lipo-Cy3-CO at 570 nm, and c) Emission of the acceptor Lipo-Cy5-N_3 C_{12} at 670 nm, for a mixture of non-DNA functionalized Lipo-Cy3-CO and Lipo-Cy5-N_3 C_{12} liposomes (λ_{ex} = 530 nm).

Several hypotheses were investigated to account for the increase in FRET signal. First, the stability of Lipo-Cy5-N_3 C_{12} liposome formulation was verified by performing a leakage assay (Figure 10). Briefly, carboxyfluorescein was incorporated at a high concentration in DiD or Lipo-Cy5-N_3 C_{12} containing liposomes. Excess unencapsulated dye was removed using size exclusion chromatography. In this leakage assay, the dye encapsulated in the liposomes exhibited low fluorescence intensity as the high dye concentration caused self-quenching. As carboxyfluorescein was released from the liposomes, the fluorescence intensity of the solution increased due to dilution of the dye in the solution surrounding the liposomes. Figure 10 shows the evolution of the fluorescence of DiD and Lipo-Cy5-N_3 C_{12} liposome solutions over time; after 30 min the liposomes were disrupted using a non-ionic surfactant (triton X-100), releasing all encapsulated carboxyfluorescein; this allowed the maximum fluorescence intensity of the solution to be evaluated, and hence allow the percentage of leakage from the liposomes to be derived. As seen in Figure 10, both DiD and Lipo-Cy5-N_3 C_{12} liposomes were stable over time and did not leak significantly. Therefore, it was concluded that the increase of FRET in the liposome fusion assay for Lipo-Cy5-N_3 C_{12} liposomes was not caused by instability of the new formulation.

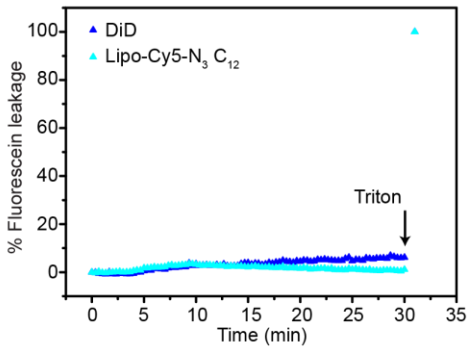

Figure 10. Carboxyfluorescein leakage assay for assessing the stability of DiD and Lipo-Cy5-N_3 C_{12} liposomes.

Next, in order to verify that the dyes were encapsulated in the lipid bilayer of liposomes and not simply adsorbed on the surface, the liposomes were subjected to extensive purification using several types of size exclusion chromatography columns. However, this did not prevent the non-specific FRET occurring when non-DNA functionalized Lipo-Cy5-N_3 C_{12} liposomes were mixed with Lipo-Cy3-CO or DiL liposomes (data not shown).

Lipids and membrane-located molecules can non-specifically migrate between liposomes by two processes: through diffusion in the aqueous phase surrounding the liposomes (when the molecule has partial aqueous solubility), or through exchange during collision events occurring between liposomes.[26] This hypothesis was tested by adding an excess of unlabelled DOPC liposomes to a 1:1 mixture of liposomes containing either a donor or an acceptor dye (Figure 11). In these conditions, the probability of Lipo-Cy5-N_3 transfer to unlabelled liposomes is greater than the probability of transfer to Lipo-Cy3-CO containing liposomes, if the exchange of dye between liposomes is non-specific. It was observed that adding an excess of unlabelled liposomes resulted in almost complete elimination of non-specific FRET between Lipo-Cy3-CO and Lipo-Cy5-N_3, as well as with DiL and Lipo-Cy5-N_3 (Figure 11a). Therefore, it was concluded that the increase of FRET signal observed upon mixing Lipo-Cy5-N_3 C_{12} liposomes with either Lipo-Cy3-CO or DiL liposomes was caused by non-specific transfer of the Lipo-Cy5-N_3 C_{12} dye between liposomes.

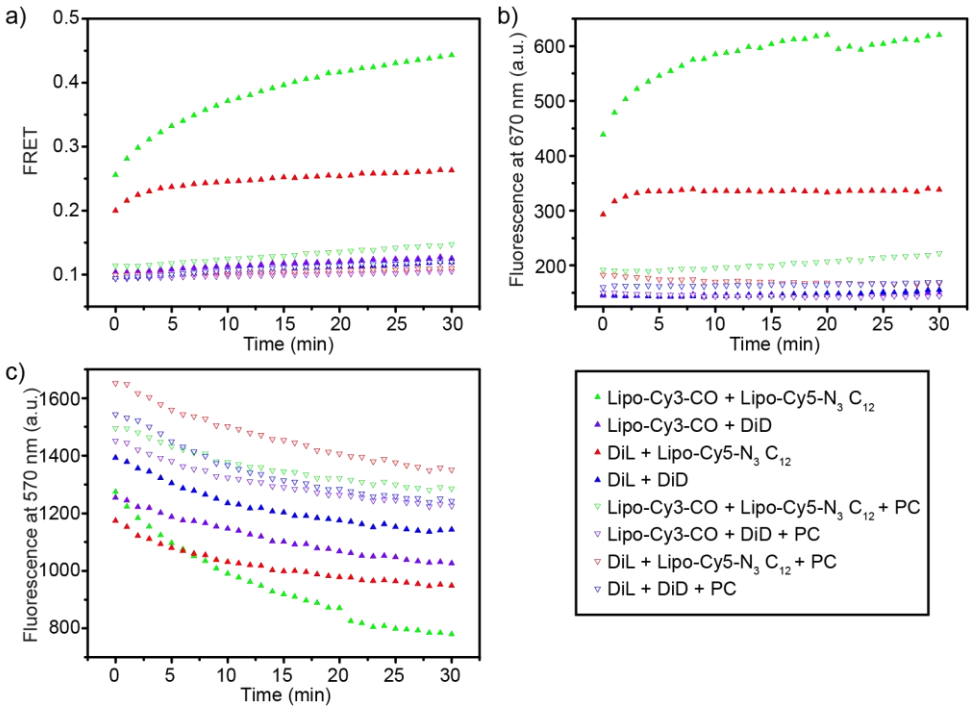

Figure 11. Fluorescence intensity evolution over time for a mixture of non-DNA functionalized liposomes in the absence (full symbols) or presence (open symbols) of excess unlabelled DOPC liposomes. a) FRET signal, b) Emission of the donor DiL/Lipo-Cy3-CO at 570 nm, and c) Emission of the acceptor DiD/Lipo-Cy5-N_3 C_{12} at 670 nm (λ_{ex} = 530 nm).

As a strategy for maximizing the retention of Lipo-Cy5-N_3 in the bilayer, the influence of the alkyl chain length and therefore lipophilicity of the molecule was studied. As shown in Figure 4, three different Lipo-Cy5-N_3 dyes were synthesized, with various alkyl chain lengths: 6-, 12-, and 16-carbons long (Figure 4, Figure 12). The lipophilicity of each dye was calculated using the ALOGPS 2.1 online program to predict logP.[17] LogP is the partition coefficient, and represents the logarithm of the ratio of concentrations of a solute between two solvents, 1-octanol and water. As such, LogP is a measure of lipophilicity. As expected, the lipophilicity (logP) of Lipo-Cy5-N_3 increased with increasing alkyl chain length (Figure 12b).

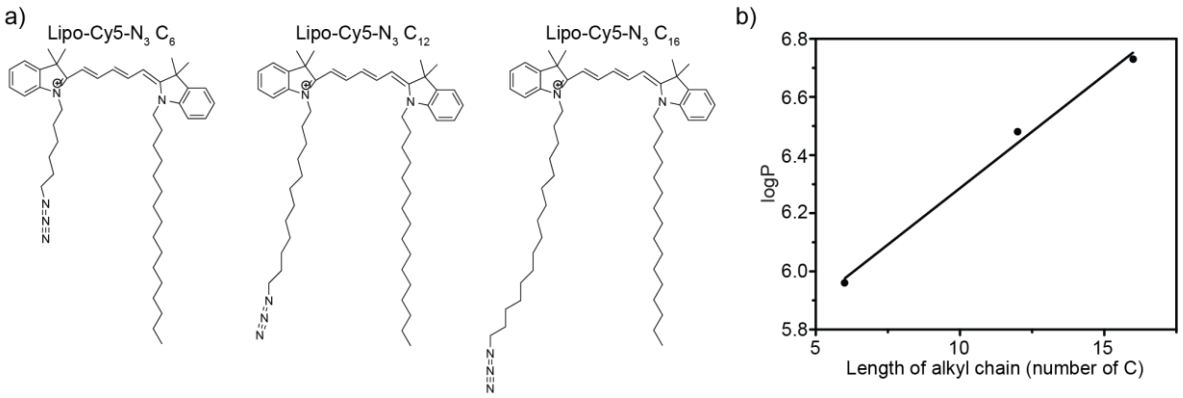

Figure 12. a) Chemical structures of Lipo-Cy5-N_3 dyes with different alkyl chain lengths. b) Plot of lipophilicity *vs* alkyl chain length.

The different Lipo-Cy5-N_3 dyes were then incorporated in liposomes, and the bilayer stability of each dye was studied by mixing Lipo-Cy5-N_3 liposomes with Lipo-Cy3-CO liposomes (non-functionalized with DNA) (Figure 13a). All Lipo-Cy5-N_3 dyes caused a non-specific increase of FRET signal. Lipo-Cy5-N_3 C_{16} led to the lowest increase in FRET over time due to dye transfer, while Lipo-Cy5-N_3 C_6 and C_{12} both yielded a high FRET efficiency (Figure 13a and c). In control experiments, non-functional dyes DiL and DiD did not cause non-specific FRET (Figure 13d), and a mixture of Lipo-Cy3-CO and DiD liposomes showed relatively low non-specific FRET (Figure 13b). Lipo-Cy5-N_3 C_{16} is more lipophilic compared to C_6 and C_{12} and therefore possesses reduced water solubility. As a result its stability within the lipid bilayer is increased, explaining its higher retention in liposomes and decreased rate of transfer.

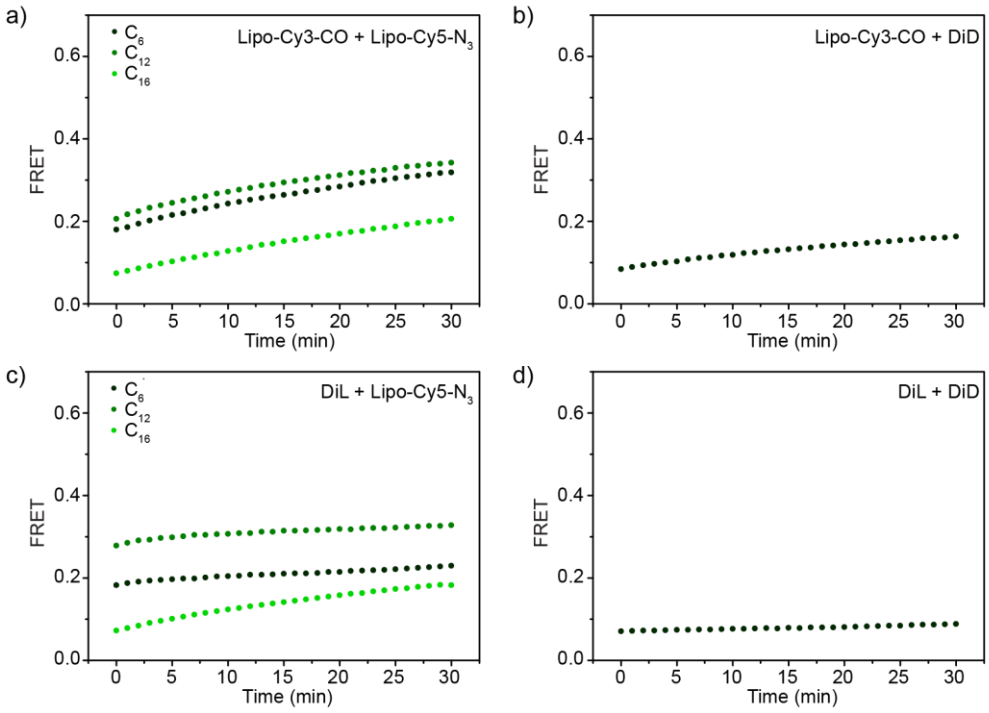

Figure 13. Influence of Lipo-Cy5-N_3 alkyl chain length on non-specific FRET signal generation. Liposomes containing either a donor or an acceptor dye from a FRET pair were mixed at equal volume, and the FRET signal was recorded. a) Lipo-Cy3-CO and Lipo-Cy5-N_3 liposomes (C_6/C_{12}/C_{16}). b) Lipo-Cy3-CO and DiD liposomes. c) DiL and Lipo-Cy5-N_3 liposomes (C_6/C_{12}/C_{16}). d) DiL and DiD liposomes.

Additionally, the insertion of Lipo-Cy5-N_3 dyes inside lipid bilayers was modelled by Dr Harund Raschid and Patrick Charchar from the group of Prof. Irene Yarovsky at RMIT University (Melbourne, Australia). Molecular dynamic simulations of the insertion of Lipo-Cy5-N_3 C_6 and C_{16} in lipid bilayers showed that Lipo-Cy5-N_3 C_6 dye diffused laterally in the upper leaflet, while Lipo-Cy5-N_3 C_{16} diffused inwards, localizing at the interface between the two lipid leaflets (Figure 14). Since Lipo-Cy5-N_3 C_{16} is integrated deeper in the lipid bilayer compared with Lipo-Cy5-N_3 C_6, this could explain why Lipo-Cy5-N_3 C_{16} is better retained in liposomes and leads to less non-specific FRET signal compared with Lipo-Cy5-N_3 C_6 and C_{12}. It can be hypothesized that upon liposome collisions, less dye transfer takes place for C_{16} as the dye is less exposed at the surface of the lipid bilayer. Moreover, this observation correlates well with the increase in lipophilicity of Lipo-Cy5-N_3 with increasing chain length; a more hydrophobic molecule will less favourably transfer through the aqueous media to another liposome and be more stable in the hydrophobic core of the lipid bilayer.

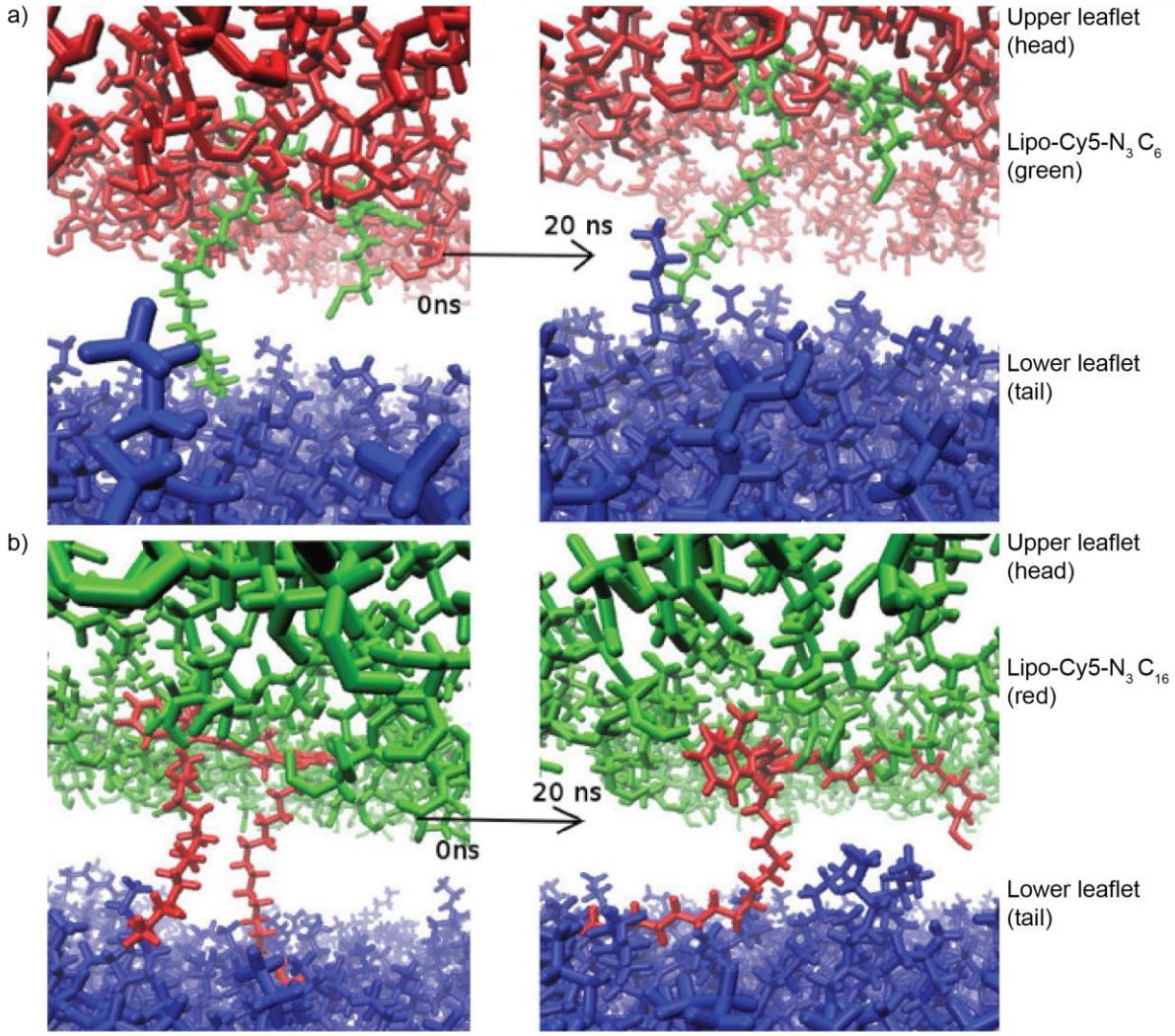

Figure 14. Modelling the insertion of Lipo-Cy5-N_3 of different alkyl chain lengths in the lipid bilayer. Representative structures of Cy5-azide molecules incorporated into a DOPC bilayer after 0 ns (left) and 20 ns (right) of MD. a) Lipo-Cy5–N_3 C_6 (green). b) Lipo-Cy5–N_3 C_{16} (red). ***For clarity, the tail molecules of the DOPC upper leaflet and solvent are not shown.*** The modelling experiments were performed by Dr Harund Raschid (RMIT University, Melbourne, Australia).

3.3.4 Quantification of the 'clicked' product formation

Formation of 'clicked' product via specific, DNA-mediated liposome fusion

With this optimised system, the formation of conjugated product upon liposome fusion was studied upon being triggered by DNA self-assembly (Figure 8, Figure 15). Liposomes containing either a donor dye (DiL or Lipo-Cy3-CO) or an acceptor dye (DiD or Lipo-Cy5-N_3) were functionalized with 100 dsDNA copies per liposome following the procedure detailed in Chapter 2. The kinetics of liposome fusion were measured for 30 min (Figure 15).

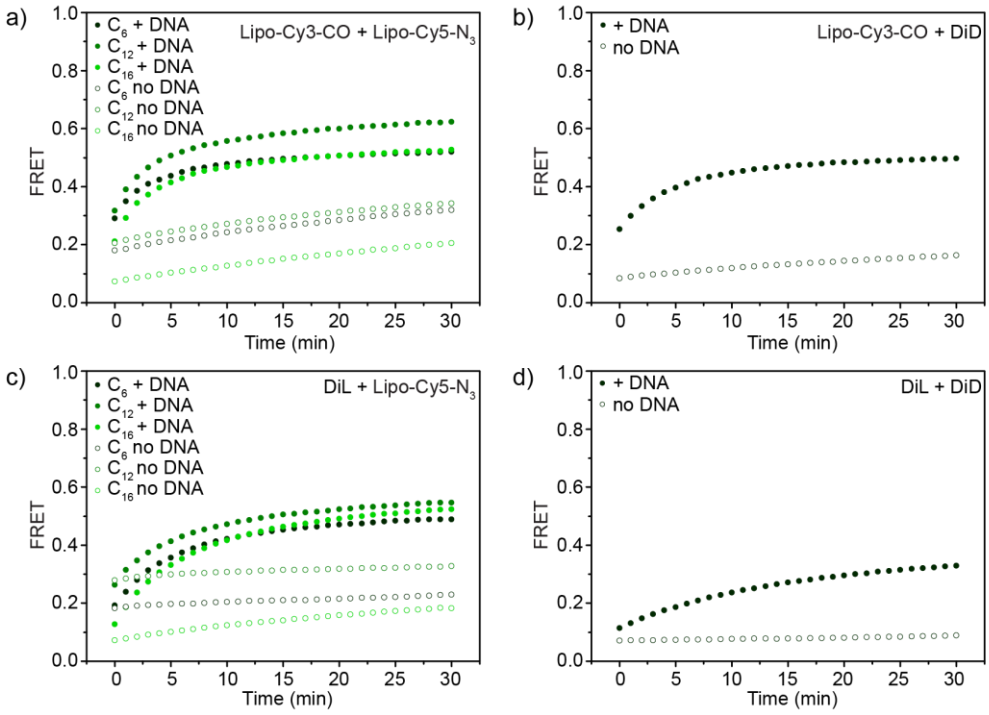

Figure 15. Influence of Lipo-Cy5-N_3 alkyl chain length on specific FRET signal generation via DNA-mediated liposome fusion. Liposomes containing either a donor or an acceptor dye from a FRET pair were mixed at equal volume, and the FRET signal was recorded (λ_{ex} = 530 nm). Liposomes were functionalized with 100 dsDNA (full symbols) or non-functionalised (hollow symbols). a) Lipo-Cy3-CO and Lipo-Cy5-N_3 liposomes ($C_6/C_{12}/C_{16}$). b) Lipo-Cy3-CO and DiD liposomes. c) DiL and Lipo-Cy5-N_3 liposomes ($C_6/C_{12}/C_{16}$). d) DiL and DiD liposomes.

When liposome fusion was triggered with DNA self-assembly, the FRET signal emitted by the functional dyes was higher than the FRET signal generated by DiL and DiD liposomes. However, a fraction of the FRET signal generated by the functional dyes can also be caused by non-specific transfer of dyes between liposomes as described above.

Disruption of the liposomes

The efficiency of the SPAAC reaction in lipid bilayers was next evaluated. In order to quantify the formation of the 'clicked' product, a method to disrupt liposomes was sought. Indeed, if the liposomes were broken down, the resulting FRET signal would emanate only from the chemically conjugated dye products, as non-covalently bound dyes would be too dilute to undergo efficient FRET. In the literature, several methods have been reported for disrupting liposomes, such as the addition of a surfactant, or of an organic solvent miscible with water.[27] The efficiency of these methods was first evaluated (Figure 16). Liposomes were prepared encapsulating both donor and acceptor DiL and DiD FRET dyes. Liposomes were diluted in buffer and split into aliquots. Various quantities of a non-ionic surfactant, triton X-100, were

added to the aliquots and the FRET signal was measured (Figure 16a). When the dyes were confined in the lipid bilayer (*i.e.* liposomes were intact), the FRET signal was high in all cases. However, as the bilayer became increasingly disrupted by the addition of surfactant, the FRET signal decreased to a minimum. This was reached after the addition of 1 % v/v of triton X-100. However, in subsequent experiments, the disruption of liposomes using triton proved to be poorly reproducible and led to false positive results; it was hypothesized that the formation of detergent micelles could favour the aggregation of the dyes and lead to misleading FRET signals. The same experiment was therefore repeated through the addition of chloroform ($CHCl_3$) to disrupt the liposomes (Figure 16b). This method did not lead to the efficient disruption of the liposomes, potentially because $CHCl_3$ and water are not miscible. Finally, the use of ethanol (EtOH) for disrupting liposomes was tested (Figure 16c and d). This method allowed the reliable disruption of the liposomes when adding more than 60 v/v % of EtOH. Furthermore, it permitted the measurement of the maximum FRET signal observed for each combination of functional dyes Lipo-Cy3-CO/Lipo-Cy5-N_3 (C_6/C_{12}/C_{16}) (Figure 16d).

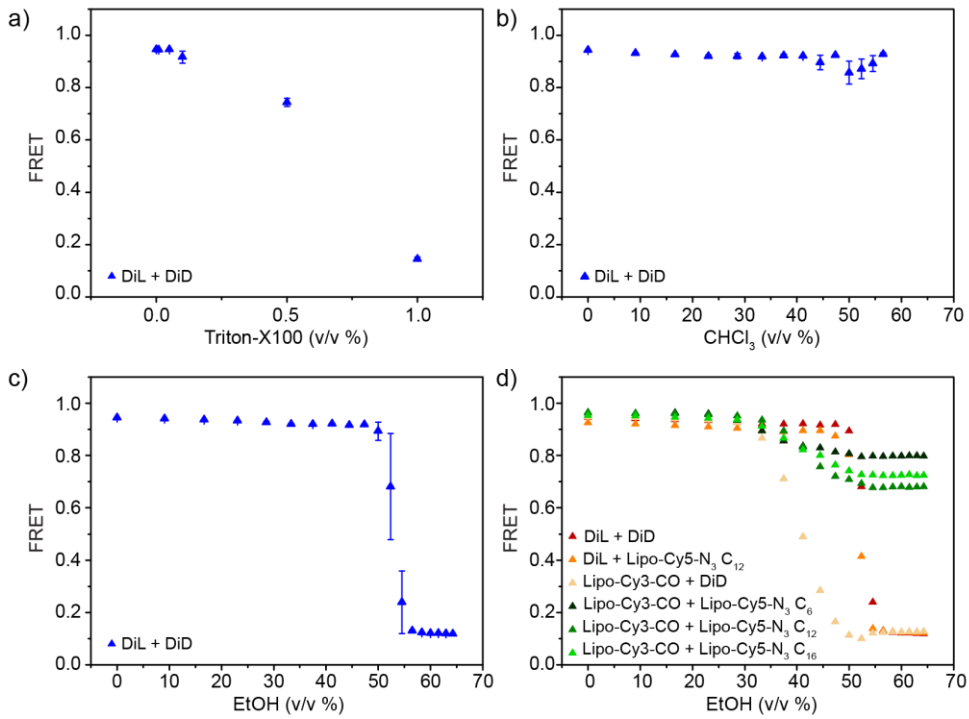

Figure 16. Evaluation of several methods for disrupting liposomes. Chemicals or solvents were added at increasing concentrations to liposome containing both donor and acceptor dyes of the FRET pair. a) Triton X-100. b) Chloroform ($CHCl_3$). c) & d) Ethanol (EtOH).

After finding an adequate method for disrupting liposomes, it was applied to the evaluation of cycloaddition product formation after DNA-mediated liposome fusion. The FRET spectra for the different dye combinations were measured directly after the liposome fusion assay (Figure 17i).

Then, a 100 molar excess of azide-functionalized polyethylene glycol (11-azido-3,6,9-trioxaundecan-1-amine, PEG-N_3) was added to the liposome mixture in order to prevent the functional dyes from reacting together after EtOH addition. Indeed, cycloaddition of functional dyes could be favoured when dissolved in EtOH; adding an excess of PEG-N_3 ensured that cycloadditions took place preferentially between Lipo-Cy3-CO and PEG-N_3, and not between Lipo-Cy3-CO and Lipo-Cy5-N_3. Finally, the FRET signal was measured again, post liposome disruption (Figure 17ii).

All dye combinations resulted in high FRET efficiency upon liposome fusion (Figure 17i). As highlighted in Table 3, the FRET efficiency was higher for mixtures of Lipo-Cy3-CO/Lipo-Cy5-N_3 liposomes compared to other liposomes mixtures, supporting the hypothesis at the outset of the study.

Table 3. FRET efficiency ($E = I_{670}/(I_{670} + I_{570})$) calculated after liposome fusion (30 min), and after disrupting these liposomes.

		E after liposome fusion	E after liposome disruption
Lipo-Cy3-CO/Lipo-Cy5-N_3	C_6	0.62	0.32
	C_{12}	0.71	0.33
	C_{16}	0.63	0.37
DiL/Lipo-Cy5-N_3	C_6	0.60	0.17
	C_{12}	0.60	0.17
	C_{16}	0.60	0.17
Lipo-Cy3-CO/DiD		0.62	0.11
DiL/DiD		0.44	0.12

The FRET signal after liposome fusion is caused by a combination of dye confinement and chemical conjugation in the lipid bilayer (in the case of Lipo-Cy3-CO/Lipo-Cy5-N_3 mixtures). Disrupting the liposomes eliminates dye confinement, and the resulting FRET signal only originates from 'clicked' dyes. As seen on Figure 17ii and Table 3, only mixtures of Lipo-Cy3-CO/Lipo-Cy5-N_3 liposomes generated FRET after liposome disruption, demonstrating the formation of cycloaddition products. Therefore, it can be concluded that the SPAAC reaction successfully took place within the lipid bilayer.

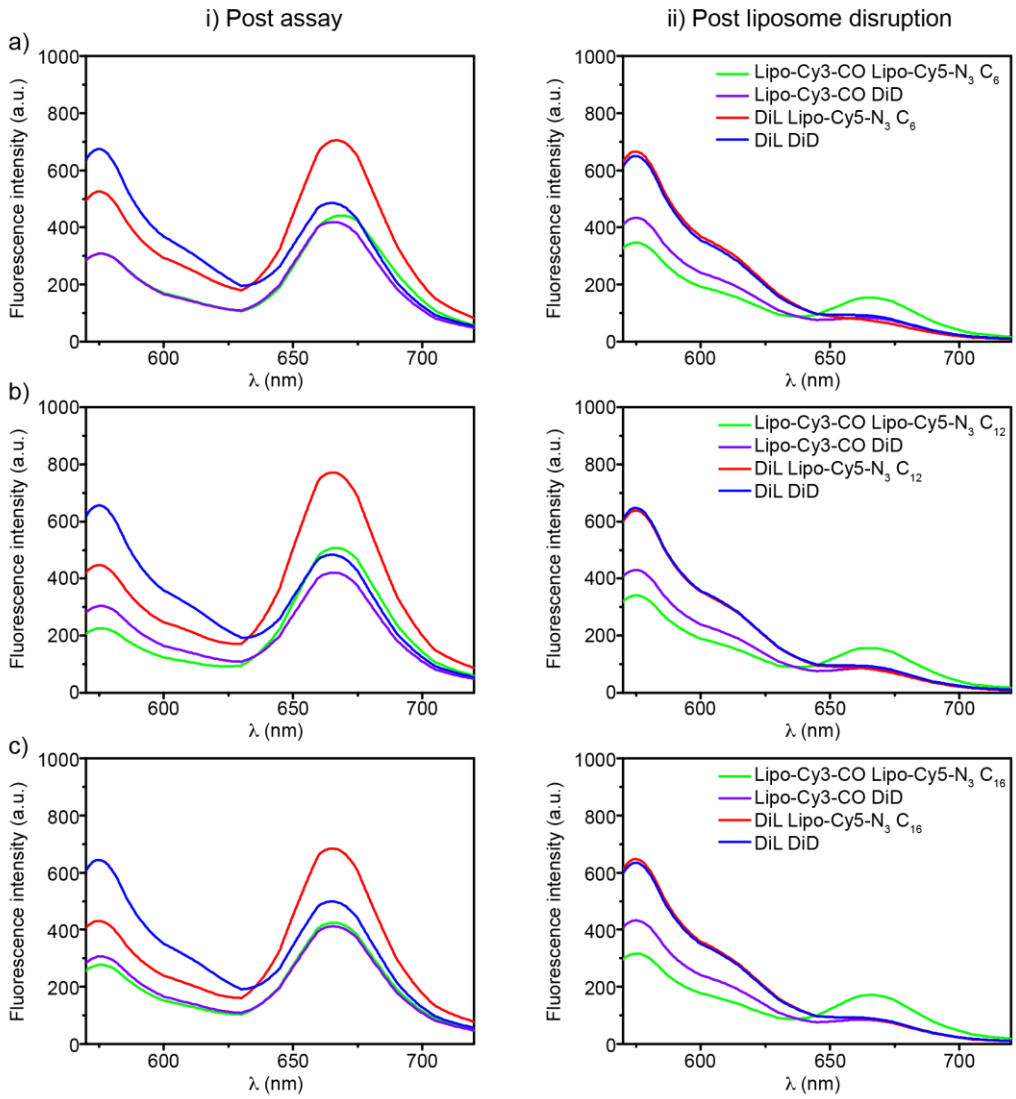

Figure 17. FRET spectra (i) post liposome fusion assay (30 min kinetics) and (ii) post liposome disruption by EtOH addition, for 1:1 mixtures of donor and acceptor liposomes. a) Lipo-Cy5-N_3 C_6. b) Lipo-Cy5-N_3 C_{12}. c) Lipo-Cy5-N_3 C_{16}.

To further confirm the formation of the 'clicked' product, aliquots of the liposomes mixtures (post liposome fusion assay) were taken, and analysed via MALDI (with the help of Dr Yiyang Lin). The results for a mixture of Lipo-Cy3-CO and Lipo-Cy5-N_3 C_{12} liposomes are presented on Figure 18. Several products can be identified: the 'clicked' product between Lipo-Cy3-CO and Lipo-Cy5-N_3 C_{12}, the 'clicked' product between Lipo-Cy3-CO and PEG-N_3, and unreacted Lipo-Cy5-N_3 C_{12}. It is to be noted that with this analytical technique, peak strength is not related to product concentration and therefore quantities cannot be determined. Peak strength depends on several factors, notably the lipophilicity and ease of ionisation of the species. Therefore, the high intensity of the peak corresponding to Lipo-Cy3-CO—PEG-N_3 relative to the peak for Lipo-

Cy3-CO—Lipo-Cy5-N_3 shown in Figure 18 does not allow to conclude on the efficiency of the cycloaddition reaction.

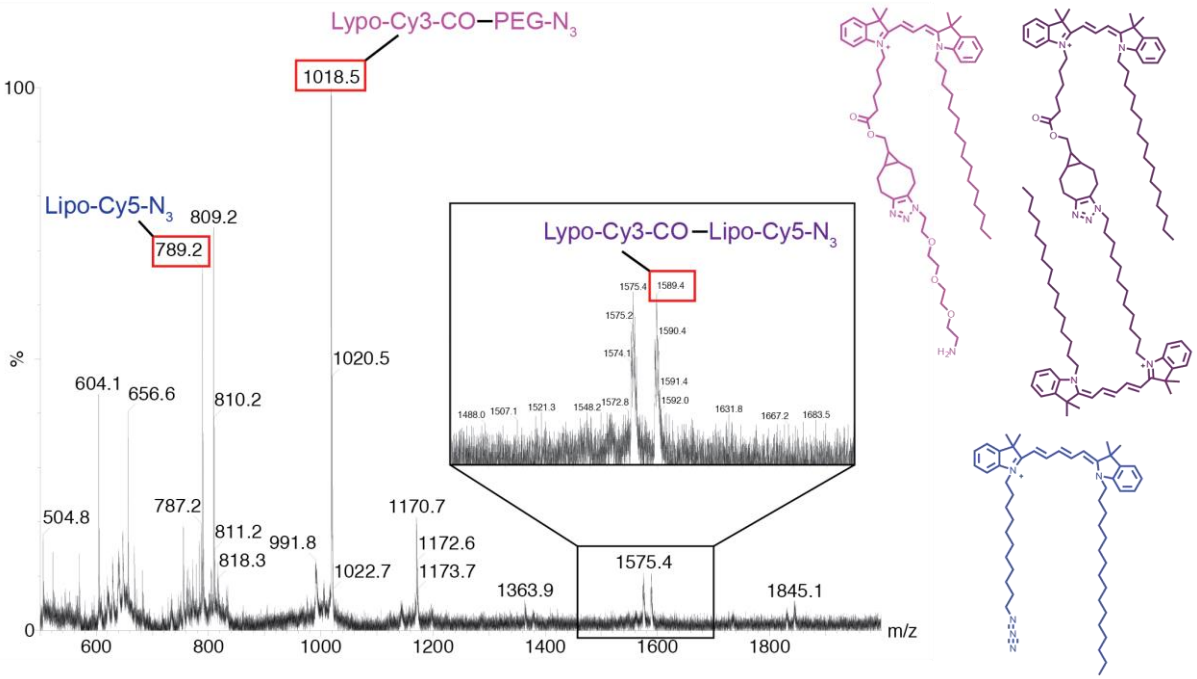

Figure 18. MALDI spectrum of a mixture of Lipo-Cy3-CO/Lipo-Cy5-N_3 liposomes after the fusion assay and after addition of a 100-molar excess of PEG-N_3, showing the formation of different products, illustrated by their chemical structures.

Kinetics of SPAAC reaction in liposomes

The kinetics of the SPAAC reaction within the lipid bilayer were studied (Figure 19). Equal volumes of Lipo-Cy3-CO and Lipo-Cy5-N_3 liposomes were mixed, and aliquots were sampled at various time intervals. The FRET spectra were measured both prior to and post liposome disruption using EtOH, enabling the kinetics of liposome fusion, as well as chemical conjugation, to be followed.

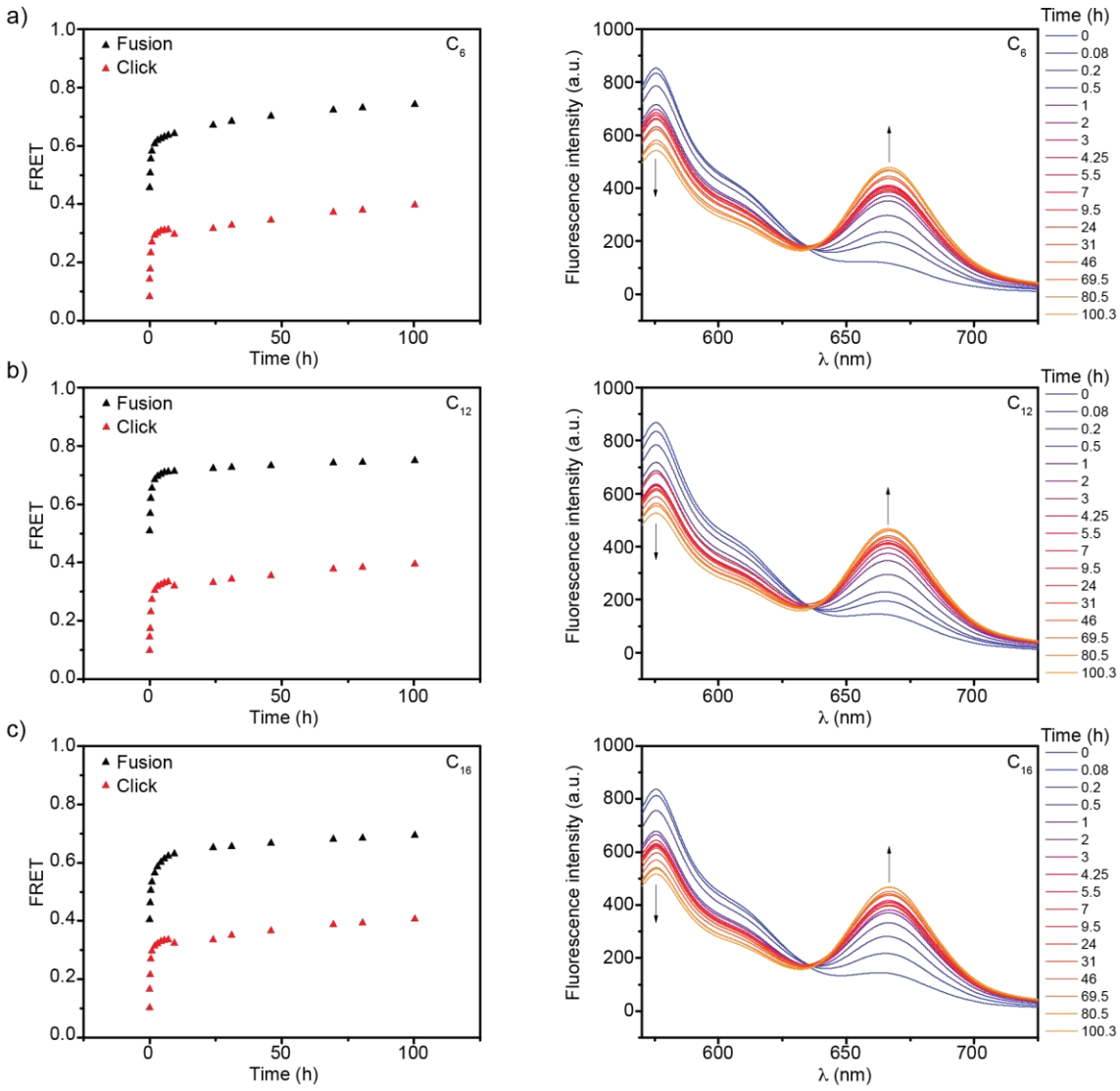

Figure 19. Kinetics of the SPAAC reaction. Equal volumes of Lipo-Cy3-CO and Lipo-Cy5-N_3 liposomes were mixed, and sampled at various time points to assess the liposome fusion extent (black symbols). Liposomes were then disrupted by EtOH addition, in order to assess the amount of 'clicked' product formed (red symbols). The FRET spectra show the increase of FRET over time post liposome disruption for mixtures of Lipo-Cy3-CO liposomes with liposomes containing a) Lipo-Cy5-N_3 C_6, b) Lipo-Cy5-N_3 C_{12}, and c) Lipo-Cy5-N_3 C_{16}.

The kinetics of product formation followed the evolution of the liposome fusion kinetics. The reduction in FRET observed post liposome disruption can be explained by the fact that when the dyes are confined in the liposomes, several donor and acceptors can interact together, which increases the FRET efficiency.[28] After liposome disruption, the FRET signal originates from interactions between one donor and one acceptor only, which are chemically conjugated.

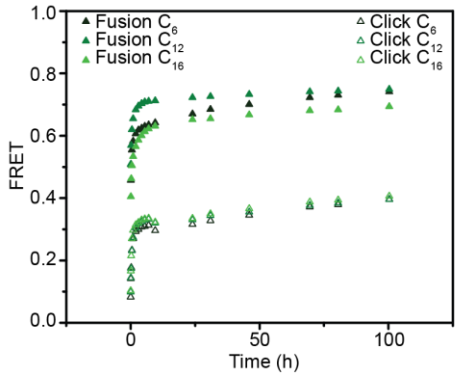

Figure 20. Kinetics of SPAAC reaction in lipid bilayer: comparison between the different Lipo-Cy5-N_3 dyes.

Little difference in SPAAC reaction kinetics were observed between dyes with different alkyl chains lengths (Figure 20). At early time points, the FRET signal from the reaction between Lipo-Cy3-CO and Lipo-Cy5-N_3 C_{16} was the highest while the extent of fusion was equal to, or lower than the other two dyes (C_6 and C_{12}). This could signify that Lipo-Cy5-N_3 C_{16} reacts faster than Lipo-Cy5-N_3 C_6 and Lipo-Cy5-N_3 C_{12}, however, further investigation is required to confirm this trend. If this observation is found to be not significant, this means that the reaction rate under these conditions is not limited by the diffusion of the functional dyes in the lipid bilayer.

3.3.5 Liposome fusion assay for the detection of miRNA

Finally, the proof of concept for using the synthesised functional dyes in a biosensing assay was tested using Lipo-Cy5-N_3 C_{16} and Lipo-Cy3-CO. The functional dyes were assessed in the liposome fusion inhibition assay described in Chapter 2 (Figure 21).

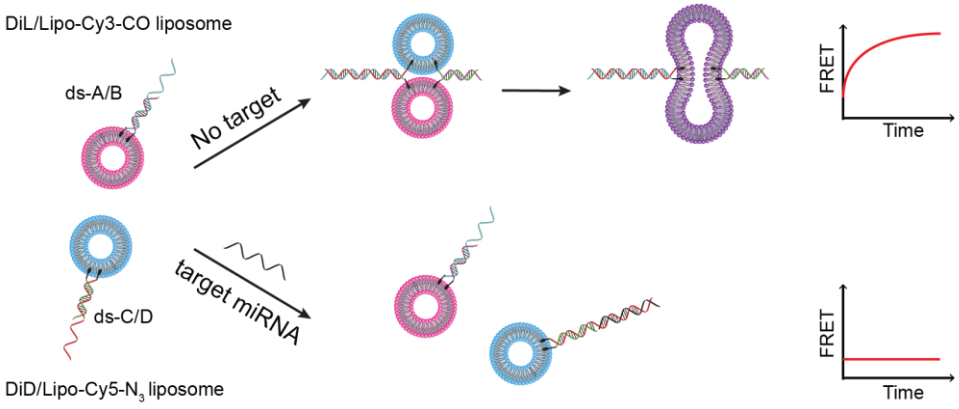

Figure 21. Liposome fusion inhibition assay. Target miRNA (black strand) is complementary to the toehold (red strand) and hybridizes to it, blocking liposome fusion. In the absence of target, liposome fusion is promoted by dsDNA A/B and C/D hybridizing in a zipper-like manner.

Liposomes containing either DiD or Lipo-Cy5-N_3 C_{16} were functionalized with ds-C/D, and incubated with 10 molar equivalents of target miRNA (the detail of the DNA and RNA sequences is included in Chapter 2 section 2.3.2). Then, equal volumes of DiL or Lipo-Cy3-CO liposomes functionalized with ds-A/B were added and the kinetics of fusion were recorded, in the presence and absence of target miRNA (Figure 22).

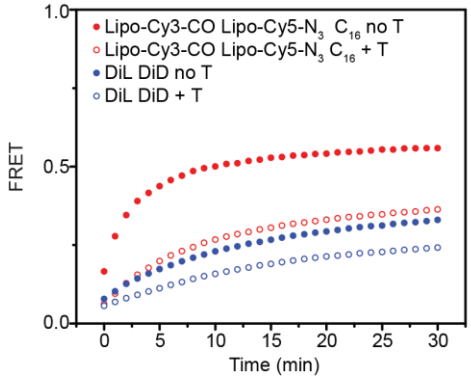

Figure 22. FRET signal measurement for assessing the kinetics of lipid mixing in the absence of target (closed symbols) or in the presence of target miRNA (T) (open symbols) for mixtures of Lipo-Cy3-CO and Lipo-Cy5-N_3 C_{16} liposomes (red symbols) or DiL and DiD liposomes (blue symbols).

The FRET signal in the absence of target was higher for the functional dyes compared to the non-functional ones. This observation cannot be attributed to the formation of 'clicked' product, however, as for instance mixtures of DiL and Lipo-Cy5-N_3 liposomes also lead to high FRET signal without covalently binding dyes in lipid bilayers (Table 3, Figure 15). It can be hypothesized that Lipo-Cy3-CO and Lipo-Cy5-N_3 dyes diffuse faster in lipid bilayers, compared with DiL and DiD, which could explain the higher FRET efficiency. Moreover, non-specific transfer of dyes between liposomes can also contribute to the increase in FRET efficiency.

In the presence of target, the FRET signal was reduced, as liposome fusion was inhibited. Not only was the dynamic margin for the functional dyes twice the value of the dynamic margin for the non-functional dyes, the fact that the FRET values are higher indicates that the liposomes containing functional dyes could be further diluted, and still lead to detectable amounts of fusion. As liposomes are diluted, the total amount in solution of dsDNA functionalizing the liposomes surface is smaller and fewer target miRNAs are needed to block liposome fusion. Therefore, using Lipo-Cy3-CO and Lipo-Cy5-N_3 dyes would allow the measurement of lower concentrations of target miRNA, and therefore increased assay sensitivity. This is a crucial requirement for miRNA detection, as such species are present at small concentrations in clinical samples (attomolar to picomolar range).[29] In future experiments, the limit of detection for the liposome fusion assay using functional dyes will need to be determined.

3.4 Conclusions

In this Chapter, a novel strategy for efficiently reporting lipid mixing upon liposome fusion was sought, with the aim of improving the limit of detection and dynamic range of the liposome fusion-based biosensing assays developed in Chapter 2. It was hypothesized that by covalently linking FRET pairs, the efficiency of FRET would be increased, providing higher signal and therefore higher sensitivity for the assay. Lipid bilayers are a complex environment, typically apolar and hydrophobic. Therefore, the choice of reaction for chemical ligation of the FRET pair inside the bilayer was limited. Strain-promoted alkyne-azide cycloaddition (SPAAC) reaction was chosen, as it is un-catalysed, the azide and alkyne functional groups are stable at physiological conditions, and its reaction rate has been showed to increase in hydrophobic conditions.

Derivatives of Cy3 and Cy5 cyanine dyes containing respectively a cyclooctyne and an azide functional group, designated Lipo-Cy3-CO and Lipo-Cy5-N_3, were successfully synthesized. Their photonic properties were measured, and were compared to their non-functional counterparts, DiL and DiD. The quantum efficiencies of the synthesized dyes were found to be similar to those of the commercial dyes. Moreover, it was shown that the functional dyes were able to undergo conjugation in solution.

Subsequently, the synthesized dyes were integrated into liposomes and the stability of the novel formulations was studied. When mixing Lipo-Cy3-CO and Lipo-Cy5-N_3 liposomes, or DiL and Lipo-Cy5-N_3 liposomes, which were not functionalised with DNA and therefore expected to not fuse, an increase of FRET signal was still observed. It was hypothesized that the non-specific FRET was caused by the transfer of Lipo-Cy5-N_3 dye between liposomes, which can occur either through transport via the aqueous environment surrounding the liposomes, or via collision events between liposomes. The non-specific transfer of dyes was verified by adding an excess of unlabelled liposomes to the mixture of dye-labelled liposomes; in these conditions the transfer of Lipo-Cy5-N_3 has a higher probability to occur towards unlabelled liposomes than towards Lipo-Cy3-CO or DiL containing liposomes. As a result, non-specific FRET was eliminated, confirming the hypothesis of dye transfer during liposome collision.

In order to study the stability of Lipo-Cy5-N_3 dye in lipid bilayers, several analogues were synthesized, with varying alkyl chain lengths: 6-, 12- and 16-carbon long. As the alkyl chain length increased, the lipophilicity of the molecule also increased. It was shown that Lipo-Cy5-N_3 C_{16} was more retained in lipid bilayers than Lipo-Cy5-N_3 C_6 and C_{12}. Molecular dynamics modelling of the insertion of the dyes in lipid bilayers showed that Lipo-Cy5-N_3 C_{16} was located

deeper with in the bilayer than Lipo-Cy5-N_3 C_6 and C_{12}. This correlates with the increase in lipophilicity observed with increased length of alkyl chain. As the lipophilicity of Lipo-Cy5-N_3 increases, its solubility in aqueous environment decreases and therefore its stability in the bilayer increases, supporting the hypothesis that Lipo-Cy5-N_3 C_{16} is better retained in lipid bilayers since transfer to other liposomes is less favourable.

The formation of the covalently bound 'clicked' product was assessed by disrupting the liposomes through the addition of an excess of ethanol; thus, the resulting FRET signal only originated from 'clicked' products rather than confined dyes in the lipid bilayer. All three dyes Lipo-Cy5-N_3 C_6, C_{12}, and C_{16} were shown to undergo cycloaddition with Lipo-Cy3-CO in lipid bilayers. The formation of 'clicked' product was further demonstrated via MALDI analysis.

The reaction kinetics of the SPAAC reaction in lipid bilayers were followed, with liposome fusion induced by DNA hybridisation. The kinetics of the SPAAC reaction followed the same evolution as the kinetics of liposome fusion, and the various functional dyes Lipo-Cy5-N_3 C_6, C_{12}, and C_{16} appeared to follow similar kinetics, indicating that under these conditions, the reaction rate was not limited by the diffusion of the dyes in lipid bilayers, but by liposome fusion events.

Finally, the proof-of-concept use of the functional dyes in biosensing assays based on liposome fusion was demonstrated. To do so, the functional dyes were tested in the liposome fusion inhibition assay developed in Chapter 2, with the presence of target miRNA inhibiting liposome fusion. The FRET signal originating from the functional dyes was higher than that obtained using non-functional dyes, potentially allowing the dilution of the liposomes. Diluting the liposomes leads to increased assay sensitivity, and will therefore enable to detect miRNAs at lower concentrations, which is advantageous due to their low abundance in clinical samples. Moreover, the assay dynamic margin when using the functional dyes was twice as high as that for non-functional dyes, which will allow the detection of a larger range of miRNA concentrations. In future work, the limit of detection for a full assay employing the functional dyes will need to be determined.

References

1. W. K. Subczynski, A. Wisniewska, J. J. Yin, J. S. Hyde, A. Kusumi. *Biochemistry*, 1994, **33**, 7670–7681.
2. J. C. Jewett, C. R. Bertozzi. *Chem. Soc. Rev.*, 2010, **39**, 1272–1279.
3. C. D. Spicer, B. G. Davis. *Nat. Commun.*, 2014, **5**, 4740–4754.
4. L. Shah, S. T. Laughlin, I. S. Carrico. *J. Am. Chem. Soc.*, 2016, **138**, 5186–5189.
5. E. Saxon, C. R. Bertozzi. *Science (80-.).*, 2000, **287**, 2007–2010.
6. E. Saxon, J. I. Armstrong, C. R. Bertozzi. *Org. Lett.*, 2000, **2**, 2141–2143.
7. Q. Wang, T. R. Chan, R. Hilgraf, V. V. Fokin, K. B. Sharpless, M. G. Finn. *J. Am. Chem. Soc.*, 2003, **125**, 3192–3193.
8. N. J. Agard, J. A. Prescher, C. R. Bertozzi. *J. Am. Chem. Soc.*, 2004, **126**, 15046–15047.
9. A. T. Blomquist, L. H. Liu. *J. Am. Chem. Soc.*, 1953, **75**, 2153–2154.
10. M. F. Debets, S. S. Van Berkel, J. Dommerholt, A. J. Dirks, F. P. J. T. Rutjes, F. L. Van Delft. *Acc. Chem. Res.*, 2011, **44**, 805–815.
11. J. A. Codelli, J. M. Baskin, N. J. Agard, C. R. Bertozzi. *J. Am. Chem. Soc.*, 2008, **130**, 11486–11493.
12. M. F. Debets, S. S. van Berkel, S. Shoffelen, F. P. J. T. Rutjes, J. C. M. van Hest, F. L. van Delft. *Chem. Commun.*, 2010, **46**, 97–99.
13. J. C. Jewett, E. M. Sletten, C. R. Bertozzi. *J. Am. Chem. Soc.*, 2010, **132**, 3688–3690.
14. H. Tian, T. P. Sakmar, T. Huber. *ChemBioChem*, 2015, **16**, 1314–1322.
15. G. I. Anderton, A. S. Bangerter, T. C. Davis, Z. Feng, A. J. Furtak, J. O. Larsen, T. L. Scroggin, J. M. Heemstra. *Bioconjug. Chem.*, 2015, **26**, 1687–1691.
16. Online SMILES Translator and Structure File Generator https://cactus.nci.nih.gov/translate/ (accessed Apr 27, 2016).
17. ALOGPS 2.1 http://www.vcclab.org/web/alogps/ (accessed Apr 27, 2016).
18. C. J. Dickson, B. D. Madej, Å. A. Skjevik, R. M. Betz, K. Teigen, I. R. Gould, R. C. Walker, A. A. Skjevik, R. M. Betz, K. Teigen, I. R. Gould, R. C. Walker. *J. Chem. Theory Comput.*, 2014, **10**, 865–879.
19. J. Wang, R. M. Wolf, J. W. Caldwell, P. A. Kollman, D. A. Case. *J. Comput. Chem.*, 2004, **25**, 1157–1174.
20. E. M. S. Stennett, N. Ma, A. Van Der Vaart, M. Levitus. *J. Phys. Chem. B*, 2014, **118**, 152–163.
21. G. Pieffet, P. A. Petukhov. *J. Mol. Model.*, 2009, **15**, 1291–1297.
22. J. C. Phillips, R. Braun, W. Wang, J. Gumbart, E. Tajkhorshid, E. Villa, C. Chipot, R. D. Skeel, L. Kalé, K. Schulten. *J. Comput. Chem.*, 2005, **26**, 1781–1802.

23. M. V. Kvach, A. V. Ustinov, I. A. Stepanova, A. D. Malakhov, M. V. Skorobogatyi, V. V. Shmanai, V. A. Korshun. *European J. Org. Chem.*, 2008, 2107–2117.

24. L. Vigderman, P. Manna, E. R. Zubarev. *Angew. Chem. Int. Ed.*, 2012, **51**, 636–641.

25. I. Texier, M. Goutayer, A. Da Silva, L. Guyon, N. Djaker, V. Josserand, E. Neumann, J. Bibette, F. Vinet. *J. Biomed. Opt.*, 2009, **14**, 54005.

26. L. R. McLean, M. C. Phillips. *Biochemistry*, 1981, **20**, 2893–2900.

27. J. Zhou, Q. Wang, C. Zhang. *J. Am. Chem. Soc.*, 2013, **135**, 2056–2059.

28. A. I. Fabian, T. Rente, J. Szollosi, L. Matyus, A. Jenei. *ChemPhysChem*, 2010, **11**, 3713–3721.

29. R. M. Graybill, R. C. Bailey. *Anal. Chem.*, 2016, **88**, 431–450.

Chapter 4

Quantum rattles as stimuli-responsive drug delivery carriers

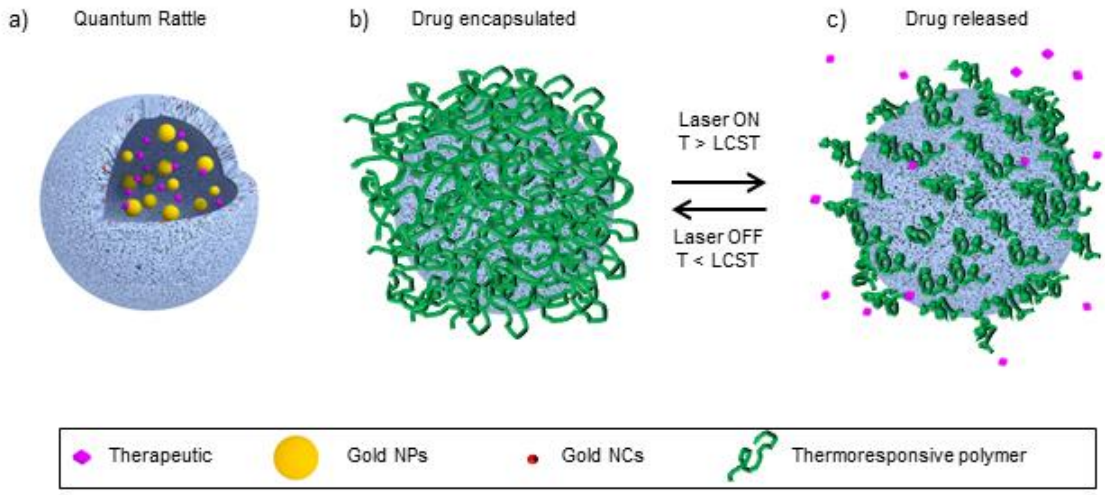

Part of this Chapter has been published in:

Hembury M, Chiappini C, Bertazzo S, Kalber TL, Drisko GL, Ogunlade O, Walker-Samuel S, Krishna KS, **Jumeaux C**, Beard P, Kumar CS, Porter AE, Lythgoe MF, Boissière C, Sanchez C, Stevens MM. Gold-Silica Quantum Rattles for Multimodal Imaging and Therapy. *Proc Natl Acad Sci USA* **2015**, 112 (7), 1959-1964.

4.1 Introduction

Cancer remains one of the world's most devastating diseases, and the number of cancer patients increases each year.[1] Clinical outcome of cancer is strongly related to the stage at which the cancer is detected, therefore early detection methods are highly desirable.[2] Current diagnostics techniques include medical imaging, tissue biopsy and bioanalytical assays of bodily fluids, all of which are not sensitive and/or specific enough to detect most types of early stage cancers.[2] Moreover, current treatments of cancer such as radiation and chemotherapy suffer from poor specificity and damage healthy tissues. Targeted therapies based on cancer-specific markers are therefore highly sought. As highlighted in Chapter 1, nanobiotechnology holds great potential for significant contributions to cancer therapy. Indeed, nanobiotechnology can provide a platform for a combination of diagnostics, therapeutics, and targeted delivery to tumours with subsequent monitoring of responses.[3]

Dr M. Hembury developed during his PhD a nanosystem called the quantum rattle (QR).[4] QR is composed of a hollow mesoporous silica shell (HS) hosting two distinct populations of gold nanostructures: gold nanoclusters and gold nanoparticles, both conferring very unique properties to the system (Figure 1). The features, properties, and *in vitro* and *in vivo* evaluation of QR have been recently published,[4] and key properties are summarized in Appendix 1. In particular, the gold nanoclusters yield near-infrared (NIR) absorption and emission in the biological window (650 - 900 nm), which were exploited *in vivo*. QR had potential for targeting cancer, demonstrated live imaging abilities via fluorescence-based optical imaging, magnetic resonance imaging and photoacoustic imaging, while providing cancer therapy via both photothermal therapy and release of anticancer drug. When irradiated by a laser emitting in the NIR, QR generated gold nanoparticle-mediated hyperthermia, which yields a high temporal and spatial control on the deployment of the therapeutic effect with minimal invasiveness. Moreover, the encapsulation and subsequent release of doxorubicin, an anticancer agent, highlighted the potential of QR as a drug delivery system.

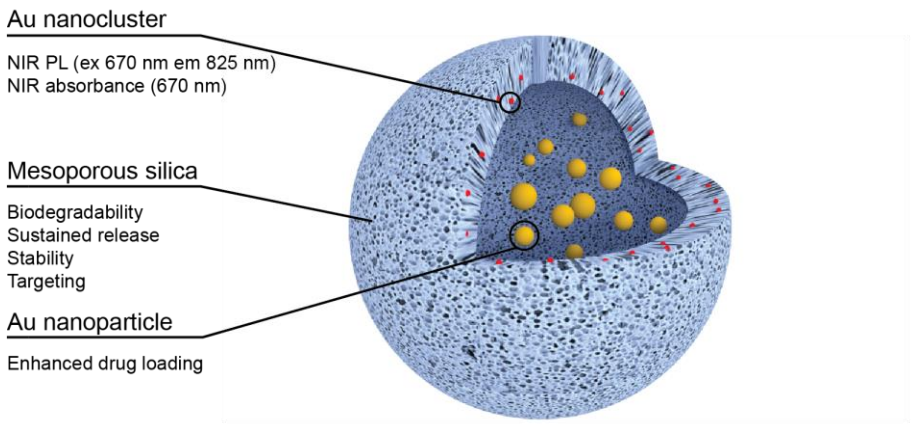

Figure 1. The quantum rattle system is composed of a hollow mesoporous silica shell, hosting two populations of gold: gold nanoparticles, in the cavity of the silica capsule, and gold nanoclusters, inside the mesopores. Modified from Hembury *et al.*[4] (NIR: near-infrared; PL: photoluminescence)

These results provide a proof of concept for the use of QR in cancer therapy. Since the particles are 150 nm-sized nanospheres, they have the potential to target tumours passively via the enhanced permeability and retention (EPR) effect, described more in details in Chapter 1, section 1.2.2. The aim of this project is to further address QR as a systemically administered multifunctional system for cancer therapy. To do so, two immediate objectives need to be fulfilled: (i) QR needs to form a stable suspension in various media; therefore the dispersibility of QR needs to be optimized, via modification of their physico-chemical properties, and (ii) no leakage of the highly toxic chemotherapeutic drug should occur before QR reaches its target, therefore triggered release of the anticancer drug needs to be engineered.

In this Chapter, requirements of dispersibility and triggered drug release are addressed by following two parallel approaches, both involving functionalizing QR surface with stimuli-responsive self-assemblies. Among the variety of stimuli and strategies that can be used for triggered drug delivery, one can take advantage of the photothermal properties of QR to design the controlled drug release system. Irradiating QR with a NIR laser results in a local hyperthermia; the increase in temperature is highly specific and can be used as a trigger. By using an external stimulus to trigger the release of chemotherapeutic drug from QR, control over both the time and location of the therapeutic effect can be achieved, improving the specificity.

The first approach undertaken echoes the work achieved in Chapter 2 where liposomes were engineered to fuse with each other. It has been known that liposomes can rupture and form a supported lipid bilayer (SLB) on silica particles.[5–7] Here, liposomes fuse with QR to form a self-assembled SLB on QR, generating a new construct advantageously combining properties of liposomes and mesoporous silica. The lipid self-assembly can be made stimuli-responsive by

carefully choosing the lipid composition (Figure 2). At a given temperature, a lipid bilayer can exist either in a solid gel or liquid phase, and the phase transition of lipids is characterized by a melting temperature T_m. The membrane permeability to drugs is higher in the liquid phase than in the gel phase,[8] therefore it is hypothesized that QR-derived hyperthermia will trigger release of therapeutics by changing the lipid bilayer structure.

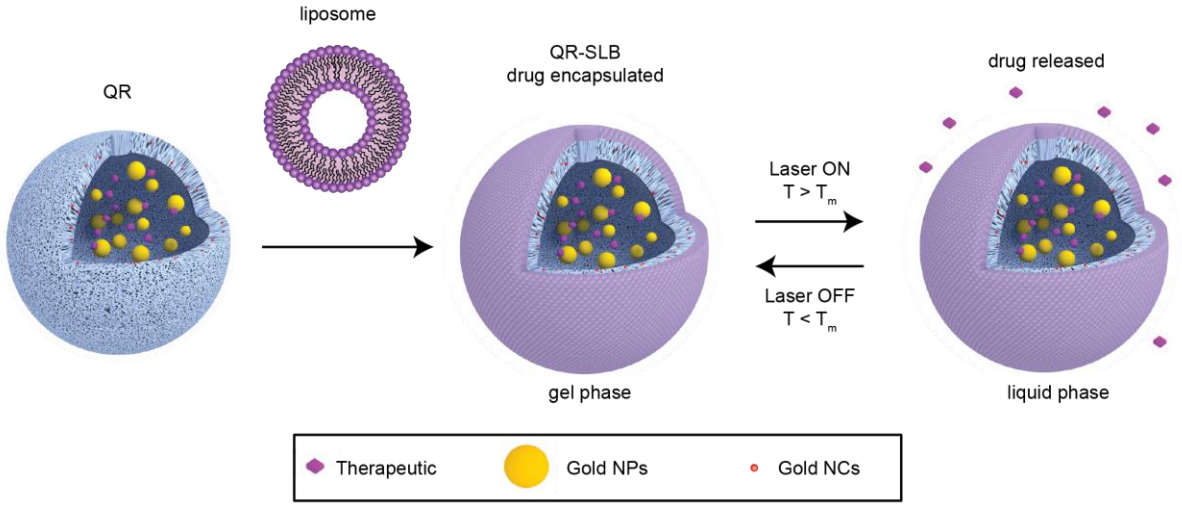

Figure 2. Schematic illustration of QR as a stimuli-responsive drug delivery system. Therapeutic molecules are encapsulated inside the mesoporous QR. Fusion of liposomes with QR results in the assembly of a supported lipid bilayer (SLB) on QR, encapsulating the therapeutic. When QRs are subjected to a temperature above the melting temperature (T_m) of the lipid bilayer, the membrane permeability to the drug increases, allowing the release of the therapeutic. The local increase in temperature causing the structural switch of the thermoresponsive polymer is generated by the local heating of gold particles contained in QR after they were irradiated by a NIR laser.

In a second approach, QR is coated with layers of a thermoresponsive polymer, which self-assemble above a critical temperature. Here, the layers of a thermoresponsive polymer are used to block the pores of QR silica shell, entrapping the encapsulated therapeutics. It only allows a diffusion-controlled release of the cargo after the polymer layers undergo a conformational change caused by a local increase of the temperature. Since QR induce hyperthermia when irradiated by a NIR laser source,[4] the increase in temperature can activate the transition of the thermoresponsive polymer from coil- to globule-structure (Figure 3). Therefore, this strategy will implement a triggered drug delivery specifically at the tumour site.

To form a polymer multilayer film on QR, the layer-by-layer (LbL) technique, which is a sequential deposition of interacting polymer pairs, was implemented.[9–14] LbL is a versatile technique, which allows the preparation of multilayer films with control over thickness, permeability, and degradation properties.[15–18]

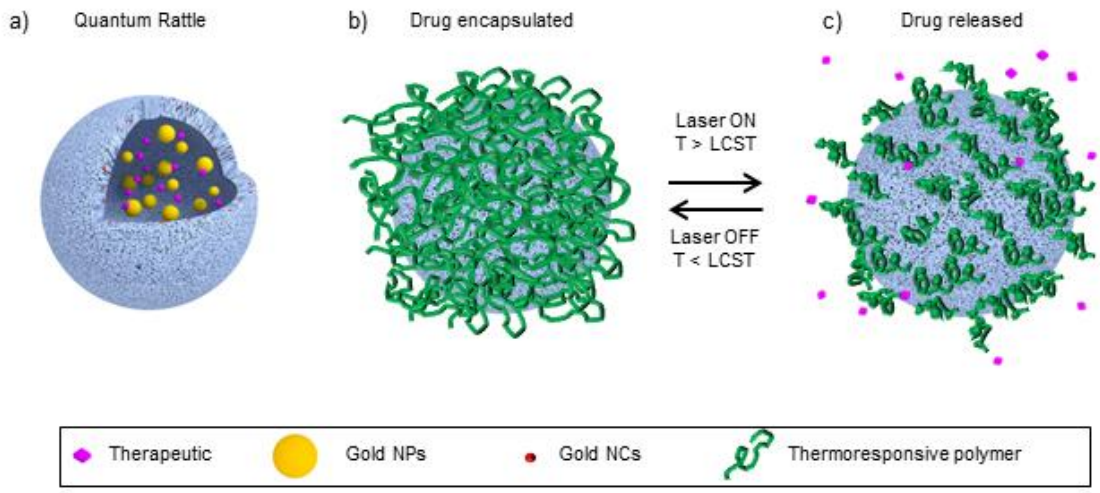

Figure 3. Schematic illustration of QR as a stimuli-responsive drug delivery system. a) Therapeutic molecules are encapsulated inside the mesoporous QR, which contain gold nanoparticles inside the cavity and gold nanoclusters inside the pores. b) Layers of thermoresponsive polymer form a protective coating around QR, preventing the diffusion of the drugs from the therapeutic carriers. c) When QRs are subjected to a temperature above the lower critical solution temperature (LCST) of the thermoresponsive polymer, the polymer undergoes a conformational change from a coil to a compact globule structure, unblocking the pores of the mesoporous silica shells and subsequently allowing the diffusion of encapsulated therapeutic molecules from QR. The local increase in temperature causing the structural switch of the thermoresponsive polymer is generated by the local heating of gold particles after they were irradiated by a NIR laser.

In order to exploit the hyperthermia generated by QR, the Lower Critical Solution Temperature (LCST) of the thermoresponsive polymer needs to be in the range of 45 to 50 °C.[4] Recently, studies demonstrated that poly[oligo(ethyleneglycol) methacrylate] polymers with different side chain lengths exhibited a highly tunable LCST[19–21] (Figure 4). These polymers are particularly relevant for *in vivo* applications, since they are principally composed of oligo(ethylene glycol) segments, and PEG has long been known as a highly biocompatible polymer.[21]

Bebis *et al* investigated the thermoresponsive behaviour of poly[oligo(ethyleneglycol) methacrylate]s across a range of concentrations and solvent systems.[22] Based on this study, poly[tri(ethyleneglycol) methacrylate] (pTEGMA) was selected as building block for the LbL polymer assembly on QR, since its LCST varied between 46 and 50 °C, depending on the concentration of the polymer.

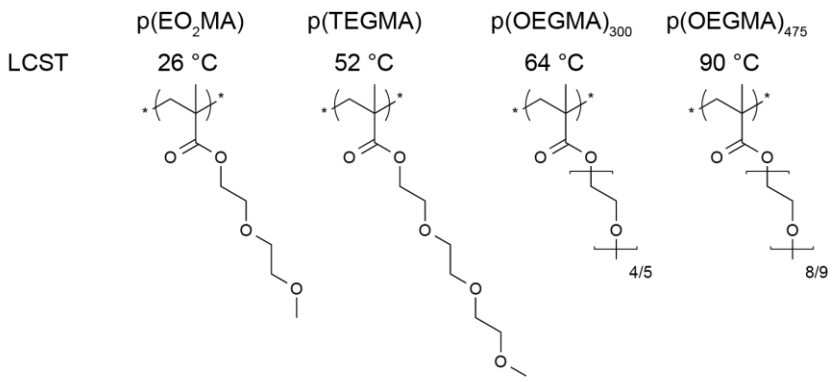

Figure 4. Various poly[oligo(ethyleneglycol) methacrylate] polymers and their corresponding LCST values in aqueous solution. p(EO_2MA): poly[2-(2′-methoxyethoxy)ethyl methacrylate]; p(TEGMA): poly[tri(ethylene glycol) methacrylate]; and p(OEGMA): poly[oligo(ethylene glycol) methacrylate]. Adapted from Lutz.[21]

In this Chapter, first, liposomes are fused with QR, forming a SLB self-assembled on QR (QR-SLB). Stability at physiological conditions and triggered release of therapeutics from QR-SLB are investigated. Then, QR is coated with layers of thermoresponsive polymer pTEGMA. The successful synthesis of pTEGMA is demonstrated, and its LCST is measured. The assembly conditions for pTEGMA multilayer film are optimized using Quartz Crystal Microbalance technique, and then transferred to QR. Finally, the temperature-triggered release of therapeutics from QR coated with layers of pTEGMA is investigated.

4.2 Materials and methods

4.2.1 Materials

All materials were purchased from Sigma-Aldrich, UK unless otherwise specified. Solvents and acids, such as chloroform, absolute ethanol, diethyl ether or nitric acid, were purchased from VWR, UK. Lipids were obtained from Avanti Polar Lipids, Inc.; Alabaster, AL.

4.2.2 Methods

Formation of supported lipid bilayer on QR

1,2-dioleoyl-*sn*-glycero-3-phosphocholine (DOPC), 1,2-dioleoyl-*sn*-glycero-3-phosphoethanolamine (DOPE), cholesterol, 1,2-distearoyl-sn-glycero-3-phosphoethanolamine-N-[methoxy-(polyethylene glycol)-2000] (PEG-2000 PE), (DOPC:DOPE:cholesterol:PEG-2000 PE = 65:4:26:5 wt%) were re-hydrated in 0.5× PBS at a concentration of 2.5 mg/mL and were passed through a 100-nm filter at least 11 times using a Mini-Extruder set (Avanti Polar Lipids, Inc.; Alabaster, AL). QRs were suspended in 0.5× PBS (25 $mg.mL^{-1}$) and exposed to an excess of liposomes (1:2 - 1:4 volumetric ratio of lipid:QR) for 30-90 minutes at room temperature. QR-SLB was stored in the presence of excess lipid for up to 3 months at 4 °C. To remove excess lipid, QR-SLB was centrifuged at 10000 rpm for 5 minutes, washed twice, and re-suspended in 0.5× PBS.

Stability of QR in buffer solution: ICP-MS study

QR, QR-SLB (prepared as described in paragraph above, using 1:3 volumetric ratio of lipid:QR) and HS were dispersed in 1× PBS (0.4 $mg.mL^{-1}$, 5 mL) and added to Amicon® Ultra-4 Centrifugal Filter Units (MWCO 100 kDa, Merck Millipore). The tubes were rotated at room temperature for the duration of the study. For each time point, the tubes were centrifuged for 1 min at 2100 rpm, and 1 mL was collected from the filtrate. The excess filtrate was added to the particles with 1 mL of 1× PBS.

Sample preparation for ICP-MS: to 0.5 mL of each sample were added 3.5 mL of HNO_3 (10 % v/v).

Determination of total silica/gold content: to 250 µL of 2 $mg.mL^{-1}$ QR or HS were added 250 µL of 2M NaOH. The samples were incubated for 24 h at 80 °C to dissolve the silica. Then, 50 µL of the solutions were mixed with 4.950 mL of HNO_3 (10 % v/v).

ICP-MS analysis of the samples was carried at King's College London with the assistance of Andy Cakebread, using a Perkin Elmer ELAN DRC Spectrometer.

QR-SLB for drug release studies

Synthesis of positively charged cholesterol derivative

3α[N-(N',N'-dimethylaminopropane)carbamoyl]cholesterol: Cholesteryl chloroformate (200 mg, 0.445 mmol), 3-(dimethylamino)-1-propylamine (136 mg, 1.336 mmol) were dissolved in 2 mL dichloromethane (DCM) in a 10 mL round bottom flask. The reaction was stirred overnight at room temperature. The mixture was then diluted in DCM and washed with saturated sodium carbonate then brine. The organic phase was dried ($MgSO_4$), filtered, and the DCM was evaporated. The expected product was obtained as a white solid (151 mg, 66 %).

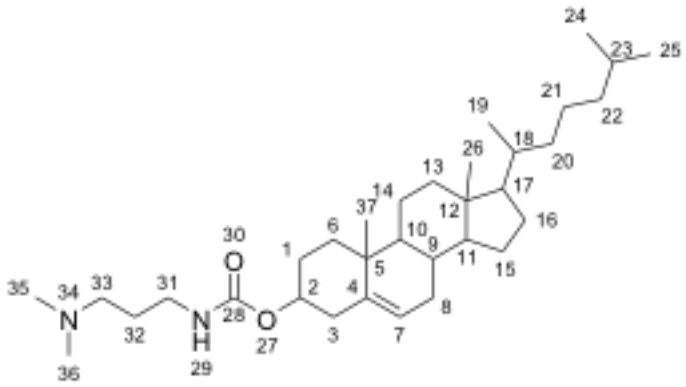

Scheme 1. Numbering system used for 3α[*N*-(*N*',*N*'-dimethylaminopropane)carbamoyl]cholesterol

^{1}H NMR (400 MHz, $CDCl_3$), δ (ppm): 0.67 (s, 3H, C<u>H</u>$_3$, C26), 0.86 (dd, *J* = 6.8 Hz, 6H, CH(C<u>H</u>$_3$)$_2$, C24 & C25), 0.91 (d, *J* = 6.4 Hz, 3H, C<u>H</u>$_3$, C19), 1.00 (s, 3H, C<u>H</u>$_3$, C37), 1.06-2.06 (m, 28H, <u>CyclicH</u> & <u>AlkylH</u>, C1, 3, 6, 8, 9, 10, 11, 13, 14, 15, 16, 17, 18, 20, 21, 22, 23), 2.27 (s, 6H, N(C<u>H</u>$_3$)$_2$, C35 & C36), 2.30-2.41 (m, 4H, N(CH$_3$)$_2$-C<u>H</u>$_2$-C<u>H</u>$_2$, C32 & C33), 3.25 (m, 2H, NH-C<u>H</u>$_2$, C31), 4.49 (m, 1H, O-C<u>H</u>, C2), 5.37 (m, 1H, C=C<u>H</u>-CH$_2$, C7).

3β[N-(N',N',N'-trimethylammoniumpropane)carbamoyl]cholesterol iodide: 3α[N-(N',N'-dimethyl-aminopropane)carbamoyl]cholesterol (40 mg, 0.077 mmol), and methyl iodide (MeI) (55 mg, 0.389 mmol) were dissolved in DCM (5 mL) in a 10 mL round bottom flask. The reaction mixture was stirred overnight at room temperature. Then, DCM and MeI were evaporated, and the resulting product was re-precipitated in diethyl ether. The precipitate was dried under vacuum, to afford the expected product as a white solid.

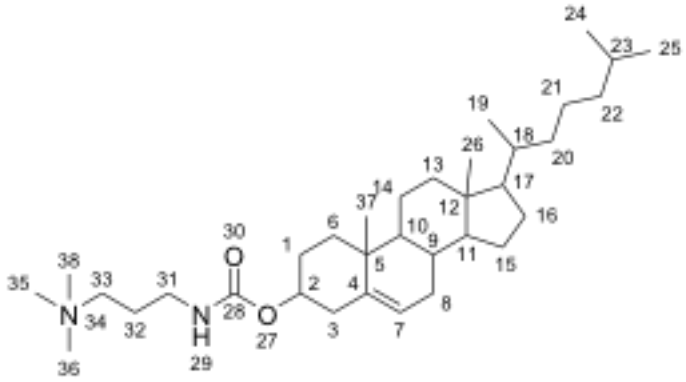

Scheme 2. Numbering system used for 3β[*N*-(*N*',*N*',*N*'-trimethylammoniumpropane)carbamoyl] cholesterol iodide.

^{1}H NMR (400 MHz, $CDCl_3$), δ (ppm): 0.67 (s, 3H, C<u>H</u>$_3$, C26), 0.86 (dd, *J* = 6.8 Hz, 6H, CH(C<u>H</u>$_3$)$_2$, C24 & C25), 0.91 (d, *J* = 6.4 Hz, 3H, C<u>H</u>$_3$, C19), 1.00 (s, 3H, C<u>H</u>$_3$, C37), 1.05-1.53 and 1.78-2.14 (m, 28H, <u>CyclicH</u> & <u>AlkylH</u>, C1, 3, 6, 8, 9, 10, 11, 13, 14, 15, 16, 17, 18, 20, 21, 22, 23), 1.60 (s, 9H, N(C<u>H</u>$_3$)$_3$, C35, C36 & C38), 2.27-2.39 (m, 4H, N(CH$_3$)$_2$-C<u>H</u>$_2$-C<u>H</u>$_2$, C32 & C33), 3.34 (m, 2H, NH-C<u>H</u>$_2$, C31), 4.45 (m, 1H, O-C<u>H</u>, C2), 5.37 (m, 1H, C=C<u>H</u>-CH$_2$, C7).

Thermoresponsive QR-SLB for drug loading and release experiments

Preparation of DPPC liposomes: in a 50 mL round bottom flask, were added 1,2-dipalmitoyl-sn-glycero-3-phosphocholine (DPPC, 12.5 mg) and 3β[N-(N',N',N'-trimethylammoniumpropane)-carbamoyl]cholesterol iodide (5.35 mg) as well as chloroform ($CHCl_3$). $CHCl_3$ was evaporated under inert atmosphere to form the lipid film, which was further dried for 1 h. The lipid film was rehydrated in 0.5× PBS (5mg.mL^{-1}), the solution was vortexed and the flask was left in a hot water bath at 50 °C for 30 min. The liposomes were extruded through a 100-nm filter 21 times using a Mini-Extruder set (Avanti Polar Lipids, Inc.; Alabaster, AL) maintained at 60 °C on a hotplate.

Rhodamine B (RhB) loading in QR: to 25 mg.mL^{-1} QR were added 50 µL of 5 mM RhB (final volume 200 µL), and the mixture was left stirring overnight. QR was washed 9 times in Milli-Q H_2O to remove the excess RhB (10000 rpm, 5 min), and the supernatant was collected to determine RhB loading in QR.

QR-SLB preparation and RhB release studies: 100 µL of 25 mg.mL^{-1} QR loaded with RhB in 0.5× PBS were heated to 50 °C in a hot water bath. To this solution were added 300 µL of 2.5 mg.mL^{-1} DPPC liposomes containing 30 % 3β[N-(N',N',N'-trimethylammoniumpropane)carbamoyl]-cholesterol iodide and the mixture was incubated at 50 °C for 30 min. After the final wash, the sample was split in two, and resuspended in a total volume of 1 mL 0.5× PBS. The release of RhB

from QR (native or with SLB) was followed at room temperature and 50 °C by centrifugating QR into pellets at each time points, collecting the supernatant and monitoring its absorbance at 544 nm on a on a plate reader (SpectraMax M5 Microplate Readers, Molecular Devices). The fraction of the total RhB released was derived from a calibration curve.

Doxorubicin loading in QR: QR (10 mg, 25 mg.mL^{-1}) was incubated overnight with doxorubicin hydrochloride (2.5 mM). QR was washed by centrifugation to remove excess doxorubicin.

QR-SLB preparation and doxorubicin release studies: 200 µL of 25 mg.mL^{-1} QR loaded with doxorubicin in 0.5× PBS were heated to 50 °C in a hot water bath. To this solution were added 600 µL of 2.5 mg.mL^{-1} DPPC liposomes containing 30 % cholesterol and the mixture was incubated at 50 °C for 30 min. QR-SLB were washed in 0.5× PBS. Then, QR was diluted to 2 mg.mL^{-1} in 1× PBS and split into 200 µL aliquots. The release of doxorubicin from QR (native or with SLB) was followed at room temperature and 50 °C, each individual aliquot corresponding to a time point. QR was centrifuged into pellets and the fluorescence of the supernatant was monitored using a plate reader (SpectraMax M5 Microplate Readers, Molecular Devices) (λ_{ex} = 470 nm, λ_{em} = 590 nm). The fraction of the total doxorubicin released was derived from a calibration curve.

Synthesis of poly[tri(ethyleneglycol) methacrylate] (pTEGMA)[22]

Triethylene glycol methacrylate was passed through an aluminium oxide column to remove the inhibitor prior to use. Triethylene glycol methacrylate (10 mmol, 2.32 g) was added to 2 mL of 1,4-dioxane in a round bottom flask. Next, 0.67 mL of 1,4-dioxane containing 0.16 M 2-cyano-2-propyl benzodithiolate (19.3 µL) and 24 mM of azobisisobutyronitrile (AIBN) (3.28 mg) was added to the reaction mixture, giving the ratios [monomer] : [initiator] : [chain transfer agent] = 100 : 0.2 : 1. The flask was sealed, and the solution was cooled down in an ice bath and degassed with argon for 15 min. Then the reaction was carried out at 70 °C for 3 h.

The round bottom flask was transferred to an ice/water bath and air was bubbled into the reaction mixture. The polymer was precipitated drop-wise in cold diethyl ether (35 mL) and then centrifuged at 6500 rpm for 10 min at 4 °C. The supernatant was removed and the precipitate was redissolved in 2 mL of THF. It was then precipitated again in cold diethyl ether containing 1 % toluene (to increase the solubility of dioxane in diethyl ether). This was centrifuged at 6500 rpm for 10 min at 4 °C. The redissolution/precipitating step was repeated twice. Isolated yield: 0.51 g, 25 %; Conversion (NMR): 50 %.

^{1}H NMR (400 MHz, $CDCl_3$), δ (ppm): 1.76-2.00 (2H, backbone-C$\underline{H_2}$), 2.17 (3H, backbone-C$\underline{H_3}$), 3.39 (3H, C(=O)-O-CH_2-CH_2-(O-CH_2-CH_2)$_2$-O-C$\underline{H_3}$), 3.50–3.74 (10H, C(=O)-O-CH_2-C$\underline{H_2}$-(O-C$\underline{H_2}$-C$\underline{H_2}$)$_2$-O-CH_3), 4.08 (2H, C(=O)-O-C$\underline{H_2}$-CH_2-(O-CH_2-CH_2)$_2$-O-CH_3).

Fluorescent Labelling of pTEGMA

Aminolysis reaction

pTEGMA (50 mg) was dissolved in tetrahydrofuran (THF) (2 mL) and ethylenediamine (11 µL) was added to the polymer solution. The reaction was stirred overnight and then the polymer was precipitated in cold diethyl ether, followed by purification by centrifugation (6500 rpm for 30 min).

Reduction of the disulphide bonds

After aminolysis, the polymer was dissolved in 3 mL of 1× PBS and tris(2-carboxyethyl) phosphine (TCEP) (120 mg in 1 mL of 1× PBS) was added to the solution. The reaction was stirred for 15 min to yield thiol-functionalized pTEGMA ($pTEGMA_{SH}$).

Conjugation of Alexa Fluor® 488

Alexa Fluor® 488 C_5-maleimide (120 µL, Invitrogen Life Technologies) was added to the $pTEGMA_{SH}$ solution and the mixture was stirred overnight at room temperature, protected from light. The product was purified by dialysis (MWCO 6000-8000 Da) against water for 48 h and the polymer was isolated via freeze-drying to obtain $pTEGMA_{SH}$-488. Prior to use, $pTEGMA_{SH}$-488 was incubated with DL-dithiothreitol (DTT) (100 $mg.mL^{-1}$) in 20 mM MOPS buffer pH 8 for at least 15 min at 37 °C, followed by dilution in 20 mM NaOAc buffer pH 4 (2 $mg.mL^{-1}$).

Cloud point temperature (T_{cp}) of pTEGMA

Solutions of pTEGMA (2 $mg.mL^{-1}$) in 1× PBS (pH 7.4) or 20 mM NaOAc buffer pH 4 were prepared. The absorbance at 500 nm of these solutions as a function of temperature was measured by a UV-vis spectrophotometer equipped with a temperature control (SpectraMax M5 Microplate Readers, Molecular Devices). The temperature was increased manually and the solution was left to equilibrate for one minute before reading the absorbance.

Quartz Crystal Microbalance (QCM)

QCM measurements (Q-sense E4) were used to characterize polymer assembly on planar surfaces. Silica-coated crystals or gold-coated crystals were cleaned in a 2 wt% sodium dodecyl sulfate solution overnight, followed by rinsing with Milli-Q H_2O and drying with nitrogen. These crystals were mounted into the chambers of the instrument and excited at multiple overtones. The changes in the resonance frequency were monitored at room temperature and normalized frequencies using the third overtone are presented. The polymers used in this study were: poly(*N*-vinylpyrrolidone) (PVP), tannic acid (TA), polyethyleneimine (PEI), poly(methacrylic acid) (PMA), and pTEGMA. The polymer solutions were prepared in 20 mM NaOAc buffer pH 4 unless otherwise stated.

SiO_2/PVP-(TA-pTEGMA)

After deposition of the initial layer of PVP (1 mg.mL^{-1}), the chamber was washed with NaOAc buffer pH 4, after which the solution of TA (2 mg.mL^{-1}) was introduced into the chamber and allowed to adsorb for 10 min. Subsequently, the chamber was washed again with NaOAc buffer and then filled with pTEGMA solution (2 mg.mL^{-1}), allowing an adsorption time of 10 min. The multilayer film was then assembled by alternating incubation of TA and pTEGMA.

Au/PEI-(TA-pTEGMA)

After deposition of the initial layer of PEI (1 mg.mL^{-1} in 0.5 M NaCl), the chamber was washed with 0.5 M NaCl solution and then NaOAc buffer, after which the solution of TA (2 mg.mL^{-1}) was introduced into the chamber and allowed to adsorb for 10 min. Subsequently, the chamber was washed again with NaOAc buffer and then filled with pTEGMA solution (2 mg.mL^{-1}), allowing an adsorption time of 10 min. The multilayer film was then assembled by alternating incubations of TA and pTEGMA, forming up to five bilayers.

SiO_2/PVP-(PMA-pTEGMA)

After deposition of the initial layer of PVP (1 mg.mL^{-1}), the chamber was washed with NaOAc buffer, after which the solution of PMA (1 mg.mL^{-1}) was introduced into the chamber and allowed to adsorb for 10 min. Subsequently, the chamber was washed again with NaOAc buffer and then filled with pTEGMA solution (1 mg.mL^{-1}), allowing an adsorption time of 10 min. The multilayer film was then assembled by alternating incubations of PMA and pTEGMA, forming up to five bilayers.

Synthesis of thiol-functionalized Poly(methacrylic acid) (PMA_{SH})

PMA samples with 14 mol% thiol modification were synthesized through functionalization of PMA with pyridine dithioethylamine (PDA). 300 mg of 30 wt% of PMA was reacted with 1-ethyl-3-(3-dimethylaminopropyl)carbodiimide (EDC) (64.6 mg, 20 $mg.mL^{-1}$ in PBS) for 15 min. Subsequently, PDA-HCl (44.5 mg, 20 $mg.mL^{-1}$ in PBS, Nanocs) was added to the mixture and the reaction was allowed to proceed overnight. The reaction mixture was purified via dialysis against water for 48 h and the polymer was isolated via freeze-drying to obtain white powder of PMA_{PD}. The thiol content of the resulting polymer was characterized by measuring the absorbance of PDA groups (λ_{max} = 343 nm) and then derived by correlation with a calibration curve of PDA. The reduced form, PMA_{SH}, was prepared by incubating PMA_{PD} in a solution of 0.5 M DTT (100 $mg.mL^{-1}$) in 20 mM MOPS buffer pH 8 for at least 15 min at 37 °C prior to dilution in NaOAc buffer (2 $mg.mL^{-1}$).

Layer-by-layer on quantum rattles

Quantum rattles were resuspended in 1 mM NaCl (1 $mg.mL^{-1}$) by ultrasonication (Sonics Vibra Cell, VCX500), at a power of 125 W. To 1 mL of QR suspension, 1 mL of 0.6 $mg.mL^{-1}$ poly(diallyldimethylammonium) chloride (PDDA) solution was added slowly while vigorously stirring. QR-PDDA was washed 2 times in 1 mM NaCl (centrifugation at 10000 rpm for 5 min). After the final wash, the particles were resuspended in 100 µL 20 mM NaOAc pH 4 buffer ([QR] = 10 $mg.mL^{-1}$). The PMA_{SH}/$pTEGMA_{SH}$-488 layers were then assembled on QR by alternatively immersing the particles in PMA_{SH} (2 $mg.mL^{-1}$) and $pTEGMA_{SH}$-488 (2 $mg.mL^{-1}$), allowing the polymers to absorb for at least 15 min. To remove excess material the polymer-coated QR were washed 3 times in 20 mM NaOAc pH 4 buffer. After each bilayer deposition, the polymer layers were cross-linked using chloramine-T hydrate: the particles were dispersed in 50 mM MES buffer pH 6 (400 µL), and chloramine-T hydrate (400 µL, 2.5 mM in MES buffer pH 6) was added. The reaction was carried out for 1 min, and the particles were washed 3 times in 20 mM NaOAc pH 4 buffer. The increase of fluorescence intensity after each bilayer deposition was monitored by flow cytometry (LSRFortessa, BD Biosciences, data acquired by Dr Rona Chandrawati) using an excitation wavelength of 488 nm. At least 20,000 particles were analysed in each experiment.

Drug loading and release experiments

Quantum rattles were resuspended in Milli-Q H_2O (5 $mg.mL^{-1}$) by ultrasonication (Sonics Vibra Cell, VCX500), at a power of 125 W. To 400 µL of QR were added 2 mL of doxorubicin solution in Milli-Q H_2O (1 $mg.mL^{-1}$) and 1.6 mL of Milli-Q H_2O ([QR] = 0.5 $mg.mL^{-1}$, [Dox] = 0.5 $mg.mL^{-1}$). QR

suspension was rotated overnight, protected from light. Then, 4 mL PDDA solution (0.3 mg.mL^{-1} in 2 mM NaCl) were added slowly while vigorously stirring. The excess polymer and unencapsulated doxorubicin were removed by washing QR 3 times in Milli-Q H_2O (centrifugation at 10000 rpm for 5 min). After the final wash, QR was resuspended in 100 µL 20 mM NaOAc pH 4 buffer. Five PMA_{SH}/$pTEGMA_{SH}$ bilayers were then assembled following the procedure described previously. As a control, five PMA_{SH}/PVP bilayers (PVP, Sigma, MW = 10000 Da) were also assembled on QR, following an identical procedure but excluding the cross-linking steps. The release of doxorubicin was initialised by resuspending QR in 1× PBS buffer. QR suspension was incubated at room temperature, 37 °C or 50 °C. For each time point QR was pelleted, the supernatant was collected and its fluorescence was measured on a plate reader (SpectraMax M5 Microplate Readers, Molecular Devices) (λ_{ex} = 470 nm, λ_{em} = 590 nm).

Dynamic Light Scattering (DLS)

Zeta potential and size distribution measurements were performed using a Zetasizer Nano ZS (Malvern). In all DLS measurements, the scattering angle was fixed at 173°.

Nuclear Magnetic Resonance (NMR)

^{1}H spectra were recorded on Bruker DPX-400 400 MHz instruments using deuterated solvents obtained from Sigma-Aldrich.

4.3 Results and discussion

4.3.1 Liposome fusion with quantum rattle

4.3.1.1 Stability of quantum rattle at physiological conditions

For demonstrating the therapeutic applications of QR on cell cultures *in vitro* as well as *in vivo* (biodistribution, safety, and efficacy), they need to form a dispersed and stable suspension at physiological conditions. Several reports state that agglomerated nanoparticles do not have the same effects as dispersed nanoparticles, leading to inaccurate evaluation of the particles' toxicity.[23–25] Indeed, when the particles are agglomerated the total surface area in contact with the organism is smaller than when the particles are well dispersed. Furthermore, while in the bloodstream, such aggregates can trigger opsonisation and make the particles more visible to the mononuclear phagocyte system.[26] The dispersibility of QR was addressed early in the project and the strategy implemented is summarized in Appendix 1. Here, the stability of QR dispersion at physiological conditions is investigated.

The flocculation of particles in aqueous solutions is governed by the DLVO theory. The stability of the dispersion depends on the balance between the attractive and repulsive forces:[24] a particle suspension becomes unstable and starts to agglomerate when the repulsive energy is not sufficient to counteract the van der Walls attractive energy.[27]

In order to form stable dispersions, it is often not sufficient to break the initial agglomerates; electrostatic and steric stabilisation is then required to provide the repulsive energy that prevents the particles from re-agglomerating.[24] In electrostatic stabilisation, the charges on the surface of the particles provide the repulsive energy, while in steric stabilisation, large molecules such as surfactants or BSA adsorb to the surface of the nanoparticles preventing them from coming too close to one another for van der Walls forces to act.[24]

In practice, measurement of the surface charge of nanoparticles in solution, referred as zeta potential, gives a good indication of their electrostatic stability. When the module of the zeta potential is more than 30 mV, particles tend to repel each other and therefore form a stable dispersion.[24,27]

The zeta potential of particles depends strongly on the pH and the ionic strength of the dispersion medium.[27] The re-dispersed QR flocculated in various buffers, such as 1× PBS (ionic strength 162.7 mM, pH 7.4). In order to study this phenomenon, the effect of ionic strength on QR stability were investigated by measuring the zeta potential and size distribution of QR in

solutions of various ionic strengths. QRs were initially resuspended in Milli-Q H_2O using ultrasonication, and then mixed with sodium chloride (NaCl) in solutions at various concentrations to a final range of ionic strengths between 10 mM and 200 mM. The zeta potential and size distribution were measured using dynamic light scattering immediately after resuspending QR in saline solution (Figure 5).

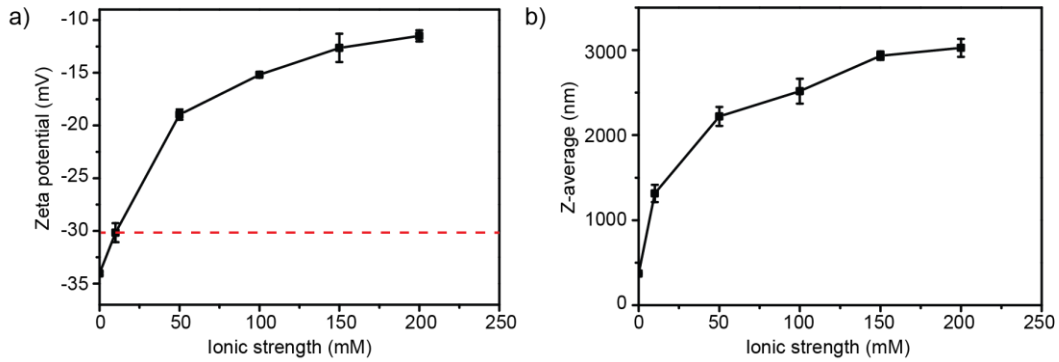

Figure 5. a) Zeta potential of QR in aqueous NaCl solutions of ionic strengths between 10 and 200 mM. The dotted line (red) represents the commonly admitted threshold for electrostatic stabilization of particle suspension. b) Z-average of QR in aqueous NaCl solutions of ionic strengths between 10 and 200 mM measured by DLS.

As seen in Figure 5a, when QRs were resuspended in Milli-Q H_2O (ionic strength 0 mM), they formed a stable suspension with a zeta potential of -34 mV. Their Z-average of 372 ± 8 nm indicated none to very little agglomeration (Figure 5b). However, when the ionic strength of the solution was increased to above 10 mM, the QR suspension was destabilized; the zeta potential increased and shifted towards more positive values (above -30 mV) and the Z-average measurements showed major agglomeration with a reported size above 1000 nm showing that QR were agglomerated together. These results implied that QR will agglomerate at physiological conditions, where the ionic strength is around 200 mM.[28] Therefore, additional means for stabilizing QR in buffer solution were sought, such as steric stabilisation of QR via surface functionalization.

4.3.1.2 Formation of a supported bilayer on QR for improved stability at physiological conditions

Recently, a new class of nanocarriers called protocells has been reported, combining the intrinsic properties of mesoporous silica particles and liposomes.[5,6] Mesoporous silica nanoparticles (MSN) are very attractive drug delivery vehicles, thanks to their high surface area allowing efficient drug packing, tunable pore size for encapsulating different sizes of drugs,[29,30] stability, safety, and ability to provide controlled drug release.[5,7,31] Liposomal carriers are very safe: several formulations have received FDA approval and are being used to treat patients,[32] and

they can encapsulate a relatively large payload of both hydrophobic and hydrophilic drugs,[32] but suffer from poor stability.[7] The outer surface of porous silica nanoparticles can be functionalized with a supported lipid bilayer to form inorganic-organic hybrids. The silica core provides increased stability of the new carrier and allows tunable drug loading and release via a combination of pore size and pore surface chemistry modifications.[5,33,34] The lipid bilayer mimics the outer layer of a natural cell membrane; additional functionalities can be imparted via easy conjugation steps such as PEGylation for increased circulation time, as well as targeting moieties for increased specificity of therapeutic delivery.[6] Functionalizing QR with a lipid bilayer containing PEG brushes will provide steric hindrance, which has great potential for stabilizing QR in solutions of high salt concentrations after redispersion.

The supported lipid bilayer (SLB) formulation used in this Chapter was adapted from the study published by Ashley *et al*.[6] The formulation contained DOPC, DOPE, and PEG-2000 PE lipids as well as cholesterol (DOPC:DOPE:cholesterol:PEG-2000 PE = 65:4:26:5 wt%). The influence of liposome size and concentration on the efficiency of SLB formation on QR was studied, and it was assessed by measuring the size of the assembly after functionalization (Figure 6).

Both 100 nm and 200 nm liposomes were able to form a SLB on QR and enabled to stabilize the QR dispersion in 0.5× PBS, as indicated by the shift in size distribution from 670 nm to sub-200 nm. As the lipid:QR ratio decreased, the QR dispersion was less stable, as evidenced by the emergence of a second peak in the size distribution profiles at > 600 nm.

Therefore, the optimized conditions selected for SLB formation on QR were: 200 nm liposomes at a lipid:QR mass ratio of 7.5. The results are summarized on Figure 7.

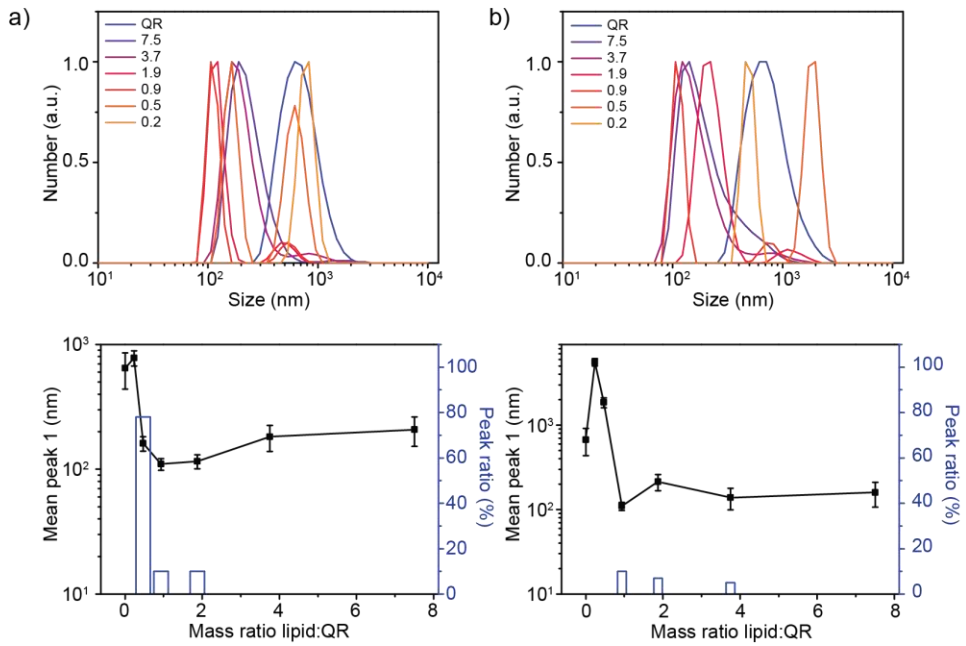

Figure 6. Size distributions of QR in 0.5× PBS functionalized with lipid bilayer using different concentrations of liposomes (numbers indicate lipid:QR mass ratio) and corresponding analysis of the different peaks. a) Using 100 nm liposomes and b) using 200 nm liposomes.

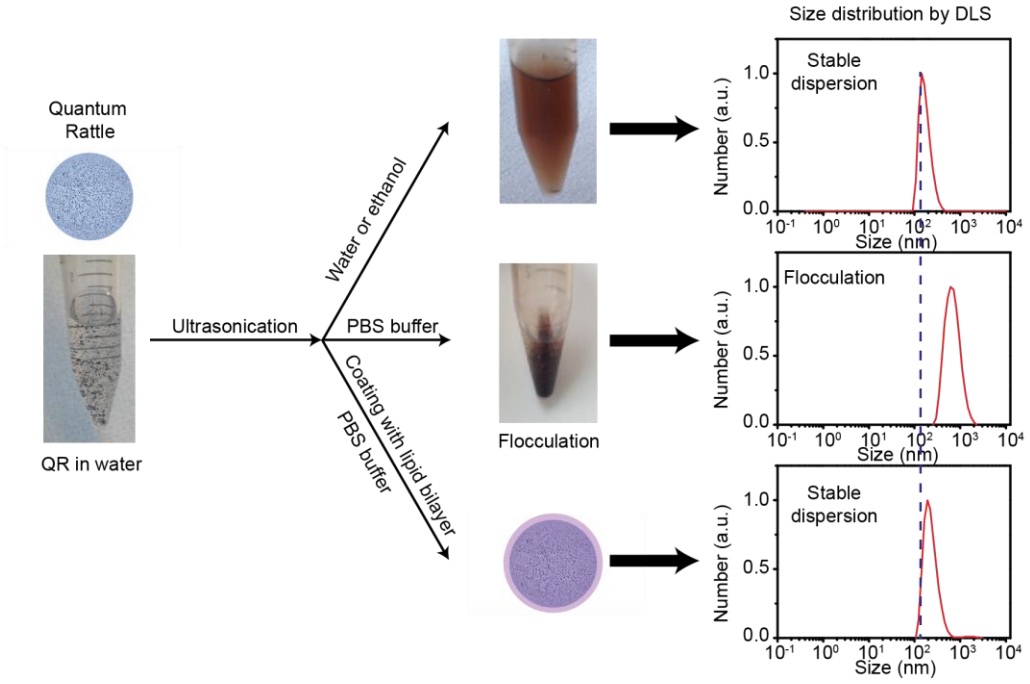

Figure 7. Summary of the SLB formation strategy to stabilize QR suspension in solutions of high salt concentration.

In addition of stabilizing QR in solutions of high salt concentrations, the SLB can potentially protect QR from degradation as the silica surface is less exposed to water, which causes hydrolysis of Si-O bonds and dissolution of the silica structure.[35]

To test this hypothesis, inductively coupled plasma mass spectrometry (ICP-MS) technique was used to measure the amount of silica and gold released overtime when QR was resuspended in 0.5× PBS buffer (Figure 8).

ICP-MS is an elemental analytical technique, which uses high-energy plasma from an inert gas (usually argon) to efficiently desolvate, vaporize, excite, and ionize atoms. The plasma is created by passing the argon gas through an alternating electric field, created by an inductively coupled coil. A detector is coupled to the instrument, such as mass spectrometry (detects ionized atoms) or atomic-emission spectroscopy (detects excited atoms, emitting electromagnetic radiations at characteristic wavelengths for each element).

As shown on Figure 8a, there was an initial fast burst release of silica ions plateauing after 24 hours, indicating a sharp hydrolysis of the silica network. The release profile was similar for QR, QR-SLB and HS, indicating that SLB formation on QR did not slow down their degradation. The release of gold followed the same trend as silica ions. However, only a fraction of the total estimated gold encapsulated in QR was released, possibly because the AuNCs are poorly soluble in water, as their surface is functionalized with lipophilic ligands.

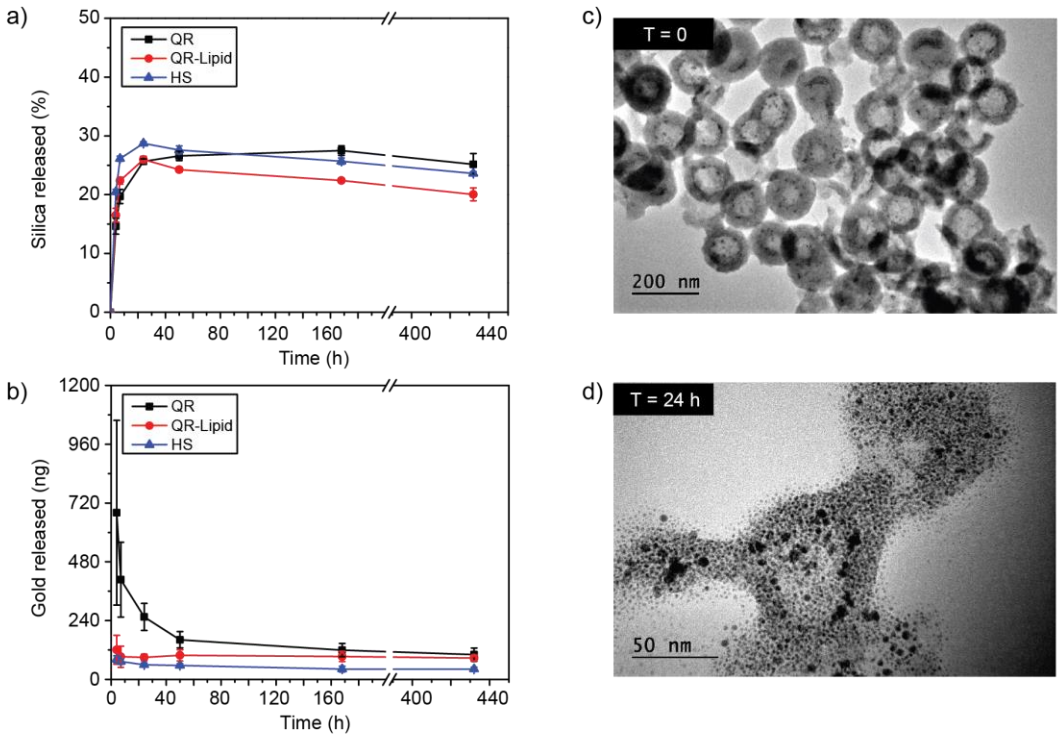

Figure 8. Degradation profile of QR, QR-SLB and HS when resuspended in 0.5× PBS. a) Release profile of silicate ions followed by ICP-MS, b) release profile of gold ions followed by ICP-MS, c) TEM imaging of QR at t = 0, and d) TEM imaging of QR at t = 24 h post resuspension in 0.5× PBS.

4.3.1.3 Formation of a supported bilayer on QR for temperature-triggered drug delivery

Here, the composition of the lipid formulation was modified to facilitate temperature-triggered release of encapsulated therapeutics from QR. Lipid bilayers can be characterized by their melting temperature T_m. Below T_m, the bilayer is in the solid-gel phase, and above T_m the bilayer is in the fluid phase, where lipids diffuse freely in the lateral plane. In the liquid phase, the membrane is more permeable to molecules than in the gel phase;[36] the permeability of the membrane to hydrophobic molecules is highest at the T_m due to the formation of grain boundaries,[8,36] and this has been exploited in several experiments for achieving temperature-triggered release of drug from liposomes.[37,38]

The lipid 1,2-dipalmitoyl-sn-glycero-3-phosphocholine (DPPC) has a T_m of 41 °C,[6] which is above body temperature and is in the temperature range of QR-generated hyperthermia.[4] Therefore, as a proof-of-concept, a simple formulation containing 70 % DPPC and 30 % cholesterol was used in this part of the project.

The temperature-triggered release of doxorubicin and rhodamine B from QR coated with a DPPC SLB was investigated (Figure 9). The release of the molecules was studied at room temperature and 50 °C. For studying the release of doxorubicin (Figure 9a), each time point

corresponded to a single aliquot, whereas for rhodamine B (Figure 9b), the same aliquot was sampled throughout the duration of the experiment.

The doxorubicin release profiles are presented on Figure 9a. There was no difference between native QR and QR-SLB, both at room temperature and at 50 °C. This could possibly be attributed to the SLB not forming uniformly on QR, therefore not preventing leakage efficiently. The release profiles at 50 °C were higher than at room temperature for up to 2 h. However, the release of doxorubicin apparently decreased over time; it was hypothesized that as QR degraded, gold nanoclusters were being released over time; they can potentially quench the fluorescence of doxorubicin, which could account for the lower fluorescent readouts of the supernatant. In addition, very little amounts of doxorubicin were released, overall less than 7 % of the total encapsulated drug.

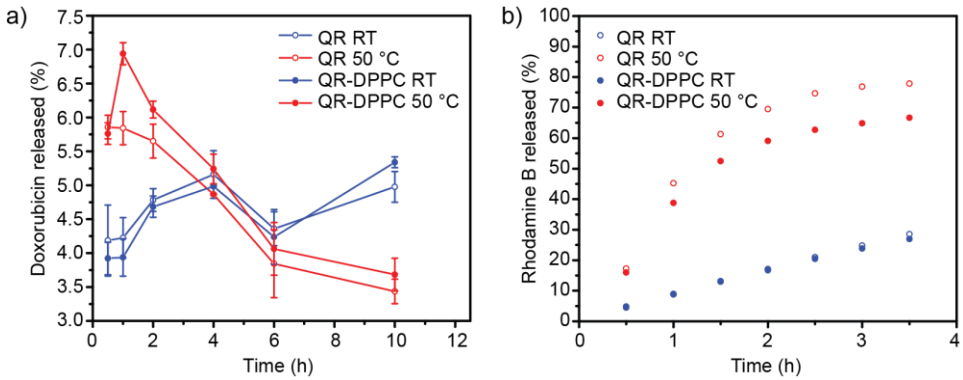

Figure 9. Drug release profiles from native QR (hollow symbols) and QR coated with thermoresponsive lipid bilayer (full symbols) at room temperature (RT, blue traces) or 50 °C (red traces). a) Release profile of doxorubicin. b) Release profile of rhodamine B.

The composition of the bilayer was improved to provide optimized surface coverage of QR: a positively charged analogue of cholesterol was synthesized, which was mixed in the lipid composition (Scheme 3). Upon fusion of the liposomes with QR, the surface charge of QR changed from negative to positive, proving successful formation of the bilayer on QR.

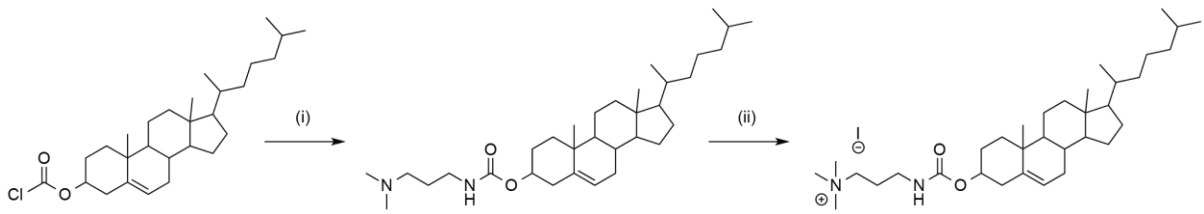

Scheme 3. Synthesis of positively-charged cholesterol analogue: (i) 3-(dimethylamino)-1-propylamine / DCM, (ii) methyl iodide / DCM.

The release of rhodamine B (RhB), a widely used model molecule for drug delivery, from these new functional QR was studied and similarly no difference in the release profiles between QR and QR-SLB was observed, either at room temperature or at 50 °C (Figure 9b). However, there was a marked difference between the release of RhB at room temperature and at 50 °C: after 3.5 h, 80 % of the encapsulated RhB was released from QR at 50 °C while only 25 % was released at room temperature.

In summary, functionalization of QR with a thermoresponsive lipid bilayer did not allow temperature-triggered drug delivery of drug molecules. It has been observed that DPPC bilayers formed on porous nanoparticles resulted in a broadening of the phase transition, with a T_m reduced to 35 °C.[6] Hence, further optimization of the bilayer composition is required in order to provide temperature-triggered release of drug from QR-SLB.

4.3.2 Layer-by-layer polymer assembly on QR

In this second approach for addressing QR as a temperature-triggered drug delivery system, layers of a thermoresponsive polymer, pTEGMA, are used to coat QR (Figure 3).

4.3.2.1 Synthesis of pTEGMA

Poly[tri(ethyleneglycol) methacrylate] (pTEGMA) was synthesised by reversible addition fragmentation chain transfer (RAFT) polymerisation of tri(ethyleneglycol) methacrylate, following a modified protocol from Bebis *et al* as illustrated on Scheme 4.[22]

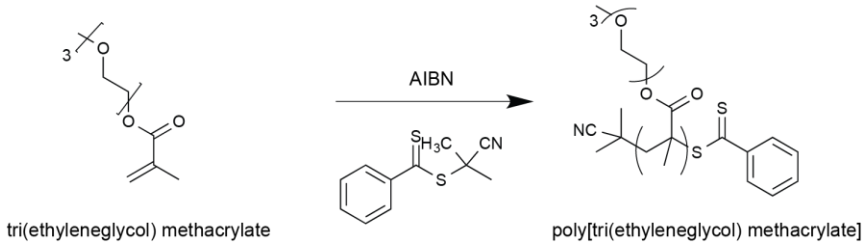

Scheme 4. Synthesis of poly[tri(ethyleneglycol) methacrylate] (pTEGMA) by RAFT polymerization of tri(ethyleneglycol) methacrylate.

Successful synthesis of pTEGMA was confirmed by ^{1}H NMR analysis.

4.3.2.2 Cloud point temperature (T_{cp}) of pTEGMA

After synthesis of pTEGMA, the thermoresponsive behaviour of the polymer was studied. As single concentration measurements were performed, the transition temperature is referred here as cloud point temperature (T_{cp}). The T_{cp} of pTEGMA was evaluated by measuring the optical transmittance of the polymer solution on a UV-vis spectrophotometer equipped with a temperature controller. Indeed, the coil-to-globule transition is accompanied by a solubility change that can be observed by monitoring the change in absorbance of the polymer solution: as the temperature increases, the hydrophobic interactions between polymer chains become more favourable than polymer-water interactions,[21] leading to a collapse of the polymer chains, which precipitate out of solution increasing its turbidity. The change in transmittance as a function of the temperature was monitored at 500 nm. Using the generated curves, the T_{cp} was defined as the abscissa of the inflection point (Figure 10).

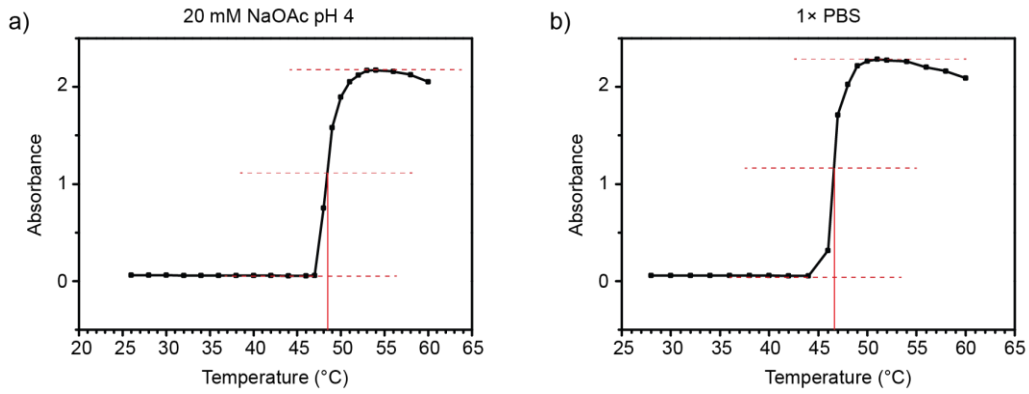

Figure 10. T_{cp} measurement profile of pTEGMA (2 mg.mL^{-1}) dissolved in a) 20 mM NaOAc buffer pH 4.0 or b) 1× PBS pH 7.4. The T_{cp} is defined as the abscissa of the inflection point of the absorption curves.

The T_{cp} of pTEGMA was evaluated in two different buffers: 20 mM NaOAc buffer pH 4.0, which represents the assembly conditions for the layer-by-layer process, and 1× PBS pH 7.4, which mimics physiological conditions. Based on the turbidimetry plot, the T_{cp} of the synthesized pTEGMA were determined to be 48 °C in NaOAc buffer pH 4 and 47 °C in 1× PBS pH 7.4. These values were consistent with the LCST values reported on the literature[22] and are in an optimal temperature range for exploiting combinatorial approach of drug delivery and photothermal therapy with QR.

4.3.2.3 Layer-by-layer on planar substrates

The potential use of pTEGMA as building block for layer-by-layer assembly was first investigated on planar substrates using Quartz Crystal Microbalance with Dissipation monitoring (QCM-D).

QCM-D technique:

This technique senses mass deposition on surfaces, and allows label-free, real-time analysis of surface phenomena, such as film deposition, interactions between molecules, as well as chemical reactions. QCM exploits the piezoelectric properties of quartz crystal. Applying mechanical strain to a piezoelectric material results in the generation of an electric field, and conversely, the application of an electric field across a piezoelectric material induces a deformation of the material. A QCM consists of a thin quartz disc coated with gold electrodes on both sides. An AC voltage is applied across the electrodes, which results in oscillations of the quartz crystal and the propagation of an acoustic wave of characteristic resonance frequency (f) through the thickness of the crystal, reflecting back into the crystal at the surface.[39]

Upon deposition of matter on the sensor, the acoustic wave propagates through it. This results in a decrease of resonance frequency (Figure 11). Therefore, the change in frequency of the oscillating crystal can be directly linked to the total mass absorbed on the crystal, including water molecules coupled to the oscillation. The relation between change in frequency and mass is quantified in the Sauerbrey equation:[40,41]

$$\Delta f = \frac{-2f_0^2 \Delta m}{A\sqrt{\mu_{Qq}\rho_q}} \quad (1)$$

where Δf (Hz) is the measured frequency change, f_0 (Hz) is the resonant frequency, Δm (g) is the mass change, A (cm^2) is the active electrode area, and μ_q and ρ_q are the shear modulus and density of the quartz crystal.

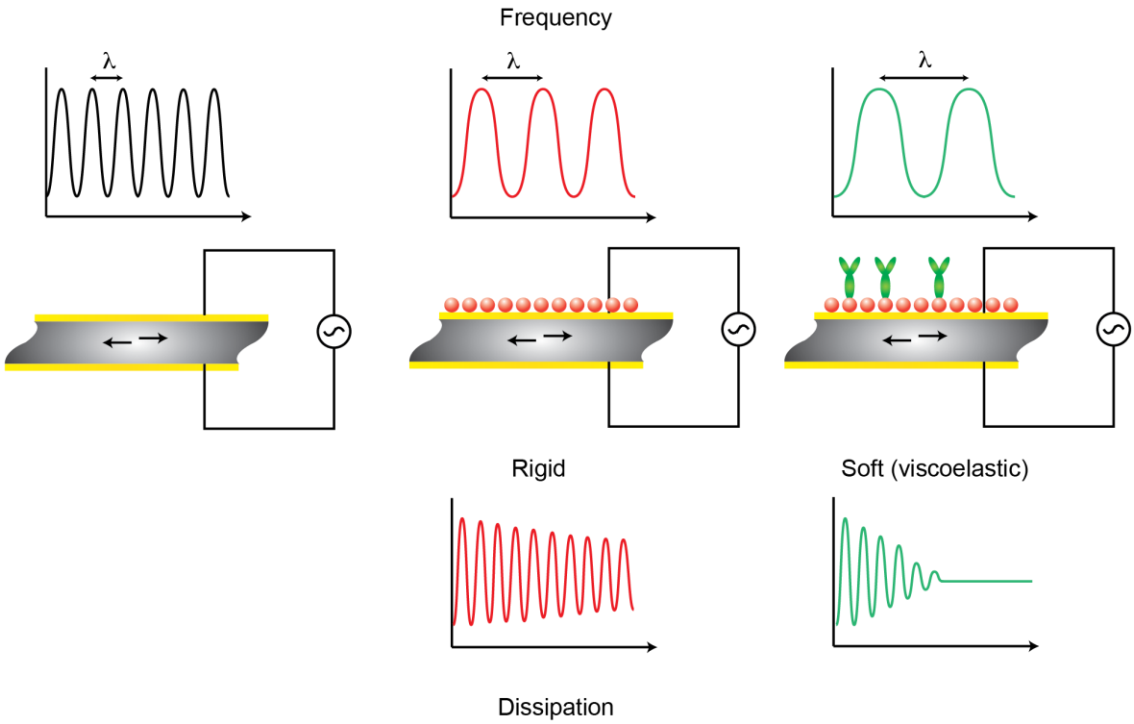

Figure 11. Schematics of QCM sensing principle. The QCM quartz sensor is sandwiched between two gold electrodes and subjected to an AC voltage. An increase of mass deposited on the QCM quartz sensor causes an increase of the wavelength of the acoustic wave, and consequently a decrease of frequency. Absorption of a soft film results in dampening of the oscillations of the crystal.

The Sauerbrey equation is only valid for rigid, uniformly distributed, thin films that do not experience any energy losses upon oscillation. In most applications, the deposited films are soft, and they do not fully couple with the oscillations of the quartz crystal, resulting in dampening of the oscillation, hence the Sauerbrey equation will underestimate the mass deposited on the surface (Figure 11).

The damping or energy dissipation D is defined as:

$$D = \frac{E_{lost}}{2\pi E_{stored}} \tag{2}$$

In practice, dissipation is determined from the time it takes the oscillation to stop when the power is disconnected.

Choice of polymer pairs for Layer-by-Layer:

Several polymer pairs were explored, in order to find the optimal and most stable system during assembly as well as at physiological conditions. pTEGMA presents a high density of hydrogen bond accepting groups, therefore it was chosen to pair with polymers or molecules capable of donating hydrogen bonds. The complementary building blocks used in this study were tannic acid (TA) which is rich in phenolic hydroxyl groups and poly(methacrylic acid) (PMA) which is rich in carboxyl groups (Figure 12).

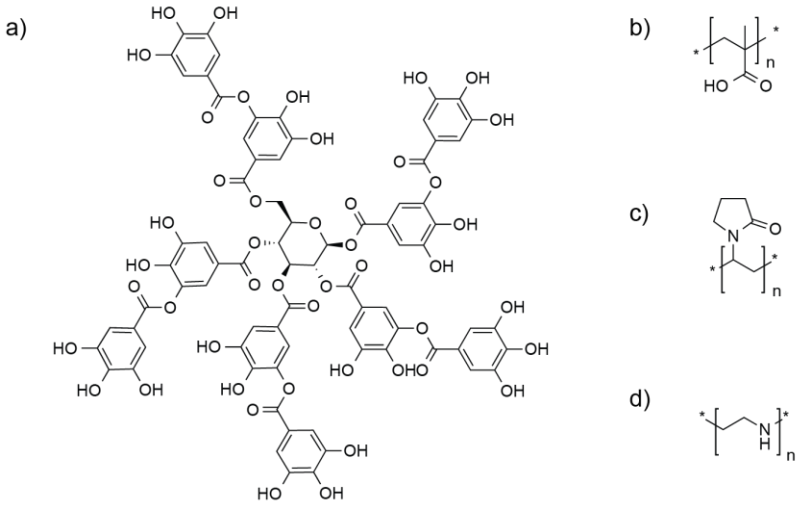

Figure 12. Chemical structures of a) tannic acid b) poly(methacrylic acid) c) poly(*N*-vinylpyrrolidone), and d) polyethyleneimine.

Layer-by-Layer of Tannic acid/pTEGMA

Tannic acid (TA) is a polyphenol of natural origin. It has been extensively used to form LbL constructs in conjunction of other polymers due to its high biocompatibility.[42] TA is a weak acid of pKa of 8.5[43] and is therefore protonated at physiological pH. TA has been shown to form self-assembled multilayer films with pTEGMA through hydrogen bonding and these films were shown to be stable at physiological conditions.[43]

The adsorption of TA/pTEGMA layers was investigated on a silicon QCM chip using PVP as a polymer precursor layer to impart a surface of hydrogen bonding sites to the substrate (Figure 13). The increase of mass on the surface, i.e., adsorption of polymers, is reflected by a negative frequency change (ΔF). Polymer desorption or other phenomenon leading to mass loss results in a positive ΔF.

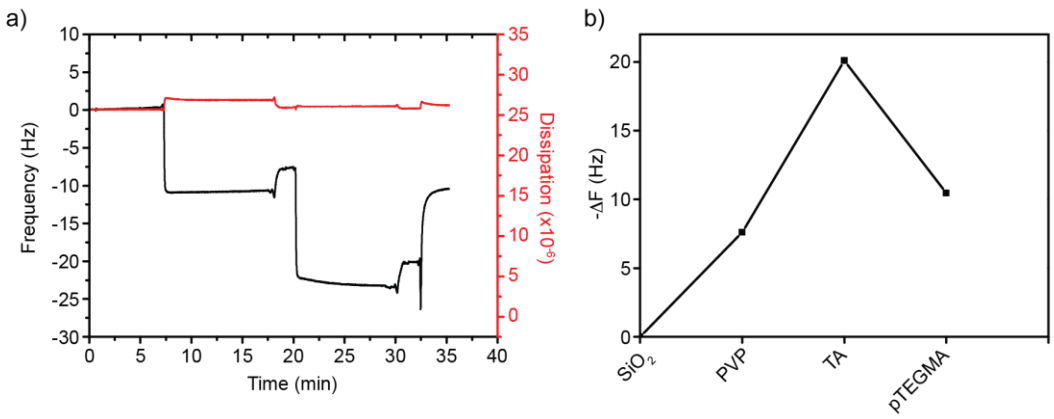

Figure 13. a) QCM frequency changes upon alternating addition of TA and pTEGMA layers on PVP-coated planar surfaces. b) Plot of the frequency changes for each successive layer. Measurements were made using the third overtone.

As shown in Figure 13, PVP and TA were sequentially adsorbed onto planar silica surfaces by hydrogen bonding. However, the addition of the next layer pTEGMA resulted in a positive frequency change indicating a loss of mass from the surface, possibly due to competitive displacement of TA via preferential interaction of pTEGMA and the underlying TA layer in comparison to PVP and TA.

In order to promote a stronger interaction of TA onto the surfaces and consequently provides a more optimal underlying support for the adsorption of pTEGMA, an alternative precursor layer, polyethyleneimine (PEI), was used.[44] The TA/pTEGMA layers were sequentially constructed on the PEI-coated substrate and the results are presented in Figure 14.

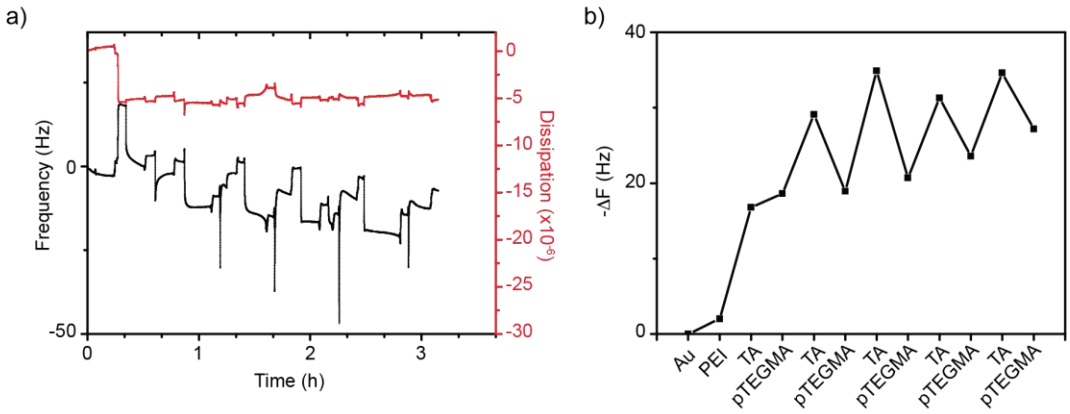

Figure 14. a) QCM frequency changes upon alternating addition of TA and pTEGMA layers on PEI-coated planar surfaces. b) Plot of the frequency changes for each successive layer. Measurements were made using the third overtone.

Similarly, sequential layering of pTEGMA and TA was not observed on the PEI-coated surface. Every addition of pTEGMA layer resulted in a positive frequency change, which indicated that TA/pTEGMA is not a suitable polymer pair to form a stable LbL construct.

Layer-by-Layer of Poly(methacrylic acid)/pTEGMA

The second polymer pair investigated in this study was poly(methacrylic acid) (PMA). This polymer is biocompatible, and has been used to create robust LbL systems.[16] The PMA/pTEGMA layers were constructed on silicon QCM chip using PVP as a precursor layer (Figure 15).

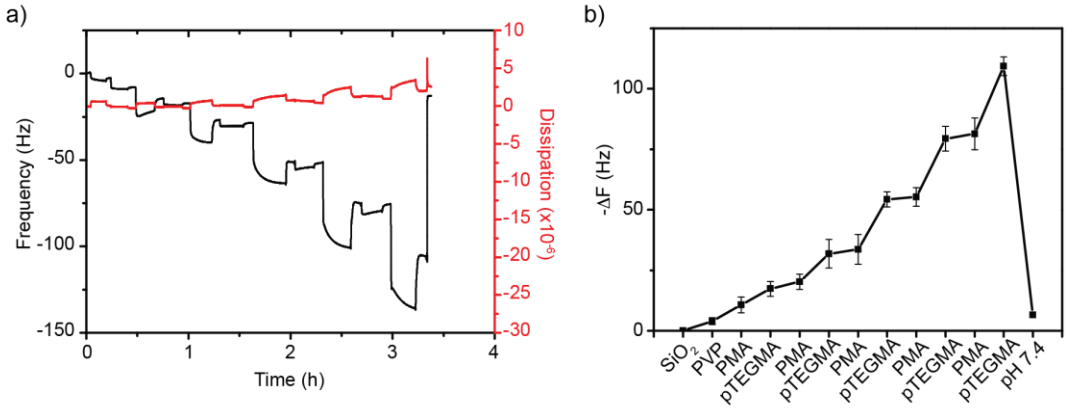

Figure 15. a) QCM frequency changes upon alternating addition of PMA and pTEGMA layers on PVP-coated planar surfaces. b) Plot of the frequency changes for each successive layer. Measurements were made using the third overtone.

Figure 15 shows the successful sequential adsorption of PMA and pTEGMA layers (up to five bilayers) at the assembly condition 20 mM NaOAc buffer pH 4 and in fact exhibited an exponential growth of the polymer layers. This allows thicker films to be deposited in comparison to linear growth, which will be beneficial for tuning the permeability of the polymer membranes. PMA has a pKa value of 6.5,[16] therefore it is deprotonated at physiological pH and loses its hydrogen bond donating capacities. When the PMA/pTEGMA system was exposed to physiological conditions (PBS pH 7.4), a significant recovery in the resonance frequency was quickly observed (Figure 15a). Hence, after the assembly at NaOAc buffer pH 4, PMA/pTEGMA layers need to be stabilized, for instance by chemical cross-linking, to prevent the disassembly at physiological pH.

4.3.2.4 Layer-by-layer on quantum rattle

The optimized film assembly conditions based on the findings on planar surfaces were used for the LbL assembly of pTEGMA on QR. In order to ensure the stability of the PMA/pTEGMA

system at physiological pH, thiol-functionalized PMA (PMA_{SH}) (Scheme 5) and thiol-functionalized pTEGMA ($pTEGMA_{SH}$) were synthesized, and thiol chemistry was used to cross-link the polymer layers.

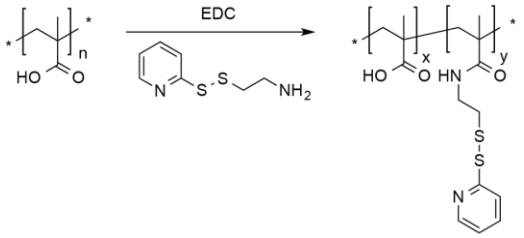

Scheme 5. Synthesis of thiol-functionalized PMA, PMA_{SH}.

pTEGMA was labelled with a fluorescent molecule (Alexa Fluor® 488) in order to facilitate the monitoring of the sequential deposition on QR by flow cytometry. The reaction scheme for the labelling of pTEGMA with Alexa Fluor® 488 is illustrated on Scheme 6.

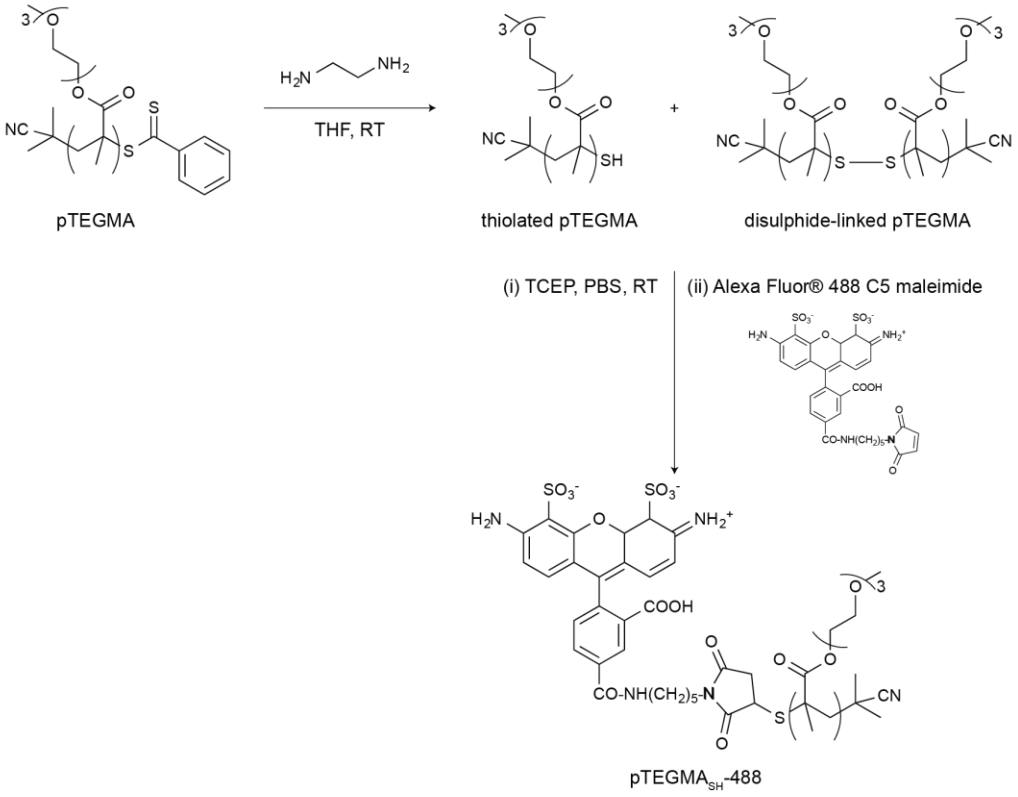

Scheme 6. Fluorescent labelling of pTEGMA: the polymer is first uncapped via an aminolysis reaction to generate thiolated-pTEGMA and disulphide-linked pTEGMA. The disulphide bonds are reduced by reacting with a reducing agent TCEP, and subsequently the polymer is conjugated with fluorophore Alexa Fluor® 488 C5 maleimide via thiol-maleimide reaction to form $pTEGMA_{SH}$-488.

As reported in Chapter 3, QR does not form stable suspensions in solutions of high salt concentration. The flocculation of QR is an issue for the LbL process, as the PMA/pTEGMA sequential deposition needs to proceed in buffered solution (pH 4) for optimal interaction between the polymer pairs. Electrostatic stabilization was used to ensure that QR remains well dispersed prior to LbL build-up. Poly(diallyldimethylammonium) chloride (PDDA) is a positively charged polymer, which has been used to stabilize dispersions of gold nanoparticles.[45] Here, it is used as a precursor layer adsorbed on QR, stabilizing them electrostatically before resuspending in 20 mM NaOAc pH 4 buffer for building up the polymer layers. The PDDA adsorption process was optimized (Figure 16b): using a high concentration of PDDA resulted in inter-particle cross-linking, with polymer chains forming a thick coating around several particles (Figure 16bi.), while reducing the concentration of PDDA led to a stable dispersion of QR, with only a slight shift in the size distribution of QR (Figure 16bii.). It was also verified that the release profile of doxorubin, a model anticancer drug, was unaffected by the deposition of the PDDA precursor layer (Figure 16d).

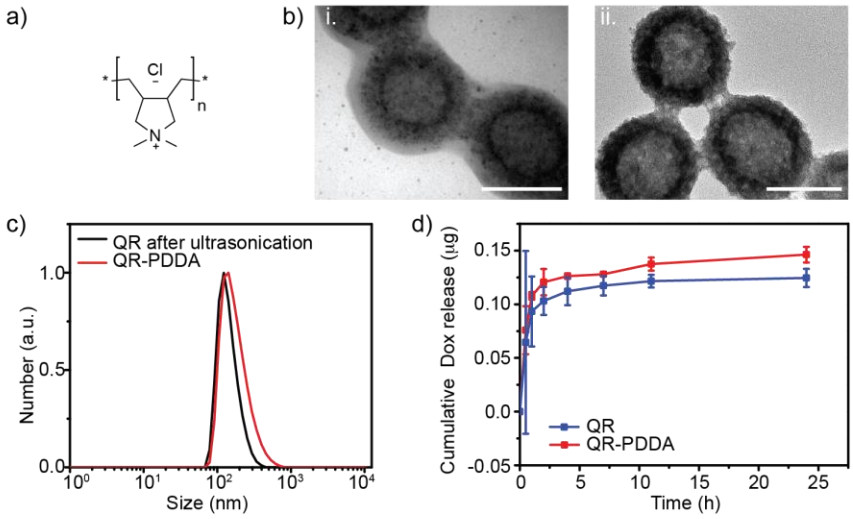

Figure 16. a) Chemical structure of PDDA. b) TEM images of QR coated with (i.) 3 mg.mL^{-1} PDDA or (ii.) 0.3 mg.mL^{-1} PDDA. c) Size distributions of QR after dispersion in water (black trace) and after coating with 0.3 mg.mL^{-1} PDDA (red trace). d) Doxorubicin release from native QR (blue trace) or from QR coated with 0.3 mg.mL^{-1} PDDA (red trace).

After stabilising QR by adsorbing a PDDA precursor layer, the PMA_{SH}/$pTEGMA_{SH}$-488 layers were then assembled on QR. In order to analyse the build-up of the polymer layers, aliquots of the particle suspension were taken after each cross-linking reaction of a deposited PMA_{SH}/$pTEGMA_{SH}$-488 bilayer. The changes in fluorescence intensity of the particles were monitored by flow cytometry (Figure 17) (flow cytometry data collection was performed by Dr Rona Chandrawati). The increase of fluorescence intensity after each addition of $pTEGMA_{SH}$-488

layer indicated the successful sequential layering of PMA/pTEGMA on QR. Upon exposure of these particles to PBS pH 7.4, there was no measurable loss of fluorescence intensity (Figure 17), indicating the stability of the LbL film at physiological conditions and therefore highlighting the necessity of the cross-linking approach.

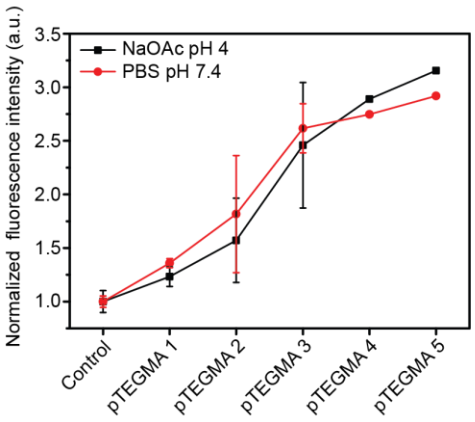

Figure 17. LbL construct of PDDA-(PMA/pTEGMA) on QR. pTEGMA was labelled with Alexa Fluor® 488 and the variations in fluorescence were measured by flow cytometry. An increase of fluorescence was observed after each bilayer deposition and the resuspension of the particles in a buffer at pH 7.4 resulted in a sustained fluorescence level, showing the stability of the cross-linked system. The fluorescence values are the average of 2 experiments; in one experiment 3 bilayers were assembled on QR while 5 bilayers were built in the second experiment.

Then, the release of a model anticancer drug, Doxorubicin, from QR coated with 3 bilayers of PMA_{SH}/$pTEGMA_{SH}$ was investigated. Doxorubicin is a fluorescent molecule and its release can be monitored by measuring the fluorescence of the supernatant at various time points. The drug was encapsulated in QR prior to building up the polymer layers, and the release was initiated by transferring the particles to 1× PBS buffer. As a control, QR coated with PMA/PVP (polyvinylpyrrolidone) was also prepared. The LCST of PVP is above 100 °C,[46] therefore the PMA/PVP multilayer film is non-thermoresponsive at the temperature range explored during the drug release experiments. The samples were incubated at 3 different temperatures: 25 °C, 37 °C (both below the LCST of pTEGMA), and 50 °C (above the LCST of pTEGMA) (Figure 18a).

During the LbL process, a lot of particles were lost, either because they were adhering to the walls of the eppendorf tubes, or because they did not aggregate in the pellet during the washing steps. There was a disparity in the amount of particles lost between the PMA_{SH}/$pTEGMA_{SH}$ and the PMA/PVP samples. The drug release profiles were tentatively normalized to the number of particles present in each sample by measuring the particle concentration in aliquots using

Nanoparticle Tracking Analysis (NTA, NanoSight LM10). However this method did not provide reliable particle concentration, due to the small size of QR and the formation of aggregates.

The drug release profiles presented on Figure 18a showed a dependence on temperature: as the temperature increased, more doxorubicin was being released, at a faster rate. However, this could not be attributed to the thermoresponsive properties of the PMA_{SH}/$pTEGMA_{SH}$ LbL multilayer film on QR, as the non-thermoresponsive construct PMA/PVP showed similar drug release profile evolution *vs* temperature. Therefore, it was concluded that the release of doxorubicin from QR was occurring by passive diffusion, rather than being triggered by a temperature-induced conformational change in the polymer structure. Additionally, the polymer multilayer film on QR did not prevent leakage of doxorubicin at room temperature.

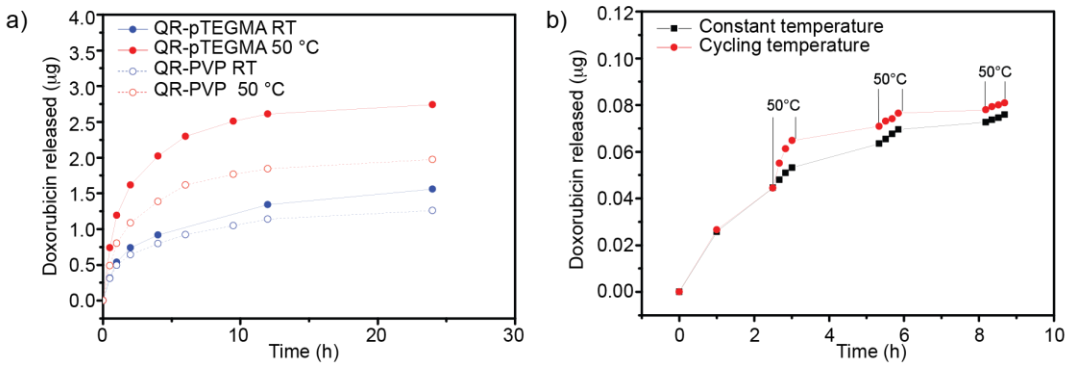

Figure 18. a) Doxorubicin release profiles from QR coated with thermoresponsive polymer assembly pTEGMA (full symbols) or non-thermoresponsive polymer assembly PVP (hollow symbols) at room temperature (blue traces) or 50 °C (red traces). b) Doxorubicin release profiles from QR coated with pTEGMA, at constant room temperature (black trace) or with temperature cycling (15 min at 50 °C, red trace).

A cycling experiment was also performed, where the same sample was incubated at room temperature for 2.5 h, then at 50 °C for 10 min, repeating this cycle 2 additional times (Figure 18b). When the temperature was first increased to 50 °C, it resulted in an increase of doxorubicin release compared to the sample kept at 25 °C. However, this increase was not observed during the next two cycles.

In order to investigate possible causes for the apparent absence of thermal response from the PMA_{SH}/$pTEGMA_{SH}$ LbL assembly, additional QCM experiments were performed to study the influence of cross-linking on the thermal response of the multilayer assembly of PMA_{SH}/$pTEGMA_{SH}$.

Figure 19 shows the sequential deposition of PMA_{SH} and $pTEGMA_{SH}$ in 20 mM NaOAc pH 4 buffer, forming 5 bilayers. After the final $pTEGMA_{SH}$ layer was added, the temperature of the

QCM chamber was slowly increased from 25 °C to 50 °C, and the changes in frequency were recorded.

The changes in frequency accompanying the change in temperature not only come from the polymer chains absorbed on the crystal, but also from the crystal itself and the water surrounding them.[47] The effect of temperature on the crystal can be derived from a control experiment, where a bare crystal is subjected to a temperature ramp. The influence of viscosity and density of liquid on QCM frequency change can be written as:[41]

$$\Delta f_\eta = -C_\eta\sqrt{\eta\rho} = -\frac{C_m}{2\sqrt{\pi f_0}}\sqrt{\eta\rho} \quad , \tag{3}$$

where η and ρ are the viscosity and density of the liquid. Additionally, the viscosity of a liquid strongly depends on temperature,

$$\eta = Ae^{\frac{B}{RT}} \quad , \tag{4}$$

where A and B are constant of viscosity and density, characteristic of a substance.

An increase of temperature will cause a decrease of the viscosity of the fluid and conversely a decrease of -Δf. Figure 19b shows the evolution of -Δf as the temperature of the QCM chamber was increased from 25 °C to 50 °C. In the 25-40 °C temperature range, a decrease of -Δf was observed, which can be attributed to an increase of the viscosity of the water surrounding the polymer film. As the temperature of the chamber approached the LCST of pTEGMA (48 °C), -Δf started to decrease. This could be an evidence for the structural transition occurring at the LCST. However, the decrease in -Δf below the LCST was unexpected as it corresponds to an apparent increase of mass, whereas when the temperature reaches the LCST of pTEGMA, the polymer chains start to collapse into globules, expulsing the water initially solubilizing it and therefore an apparent decrease of mass was expected. The dissipation, which reflects the structural characteristics of the film formed on the QCM crystal (rigid *vs* soft), did not show dramatic changes around the LCST value.

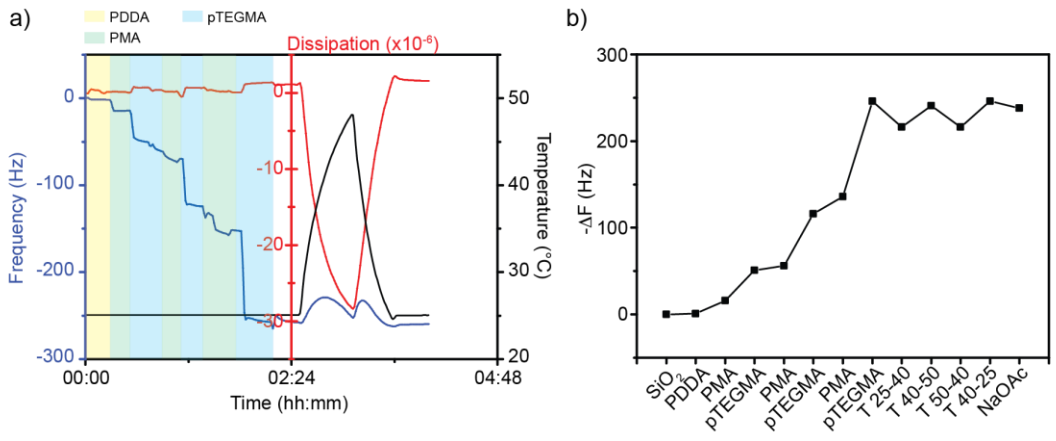

Figure 19. a) QCM frequency changes upon alternating addition of PMA and pTEGMA layers on PDDA-coated planar surfaces, followed by temperature cycling 25 °C → 50 °C → 25 °C. b) Plot of the frequency changes for each successive layer.

The LbL multilayer film build-up on QCM was repeated, this time with cross-linking after each bilayer deposition (Figure 20). Figure 20b shows the temperature dependence of the frequency shift (-Δf) of the LbL film. The evolution of -Δf in the temperature range 25-50 °C was different from the previous experiment where no cross-linking was used: -Δf increased continuously and did not drop when the temperature reached the LCST value for pTEGMA.

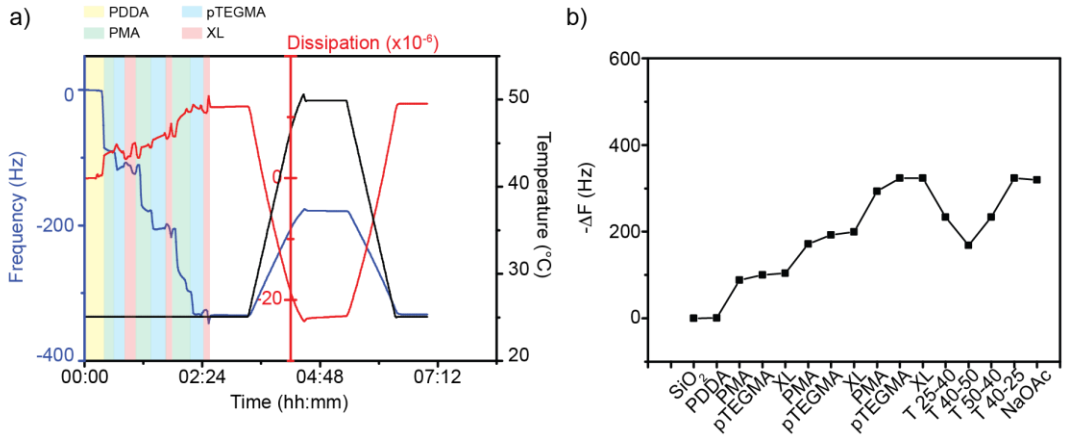

Figure 20. a) QCM frequency changes upon alternating addition of PMA and pTEGMA layers on PDDA-coated planar surfaces, after each bilayer deposition a cross-linking reaction step is implemented, followed by temperature cycling 25 °C → 50 °C → 25 °C. b) Plot of the frequency changes for each successive layer.

Studies of Poly(N-isopropylacrylamide) (PNIPAM) polymer brushes grafted to a QCM crystal have also revealed discrepancies in the temperature-responsive behaviour of end-grafted polymers chains *vs* polymer chains free in solution.[47] The conformational change of polymer chains with high grafting density only showed a gradual transition across the LCST.[48] Similarly,

studies have shown that grafted PNIPAM brushes of low molecular weight do not show a collapse transition even well above their LCST.[47,48]

In summary, the QCM measurements showed a discrepancy between non-cross-linked and cross-linked polymer assemblies; cross-linking the end of pTEGMA chains resulted in the chains behaving differently in response to an increase of temperature, and did not show a dramatic change in structure around the LCST value. In Chapter 5, an alternative strategy to cross-linking for the build-up of the multilayer polymer film is investigated.

4.4 Conclusion

In this Chapter, the engineering of QR as smart therapeutic carriers for triggered release of the therapeutics at the tumour site was explored. An increase in temperature generated from the photothermal properties of QR was used as a stimulus. Two parallel strategies were investigated. In one approach, QR was fused with liposomes to form a self-assembled, supported lipid bilayer (SLB) on QR. This new construct advantageously combined the propertied of QR and of liposomes; and it allowed stabilization of QR dispersion in solutions of high salt concentration, as would be encountered at physiological conditions. The lipid composition was then modified to impart thermoresponsive properties to the bilayer. Liposomes composed of DPPC display a phase transition characterized by a melting temperature (T_m) of 41 °C; the bilayer permeability to molecules is typically higher above T_m and maximal at T_m. The release profiles of doxorubicin (a model anticancer drug) and rhodamine B (a model dye molecule) from QR were similar for native QR and QR-SLB, therefore this approach was not successful for triggering the release of molecules from QR using an increase in temperature.

In a second approach, thermoresponsive polymers were incorporated into the platform using the layer-by-layer (LbL) technique, with the aim of allowing encapsulated molecules to be released only by the temperature trigger. Thermoresponsive polymer poly[tri(ethylene glycol) methacrylate] (pTEGMA) was successfully synthesized and its LCST was measured to be 47 °C in 1× PBS. The optimal conditions for the film deposition were established in Quartz Crystal Microbalance (QCM) experiments: alternating layers of poly(methacrylic acid) (PMA) and pTEGMA via hydrogen bonding. This optimized LbL assembly strategy was translated to QR. In order to detect the deposition of the layers, pTEGMA was fluorescently labelled with Alexa Fluor®488, and the increase of fluorescence intensity of the coated particles was detected using flow cytometry. The PMA/pTEGMA construct, however, was only stable at pH below pKa of PMA (6.5), since above this pH PMA was deprotonated and therefore was not able to interact with pTEGMA via hydrogen bonding. To achieve stability at physiological conditions, chemical cross-linking was performed on thiol-functionalized PMA and thiol-functionalized pTEGMA to form disulphide bond and the cross-linked construct on QR was found to be stable at pH 7.4. Doxorubicin was loaded in QR prior to the LbL polymer deposition, and its release was studied at temperatures both below and above the LCST of pTEGMA. The higher temperatures yielded an increased release rate of doxorubicin, but this was not specific to the thermoresponsive PMA_{SH}/$pTEGMA_{SH}$ assembly. QCM experiments showed a difference of behaviour between the 'free' and cross-linked PMA_{SH}/$pTEGMA_{SH}$ assemblies when the temperature was ramped up above the LCST of pTEGMA, suggesting that end-cross-linked $pTEGMA_{SH}$ polymer chains might

not show a drastic structural transition at the LCST. Therefore, there is a need for polymer structures, which are suitable for LbL assembly while maintaining their LCST. This is explored in Chapter 5, with the synthesis of novel thermoresponsive block copolymers.

References

1. P. Boyle, B. Levin. *World cancer report 2008.*; 2008.
2. A. M. Smith, S. Dave, S. Nie, L. True, X. Gao. *Expert Rev. Mol. Diagn.*, 2006, **6**, 231–244.
3. L. T. M. Sa, M. D. S. Albernaz, B. F. D. C. Patricio, M. V. Falcão, B. F. Coelho, A. Bordim, J. C. Almeida, R. Santos-Oliveira. *J. Pharm. Biomed. Anal.*, 2012, **70**, 602–604.
4. M. Hembury, C. Chiappini, S. Bertazzo, T. L. Kalber, G. L. Drisko, O. Ogunlade, S. Walker-Samuel, K. S. Krishna, C. Jumeaux, P. Beard, C. S. S. R. Kumar, A. E. Porter, M. F. Lythgoe, C. Boissière, C. Sanchez, M. M. Stevens. *Proc. Natl. Acad. Sci. U. S. A.*, 2015, **112**, 1959–1964.
5. J. Liu, A. Stace-Naughton, X. Jiang, C. J. Brinker. *J. Am. Chem. Soc.*, 2009, **131**, 1354–1355.
6. C. E. Ashley, E. C. Carnes, G. K. Phillips, D. Padilla, P. N. Durfee, P. A. Brown, T. N. Hanna, J. Liu, B. Phillips, M. B. Carter, N. J. Carroll, X. Jiang, D. R. Dunphy, C. L. Willman, D. N. Petsev, D. G. Evans, A. N. Parikh, B. Chackerian, W. Wharton, D. S. Peabody, C. J. Brinker. *Nat. Mater.*, 2011, **10**, 389–397.
7. X. Liu, A. Situ, Y. Kang, K. R. Villabroza, Y. Liao, C. H. Chang, T. Donahue, A. E. Nel, H. Meng. *ACS Nano*, 2016, **10**, 2702–2715.
8. B. Kneidl, M. Peller, G. Winter, L. H. Lindner, M. Hossann. *Int. J. Nanomedicine*, 2014, **9**, 4387–4398.
9. Y. Lvov, G. Decher, H. Moehwald. *Langmuir*, 1993, **9**, 481–486.
10. G. Decher. *Science*, 1997, **277**, 1232–1237.
11. K. Ariga, J. P. Hill, Q. Ji. *Phys. Chem. Chem. Phys.*, 2007, **9**, 2319–2340.
12. J. F. Quinn, A. P. R. Johnston, G. K. Such, A. N. Zelikin, F. Caruso. *Chem. Soc. Rev.*, 2007, **36**, 707–718.
13. B. G. De Geest, S. De Koker, G. B. Sukhorukov, O. Kreft, W. J. Parak, A. G. Skirtach, J. Demeester, S. C. De Smedt, W. E. Hennink. *Soft Matter*, 2009, **5**, 282–291.
14. Y. Yan, M. Björnmalm, F. Caruso. *Chem. Mater.*, 2014, **26**, 452–460.
15. Y. Ma, W.-F. Dong, M. a Hempenius, H. Möhwald, G. J. Vancso. *Nat. Mater.*, 2006, **5**, 724–729.
16. A. Zelikin, Q. Li, F. Caruso. *Chem. Mater.*, 2008, **20**, 2655–2661.
17. Y. Yan, A. P. R. Johnston, S. J. Dodds, M. M. J. Kamphuis, C. Ferguson, R. G. Parton, E. C. Nice, J. K. Heath, F. Caruso. *ACS Nano*, 2010, **4**, 2928–2936.
18. R. Chandrawati, F. Caruso. *Langmuir*, 2012, **28**, 13798–13807.
19. J.-F. Lutz, A. Hoth. *Macromolecules*, 2006, **39**, 893–896.
20. J.-F. Lutz, O. Akdemir, A. Hoth. *J. Am. Chem. Soc.*, 2006, **128**, 13046–13047.
21. J.-F. Lutz. *J. Polym. Sci. Part A Polym. Chem.*, 2008, **46**, 3459–3470.

22. K. Bebis, M. W. Jones, D. M. Haddleton, M. I. Gibson. *Polym. Chem.*, 2011, **2**, 975.

23. T. M. Sager, D. W. Porter, V. a. Robinson, W. G. Lindsley, D. E. Schwegler-Berry, V. Castranova, G. William. *Nanotoxicology*, 2007, **1**, 118–129.

24. P. Bihari, M. Vippola, S. Schultes, M. Praetner, A. G. Khandoga, C. a Reichel, C. Coester, T. Tuomi, M. Rehberg, F. Krombach. *Part. Fibre Toxicol.*, 2008, **5**, 14.

25. L. Foucaud, M. R. Wilson, D. M. Brown, V. Stone. *Toxicol. Lett.*, 2007, **174**, 1–9.

26. M. K. Yu, J. Park, S. Jon. *Theranostics*, 2012, **2**, 3–44.

27. N. Mandzy, E. Grulke, T. Druffel. *Powder Technol.*, 2005, **160**, 121–126.

28. A. Stein, J. P. Whitlock, M. Bina. *Proc. Natl. Acad. Sci.*, 1979, **76**, 5000–5004.

29. C. Xu, M. Yu, O. Noonan, J. Zhang, H. Song, H. Zhang, C. Lei, Y. Niu, X. Huang, Y. Yang, C. Yu. *Small*, 2015, 1–7.

30. J.-G. Wang, H.-J. Zhou, P.-C. Sun, D.-T. Ding, T.-H. Chen. *Chem. Mater.*, 2010, **22**, 3829–3831.

31. S.-H. Wu, Y. Hung, C.-Y. Mou. *Chem. Commun.*, 2011, **47**, 9972–9985.

32. P. R. C. Theresa M. Allena. *Adv. Drug Deliv. Rev.*, 2013, **65**, 36–48.

33. W. Xu, J. Rytkönen, S. Rönkkö, T. Nissinen, T. Kinnunen, M. Suvanto, A. Närvänen, V. P. Lehto. *Chem. Mater.*, 2014, **26**, 6734–6742.

34. X. Wu, Z. Wang, D. Zhu, S. Zong, L. Yang, Y. Zhong, Y. Cui. *ACS Appl. Mater. Interfaces*, 2013, **5**, 10895–10903.

35. K. Chen, J. Zhang, H. Gu. *J. Mater. Chem.*, 2012, **22**, 22005.

36. H. Grüll, S. Langereis. *J. Control. Release*, 2012, **161**, 317–327.

37. M. B. Yatvin, J. N. Weinstein, W. H. Dennis, R. Blumenthal. *Science*, 1978, **202**, 1290–1293.

38. J. N. Weinstein, R. L. Magin, M. B. Yatvin, D. S. Zaharko. *Science*, 1979, **204**, 188–191.

39. C. K. O'Sullivan, G. G. Guilbault. *Biosens. Bioelectron.*, 1999, **14**, 663–670.

40. G. Sauerbrey. *Zeitschrift fur Phys.*, 1959, **155**, 206–222.

41. K. A. Marx. *Biomacromolecules*, 2003, **4**, 1099–1120.

42. V. Kozlovskaya, E. Kharlampieva, I. Drachuk, D. Cheng, V. V. Tsukruk. *Soft Matter*, 2010, **6**, 3596.

43. Y. Cao, W. He. *Acta Biomater.*, 2013, **9**, 4558–4568.

44. H. Lomas, A. P. R. Johnston, G. K. Such, Z. Zhu, K. Liang, M. P. van Koeverden, S. Alongkornchotikul, F. Caruso. *Small*, 2011, **7**, 2109–2119.

45. H. Chen, Y. Wang, Y. Wang, S. Dong, E. Wang. *Polymer*, 2006, **47**, 763–766.

46. P. Sakellariou. *Polymer*, 1992, **33**, 1339–1342.

47. G. Liu, G. Zhang. *J. Phys. Chem. B*, 2005, **109**, 743–747.

48. N. Ishida, S. Biggs. *Langmuir*, 2007, **23**, 11083–11088.

Chapter 5

Design and synthesis of thermoresponsive block copolymers based on polyvinylpyrrolidone and poly(triethylene glycol methacrylate)

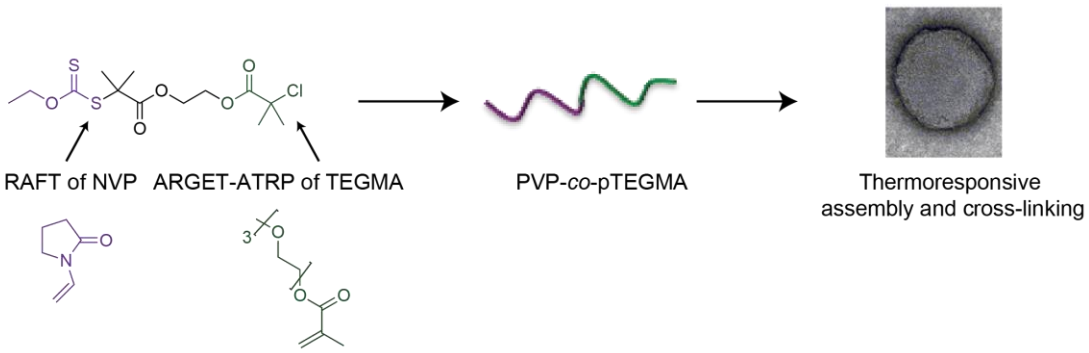

Part of this Chapter was published in:

C. Jumeaux, R. Chapman, R. Chandrawati, M. M. Stevens. Synthesis and self-assembly of temperature-responsive copolymers based on *N*-vinylpyrrolidone and triethylene glycol methacrylate. *Polym. Chem.*, 2015, **6**, 4116–4122.

5.1 Introduction

To further the aim in addressing QR in therapeutic applications, this platform is developed as a smart mesoporous silica-based drug delivery system that allows triggered release of drugs. In Chapter 4, layers of a thermoresponsive polymer, poly(triethylene glycol methacrylate) (pTEGMA), were used to coat QR and seal the pores of the silica shells, entrapping the encapsulated therapeutics. An increase in temperature was used as the external stimulus, initially achieved by heating up the solution, and with the future goal of deriving it by irradiating QR with a near-infrared laser. The increase in temperature above the LCST of pTEGMA results in a change of the structure of the polymer chains, called coil-to-globule transition, which then triggers the release of drugs from QR. The assembly of pTEGMA layers on QR was demonstrated, however, results suggested that the thermoresponsive properties of pTEGMA chains integrated in a cross-linked multilayer film were not retained, hindering the ability to repeatedly switch 'on' and 'off' the release of the encapsulated drugs.

To overcome this, in this Chapter a more advanced system is designed, involving the synthesis of novel block copolymers composed of a thermoresponsive polymer segment linked to an anchoring polymer segment allowing the build-up of the multilayer film.

The building blocks selected for this study are polyvinylpyrrolidone (PVP), pTEGMA, and tannic acid (TA). PVP is a non-toxic, non-ionic, water-soluble polymer with unique physicochemical properties. Its biocompatibility and anti-fouling properties are particularly attractive and have resulted in the application of PVP in the development of biomaterials and drug delivery carriers.[1–4] Here, PVP acts as a hydrogen bond acceptor to the tannic acid in the layer-by-layer assembly,[5] and as a handle for pTEGMA incorporation. pTEGMA is a thermoresponsive polymer and its properties have been listed in Chapter 4. This Chapter describes the synthesis of a library of block copolymers PVP-*co*-pTEGMA using advanced polymerisation techniques, the characterisation of the thermoresponsive behaviour, and finally the application of these new materials for the assembly of multilayer films, both on QR and on sacrificial templates to form hollow capsules.

5.2 Materials and methods

5.2.1 Materials

Acetone, ascorbic acid, azobisisobutyronitrile (AIBN), 2,2'-bipyridine, α-bromoisobutyryl bromide, copper(II) chloride ($CuCl_2$), ethylene glycol, 1,4-dioxane, methacryloyl chloride, potassium ethyl xanthogenate, potassium persulphate, tetrahydrofuran (THF), triethylamine, triethylene glycol monomethyl ether, tris(pyridin-2-ylmethyl)amine (TPMA), 1,3,5-trioxane, *N*-vinylpyrrolidone (NVP) were purchased from Sigma Aldrich (UK) and were used without further purification. Dichloromethane (DCM) was purchased from AGTC Bioproducts (UK). Ethyl acetate and hexane were purchased from VWR Chemicals (UK). Copper(I) chloride (CuCl) was purchased from Sigma Aldrich (UK) and purified prior to use by stirring the powder in glacial acetic acid for 2 h. The white solids were filtered, washed thoroughly with cold ethanol, dried *in vacuo*, and stored under nitrogen.

5.2.2 Methods

Synthesis of triethylene glycol methacrylate (TEGMA)

Triethylene glycol monomethyl ether (5.0 g, 30 mmol) was added in a 50 mL two-necked round-bottom flask at 0 °C. The flask was equipped with a magnetic stirrer and an isobar addition funnel, and flushed with nitrogen (N_2). Dry DCM (20 mL) was added, followed by triethylamine (5.5 mL, 40 mmol), and dropwise addition of methacryloyl chloride (6.3 g, 60 mmol) in DCM (10 mL). After addition, the funnel was further rinsed with 5 mL of DCM and the mixture was stirred for 1 h at 0 °C and 17 h at room temperature. After addition of methanol to quench the reaction, the mixture was filtered to remove the triethylammonium chloride salt. The organic phase was washed with aqueous HCl (pH 2, 2 × 50 mL), aqueous NaOH (pH 12, 2 × 50 mL) and brine (2 × 50 mL), and dried over magnesium sulphate ($MgSO_4$) to yield the product as a yellow viscous oil (7.7 g, quantitative). ^{1}H-NMR (400 MHz, $CDCl_3$, δ, ppm): 6.13-6.10 (m, 1H, =C$\underline{H}$H), 5.58-5.54 (m, 1H, =CH$\underline{H}$), 4.30-4.28 (m, 2H, COOC$\underline{H_2}$CH$_2$O), 3.75-3.72 (m, 2H, COOCH$_2$C$\underline{H_2}$O), 3.67-3.62 (m, 6H, OC$\underline{H_2}$C$\underline{H_2}$OC$\underline{H_2}$), 3.55-3.52 (m, 2H, C$\underline{H_2}$OCH$_3$), 3.37 (s, 3H, OC$\underline{H_3}$), 1.93 (s, 3H, C$\underline{H_3}$).

Synthesis of chloroxanthate CTA

2-hydroxyethyl 2-bromo-2-methylpropanoate (**1**): Ethylene glycol (31.03 g, 0.5 mol) and pyridine (0.72 g, 0.01 mol) were introduced to a 100 mL round bottom flask with dry THF (10 mL). The reaction mixture was cooled in an ice-water bath, and a solution of α-bromoisobutyryl bromide

(1.07 mL, 0.01 mol) in dry THF (5 mL) was slowly added while stirring. The reaction mixture was stirred at 0 °C for 1 h and then at room temperature for 16 h. The reaction mixture was then diluted in aqueous HCl (pH 2) and extracted with DCM. The organic fractions were combined, extracted with water, washed with brine, dried on $MgSO_4$, filtered and evaporated to dryness to afford the product **1** as a colourless oil (1.83 g, 87 %). ^{1}H-NMR (400 MHz, $CDCl_3$, δ, ppm): 4.35-4.30 (m, 2H, C$\underline{H_2}$CH_2OH), 3.92-3.85 (m, 2H, C$\underline{H_2}$OH), 1.96 (s, 6H, (C$\underline{H_3}$)$_2$).

S-2-[(2-Hydroxyethoxy)carbonyl] propan-2-yl O-ethyl carbondithioate (**2**): Potassium ethyl xanthogenate (726 mg, 4.5 mmol) and acetone (10 mL) were added to a 50 mL round bottom flask equipped with a magnetic stirrer and a dropping funnel. A solution of 2-hydroxyethyl 2-bromo-2-methylpropanoate **1** (853 mg, 4.0 mmol) in acetone (10 mL) was added dropwise over 30 min and the reaction mixture was stirred for 17 h at room temperature. After filtration to eliminate the salts, the mixture was concentrated *in vacuo* to afford a yellow viscous solid. This was diluted using DCM (100 mL), washed with water (2 × 50 mL), dried over $MgSO_4$ and evaporated to dryness. The yellow viscous solid obtained was purified over a silica column (hexane : ethyl acetate 1:1), and the relevant fractions were combined and concentrated to afford the product **2** as a yellow viscous liquid (0.7 g, 67 %). ^{1}H-NMR (400 MHz, $CDCl_3$, δ, ppm): 4.61 (q, *J* = 7.1 Hz, 2H, C$\underline{H_2}$CH_3), 4.28-4.24 (m, 2H, C$\underline{H_2}$CH_2OH), 3.85-3.81 (m, 2H, C$\underline{H_2}$OH), 1.64 (s, 6H, (C$\underline{H_3}$)$_2$), 1.40 (t, *J* = 7.1 Hz, 3H, CH_2C$\underline{H_3}$).

S-[1,2-dimethyl-4-(6-bromoisobutyrate) ethyl acetate] O-ethyl dithiocarbonate (**3**): In a two-necked 50 mL round bottom flask, **2** (500 mg, 2.0 mmol) and triethylamine (378 μL, 2.7 mmol) were dissolved in dry THF (5 mL) under inert atmosphere (N_2). The reaction mixture was cooled in an ice-water bath and a solution of α-bromoisobutyryl bromide (276 μL, 2.5 mmol) in dry THF (5 mL) was slowly added while stirring. The mixture was stirred in the ice bath for 1 h and then at room temperature for 17 h. Excess of α-bromoisobutyryl bromide was neutralised with water and the reaction mixture was poured into aqueous HCl (pH 2) and extracted with DCM. The combined organic layers were washed with saturated sodium carbonate (2 × 50 mL) and brine (2 × 50 mL), dried over $MgSO_4$ and concentrated *in vacuo*. The yellow viscous solid obtained was purified over a silica column (hexane:ethyl acetate 8:2), and the relevant fractions were combined and evaporated to afford the product **3** as a yellow viscous liquid (0.4 g, 55 %). ^{1}H-NMR (400 MHz, $CDCl_3$, δ, ppm): 4.60 (q, *J* = 7.1 Hz, 2H, C$\underline{H_2}$CH_3), 4.42-4.35 (m, 4H, OC$\underline{H_2}$C$\underline{H_2}$O), 1.93 (s, 6H, C(C$\underline{H_3}$)$_2$), 1.62 (s, 6H, (C$\underline{H_3}$)$_2$), 1.39 (t, *J* = 7.1 Hz, 3H, C$\underline{H_3}$).

S-[1,2-dimethyl-4-(6-chloroisobutyrate) ethyl acetate] O-ethyl dithiocarbonate (**4**): The final chloroxanthate CTA **4** was prepared using a halogen exchange reaction. A 100 mL Schlenk flask was charged with **3** (2.21 g, 13.7 mmol), 2,2'-bipyridine (5.16 g, 82.4 mmol), and dry acetone

(20 mL), and deoxygenated using three freeze-pump-thaw cycles. CuCl (236 mg, 2.39 mmol) and $CuCl_2$ (146 mg, 1.09 mmol) were quickly added to the frozen mixture, and the oxygen removed by a further three freeze-pump-thaw cycles. After stirring for 24 h at 50 °C, the acetone was removed and the mixture was diluted with DCM (15 mL) before passing it over a column of neutral alumina. The solution was diluted with DCM (35 mL) and washed with EDTA (100 mM, 3 × 50 mL), saturated sodium bicarbonate (1 × 50 mL) and brine (2 × 50 mL). The organic fraction was dried over $MgSO_4$, and the concentrated mixture was purified over a silica column (hexane : ethyl acetate 3:1). After combination and concentration of the relevant fractions, the product **4** was obtained as a yellow oil (0.2 g, 52 %). MS (MALDI-TOF, CHCA matrix) m/z calcd. for $C_{13}H_{21}ClO_5S_2Na$ $[M+Na]^+$ 379.1, Found. 379.1; ^{1}H-NMR (400 MHz, $CDCl_3$, δ, ppm): 4.60 (q, *J* = 7.1 Hz, 2H, $C\underline{H_2}CH_3$), 4.41-4.36 (m, 4H, $OC\underline{H_2}C\underline{H_2}O$), 1.77 (s, 6H, $C(C\underline{H_3})_2$), 1.62 (s, 6H, $(C\underline{H_3})_2$), 1.39 (t, *J* = 7.0 Hz, 3H, $C\underline{H_3}$); ^{13}C-NMR (100 MHz, $CDCl_3$, δ, ppm): 211.0 (C=S), 173.0 (C=O, ATRP side), 171.5 (C=O, RAFT side), 70.0 ($\underline{C}(CH_3)_2Cl$), 64.5 ($\underline{C}(CH_3)_2S$), 63.5 ($\underline{C}H_2OC(O)C(CH_3)_2Cl$), 63.2 ($\underline{C}H_2CH_2OC(O)C(CH_3)_2Cl$), 54.2 ($CH_3\underline{C}H_2$), 30.0 ($C(\underline{C}H_3)_2Cl$), 26.0 ($C(\underline{C}H_3)_2S$), 13.5 ($\underline{C}H_3CH_2$).

RAFT of NVP

In a typical experiment, the chloroxanthate CTA (40 mg, 0.1 mmol), AIBN (1.84 mg, 0.01 mmol) and NVP (1.87 g, 16.8 mmol) were charged to a 10 mL round bottom flask equipped with a magnetic stirrer bar and a septum with 3.4 mL of 1,4-dioxane. 1,3,5-Trioxane (90 mg, 1 mmol) was also added to the reaction mixture as a reference for calculating monomer conversion. The reaction mixture was degassed by argon bubbling, and then transferred to a pre-heated oil bath at 65 °C for 17 h. The reaction was stopped by introducing oxygen, and 1,4-dioxane was removed under vacuum. The viscous liquid was solubilised in DCM and the polymer was purified by precipitation in hexane. Monomer conversion was determined by 1H-NMR using 1,3,5-trioxane as internal standard.

ATRP of TEGMA

Purification of CuCl

CuCl (1 g) was mixed with glacial acetic acid (100 mL) and stirred for 2 h. The solids were filtered under N_2 flow, and were washed with glacial acetic acid then dried using absolute ethanol. The powder was transferred to a 50 mL falcon, dried under vacuum overnight, and then stored under inert atmosphere, protected from light.

ATRP of TEGMA

In a typical experiment, PVP macroinitiator (250 mg, 10.4 μmol) was mixed with TEGMA (1200 mg, 5.2 mmol, 500 eq.) and 1.5 mL 1,4-dioxane in a Schlenk tube. The mixture was degassed by performing five freeze-pump-thaw cycles. In a 7 mL glass vial were weighed $CuCl_2$ (1.05 mg) and CuCl (4.4 mg) (vial A), and in a separate glass vial tris(2-pyridylmethyl)amine (TPMA) (15.1 mg) and 2.5 mL 1,4-dioxane (vial B). These vials contained five times excess reagents needed for the polymerisation; the final equivalent ratios were PVP/$CuCl_2$/CuCl/TPMA/TEGMA 1/0.85/0.15/1/500. The vials were equipped with a septum, and degassed under N_2. The content of vial B was transferred to vial A via a cannula. Using a syringe filled with N_2, 0.5 mL of the Cu/TPMA mixture was added to the frozen content of the Schlenk tube. Three additional freeze-pump-thaw cycles were performed. The reaction was initiated by transferring the vial to an oil bath heated to 40 °C.

ARGET-ATRP of TEGMA

In a typical experiment, PVP macroinitiator (162 mg, 1.8 μmol) was mixed with TEGMA (100 mg, 430 μmol, 40 eq.), $CuCl_2$ (1.4 mg, 1.8 μmol) and the ligand TPMA (3.1 mg, 1.8 μmol) in IPA/water (50 % v/v) such that the monomer concentration in the final mixture was 0.5 M. Separately, a solution of ascorbic acid (28 $mg.mL^{-1}$) in IPA/water (50 % v/v) was prepared, and both solutions were degassed by argon bubbling. Ascorbic acid solution (0.75 eq. relative to the initiator) was added to start the polymerisation, which was conducted at 40 °C.

Cross-linking of self-assembled block copolymers

PVP-*co*-pTEGMA (0.4 mg) was dissolved in 800 μL of sodium acetate buffer (20 mM, pH 4) in a glass vial equipped with a septum and a magnetic stirrer. Cross-linker potassium persulphate (1.8 mM) was added to the polymer solution, followed by degassing by argon bubbling. The reaction mixture was transferred to a pre-heated oil bath at 80 °C for 2 h and then cooled down to room temperature to confirm the structural integrity of the cross-linked structures. Prior to Transmission Electron Microscopy (TEM) imaging, the cross-linked assemblies were subjected to dialysis against water, using a Slide-A-Lyzer MINI Dialysis Device, 2 kDa MWCO (Thermo Scientific).

Characterization methods

NMR spectra were recorded on Bruker DPX-400 400 MHz instruments using deuterated solvents obtained from Sigma-Aldrich. Conversion for polymerisations of NVP and TEGMA were determined by ^{1}H-NMR. Molecular weight distributions of the resulting polymers were

characterised using size exclusion chromatography (SEC) over two PSS GRAM columns in series using DMF (+ 0.075 % w/v LiBr) as the eluent, at the exception of copolymers obtained via ATRP, where THF was used as the eluent. Retention times were normalised using water as a flow rate marker and molecular weights were calculated without correction relative to a set of narrow polystyrene standards. Matrix-assisted laser desorption/ionisation (MALDI) time of flight (ToF) spectra were collected on a Waters Micromass MALDI-ToF in positive ion reflectron mode, calibrated using poly(ethylene glycol) standards. TEM images of the polymer nanostructures were recorded on a JEOL JEM 2100 field emission electron microscope, operating with an acceleration voltage of 200 kV. The TEM samples were prepared by dropping 5 µL of a solution of the cross-linked self-assembled copolymers onto mesh copper grids and subsequently dried at room temperature. The grids were stained with a solution of 0.2 % w/w uranyl acetate. Size distribution measurements were performed using a Zetasizer Nano ZS (Malvern). In all dynamic light scattering (DLS) measurements, the scattering angle was fixed at 173°. DLS was also used to measure the thermoresponsive behaviour of PVP-*co*-pTEGMA. Solutions of PVP-*co*-pTEGMA (2 $mg.mL^{-1}$ in 20 mM NaOAc pH 4) were submitted to a temperature ramp (1 °C) with 30 s equilibration time. Each data point corresponds to the average of 5 measurements of 10 s with an attenuator value fixed at 8 and a measurement position set at 4.65 mm.

Quartz Crystal Microbalance (QCM)

QCM measurements (Q-sense E4) were used to characterize polymer assembly on planar surfaces. Silica-coated crystals were cleaned in a 2 wt% sodium dodecyl sulfate solution overnight, followed by rinsing with Milli-Q H_2O and drying with nitrogen. These crystals were mounted into the chambers of the instrument and excited at multiple overtones. The changes in the resonance frequency were monitored at room temperature and normalized frequencies using the third overtone are presented.

The initial layer of PVP-*co*-pTEGMA was deposited by injecting the polymer solution into the QCM chamber, and allowed to adsorb for 10 min. The chamber was then washed with NaOAc buffer pH 4, after which the solution of TA was introduced into the chamber and allowed to adsorb for 10 min. The multilayer film was then assembled by alternating incubation of TA and PVP-*co*-pTEGMA.

Fluorescent Labelling of pTEGMA

Aminolysis reaction

PVP-*co*-pTEGMA (10 mg) was dissolved in tetrahydrofuran (THF) (300 µL) and ethylenediamine (1.8 µL) was added to the polymer solution. The reaction was stirred overnight and then the polymer was precipitated in cold diethyl ether, followed by purification by centrifugation (6500 rpm for 30 min).

Reduction of the disulphide bonds

After aminolysis, the polymer was dissolved in 1 mL of 1× PBS and tris(2-carboxyethyl) phosphine (TCEP) (19.2 mg in 500 µL of 1× PBS) was added to the solution. The reaction was stirred for 15 min to yield thiol-functionalized PVP-*co*-pTEGMA (PVP-*co*-pTEGMA$_{SH}$).

Conjugation of Alexa Fluor® 488

Alexa Fluor® 488 C_5-maleimide (20 µL, Invitrogen Life Technologies) was added to the PVP-*co*-pTEGMA$_{SH}$ solution and the mixture was stirred overnight at room temperature, protected from light. The product was purified by dialysis (using Float-A-Lyzer® G2 device, MWCO 3.5-5 kDa, Spectrum Labs) against water for 24 h and the polymer was isolated via freeze-drying to obtain PVP-*co*-pTEGMA$_{SH}$-488. Prior to use, pTEGMA$_{SH}$-488 was incubated with DL-dithiothreitol (DTT) (100 mg.mL^{-1}) in 20 mM MOPS buffer pH 8 for at least 15 min at 37 °C, followed by dilution in 20 mM NaOAc buffer pH 4.

Layer-by-layer on colloidal silica microparticles

Silica microparticles from microParticles GmbH (200 µL, 5 wt%, 2.79 µm-diameter) were washed 3 times in 20 mM NaOAc pH 4 buffer. They were resuspended in 100 µL of 20 mM NaOAc pH 4 buffer and 100 µL of PVP-*co*-pTEGMA-488 (PVP$_{9kDa}$-*co*-pTEGMA$_{6kDa}$, 0.1 mg.mL^{-1} in NaOAc buffer) were added. The polymers were allowed to adsorb for 15 min at room temperature, and then the particles were washed 3 times in NaOAc buffer. The PVP-*co*-pTEGMA-488/TA layers were then assembled by alternatively immersing the particles in polymer solution (0.1 mg.mL^{-1}) for at least 15 min. To remove excess material the polymer-coated particles were washed 3 times in NaOAc buffer. Five bilayers were built on the silica particles. The increase of fluorescence intensity after each bilayer deposition was monitored by flow cytometry (LSRFortessa, BD Biosciences, data acquired by Dr Rona Chandrawati) using an excitation wavelength of 488 nm. At least 10,000 particles were analysed in each experiment.

Drug loading and release experiments

Quantum rattles were resuspended in Milli-Q H_2O (5 mg.mL^{-1}) by ultrasonication (Sonics Vibra Cell, VCX500), at a power of 125 W. To 1.2 mL of QR were added 1.2 mL of doxorubicin solution in milliQ H_2O (0.5 mg.mL^{-1}) ([QR] = 2.5 mg.mL^{-1}, [Dox] = 0.25 mg.mL^{-1}). QR suspension was rotated overnight, protected from light. The unencapsulated doxorubicin was removed by washing QR 3 times in Milli-Q H_2O (centrifugation at 14000 rpm for 5 min). After the final wash, QR was resuspended in 1.2 mL Milli-Q H_2O and split into 100 µL aliquots: "QR", "QR/PVP-*co*-pTEGMA(1)" and "QR/PVP-*co*-pTEGMA(2)" which were functionalized with respectively 0, 1 and 2 layers of PVP-*co*-pTEGMA. Briefly, the PVP-*co*-pTEGMA/TA layers were assembled on QR by alternatively adding to the particles 100 µL of PVP-*co*-pTEGMA ($MW_{NMR,PVP}$ = 23 kDa, $MW_{NMR,pTEGMA}$ = 70 kDa, 0.2 mg.mL^{-1} stock solution in Milli-Q H_2O) or TA (0.2 mg.mL^{-1}), allowing the polymers to absorb for at least 15 min. To remove excess material the polymer-coated QR were washed 3 times in Milli-Q H_2O. For "QR/PVP-*co*-pTEGMA(2)", this step was repeated another time. The release of doxorubicin was initialised by resuspending QR in 1× PBS buffer (200 µL). QR suspension was incubated at room temperature, or 50 °C. For each time point QR was pelleted, the supernatant was collected and its fluorescence was measured on a plate reader (SpectraMax M5 Microplate Readers, Molecular Devices) (λ_{ex} = 470 nm, λ_{em} = 590 nm).

Synthesis of PVP-co-pTEGMA hollow capsules

Photothermal properties of materials

Graphene oxide (GO), reduced graphene oxide (rGO) and gold nanoclusters (AuNC) were provided by Dr Yiyang Lin. The photothermal properties of solutions of GO, rGO (0.1 mg.mL^{-1} in Milli-Q H_2O) and AuNC (0.1 mM in Milli-Q H_2O) were measured. 100 µL of each solution were added to wells of a 96-well plate, which were placed in the path of a 146 mW, 785 nm laser. The temperature profile of the solution was recorded using a mini-hypodermic probe, type T thermocouple (Omega, UK) and a RTD thermometer (Omega, UK). The experiments were repeated twice.

Synthesis of hybrid PVP-co-pTEGMA/GO/TA capsules

Silica microparticles (2.79 µm, microParticles GmbH, Germany) were washed with three centrifugation/redispersion cycles (1000 g, 30 s) with 20 mM NaOAc buffer pH 4. Assembly of polymer multilayers was achieved by alternately incubating the particles with PVP-*co*-pTEGMA (**8**g, 0.1 mg.mL^{-1}, 15 min), graphene oxide (GO, 0.1 mg.mL^{-1}, 15 min) and tannic acid (TA, mg.mL^{-1}, 15 min) in NaOAc buffer with constant shaking. The particles were washed with three centrifugation/redispersion cycles (1000 g, 30 s) with NaOAc buffer between layers and the

process was cycled five times. The dissolution of the sacrificial silica templates was performed by Dr Rona Chandrawati. Hollow capsules were obtained by dissolving the SiO_2 cores using a 2 M hydrofluoric acid (HF)/8 M ammonium fluoride (NH_4F) solution for 2 min, followed by multiple centrifugation/washing cycles (4500 g, 3 min). *Caution! HF and NH_4F are highly toxic. Extreme care should be taken when handling HF and NH_4F solutions and only small quantities should be prepared.*

Characterization by Raman spectroscopy

Raman analysis was performed with the help of Dr Mads Bergholt. Capsules were diluted five times, and dried on a MgF_2 slide. Images were acquired with a 41 mV, 532 nm laser with 0.5 s integration time.

5.3 Results and discussion

5.3.1 Polymer synthesis

Finely tuning the molecular weight and architecture of polymers enables precise control over the polymers' properties. This can be achieved thanks to recent advances in polymerisation techniques, most notably with the development of reversible deactivation radical polymerisation (RDRP) methods such as Nitroxide Mediated Polymerisation (NMP),[6,7] Atom Transfer Radical Polymerisation (ATRP),[8–11] and Reversible Addition-Fragmentation chain Transfer (RAFT).[12–14] In RDRP the majority of polymer chains are maintained in dormant form via the presence of reagents that are capable or reversibly deactivating the propagating radicals.

While the synthesis of PVP via ATRP has only rarely been reported,[15] several groups successfully synthesised PVP via RAFT.[16,17] RAFT is a versatile polymerisation technique, discovered in 1998 at CSIRO.[12,18,19] It allows the controlled polymerisation of a broad range of monomers over a variety of experimental conditions, including water-soluble materials, and is tolerant of unprotected functionality in monomer and solvent.[12,18,19] Control over the radical polymerisation in RAFT is obtained via a degenerative chain transfer process, facilitated by a thiocarbonylthio chain transfer (CTA) or RAFT agent (RSC(Z)=S). The mechanism for RAFT polymerisation is illustrated on Scheme 1. The initiation and termination steps occur as in conventional radical polymerisation, and the rapid equilibrium between the growing polymer chains $P_n^{\bullet}$ and $P_m^{\bullet}$ and the dormant polymeric thiocarbonylthio compounds provide an equal opportunity for all chains to grow, yielding polymers with narrow polydispersity.

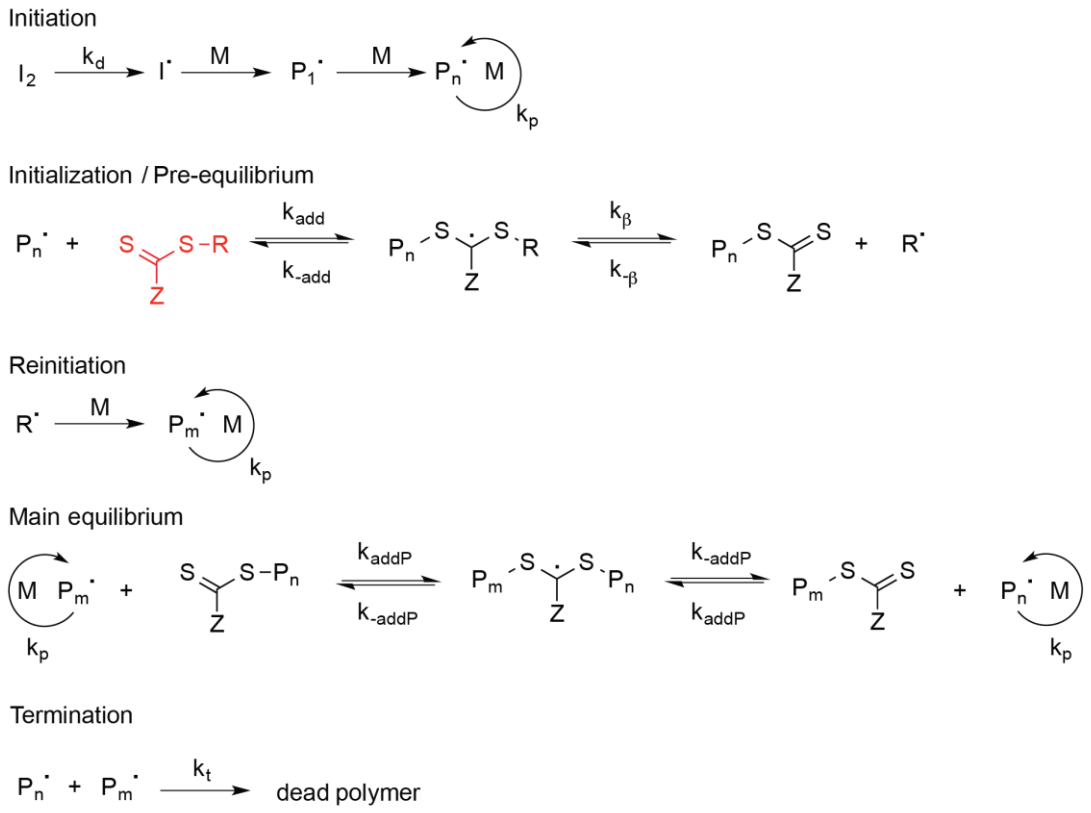

Scheme 1. Mechanism of RAFT polymerisation. Adapted from Moad *et al.*[18]

The simplest and most used method to obtain block copolymers using RAFT polymerisation is to introduce each monomer sequentially: the first monomer is polymerised, and after purification this block is extended by adding a second monomer, the first polymer acting as a macro-RAFT agent for the second polymerisation step.[20]

However, to synthesize the block copolymer PVP-*co*-pTEGMA, a more sophisticated approach is required, as the monomers possess divergent reactivities. In RAFT polymerisation, the choice of the CTA is based on the monomers and is crucial for obtaining a suitable equilibrium between dormant and active species and robust control over the molecular weight of the polymer (Figure 1a). The monomer *N*-vinylpyrrolidone (NVP) has a low activity: it is non-conjugated and its radicals are poorly stable. Therefore, the Z group of the CTA must also be poorly stabilising in order to enable fast fragmentation of the polymer growing chains. This is typically done using a xanthate or dithiocarbamate CTA due to their reduced reactivity, allowing both radical addition and fragmentation.[14,21,22] TEGMA is a more activated monomer, which reacts more readily with radicals than less activated monomers, and the radicals created from the propagating chains are well stabilized by resonance stabilization effect of the radical centre through the close proximity of the carbonyl group. The polymerisation of methyl methacrylate is generally well controlled

using CTA such as dithioester or S-alkyl trithiocarbonates, as these functional groups provide a high rate of radical addition and fragmentation with respect to propagation. In summary, the preparation of block copolymers with PVP is challenging since all available RAFT agents for controlling its polymerisation are not suitable for the polymerisation of more active conjugated monomers such as styrene, acrylate and methacrylate (Figure 1b).[12,18]

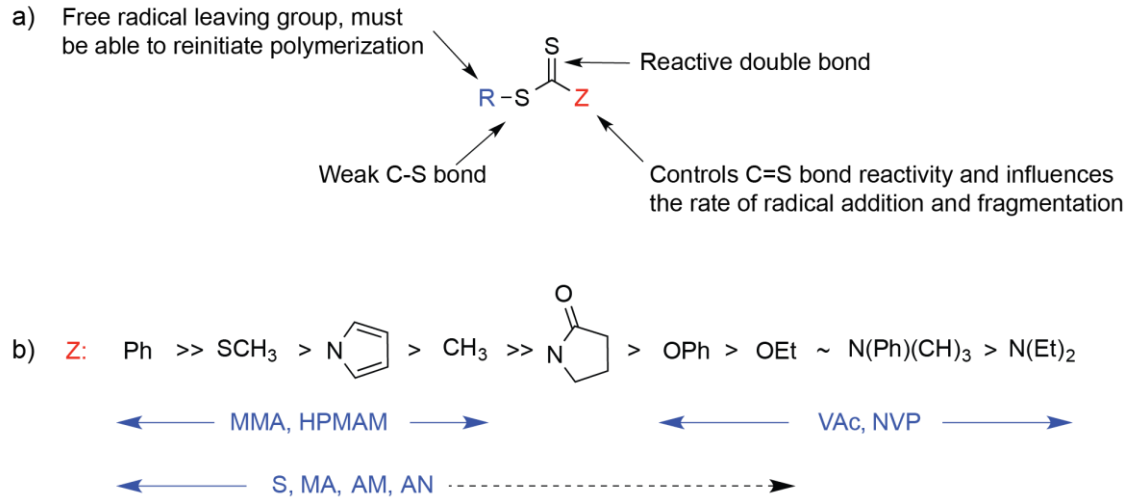

Figure 1. a) Structure of a suitable RAFT agent. b) Guidelines for the choice of Z group for the polymerisation of various monomers (MMA = methyl methacrylate, HPMAM = N-(2-hydroxypropyl)methacrylamide, S = styrene, MA = methacrylate, AM = acrylamide, AN = acrylonitrile, VAc = vinyl acetate, NVP = N-vinylpyrrolidone). Dashed line indicates partial control over polymerisation. Adapted from Moad *et al.*[18]

Several strategies exist to prepare block copolymers of monomers with divergent activity.[20] The first approach is to use click chemistry to link together two independently-prepared homopolymers.[23] However, the synthetic complexity involved makes this process unattractive for high molecular weight copolymers where complete reaction conversions are difficult to achieve. An alternative approach is to use 'switchable', stimuli-responsive dithiocarbamate RAFT agents, where protonation/deprotonation of the amide results in modulation of the strength of the Z-C=S bond, and in turn of its reactivity towards different monomers. This enables the synthesis of block copolymers with monomers of disparate reactivities by introduction of a Lewis acid between the two polymerisations.[24,25] However, this technique has yet to be applied to the preparation of a wide range of copolymers. A third strategy involves the independent use of two different polymerisation mechanisms for each block extension.[26] This approach has been exploited to prepare PVP-*co*-poly(ε-caprolactone) block copolymers using either RAFT,[27] or ATRP,[28] to polymerise the NVP and ring opening polymerisation for the caprolactone. Matyjaszewski and coworkers recently used a dual RAFT / ATRP chloroxanthate CTA to prepare

block copolymers of NVP with styrene (St), methyl acrylate (MA), and methyl methacrylate (MMA).[29] In this example the CTA was able to control the NVP polymerisation by RAFT, and then initiate chain extension with the more active monomer by ATRP, enabling the versatility of free radical polymerisation to be exploited in both blocks.[29]

Here, a similar approach was used to explore the synthesis of a range of PVP-*co*-pTEGMA block copolymers: these polymers were prepared through a control agent able to act as both a chain transfer agent in RAFT polymerisation and as an initiator for ATRP reactions. It was decided to use RAFT to control NVP polymerisation following promising findings in literature studies.[16,17] Since NVP is the less active monomer, this reaction was performed before chain extension of the polymer from the ATRP initiator with TEGMA. The CTA (Figure 2, compound **4**) was therefore designed to have a Z group suitable for NVP, following previous work by Matyjaszewski and coworkers.[30] Unlike in their study, two methyl substituents rather than one substituent were included on the R group of the RAFT agent in an attempt to reduce the inhibition period at the start of the RAFT polymerisation. Since bromoxanthate CTAs have been shown to lead to almost quantitative dimerisation of NVP in RAFT polymerisations,[29] a chloroxanthate CTA was used for initiation of the ATRP reaction. No such dimerisations have been observed with chloroxanthate agents.[29] Additionally, xanthate CTA has been shown to have a very low efficiency as a radical transfer agent for methyl methacrylates,[29] ensuring the regioselectivity of the ATRP of TEGMA without interference of the RAFT moiety in the CTA.

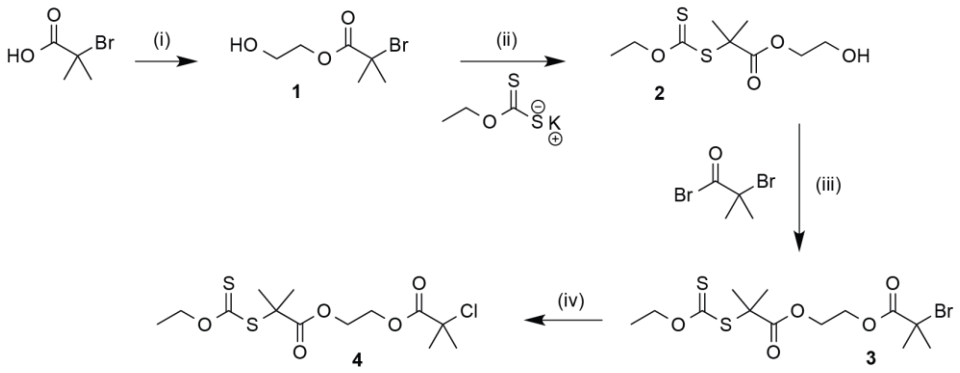

Figure 2. Synthesis of chloroxanthate chain transfer agent (CTA) (compound 4). (i) Ethylene glycol/pyridine/THF, (ii) acetone, (iii) triethylamine/THF, (iv) CuCl/$CuCl_2$/2,2'-bipyridine/acetone. Adapted from Jumeaux *et al*,[31] with permission from the Royal Society of Chemistry.

A schematic of RAFT polymerisation of NVP, using a M:CTA:I ratio of 200:1:0.1 is shown in Figure 3a. Robust control was observed even at a high monomer concentration of 5 M as seen by the pseudo-first order kinetics (Figure 3b), a linear increase of molecular weight *versus*

monomer conversion, and narrow molecular weight distribution (M_w/M_n < 1.3, Figure 3c-d). No significant inhibition period was observed as had been reported in previous work with a similar RAFT agent,[30] presumably due to the additional methyl substituent on the R group that was used. Table 1 summarises the properties of PVP homopolymers synthesized.

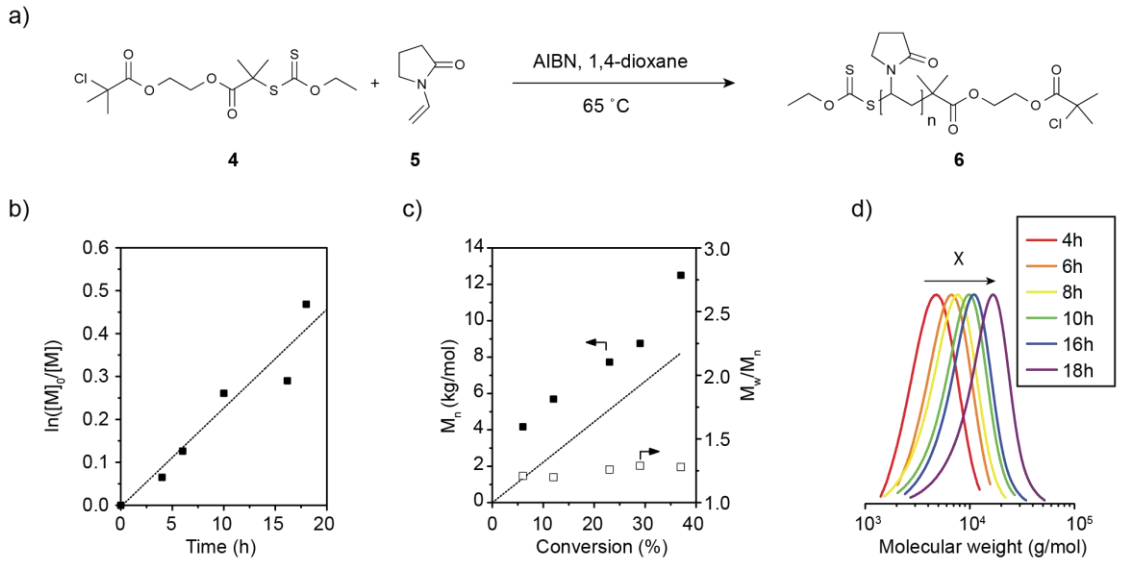

Figure 3. Synthesis of PVP by RAFT (compound 6). a) Synthetic scheme. b) Kinetic plot of monomer conversion versus time. c) Plots showing the evolution of Mn (filled squares) and dispersity (open squares) versus conversion. d) Evolution of GPC traces during NVP polymerisation. ([CTA] / [I] / [NVP] = 1 / 0.1 / 200; [NVP] = 5 M). Adapted from Jumeaux et al,[31] with permission from the Royal Society of Chemistry.

Table 1. Library of PVP polymers synthesized. Adapted from Jumeaux *et al*,[31] with permission from the Royal Society of Chemistry.

#	[NVP]:[CTA]	Time (h)	X (%)	M_n (Da) (NMR)	M_n (Da) (GPC)	M_w/M_n
6a	160	17	27	4800	6220	1.22
6b	300	17	27	9000	17130	1.25
6c	400	17	31	13780	16490	1.26
6d	500	17	27	15000	18220	1.27
6e	750	17	22	18340	22530	1.34
6f	300	17	70	23000	-	-

The second monomer, TEGMA, was synthesized following a procedure adapted from the literature.[32]

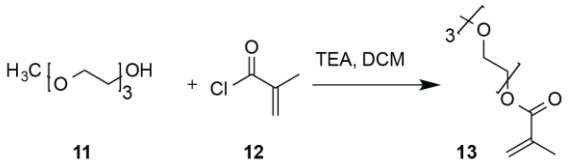

Figure 4. Synthesis of TEGMA. Adapted from Jumeaux *et al*,[31] with permission from the Royal Society of Chemistry.

The chain extension of PVP macroinitiators was first attempted via ATRP. The general transition metal-catalysed ATRP mechanism is illustrated on Scheme 2. The process is initiated by the reaction of a transition metal-ligand complex (usually copper) with an alkyl halide to produce a radical R• and a metal halide complex in which the metal is oxidised to a higher oxidation state.[13] R• reacts with the monomer to form polymeric propagating radicals, which are reversibly transformed in dormant species (P-X) by transfer of the halogen from the metal complex. Irreversible radical termination processes by coupling or disproportionation always occur in ATRP reactions.[33]

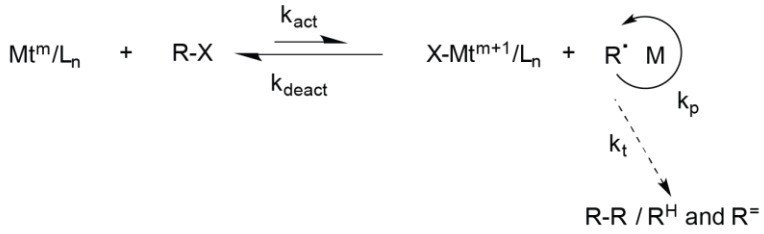

Scheme 2. ATRP mechanism. Adapted from Matyjaszewski.[13]

The library of copolymers synthesized via ATRP extension of PVP macroinitiatior is presented in Table 2.

Table 2. Library of PVP-*co*-pTEGMA polymers synthesized via ATRP. *Polymerisation was carried at 60 °C.

#	PVP M_w kDa	[TEGMA]:[CTA]	Time (h)	X (%)	M_n (Da) (NMR)	M_n (Da) (GPC)	M_w/M_n
8a	23.0	500	17	45	52000	66000	1.86
8b*	23.0	500	17	60	70000	-	-
8c	18.3	800	1	9	16700	51000	1.35
8d	18.3	800	2.5	12	22000	53000	1.44
8e	18.3	800	3	13	24000	54000	1.38

In ATRP, each termination step leads to the irreversible conversion of the catalyst Cu^I to Cu^{II},[10] therefore the initial concentration of Cu^I needs to be relatively large (0.1-1 mol % relative to monomer). At the end of the polymerisation there is a large amount of toxic residual metal. In order to solve this problem, several methods have been developed, notably Activator ReGenerated by Electron Transfer (ARGET)-ATRP (Scheme 3), which employs a reducing agent to regenerate Cu^I from Cu^{II}, allowing carrying the reaction using lower concentrations of catalyst. In addition, Cu^{II} is more oxygen stable than Cu^I, therefore by using ARGET-ATRP rather than standard ATRP, which has been used in the only other example of a PVP chain extension,[29] the demand for copper and intolerance to oxygen is reduced, leading to easier purification of the product and simpler experimental setup.

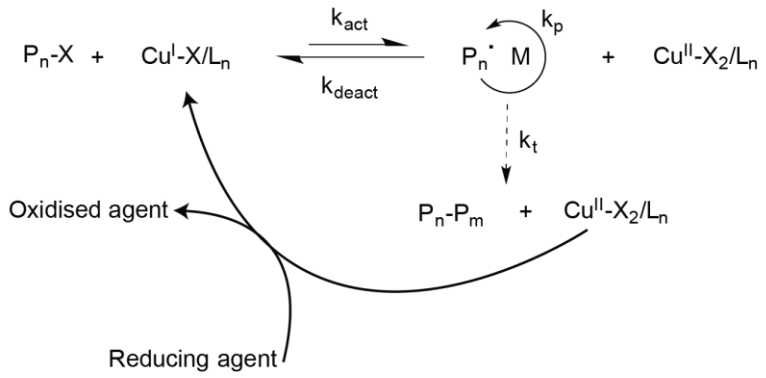

Scheme 3. ARGET-ATRP mechanism. Adapted from Matyjaszewski.[13]

Two homopolymers, PVP 9 kDa and 15 kDa (**6**b and **6**d, respectively), were chosen as macroinitiators for the subsequent block extension with TEGMA via ARGET-ATRP, as their polydispersities were below 1.3 and it was interesting to see if the difference in molecular weight of the PVP block would lead to variation in the properties of the block copolymers.

The chain extension of the two different PVP macroinitiators (9 kDa and 15 kDa) was performed using ARGET-ATRP (Figure 5a). The polymerisations were carried with the help of Dr Rob Chapman. The reaction demonstrated linear pseudo-first order kinetics (Figure 5b), and a linear evolution of molecular weight *versus* conversion (Figure 5c). The molecular weight distribution stayed in a relatively narrow range ($M_w/M_n \leq 1.5$) with only a small amount of tailing (Figure 3c-d), which demonstrated the successful synthesis of well-defined PVP-*co*-pTEGMA block copolymers. The library of copolymers synthesised is reported in Table 3.

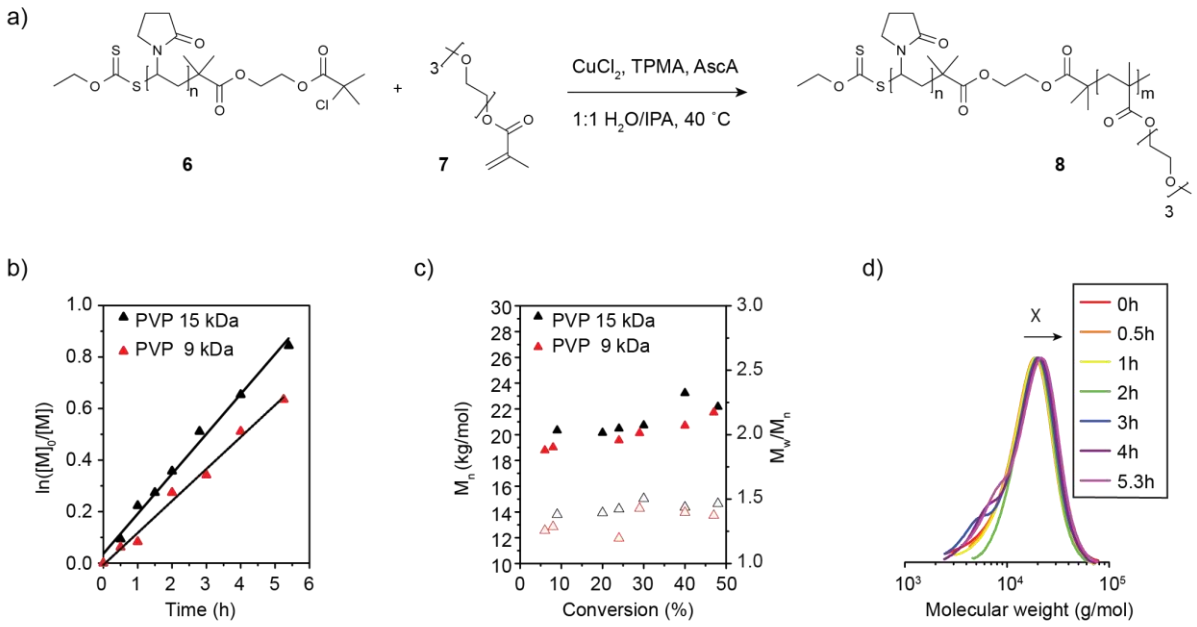

Figure 5. Synthesis of PVP-*co*-pTEGMA block copolymers via chain extension of PVP macroinitiators with TEGMA by ARGET-ATRP (compound **8**). a) Synthetic scheme. b) Kinetic plots of monomer conversion *versus* time. c) Plots showing the evolution of M_n (filled symbols) and dispersity (open symbols) *versus* conversion. d) Evolution of GPC traces during TEGMA polymerisation. ([TEGMA] / [CTA] = 40 / 1; [TEGMA] = 0.5 M). Adapted from Jumeaux *et al*,[31] with permission from the Royal Society of Chemistry. Reactions were performed with the assistance of Dr Rob Chapman.

Table 3. Library of PVP-*co*-pTEGMA block copolymers synthesized via ARGET-ATRP. Adapted from Jumeaux *et al*,[31] with permission from the Royal Society of Chemistry.

#	PVP M_w (kDa)	[TEGMA] /[CTA]	Time (h)	X (%)	M_n (Da) (NMR)	M_n (Da) (GPC)	M_w/M_n	wt % TEGMA	T_{cp} (°C)	Z-average (nm) (PDI) Pre-XL @ 65 °C	Z-average (nm) (PDI) Post-XL @ 25 °C
8f	9.0	40	5	47	5030	14420	1.38	33%	61	217 (0.17)	274 (0.10)
8g	9.0	75	17	37	6270	16630	1.54	42%	54	212 (0.13)	136 (0.07)
8h	15.0	40	5.4	57	4180	17660	1.41	26%	60	221 (0.18)	225 (0.10)
8i	15.0	75	17	47	11610	18590	1.62	35%	57	185 (0.10)	110 (0.09)
8j	15.0	40	17	99	-	26780	1.50	38%	58	277 (0.10)	175 (0.10)

5.3.2 Self-assembly and cross-linking

Following the successful synthesis of PVP-*co*-pTEGMA, the thermoresponsive behaviour of these block copolymers was investigated. Both pTEGMA and PVP homopolymers are known to display thermoresponsive behaviour.[34,35] The LCST for PVP can be observed above the boiling temperature of water,[35] while the LCST for pTEGMA is around 52 °C.[34] It was hypothesised that while PVP-*co*-pTEGMA copolymers should be soluble in water at room temperature, at the LCST of pTEGMA the polymer will undergo a drastic conformational and solubility change (known as the coil-globule transition) driven by the sensitive dehydration behaviour and leading to a collapse of the polymer chains caused by the increased favourability of hydrophobic interactions between polymer chains relative to polymer-water interactions.[34] To confirm this, the cloud point temperature (T_{cp}) of PVP-*co*-pTEGMA copolymers using Dynamic Light Scattering (DLS) was determined. Figure 6a shows the evolution of count-rate at 1 °C resolution as the temperature in the instrument was ramped. Each measurement was made at a fixed position and with a fixed attenuator, so the count-rate is proportional to the total intensity of scattered light, and therefore the assembly of the copolymers. T_{cp} was determined by the inflection points of the curves and it was found that the T_{cp} of the copolymers varied between 54 °C and 61 °C (Figure 6a, Table 3), in accordance with the LCST for pTEGMA previously reported.[34] Studies have reported the very small influence of the DP_n of poly(oligo[ethylene glycol] methacrylates) on the value of their LCST,[36,37] which is in agreement with this study.

Contrary to pTEGMA homopolymers, these copolymer solutions did not evolve into cloudy, opaque solutions when the temperature reached the T_{cp} of pTEGMA, indicating that copolymers were self-assembling instead of forming precipitates. To confirm this phenomenon, the size distribution of the copolymer assemblies was studied (PVP-*co*-pTEGMA copolymers **8**f-**8**j in Table 3) at 65 °C, above the T_{cp}, by DLS (Figure 6b). The size of the resulting structures varied between 180 nm and 280 nm in diameter (Figure 6b, Table 3). When these structures were subjected to temperature below their T_{cp}, significant changes in size distributions to below 10 nm for all of the copolymer assemblies were observed (Figure 6b), indicating the disassembly of the structures.

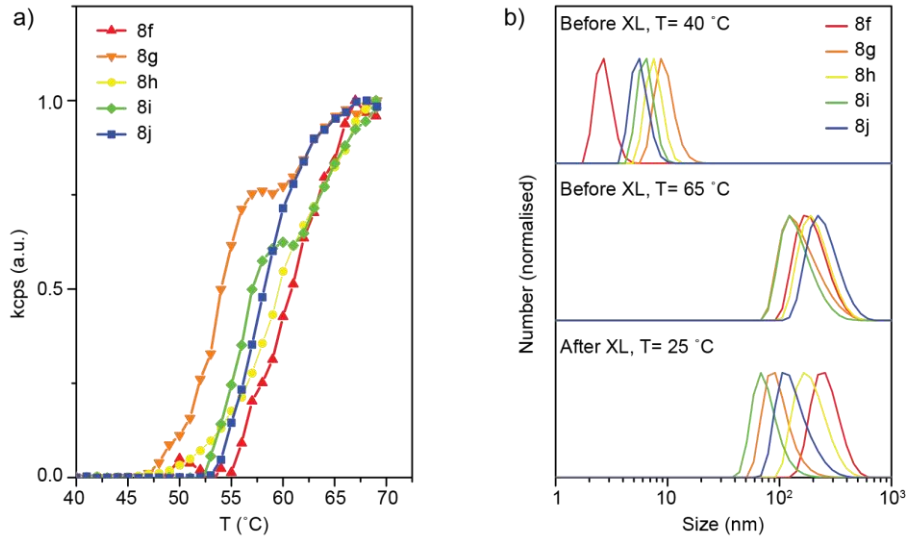

Figure 6. Temperature-triggered self-assembly of PVP-*co*-pTEGMA block copolymers. a) Evolution of count-rate *versus* temperature measured by DLS. The cloud point temperature (T_{cp}) of each copolymer was determined by the inflection points of the curves. b) Normalised size distribution as determined by DLS of PVP-*co*-pTEGMA (2 mg.mL^{-1} copolymer solution in 20 mM NaOAc pH 4) below the T_{cp} at 40 °C, and self-assembled PVP-*co*-pTEGMA before and after cross-linking (XL) with potassium persulphate, at 65 °C and 25 °C, respectively, confirming the structural integrity of the cross-linked structures below the T_{cp}. Adapted from Jumeaux *et al*,[31] with permission from the Royal Society of Chemistry.

To obtain self-assembled structures that can retain their integrity at physiological conditions, the copolymers need to be cross-linked. PVP is a versatile polymer with ease of cross-linking by gamma rays, strong alkaline, peroxides, and inorganic persulphates.[38] This was exploited to covalently cross-link the self-assembled PVP-co-pTEGMA structures using potassium persulphate.[38] The mechanism of cross-linking of PVP with potassium persulphate is believed to proceed via self-condensation of the PVP, following abstraction of an hydrogen atom on the polymer backbone.[38] The size of the self-assembled PVP-co-pTEGMA structures after cross-linking with potassium persulphate are shown in Figure 6b and Table 3, confirming the successful cross-linking and the stability of the structures below the Tcp. Dialysis against water did not affect the size of the aggregates (Figure 7), confirming the stability of the cross-linking mechanism in solutions of various ionic strengths.

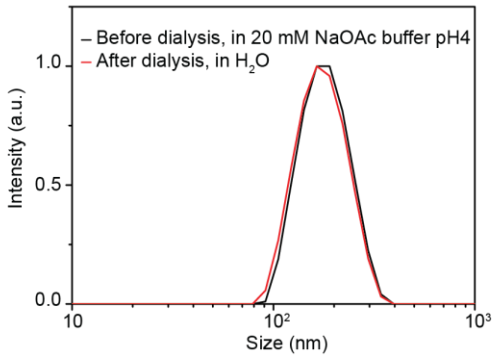

Figure 7. Stability of cross-linked self-assembled PVP-*co*-pTEGMA structures in buffer and in water. Size distribution by intensity of self-assembled PVP-*co*-pTEGMA **8**h (0.5 mg.mL^{-1} copolymer solution) at 25 °C after cross-linking with potassium persulphate in 20 mM NaOAc pH 4 (black line), followed by dialysis of the cross-linked assemblies for 24 h in H_2O (red line), as determined by DLS, confirming the stability of the cross-linked structures upon removal of the salt. Adapted from Jumeaux *et al*,[31] with permission from the Royal Society of Chemistry.

To further confirm the morphology of the self-assembled PVP-*co*-pTEGMA structures, Transmission Electron Microscopy (TEM) was used to image the dialysed cross-linked PVP-co-pTEGMA polymers (Figure 8). Relatively monodisperse spherical aggregates were observed, with sizes that corresponded well to the DLS measurements (Figure 6b, Table 3) and which are consistent with other polymersomes in the literature.[39] This temperature triggered self-assembly of PVP-co-pTEGMA into precise architectures at the nanoscale is particularly interesting for applications in drug delivery and the design of smart, stimuli-responsive materials.

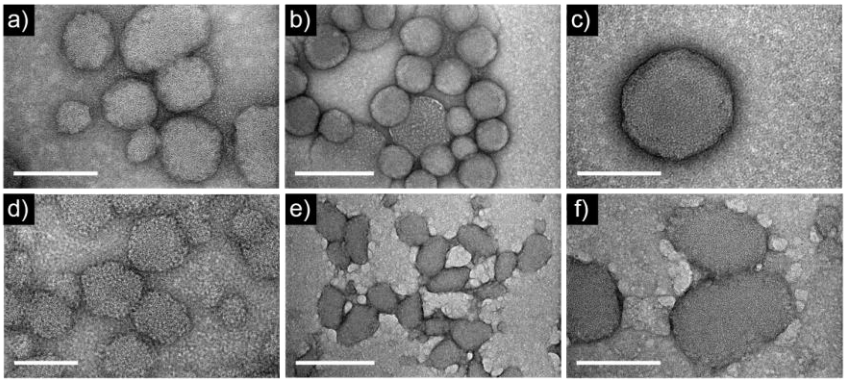

Figure 8. TEM images illustrating the structures of self-assembled PVP-*co*-pTEGMA *post* cross-linking with potassium persulphate. a) **8**g (scale bar 200 nm), b) **8**h (scale bar 500 nm), c) **8**h at higher magnification (scale bar 200 nm), d) **8**i (scale bar 100 nm), e) **8**j (scale bar 500 nm), f) **8**j at higher magnification (scale bar 200 nm). Adapted from Jumeaux *et al*,[31] with permission from the Royal Society of Chemistry.

5.3.3 PVP-*co*-pTEGMA block copolymers applied to the design of new materials

After having synthesized and characterized a library of PVP-*co*-pTEGMA block copolymers, their applications for the design of stimuli-responsive materials were investigated. PVP-*co*-pTEGMA was used as a dual-function building block in the layer-by-layer (LbL) assembly of polymer films: the PVP block serves as an anchoring segment allowing the build-up of the multilayer film through hydrogen bonding interactions, and the thermoresponsive properties of the assembly are derived from the pTEGMA block. Building up from the results obtained in Chapter 4, in a first example PVP-*co*-pTEGMA was used to functionalize QR surface in order to implement a smart, thermoresponsive drug delivery carrier for the triggered release of doxorubicin, a model anti-cancer drug. In a second example, PVP-*co*-pTEGMA served as the building block for the assembly of hybrid capsules with graphene oxide.

5.3.3.1 Layer-by-layer assembly of PVP-*co*-pTEGMA / tannic acid

The layer-by-layer assembly of PVP-*co*-pTEGMA was first optimized on planar substrates by performing QCM-D measurements. In order to have a stable multilayer film at physiological pH, tannic acid (TA) was chosen as the hydrogen bond donor as it remains protonated at physiological pH value (pKa = 8.5) (see Chapter 4, section 4.3.2.3).[40]

Successive layers of PVP-*co*-pTEGMA (**8**j) and TA were deposited on a silicon QCM chip (Figure 9). Initially, polymer stock solutions at a concentration of 2 $mg.mL^{-1}$ were injected in the QCM chamber, but these conditions did not allow the build-up of a stable multilayer film (Figure 9a): an initial deposition of polymer mass was observed, which was followed by the peeling off of PVP-*co*-pTEGMA from the QCM chip after each addition of the polymer (black arrows). A study of PVP/TA polymer layers assembly showed that the film formation was concentration-dependant: at high concentrations, TA aggregated and was solubilized by the subsequent addition of PVP.[41] The QCM-D study of PVP-*co*-pTEGMA/TA layers deposition was repeated using a lower polymer concentration of 0.1 $mg.mL^{-1}$ (Figure 9b): diluting the polymer solutions prevented their aggregation and allowed the successful build-up of the multilayer film as shown by the continuous decrease in frequency observed after each polymer addition.

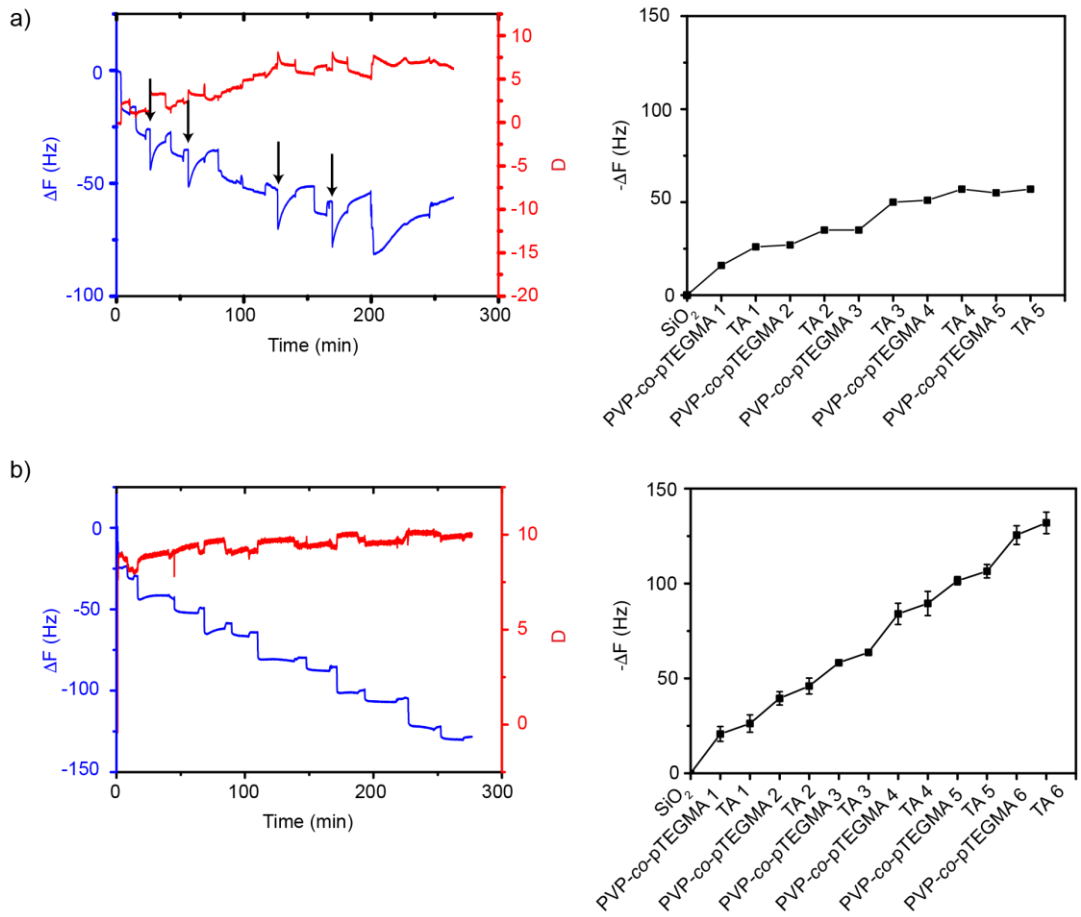

Figure 9. QCM frequency changes upon alternating addition of PVP-*co*-pTEGMA and TA layers on planar surfaces and plot of the frequency changes for each successive layer for a) 2 mg.mL^{-1} polymer solutions, and b) 0.1 mg.mL^{-1} polymer solutions. Measurements were done using the third overtone.

After having optimized the layering conditions on planar substrates, these were translated to colloidal substrates. PVP-*co*-pTEGMA was labelled with Alexa Fluor® 488 and successive layers of this block copolymer and TA were deposited on silica microparticles (2.79 µm, microParticles GmbH, Germany). For this study, the block copolymer used was **8**a as this polymer has a low T_{cp} (45 °C). After each bilayer deposition, aliquots of the particle suspension were taken and the change in fluorescence of the particles was monitored by flow cytometry (flow cytometry data was collected by Dr Rona Chandrawati). The increase in fluorescence intensity after each bilayer deposition demonstrated the successful deposition of up to five bilayers of PVP-*co*-pTEGMA/TA on colloidal silica particles (Figure 10).

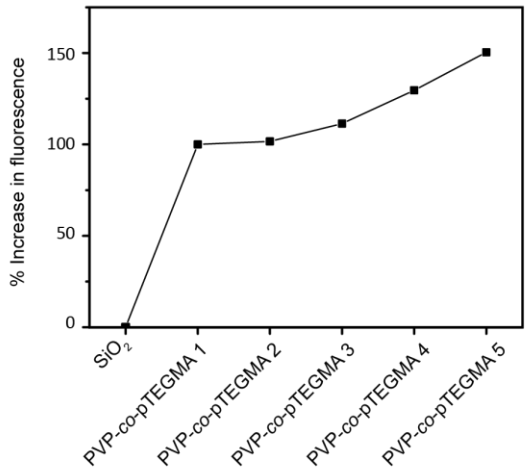

Figure 10. LbL construct of PVP-*co*-pTEGMA/TA on colloidal silica particles. PVP-*co*-pTEGMA was labelled with Alexa Fluor® 488 and the variations in fluorescence were measured by flow cytometry. An increase of fluorescence was observed after each bilayer deposition, demonstrating the successful build-up of up to 5 bilayers of PVP-*co*-pTEGMA/TA.

5.3.3.2 Temperature-triggered release of doxorubicin

Doxorubicin was encapsulated in QR, which was functionalized with 1 or 2 bilayers of PVP-*co*-pTEGMA/TA using the layer-by-layer technique described in the section above. The block copolymer PVP-*co*-pTEGMA used in this study was **8**b, as it has a T_{cp} of 45 °C and QR have been shown to generate a hyperthermia of up to 50 °C in an *in vivo* experiment.[42] The release of doxorubicin was initiated by transferring the particles to 1× PBS buffer, and the experiment was conducted at room temperature and 50 °C. The release of doxorubicin was monitored by measuring the fluorescence of aliquots of the supernatant at regular time intervals and the quantity of doxorubicin was derived from a calibration curve (Figure 11).

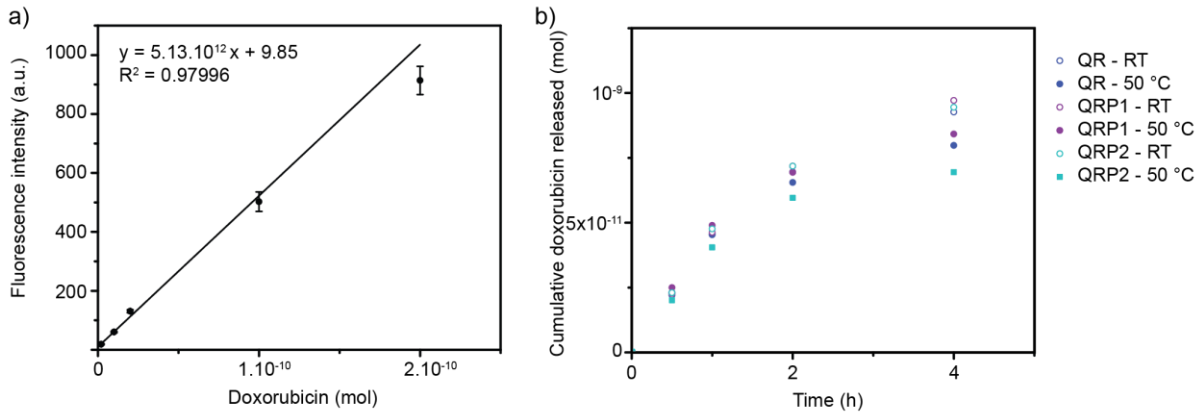

Figure 11. a) Calibration curve for doxorubicin obtained in PBS. λ_{ex} = 470 nm, λ_{em} = 590 nm. b) Release of doxorubicin from QR functionalized with 0, 1 or 2 PVP-*co*-pTEGMA/TA bilayers at room temperature or 50 °C.

The release profiles of doxorubicin from QR show very little difference between all conditions and functionalization. Assuming quantitative loading of doxorubicin into QR, it can be extrapolated that only 0.42 % of doxorubicin had been released after 4 hours, in the case of the highest release profile. Several factors could explain the slow release of doxorubicin from QR. The state of doxorubicin (free, self-associated, complexed, or precipitated) varies depending on its environment. In order to achieve high encapsulation efficiencies, active loading of doxorubicin into liposomes is achieved using pH-, manganese-, sulphate-, citrate- or phosphate-gradients.[43] The underlying principle relies on the diffusion of free doxorubicin inside the liposomes, where a change in the milieu composition triggers a modification in the drug structure, preventing doxorubicin from re-traversing the lipid bilayer. It has been shown that doxorubicin can precipitate in the presence of ions, notably phosphate ions, although at higher concentration than the one used in this study.[43] The solubility of doxorubicin also decreases with increasing pH value.[43] Additionally, doxorubicin can self-associate via π-π stacking, which could influence its transport in QR pores.[44] Essentially, all these phenomena could potentially occur when doxorubicin is confined into QR pores and the media is changed to PBS, entrapping doxorubicin inside QR. In addition, it has been demonstrated that doxorubicin has a high affinity for gold surfaces;[45,46] therefore doxorubicin can be adsorbed on the gold particles (AuNC and AuNP) present in QR, preventing its release from QR.

In summary, doxorubicin, despite being a convenient model anticancer drug for studying drug release from QR due to its photonic properties, may not be the most appropriate drug for the study of temperature-triggered release from QR, as it is too well retained inside QR. Current efforts are focused towards selecting a more suitable drug candidate, which fulfils the following requirements: the drug can be loaded in QR but does not stay entrapped, with easy to maintain

sink conditions, the drug release can be quantified using methods available in the lab (UV-vis, fluorescence, HPLC, ICP-AES) and the drug needs to work in synergy with photothermal therapy.[47] Preliminary results suggest mitomycin C is a promising candidate.

5.3.3.3 Formation of PVP-*co*-pTEGMA/TA capsules

Multilayers of interacting polymer pairs can also be assembled on sacrificial particles templates to form hollow capsules, which can encapsulate a range of molecule sizes.[48–50] The release of cargo can be finely tuned by controlling the porosity and thickness of the polymer layers.

In order to take advantage of the thermoresponsive properties of PVP-*co*-pTEGMA and with the aim of building holistic stimuli-responsive capsules, a photothermal agent was incorporated in the capsules. Near-infrared (NIR) light is best suited for biomedical applications as light at these wavelengths is less absorbed by tissues, with negligible damage.[51] Therefore, suitable photothermal agents should convert NIR light to heat. Such materials include gold nanostructures, carbon nanotubes, and graphene.[52] Graphene oxide (GO), an oxidised form of graphene, has recently emerged as a promising novel carbon-based material, owing to its absorption and photothermal conversion properties, water-solubility and lower cost compared to metal-based nanoparticles.[53,54] Reduced graphene oxide (rGO) is prepared by reduction of GO using chemical, thermal or electrical treatments.[55] Owing to their high absorbance in the NIR, the use of GO and rGO has been explored for photothermal therapy.[56–58]

The photothermal properties of several materials were evaluated. Suspensions of graphene oxide (GO, 0.1 $mg.mL^{-1}$), reduced graphene oxide (rGO, 0.1 $mg.mL^{-1}$) and gold nanoclusters (AuNC, 0.1 mM) in Milli-Q H_2O were irradiated with a NIR laser (785 nm, 146 mW) and the evolution of the temperature profiles was measured using a needle-like temperature probe (Figure 12). The highest increase in temperature was observed for rGO (green curve), followed by GO (blue curve), which was expected as the absorbance of rGO in the NIR is higher than the one of GO.[59] At the concentration used in this study, AuNC (red curve) did not cause a significant increase of temperature compared to the control (water only, black curve).

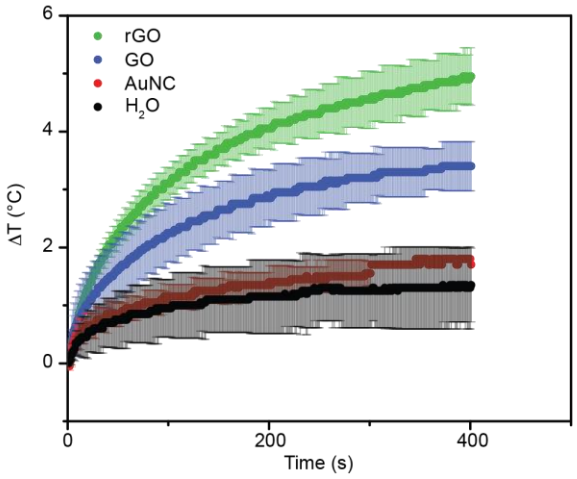

Figure 12. Evolution of the temperature profiles of solutions in Milli-QH_2O of reduced graphene oxide (rGO, green curve), graphene oxide (GO, blue curve), gold nanoclusters (AuNC, red curve), compared with water only (black curve), when irradiated with a 785 nm, 146 mW laser (n=2).

GO was selected as the photothermal agent to be included in the LbL capsules, as its water solubility is higher than rGO, which aggregates in the buffer solution used for LbL assembly. The multilayer capsules were assembled by sequential deposition of PVP-*co*-pTEGMA (compound **8**g) and TA on colloidal silica (2.79 um, microParticle GmbH). GO interacts with PVP via hydrogen-bonding,[60,61] therefore it was introduced after each deposition of PVP-*co*-pTEGMA. Hollow capsules were obtained by dissolving the SiO_2 cores using a buffered HF treatment (capsule dissolution was performed by Dr Rona Chandrawati). *Caution! HF is highly toxic. Extreme care should be taken when handling HF solutions and only small quantities should be prepared.*

The presence and morphology of the capsules was observed using phase contrast microscopy and TEM imaging (Figure 13).

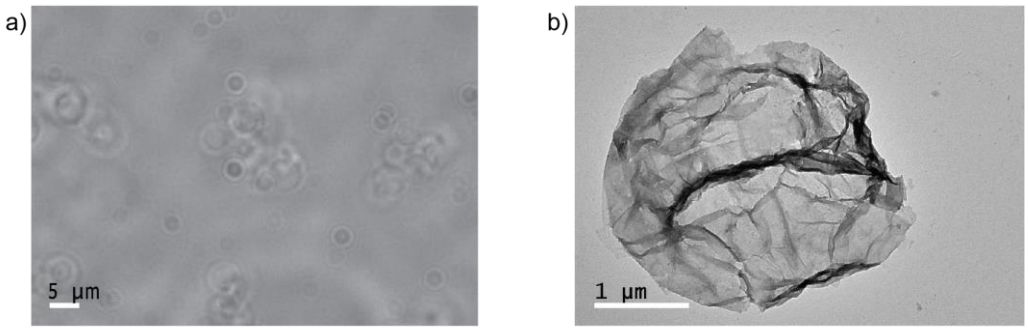

Figure 13. PVP-*co*-pTEGMA/GO/TA capsules imaged by a) phase contrast imaging and b) TEM imaging (stained with 1 w/w % uranyl acetate).

The presence of GO in the capsules was verified using Raman spectroscopy (data collection was performed with Dr Mads Bergholt). This spectroscopy technique probes the fundamental vibration modes of the molecules within a sample, each molecule can be identified by its unique fingerprint. The Raman spectrum of GO has two characteristics bands, G (1350 cm^{-1}) and D (1600 cm^{-1}).[54] The capsules were dried on a MgF_2 slide, and the Raman spectrum of an isolated capsuled showed the characteristic bands for GO at 1340 and 1620 cm^{-1}, confirming that GO is associated with the capsules (Figure 14a). The heat map of a scanned area on the slide showed that GO was only present in the capsules (Figure 14b).

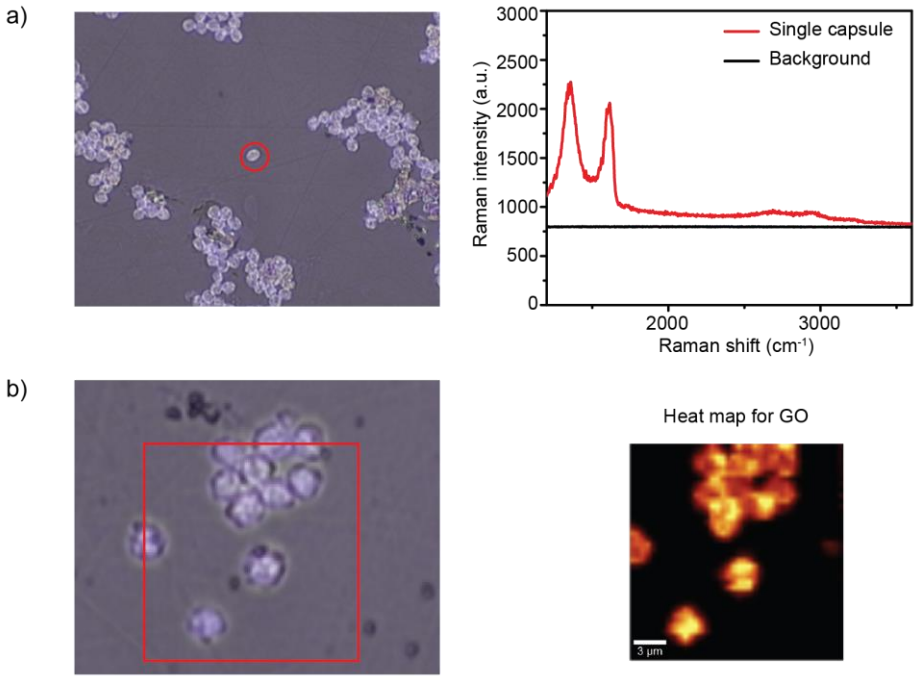

Figure 14. Raman spectroscopy of PVP-*co*-pTEGMA/GO/TA capsules. a) Single Raman spectrum on isolated capsule, showing characteristic bands for GO. b) Heat map of GO. Measurements were performed with the assistance of Dr Mads Bergholt.

In summary, the formation of stable PVP-*co*-pTEGMA hybrid capsules incorporating graphene oxide was demonstrated. In future experiments, the thermoresponsive behaviour of the capsules will be investigated.

5.4 Conclusions

In this Chapter, the successful synthesis of well-defined PVP-*co*-pTEGMA block copolymers was demonstrated. Due to the divergent reactivities of NVP and TEGMA, these monomers cannot be polymerised using the same RAFT agent. To solve this problem, a dual-function chain transfer agent (CTA) was synthesized, able to act as both a CTA in RAFT polymerisation and as an initiator for ATRP reactions. The xanthate CTA was able to control the RAFT polymerisation of NVP, generating polymers with polydispersities inferior to 1.4. The chain extension of PVP macro-CTA with TEGMA was performed either via ATRP or ARGET-ATRP; the latter method advantageously reduces the amount of copper needed for the polymerisation and the intolerance to oxygen. It was showed that PVP-*co*-pTEGMA block copolymers self-assembled above their cloud point temperature (T_{cp}) into large spherical nanostructures, and that these assemblies could be stabilised below their T_{cp} by cross-linking them through the PVP block using potassium persulphate.

Two applications for these new materials were explored. First, PVP-*co*-pTEGMA was used as a dual building block in the layer-by-layer (LbL) assembly of multilayer polymer films on quantum rattle (QR): the PVP block served as a hydrogen bond accepting agent to tannic acid, and the pTEGMA provided thermoresponsive properties. This polymer film is stable at physiological pH and does not require cross-linking, which answers the requirements raised in the conclusion of Chapter 4. The LbL assembly was first explored on planar surfaces using quartz crystal microbalance (QCM), and the optimized layering conditions were transferred to QR. Doxorubicin, a model anticancer drug, was encapsulated and the release profiles of the drug from QR coated with PVP-*co*-pTEGMA/TA bilayers were studied, at room temperature and above the T_{cp} of TEGMA. The polymer coating on QR did not influence the release profile of doxorubicin.

In a second application, PVP-*co*-pTEGMA was used to build hollow hybrid capsules with graphene oxide as a photothermal agent for converting near-infrared light to heat. The formation of stable capsules was demonstrated, and the incorporation of graphene oxide was verified using Raman spectroscopy. These hybrid capsules may find potential applications in drug delivery as well as combination therapy with photothermal therapy.

References

1. S. Lowe, N. M. O'Brien-Simpson, L. A. Connal. *Polym. Chem.*, 2015, **6**, 198–212.
2. A. N. Zelikin, G. K. Such, A. Postma, F. Caruso. *Biomacromolecules*, 2007, **8**, 2950–2953.
3. W. Sun, Z. Araci, M. Inayathullah, S. Manickam, X. Zhang, M. A. Bruce, M. P. Marinkovich, A. T. Lane, C. Milla, J. Rajadas, M. J. Butte. *Acta Biomater.*, 2013, **9**, 7767–7774.
4. R. Chandrawati, S.-F. Chong, A. N. Zelikin, L. Hosta-Rigau, B. Städler, F. Caruso. *Soft Matter*, 2011, **7**, 9638–9646.
5. M. Dierendonck, K. Fierens, R. De Rycke, L. Lybaert, S. Maji, Z. Zhang, Q. Zhang, R. Hoogenboom, B. N. Lambrecht, J. Grooten, J. P. Remon, S. De Koker, B. G. De Geest. *Adv. Funct. Mater.*, 2014, **24**, 4634–4644.
6. C. J. Hawker, A. W. Bosman, E. Harth. *Chem. Rev.*, 2001, **101**, 3661–3688.
7. R. B. Grubbs. *Polym. Rev.*, 2011, **51**, 104–137.
8. K. Matyjaszewski, J. Xia. *Chem. Rev.*, 2001, **101**, 2921–2990.
9. T. Pintauer, K. Matyjaszewski. *Chem. Soc. Rev.*, 2008, **37**, 1087–1097.
10. K. Matyjaszewski, N. V Tsarevsky. *Nat. Chem.*, 2009, **1**, 276–288.
11. M. Ouchi, T. Terashima, M. Sawamoto. *Chem. Rev.*, 2009, **109**, 4963–5050.
12. G. Moad, E. Rizzardo, S. H. Thang. *Aust. J. Chem.*, 2005, **58**, 379–410.
13. K. Matyjaszewski. *Macromolecules*, 2012, **45**, 4015–4039.
14. K. Nakabayashi, H. Mori. *Eur. Polym. J.*, 2013, **49**, 2808–2838.
15. X. Lu, S. Gong, L. Meng, C. Li, S. Yang, L. Zhang. *Polymer*, 2007, **48**, 2835–2842.
16. R. Devasia, R. L. Bindu, R. Borsali, N. Mougin, Y. Gnanou. *Macromol. Symp.*, 2005, **229**, 8–17.
17. D. Wan, K. Satoh, M. Kamigaito, Y. Okamoto. *Macromolecules*, 2005, **38**, 10397–10405.
18. G. Moad, E. Rizzardo, S. H. Thang. *Aust. J. Chem.*, 2006, **59**, 669–692.
19. G. Moad, E. Rizzardo, S. H. Thang. *Aust. J. Chem.*, 2009, **62**, 1402–1472.
20. D. J. Keddie. *Chem. Soc. Rev.*, 2014, **43**, 496–505.
21. A. Postma, T. P. Davis, G. Li, G. Moad, M. S. O'Shea. *Macromolecules*, 2006, **39**, 5307–5318.
22. J. Chiefari, R. T. Mayadunne, C. L. Moad, G. Moad, E. Rizzardo, A. Postma, M. A. Skidmore, S. H. Thang. *Macromolecules*, 2003, **36**, 2273–2283.
23. D. Quémener, T. P. Davis, C. Barner-Kowollik, M. H. Stenzel. *Chem. Commun.*, 2006, 5051–5053.
24. M. Benaglia, J. Chiefari, Y. K. Chong, G. Moad, E. Rizzardo, S. H. Thang. *J. Am. Chem. Soc.*, 2009, **131**, 6914–6915.

25. D. J. Keddie, C. Guerrero-Sanchez, G. Moad, E. Rizzardo, S. H. Thang. *Macromolecules*, 2011, **44**, 6738–6745.

26. K. V. Bernaerts, F. E. Du Prez. *Prog. Polym. Sci.*, 2006, **31**, 671–722.

27. H. U. Kang, Y. C. Yu, S. J. Shin, J. Kim, J. H. Youk. *Macromolecules*, 2013, **46**, 1291–1295.

28. A. Veeren, A. Bhaw-Luximon, D. Jhurry. *Eur. Polym. J.*, 2013, **49**, 3034–3045.

29. C. F. Huang, R. Nicolay, Y. Kwak, F. C. Chang, K. Matyjaszewski. *Macromolecules*, 2009, **42**, 8198–8210.

30. R. Nicolaÿ, Y. Kwak, K. Matyjaszewski. *Chem. Commun.*, 2008, 5336–5338.

31. C. Jumeaux, R. Chapman, R. Chandrawati, M. M. Stevens. *Polym. Chem.*, 2015, **6**, 4116–4122.

32. R. Auvergne, M. H. Morel, P. Menut, O. Giani, S. Guilbert, J. J. Robin. *Biomacromolecules*, 2008, **9**, 664–671.

33. J. M. Muñoz-Molina, T. R. Belderraín, P. J. Pérez. *Macromolecules*, 2010, **43**, 3221–3227.

34. J. F. Lutz. *J. Polym. Sci. Part A Polym. Chem.*, 2008, **46**, 3459–3470.

35. P. Sakellariou. *Polymer*, 1992, **33**, 1339–1342.

36. J.-F. Lutz, O. Akdemir, A. Hoth. *J. Am. Chem. Soc.*, 2006, **128**, 13046–13047.

37. C. Weber, R. Hoogenboom, U. S. Schubert. *Prog. Polym. Sci.*, 2012, **37**, 686–714.

38. C. C. Anderson, F. Rodriguez, D. A. Thurston. *J. Appl. Polym. Sci.*, 1979, **23**, 2453–2462.

39. R. P. Brinkhuis, F. P. J. T. Rutjes, J. C. M. van Hest. *Polym. Chem.*, 2011, **2**, 1449–1462.

40. Y. Cao, W. He. *Acta Biomater.*, 2013, **9**, 4558–4568.

41. C. Sample. Hydrogen-bonded layer-by-layer assembly of poly(vinyl alcohol) and tannic acid, 2014.

42. M. Hembury, C. Chiappini, S. Bertazzo, T. L. Kalber, G. L. Drisko, O. Ogunlade, S. Walker-Samuel, K. S. Krishna, C. Jumeaux, P. Beard, C. S. S. R. Kumar, A. E. Porter, M. F. Lythgoe, C. Boissière, C. Sanchez, M. M. Stevens. *Proc. Natl. Acad. Sci. U. S. A.*, 2015, **112**, 1959–1964.

43. A. Fritze, F. Hens, A. Kimpfler, R. Schubert, R. Peschka-Suss. *Biochim. Biophys. Acta - Biomembr.*, 2006, **1758**, 1633–1640.

44. K. Karatasos. *J. Phys. Chem. B*, 2013, **117**, 2564–2575.

45. D. Curry, A. Cameron, B. MacDonald, C. Nganou, H. Scheller, J. Marsh, S. Beale, M. Lu, Z. Shan, R. Kaliaperumal, H. Xu, M. Servos, C. Bennett, S. MacQuarrie, K. D. Oakes, M. Mkandawire, X. Zhang. *Nanoscale*, 2015, **7**, 19611–19619.

46. J. You, G. Zhang, C. Li. *ACS Nano*, 2010, **4**, 1033–1041.

47. H. H. Kampinga. *Int. J. Hyperth.*, 2006, **22**, 191–196.

48. A. L. Becker, A. P. R. Johnston, F. Caruso. *Small*, 2010, **6**, 1836–1852.

49. A. J. Gormley, R. Chandrawati, A. J. Christofferson, C. Loynachan, C. Jumeaux, A. Artzy-

Schnirman, D. Aili, I. Yarovsky, M. M. Stevens. *Chem. Mater.*, 2015, **27**, 5820–5824.

50. S. F. Chong, R. Chandrawati, B. Städler, J. Park, J. Cho, Y. Wang, Z. Jia, V. Bulmus, T. P. Davis, A. N. Zelikin, F. Caruso. *Small*, 2009, **5**, 2601–2610.

51. A. Vogel, V. Venugopalan. *Chem. Rev.*, 2003, **103**, 577–644.

52. J. T. Robinson, S. M. Tabakman, Y. Liang, H. Wang, H. Sanchez Casalongue, D. Vinh, H. Dai. *J. Am. Chem. Soc.*, 2011, **133**, 6825–6831.

53. K. Yang, L. Feng, X. Shi, Z. Liu. *Chem Soc Rev*, 2013, **42**, 530–547.

54. R. Kurapati, A. M. Raichur. *Chem. Commun.*, 2013, **49**, 734–736.

55. J.-L. Li, X.-L. Hou, H.-C. Bao, L. Sun, B. Tang, J.-F. Wang, X.-G. Wang, M. Gu. *J. Biomed. Mater. Res. A*, 2014, **102**, 2181–2188.

56. K. Yang, S. Zhang, G. Zhang, X. Sun, S. T. Lee, Z. Liu. *Nano Lett.*, 2010, **10**, 3318–3323.

57. J. L. Li, H. C. Bao, X. L. Hou, L. Sun, X. G. Wang, M. Gu. *Angew. Chemie - Int. Ed.*, 2012, **51**, 1830–1834.

58. M. Li, X. Yang, J. Ren, K. Qu, X. Qu. *Adv. Mater.*, 2012, **24**, 1722–1728.

59. S. Yang, W. Yue, D. Huang, C. Chen, H. Lin, X. Yang. *RSC Adv.*, 2012, **2**, 8827–8832.

60. L. Sheng, J. Ren, Y. Miao, J. Wang, E. Wang. *Biosens. Bioelectron.*, 2011, **26**, 3494–3499.

61. S. Chen, B. Cheng, C. Ding. *J. Macromol. Sci.*, 2015, **2348**, 37–41.

Chapter 6

Conclusions and perspectives

Motivation

This thesis aimed at exploring the use of nanostructured materials for biosensing and drug delivery in cancer therapy, using self-assembly as a way of controlling the properties and function of such nanomaterials, introducing specificity in behaviour, or responsiveness to an external stimulus. Being able to control the organization of materials at the nanoscale opens up tremendous opportunities for the development of systems interacting with biological elements with high precision and predictability.

For instance, detection of a target of interest with high specificity is a key requirement for developing a biosensor, which will efficiently allow the diagnostic of diseases. Furthermore in cancer therapy, the Holy Grail resides in the development of drug delivery platforms, which will specifically target cancerous cells, in order to circumvent the deleterious side effects caused by the high toxicity of the chemotherapeutic drugs, and the risk of multidrug resistance.

Liposome fusion as a signal transducer for biosensing

As highlighted in Chapter 1, specific detection of miRNAs is challenging, mainly due to their short sequence size, leading to high sequence homology, and a low T_m inducing poor duplex stability. State-of-the art detection methods are mostly based on the hybridization of the target miRNA to a capture probe, and most of these methods suffer from poor specificity. The field has evolved to using more complex capture probe structures, such as stem-loops or modified nucleic acids. The study carried in Chapter 2 illustrates well this paradigm, as it emerged that the mechanism based on hairpin displacement for miRNA detection enabled the detection of miR-29a with a much higher specificity compared with the mechanism where miR-29a hybridizes on the dsDNA toehold. Furthermore, due to the low abundance of miRNAs in clinical samples it is important to have biosensors able to detect low miRNAs concentrations, typically in the aM to pM range. Currently, in the literature, enzyme-based target amplification steps are required to reach these concentrations. The use of enzymes introduces complexity in the experimental design and protocol, increases the cost, and increases the risk of error due to the existence of secondary enzymatic activities. As an alternative to enzyme-based target amplification, this thesis intended to explore whether DNA-mediated liposome fusion could be controlled by interaction with specific nucleic acids targets, and whether this mechanism could form the basis of a detection assay. Mimicking natural membrane fusion mechanisms for the purpose of biological sensor development holds great potential for highly amplified detection, where relatively few targets lead to fusion and interaction of a large payload of signal-generating molecules. Two mechanisms were designed, where the self-assembly of a specific miRNA with

specially engineered double-stranded DNA strands (dsDNA) functionalizing liposomes surface either inhibited or promoted liposome fusion. By encapsulating DiL and DiD fluorophores in the membranes of separate liposome populations, fusion can be tracked by Förster Resonance Energy Transfer (FRET). It was demonstrated for both mechanisms that the presence of target miRNA was able to modulate the event of liposome fusion in a dose-dependent fashion, enabling the build-up of dose-response curves for the detection of miR-29a. As such, this study constitutes the first example of target-mediated control over liposome fusion. The field of model systems mimicking membrane fusion in the literature is currently only focused on studying the mechanism of this complex phenomenon, therefore this study presents new exciting insights for the design of biomimetic sensors. The mechanisms developed in this study successfully demonstrated sensitive and specific detection of target miRNA at nanomolar to sub-nanomolar concentrations. In order to further develop this assay towards clinical relevance, the sensitivity requires to be improved, and two parallel approaches were undertaken. First, using 2-color fluorescence correlation microscopy analysis and a novel intensity fluctuation analysis, an increase in the sensitivity of detection was observed via a shift in the dose-response curve by ca. two orders of magnitude, which demonstrated the utility of such a setup in both the study of liposome fusion and application in a biosensing system. Then, in Chapter 3, covalent binding of FRET pair dyes inside lipid bilayers was investigated as a mean to improve FRET efficiency for the liposome fusion assay. FRET efficiency is highly sensitive to the distance separating the donor and acceptor; therefore it was hypothesized that dyes, which are maintained at close proximity through covalent bonding, would have a higher FRET efficiency than dyes, which are freely diffusing in liposomes membranes. Using Lipo-Cy3-CO and Lipo-Cy5-N_3 dyes enabled the generation of a higher FRET signal compared to DiL and DiD, with a two-fold increase of dynamic margin. As the FRET signal is higher, the liposomes can be further diluted, which would increase the assay sensitivity and allow the detection of lower concentrations of miRNAs. Therefore, a key validation for the use of Lipo-Cy3-CO and Lipo-Cy5-N_3 in biosensing assays will be the determination of the limit of detection for miRNA in optimized (diluted) conditions. Not only these novel functional dyes proved useful for biosensing, this study also shed a light on the features of strain-promoted alkyne-azide cycloaddition in lipid bilayers, and represents the first example of liposome fusion-triggered chemical reaction. In the literature, the field of bioconjugation is currently generating a lot of interest as it is enabling the study of complex biological phenomenon in their native environment, and this study without doubt offers great potential for novel bioconjugation strategies by specifically triggering the cycloaddition reaction via liposome fusion.

Quantum rattle as a stimuli-responsive drug delivery platform for cancer therapy

Nanobiotechnology holds great potential for significant contributions to cancer therapy. Indeed, nanobiotechnology can provide a platform for a combination of diagnostics, therapeutics, and targeted delivery to tumours with subsequent monitoring of responses, which constitutes the ultimate goal in cancer therapy, as outlined in Chapter 1. The field of nanotechnology for cancer therapy has been booming since the discovery of the (now disputed) EPR effect, however, there is a huge discrepancy between the abundance of systems presented in the literature and the examples of clinical trials of such systems. This lack in successful translation can partially be explained by the fact that a lot of these systems present complex designs hampering their scalability for manufacturing, and by the hurdles faced when attempting to transfer successful *in vitro* studies to more relevant *in vivo* systems, such as non-adequate biodistribution, dosage requirements, and emerging toxicity. The quantum rattles (QR), initially developed by Dr M. Hembury and used in this PhD project, represent promising carriers for therapeutic delivery of anticancer agents, combined with gold-mediated photothermal therapy, and live *in vivo* imaging. Mesoporous silica nanoshells act as reservoirs for drug encapsulation, while gold nanoparticles and gold nanoclusters mediate photothermal therapy and multimodal imaging. QR most definitely embodies a breakthrough from the existing literature, as its properties emerge from a simple, holistic design, and function synergistically instead of requiring design compromise. QR present the advantage of being easily scalable, and multifunctional. The properties of QR were published in a study, which highlighted their great potential for anticancer treatment, culminating with an *in vivo* model study where QR were injected intratumourally in a mouse tumour model, showing reduction of tumour mass via QR-mediated photothermal therapy. In order to advance the development of QR towards clinical applications, two requirements were examined in this thesis, the stabilisation of QR suspension at physiological conditions, and the spatiotemporal control over drug release by using an external trigger. These requirements are needed to insure that QR are able to circulate in the body in order to passively accumulate in the tumour, where they specifically deliver the therapeutic effect via triggered drug release. An increase in temperature generated from the photothermal properties of QR was used as a stimulus. Two approaches were undertaken to impart thermoresponsive features to QR. Echoing Chapter 2, where liposomes fused with each other, in Chapter 4 liposomes were fused with QR. Such constructs of supported lipid bilayer (SLB) on silica nanoparticles already exist in the literature; however, engineering them to be thermoresponsive represents a new step forward. By choosing a lipid composition with a high melting temperature, the drug permeability through the self-assembled SLB on QR (QR-SLB) can be modulated above and below body temperature.

While this strategy proved successful for stabilising QR suspensions at physiological conditions, temperature-triggered drug release of small molecules from QR-SLB could not be achieved, as the presence of SLB on QR did not modify drug release profiles, possibly due to a modification of the lipid phase transition properties upon adsorption of the bilayer on QR. Another approach used thermoresponsive polymers, which are incorporated into the QR platform, allowing encapsulated molecules to be released only by the temperature trigger, using temperature-triggered polymer self-assembly. The polymer layers on QR are built using the layer-by-layer (LbL) assembly technique. In the existing literature, polymer multilayer film assembly is achieved using particles as sacrificial templates to form hollow capsules; this study represents the first example of forming such assemblies while keeping the silica cores, allowing the drug release to be controlled both by the silica pore geometry and the characteristics of the LbL polymer film (number of layers, porosity). The study highlighted the importance of polymer design in the build-up of the LbL film; a first attempt at using cross-linked assembly of thermoresponsive polymer pTEGMA layered with PMA did not allow temperature-triggered release of small molecules from QR. A new generation of block polymers, PVP-*co*-pTEGMA, was created, to allow the build-up of a multilayer film stable at physiological conditions without the need for cross-linking, while retaining their thermoresponsive properties. The block copolymers PVP-*co*-pTEGMA were synthesized through successive Reversible Addition-Fragmentation chain Transfer (RAFT) of NVP and Activator ReGenerated by Electron Transfer Atom Transfer Radical Polymerisation (ARGET-ATRP) of TEGMA, and this work is the first report of controlled synthesis of these novel block copolymers, which were virtually unexplored using traditional polymerization strategies due to disparate reactivity of monomers, and represents an advance in the state-of-the-art polymerization of PVP. The successful synthesis of PVP block copolymers in this study will significantly expand the scope of this polymeric material. Furthermore, the temperature-triggered self-assembly of PVP-*co*-pTEGMA copolymers into vesicular structures was highlighted and a novel cross-linking approach to stabilize the structures at physiological conditions was reported. The temperature-triggered release of doxorubicin from the assembly of PVP-*co*-pTEGMA with TA was studied, however results were mitigated by the high retention of doxorubicin by QR.

Outlook

In order to transfer the potential of nanostructured materials into real outcomes, *i.e.* applications benefiting patients and improving their lives, efforts need to be achieved towards validating the current available technologies in model systems, which are more relevant for clinical applications. In the case of biosensing, this includes testing samples collected from patients. For the liposome fusion-based mechanism developed in this thesis, a trade-off is likely

to be faced as components of the serum, which are present in clinical samples, are expected to hamper liposome fusion by stabilizing liposomes upon surface adsorption, and most probably decrease the assay sensitivity. Hence, appropriate sample preparation steps will need to be implemented, such as centrifugation or filtration, to remove the interfering components. Regarding drug delivery for cancer therapy using nanoparticles, it is important to understand the limitations faced by these platforms in order to move forward and maximize their capabilities. For instance, a majority of injected nanoparticles accumulate at other sites than the tumour. By ensuring that nanoparticles are encapsulating and releasing in a spatio-temporally controlled manner a large payload of therapeutic drugs, their advantage over the use of single drug molecules will be clearly demonstrated. In particular for QR, there is a need to find an anticancer drug, which will be readily released from QR upon thermal trigger and have synergistic effects when used in combination with photothermal therapy. The study of the synthesis of PVP-*co*-pTEGMA block copolymers highlighted the need for controlling the polymer architecture for fine-tuning of their properties. As a result of the hydrogen bonding and biological properties of PVP, it is expected that block copolymers of PVP and stimuli-responsive polymers will be very attractive for the preparation of complex architectures and nanomaterials for controlled drug release applications. As a first step, PVP-*co*-pTEGMA copolymers were applied to the formation of polymer capsules incorporating graphene oxide as a NIR photothermal agent, using silica particles as sacrificial templates. These capsules will be evaluated for potential applications in temperature-triggered drug delivery as well as combination therapy with photothermal therapy. The synthesis of thermoresponsive anti-fouling polymers is not only of great interest for the design of thermoresponsive drug delivery carriers but also for surface modification for the development of cell sheet engineering in regenerative medicine.

Appendix 1

Synthesis and properties of quantum rattles

Dr. M. Hembury reported the synthesis of tailorable and multipurpose hybrid gold/silica particles which combine the functions necessary for multimodal therapy and diagnostic for cancer treatment.[1] While very often multiple step synthetic processes are required for generating such multifunctional particles, therefore adding more complexity, the synthesis of quantum rattle (QR) follows a very simple pathway, described on Figure 1.

QR was obtained by infusing and *in situ* reducing gold (I) salt in the pores and cavities of hollow mesoporous silica nanospheres. Two nanostructures of gold were formed during the synthesis: gold nanoparticles inside the cavity of the hollow silica shells, and gold nanoclusters inside the pores of the silica shells.[1]

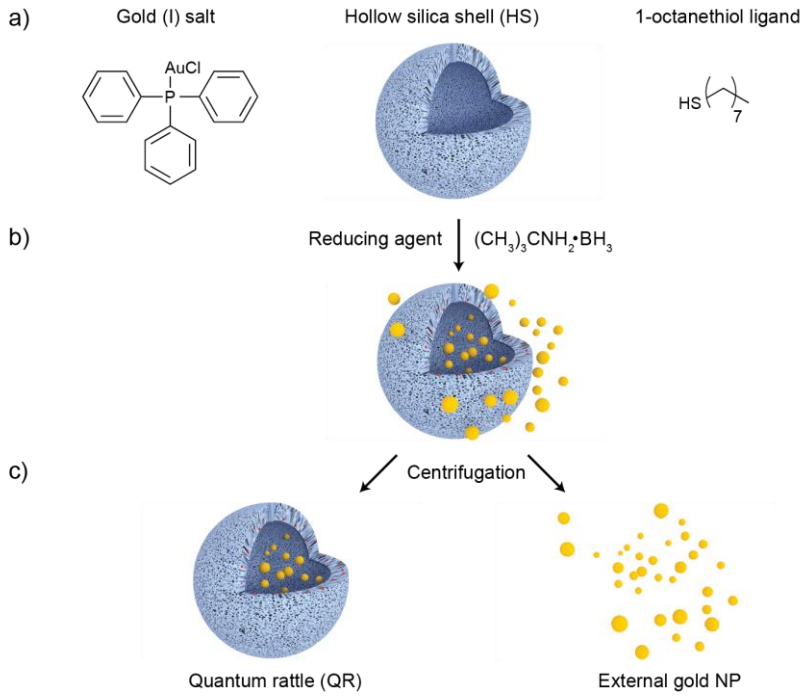

Figure 1. Schematic illustration of quantum rattles synthesis. a) Chloro(triphenylphosphine) gold (I) salt and 1-octanethiol were infused into the hollow mesoporous silica shells (HS). b) The gold nucleated in situ following the addition of the reducing agent borane tert-butylamine complex. c) The particles were purified by precipitation to remove free gold nanoparticles from the quantum rattles.[1]

This project was initiated by reproducing the synthesis of the hollow silica shells (HS) and QR previously reported by M. Hembury. The properties of the synthesized QR were evaluated to ensure the reproducibility of the synthesis.

Hollow silica shells

Silica shells were synthesized following a protocol published by collaborators at College de France.[2] Briefly, the synthesis involved a dual-templating method to create the network of pores

and the hollow cavity in the silica nanospheres. Anionic polymer latex nanoparticles were used as a template for the core, and a surfactant, cetyltrimethylammonium bromide (CTAB), was used for the formation of radially-oriented mesopores. The use of a hard core template combined with a surfactant co-template allowed the synthesis of highly hierarchically structured particles, with a great control over morphology.[2]

The polystyrene nanoparticles were synthesized via emulsion polymerisation; this method allowed the formation of monodispersed polymer nanoparticles with good control on their size and morphology.[3] Dynamic light scattering results showed that a population of polystyrene nanoparticles of diameter 113.2 nm ± 1.2 nm was synthesized. The polydispersity index of 0.04 indicated that highly monodispersed nanoparticles were obtained with a narrow size distribution, which was crucial for the next step of the synthesis, i.e., formation of the hollow mesoporous silica shells.

The silica nanospheres were subsequently obtained by sol-gel condensation of a silica precursor, tetraethyl orthosilicate (TEOS), organized by the co-templates, polystyrene nanoparticles and CTAB. The organic templates were then removed during calcination of the silica particles, creating the hollow cavity and the radially-orientated mesoporous network.

The nitrogen adsorption and desorption isotherms of the particles obtained after calcination are presented on Figure 2b-c. They were described as type IV isotherms according to the IUPAC nomenclature, characteristics of mesoporous materials.[4] The surface area value of the particles, obtained from the BET model, was of 1235 $m^2.g^{-1}$, and the particles presented a narrow pore size distribution, centred on a 2 nm-diameter, according to the BJH model.

Quantum rattles

QR were obtained following the synthetic path represented on Figure 1. Briefly, HS nanospheres were infused with gold (I) salt and 1-octanethiol, allowing the chemicals to diffuse into the mesoporous structure. The nucleation of the gold was then triggered by the addition of the reducing agent, borane-*tert*-butylamine, at 55 °C. The product was purified by precipitation of the hydrophilic QR from the free hydrophobic gold nanoparticles.

The synthesized QR were spherical in shape, presenting hollow cavities hosting gold nanoparticles (Figure 2a and d). QR showed an extinction peak at 411 nm and another one at 672 nm (Figure 2e). These extinction peaks were attributed to the gold nanoclusters hosted within the mesopores of the silica.[5] The photoluminescence spectra showed an excitation peak centred at 672 nm excited an emission peak centred at 825 nm (Figure 2f).

The optical properties of QR were highly conserved during this new synthesis, matching previous observations.[6] Therefore these newly synthesized QR were used for the remaining of the project.

Doxorubicin loading experiments confirm that QR can encapsulate this drug with higher efficiency than HS (Figure 2g-h). The release profile of doxorubicin from QR, both at room temperature and 50 °C are presented on Figure 2i; only a small fraction of total encapsulated doxorubicin was released over time.

The cytotoxic effects of QR on human cervical cancer HeLa cells were evaluated using MTS cell proliferation assay. MTS assay is a colourimetric test, based on the reduction of MTS tetrazolium compound by viable, metabolically-active cells, to produce coloured formazan product, which has an absorbance maximum at 490 nm. QR suspensions of various concentrations were prepared in 1× PBS. HeLa cells were incubated with various concentrations of QR and the mitochondrial enzymatic activities were assessed after 24 h. The statistical analysis of the MTS assay showed that QR:cell ratios of 10^2, 10^3, 10^4, and 10^5 were not significantly different from control and therefore did not affect the cells' viability. QR:cell ratios of 10^6 and 10^7 were significantly different from the control and showed cytotoxic effect on the cells metabolic activity and a reduced cell viability. Therefore, the cytotoxicity of quantum rattles on HeLa cells was dose dependant.

The photothermal properties of QR are presented on Figure 2k-l. When irradiated with a NIR laser, QR generated a hyperthermia both in solution and *in vivo*, with the temperature reaching up to 51 °C in the tumour mouse model system.

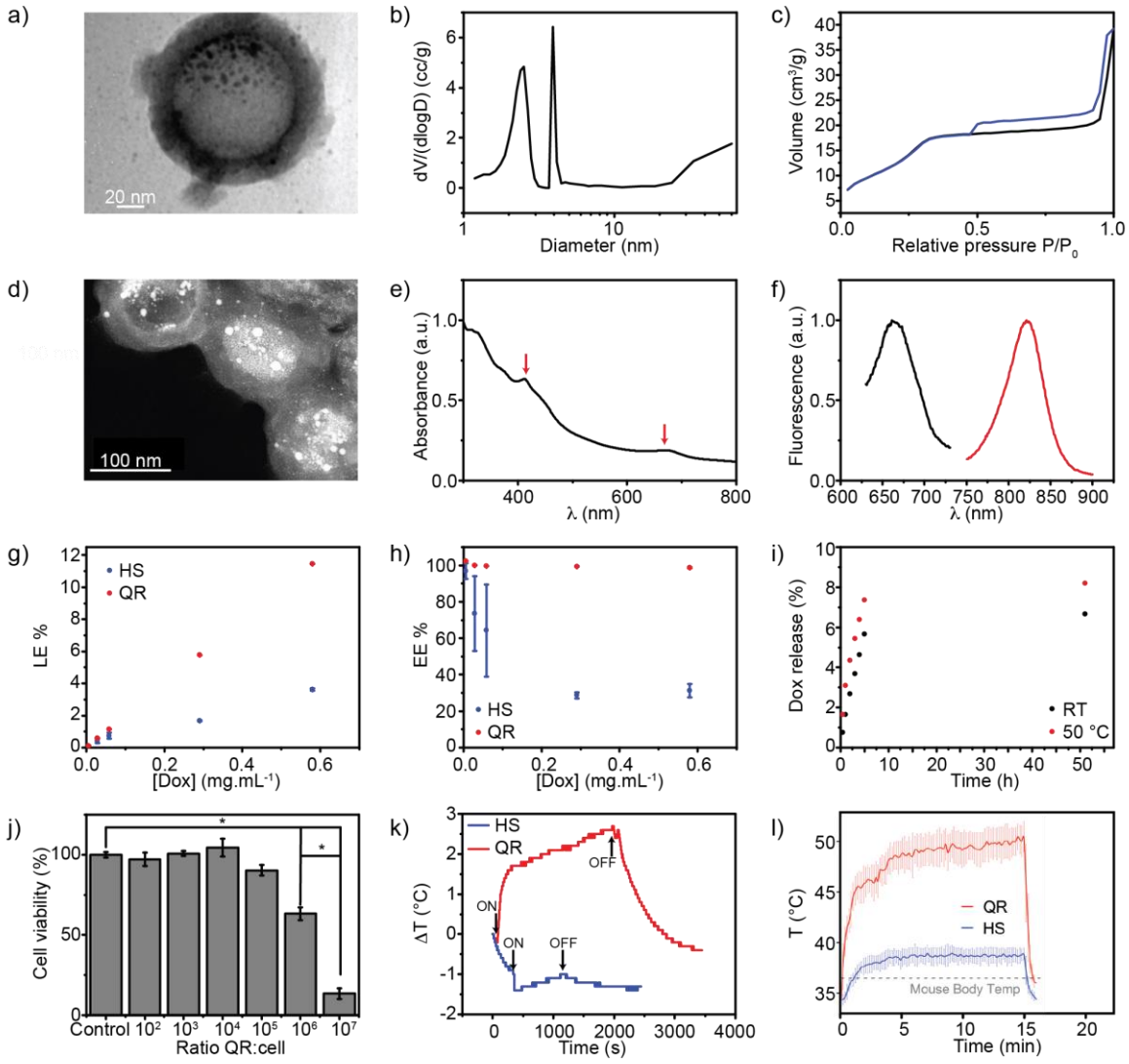

Figure 2. a) Image of quantum rattles with gold nanoparticles in the silica cavity. b) Pore size distribution of the hollow mesoporous silica nanospheres after calcination, indicating the presence of 2 nm pores on the silica shells. c) Nitrogen adsorption and desorption isotherms of the hollow mesoporous silica nanoparticles after calcination. They were type IV isotherms and exhibited an important hysteresis. d) High angle annular dark field scanning TEM (HAADF- STEM) image of QR showing the presence of gold particles. e) UV-vis spectrum of as-synthesized quantum rattles, resuspended in ethanol, showing an extinction peak centred at 411 nm and an extinction peak centred at 672 nm. f) Photoluminescence spectra of as-synthesized quantum rattles suspended in ethanol, showing an excitation peak centred at 672 nm and an emission peak centred at 825 nm. Emission spectrum (λ_{ex} = 672 nm, red) and excitation spectrum (λ_{em} = 827 nm, black). g) Loading efficiency of doxorubicin (%LE = [Entrapped drug/nanoparticles weight]×100) for hollow silica (HS, blue symbols), and QR (red symbols). h) Entrapment efficiency of doxorubicin (%EE = [(Drug added - Free drug)/Drug added]×100) for hollow silica (HS, blue symbols), and QR (red symbols). i) Release of Doxorubicin from QR at room temperature

(black symbols) or 50 °C (red symbols). j) *In vitro* cytotoxicity of QR on human cervical cancer HeLa cells evaluated by MTS assay. Data shown are average ± STD (n=2). *Significant difference (Tukey's test, $p<0.01$). k) Photothermal properties of QR. Temperature profiles for HS (blue trace) and QR (red trace) in solution upon irradiation with a 671 nm laser (38 W.cm-2), monitored using a thermocouple probe. l) Temperature profiles of tumours treated with either QR (red trace) or HS (blue trace) (100 µL, 5.7×10^{12} particles.mL^{-1}), monitored with a thermal camera, showing a 15.1 °C temperature increase from the mouse body temperature in the QR-treated samples upon irradiation with a 671 nm laser (0.9 $W.cm^{-2}$, 5 mm spot) compared to 3.2 °C for the HS-treated controls. The QR-treated areas reached temperatures above 51 °C after less than 1 min irradiation, while HS-treated control areas plateau at 39 °C after approximately 5 min. Data for panel (l) was acquired by Dr. Mathew Hembury and was reproduced with permission from Hembury *et al.*[1]

In conclusion, QR were successfully synthesized with conserved morphology, physico-chemical and photonic properties. However, QR, since their original formulation, formed supramicronmetre-size aggregates after the synthesis. The aggregation of nanoparticles poses serious concerns for the development of an injectable therapeutic system; and requires addressing in order to overcome it.

The cause of the agglomeration was unclear, and several possibilities were considered. A first hypothesis is that the particles interacted closely with each other by strong attractive forces, generated when the particles were subjected to thermal treatment. For instance, Blas *et al.* observed that the diameter of silica nanoparticles decreased after calcination, resulting of a constriction phenomenon occurring in the silica.[2] This phenomenon may have been the cause of reorganization of the silica structure, sintering the particles together. Moreover, calcination of silica results in a decrease in the concentration of the surface hydroxyls,[7] which could also potentially contribute to agglomeration of silica nanoparticles and affect their dispersibility, as hydroxyl functional groups favour water dispersibility. These hypotheses prompted a reflection on the role of calcination in the synthetic process of the hollow mesoporous silica nanospheres.

Originally, calcination was implemented as a method to remove the organic templates from the silica shells, creating the pores and the cavities of the nanospheres. In this particular process, the silica nanospheres are first calcined in air at 250 °C, inducing thermal decomposition of the pore-templating surfactant cetyltrimethylammonium bromide (CTAB).[7] The temperature is then gradually increased to 550 °C to remove the polystyrene templates. Complete removal of all organic templates by calcination[2] was also performed to minimize the cytotoxicity of the mesoporous silica nanospheres as previous studies demonstrated the inherent cytotoxicity of the surfactant CTAB to cells at sub-micromolar dose.[8]

In order to avoid calcination, an alternative strategy for the removal of the CTAB pore template was necessary. Following calcination, the second most-used method for the removal of organic surfactants from silica based particles is acidic extraction.[9] Briefly, the acid extraction began by refluxing overnight the as-synthesized silica nanoparticles in HCl (10 v/v % in ethanol), followed by thorough washing of the particles in water and ethanol. The process was repeated three times to maximize the removal of the CTAB. The removal of CTAB was assessed by comparing the FT-IR spectra of the particles before and after extraction (Figure 3). The spectra showed the disappearance of the characteristic peaks[10] for CTAB at 2845 and 2920 cm^{-1} following extraction, showing that the extraction successfully removed the CTAB.

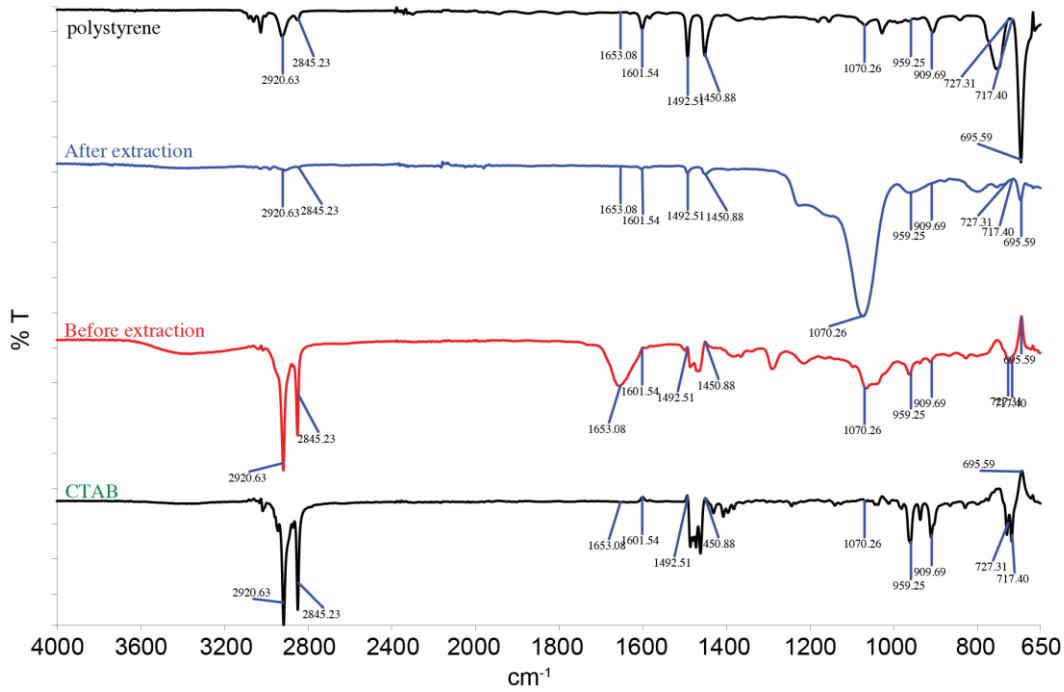

Figure 3. FTIR spectra of: (from top to bottom) polystyrene nanoparticles – silica nanoparticles after acidic extraction of CTAB – silica nanoparticles prior to the acidic extraction – CTAB. The spectrum of the particles after extraction did not present the bands characteristic for CTAB between 2800 and 3000 cm^{-1}. Spectra were measured by Dr Glenna Drisko (Collège de France).

These results were very promising and showed that it was possible to remove CTAB from the silica nanoparticles using acidic extraction. Moreover, it was found that the polystyrene core could be removed from silica nanoparticles by dissolution in solvents such as tetrahydrofuran.[11] By coupling these two approaches, hollow mesoporous silica nanospheres free of organic templates could be generated, with no need for calcination for the removal of the templates.

The influence of the organic template removal method on the resulting hollow silica (HS) particles cytotoxicity was evaluated using human cervical cancer HeLa cells, comparing HS

obtained via calcination with HS obtained via acidic extraction. Briefly, cells were seeded in wells of a multi-well plate, and incubated with a range of HS concentrations for 24 h. The toxicity of the particles on the cells was evaluated using MTS cell proliferation assay. MTS assay is a colourimetric test, based on the reduction of MTS tetrazolium compound by viable, metabolically-active cells, to produce coloured formazan product, which has an absorbance maximum at 490 nm. The results of the assay are presented on Figure 4. In the case of HS obtained via calcination (Figure 4a), for all HS concentrations tested, the metabolic activity of the cells was not different from the control. In the case of HS obtained via acidic extraction (Figure 4b), only the ratio HS:cell = 10^7 was statistically different from all other conditions, showing an increase in the cells' metabolic activity. In summary, HS obtained via acidic extraction did not have an increased toxicity for HeLa cells compared to HS obtained via calcination, confirming the efficient removal of the surfactant CTAB and the absence of deleterious effect of the solvents used during this process.

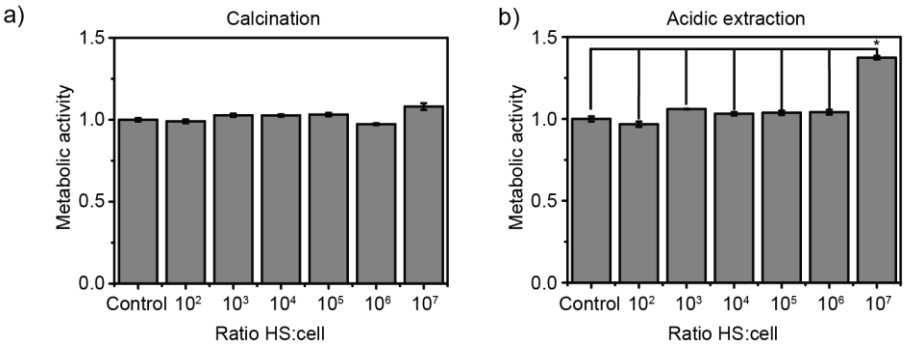

Figure 4. *In vitro* cytotoxicity of HS on human cervical cancer HeLa cells evaluated by MTS assay for a) HS obtained via calcination, and b) a) HS obtained via acidic extraction. Data shown are average ± STD (n=3). *Significant difference (Tukey's test, $p<0.01$).

As an alternative to strategies that prevented the aggregation of QR, methods to re-disperse QR efficiently after their synthesis were explored. The main strategies used for breaking agglomerates are milling and ultrasonication.[12,13]

In practice, measurement of the surface charge of nanoparticles in solution, referred as zeta potential, gives a good indication of their electrostatic stability. When the module of the zeta potential is more than 30 mV, particles tend to repel each other and therefore form a stable dispersion.[12,13] In this study, the dispersibility and stability of QR were assessed by measuring the size distribution of the QR suspension using dynamic light scattering (DLS), and measurement of the zeta potential indicated the stability of the dispersion.

QR have been successfully dispersed in water and ethanol using ultrasonication (Sonics Vibra Cell, VCX500). Typically, agglomerates of QR in water or ethanol (1 mg.mL^{-1}) were ultrasonicated using a power of 125 W until dispersion was achieved.

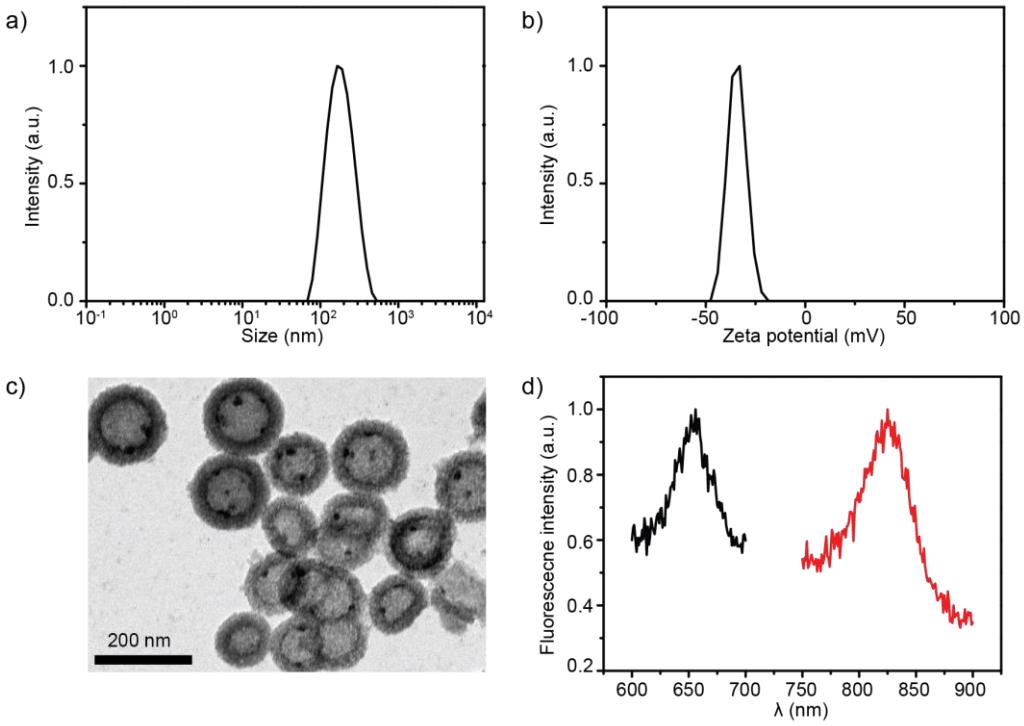

Figure 5. Properties of QR post ultrasonication at 125 W for 30 min. a) DLS size distribution centred around 170 nm. b) Zeta potential distribution centred around -34 mV. c) TEM image of QR showing that the silica nanoshells remained intact. d) Photoluminescence spectra of QR post ultrasonication, showing an excitation peak centred at 672 nm and an emission peak centred at 827 nm. Emission spectrum (λ_{ex} = 672 nm, red) and excitation spectrum (λ_{em} = 827 nm, black).

The ultrasonicated QR formed a monodispersed 170 nm-sized population (PdI: 0.1) as measured by DLS (Figure 5a). The zeta potential of dispersed QR in water was -34 mV (Figure 5b), showing a good stability of the dispersion. The absence of breakage in the silica shells was confirmed by TEM imaging (Figure 5c) and the photonic properties of QR were retained (Figure 5d). QR formed a stable suspension for up to 7 days (measured by DLS, data not shown).

These results showed that the agglomerates of as-synthesized QR could be successfully dispersed by ultrasonication, while retaining structure and photonic properties. This approach to obtain a dispersed suspension of QR is simpler and more straightforward than the synthesis of dispersed silica shells by avoiding calcination, and was therefore preferred as a strategy to attain dispersed QR.

Surface functionalization with poly(ethylene glycol) (PEGylation) has been shown to increase the stability of silica nanoparticles dispersions via steric stabilization.[14] Moreover, PEGylation can provide a shielding effect from the mononuclear phagocyte system (MPS), increasing the circulation time of the nanoparticles in the organism, and the efficacy of the EPR effect.[15]

Two molecules were investigated for the surface functionalization of QR (Figure 6): mPEG-Silane, and (3-aminopropyl)triethoxysilane (APTES).

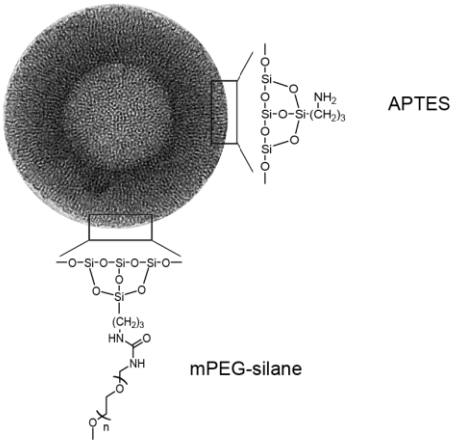

Figure 6. Surface functionalization strategies to increase the stability of QR. The surface of the silica shells is modified by mPEG-Silane, (3-aminopropyl)triethoxysilane (APTES), or (3-mercaptopropyl)trimethoxysilane (MPTS) followed by bifunctional PEG maleimide (mal-PEG-mal).

First, the silica surface was functionalized with PEG using mPEG-silane. $mPEG_{5000}$ was chosen for this study to limit the increase in the hydrodynamic radius of QR while providing charge screening. Very long PEG molecules would further increase the QR diameter and could shorten their half-life while in the systemic circulation.[16]

mPEG-silane was added to a suspension of QR in ethanol and was left to react for 2 h. The conjugation of mPEG-silane to the silanol groups on the silica surface occurs through hydrolysis/condensation reactions. While purifying the functionalized products by washing them with ethanol, the supernatant solution had an unusual yellow colour, while QR suspension had shifted from yellow towards red. This observation prompted the investigation into possible changes in the photonic properties of QR following functionalization.

The UV-vis spectrum of QR functionalized with mPEG-silane (Figure 7) displayed one broad peak centred at 520 nm, corresponding to the LSPR of gold nanoparticles.[17] However, none of the characteristic absorption peaks for the Au_{25} nanoclusters (at 411 nm and 672 nm)[5] present

in the original QR could be observed following functionalization. The photoluminescence spectra of mPEG-functionalized QR (Figure 7a) showed an extremely weak excitation peak centred at 672 nm and an emission peak centred at 827 nm compared to original QR of similar concentration. Therefore, the PEGylation of QR resulted in a loss of the photonic properties originating from the AuNC.

In parallel, the photonic properties of the supernatant from the reaction were analysed. Its UV-vis spectrum (Figure 7) displayed both 411 nm and 672 nm extinction peaks and the photoluminescence spectra (Figure 7b) showed strong excitation peak centred at 672 nm with associated emission peak centred at 827 nm. Therefore, AuNC were released from QR into the supernatant: the surface functionalization of QR with mPEG-silane induced a displacement of AuNC, from the mesopores of the silica to the dispersion media.

The origin of this phenomenon remained unclear. It was hypothesized that the silanization reaction could potentially result in changes in the porosity of QR, leading to an increase of the pore diameter and hence the release of the nanoclusters. Alternatively, the surface modification of QR can have modified the surface charge or lipophilicity of the silica surface, creating a gradient that forced the clusters out of the silica pores.

Functionalizing QR with (3-Aminopropyl)triethoxysilane (APTES) yielded the same results as those observed for mPEG-silane (Figure 7).

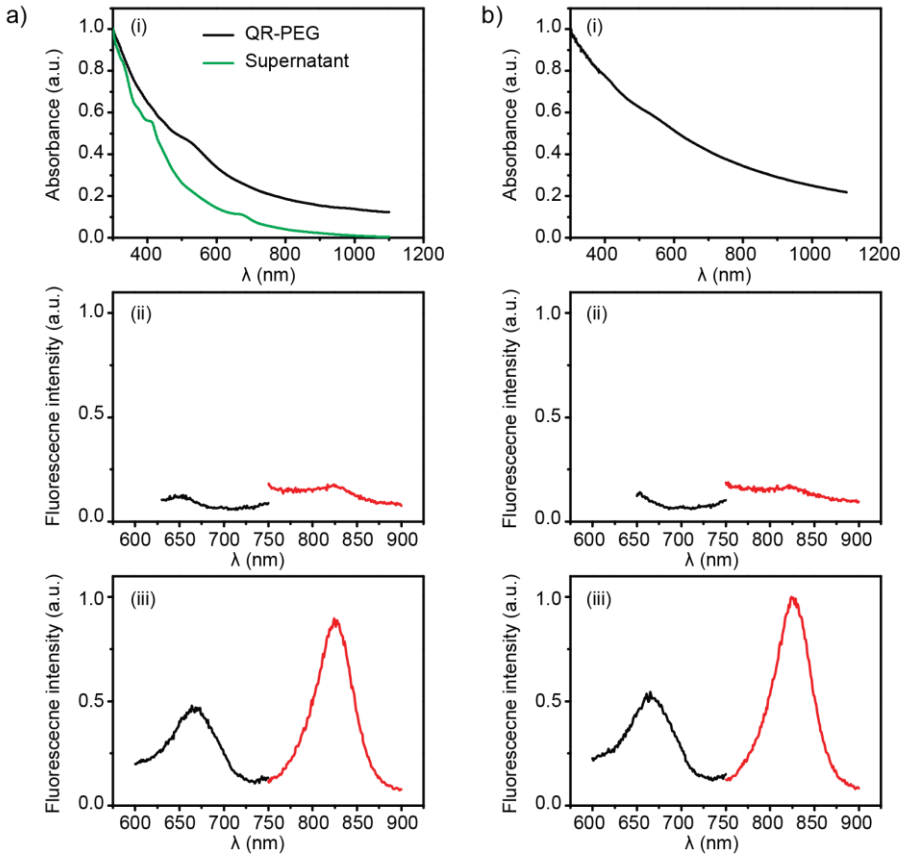

Figure 7. Photonic properties of QR functionalised with a) PEG and b) APTES. (i) UV-vis spectra of QR, (ii) Emission spectrum (λ_{ex} = 672 nm, red) and excitation spectrum (λ_{em} = 827 nm, black) of QR post functionalization showing a weak excitation peak centred at 672 nm and a weak emission peak centred at 827 nm and (iii) Emission spectrum (λ_{ex} = 672 nm, red) and excitation spectrum (λ_{em} = 827 nm, black) of the supernatant obtained after QR functionalization showing an excitation peak centred at 672 nm and an emission peak centred at 827 nm.

The reaction conditions for APTES functionalization were optimized by changing the concentration of APTES as well as the solvent. When performing the reaction in water, QR was successfully functionalized with APTES and conserved the photonic properties, indicating that the Au nanoclusters were retained within the silica shell.

Collaborators from the group of Prof. Irene Yarovsky Collaborators at RMIT University (Melbourne, Australia) have performed simulations of gold nanoclusters $Au_{25}(S(CH_2)_7CH_3)_{18}$ in ethanol and water environments to obtain insight into the effect solvent has on the overall shape/structure of the nanoclusters. The key finding from this simulation was that when AuNC are surrounded with water, ligands favour self-interactions and collapse on the cluster surface to minimise exposure to water due to their hydrophobic nature, while in ethanol the ligands are able to interact with the solvent more favourably and adopt more extended conformations

(Figure 8). The preferential affinity of the ligands for ethanol compared with water could explain why the AuNC leak from QR when they were re-dispersed in ethanol.

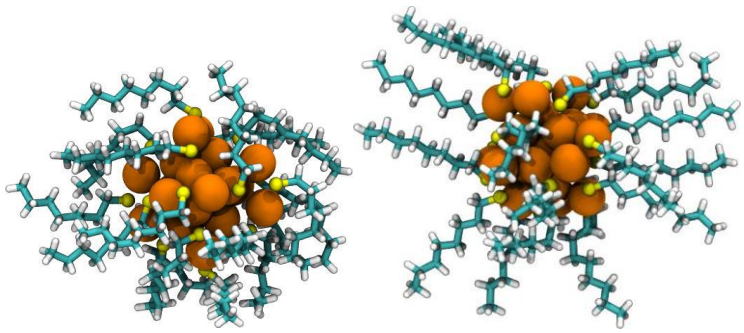

Figure 8. Snapshots of $Au_{25}(S(CH_2)_7CH_3)_{18}$ nanoclusters in water (left) and ethanol (right). Modelling experiments were performed by Patrick Charchar (RMIT University, Melbourne, Australia).

Materials and methods

Materials

All chemical reagents were purchased from Sigma-Aldrich and used as supplied unless otherwise indicated.

Methods

Polystyrene particle synthesis

Polystyrene particles were prepared by emulsion polymerisation with an anionic initiator, potassium persulfate (KPS). Dihexylsulfosuccinate sodium salt (2.6 g), MilliQ H_2O (206 mL), sodium bicarbonate (0.43 g) and styrene (30.2 g) were mixed in a round bottom flask. The solution was degassed over 30 min by bubbling with argon and then heated at 90 °C using an oil bath. As styrene auto-initiates at this temperature, the initiator, KPS (0.43 g) in MilliQ H_2O (14.9 mL), was promptly added to the hot solution via syringe. The reaction was performed for 6 h under a slight positive pressure of argon. The resulting particles were dialysed over one week producing an 8.9 wt% polystyrene dispersion.

Hollow mesoporous silica shell synthesis

Mesoporous silica was grown on the polystyrene particles, which served as templates for the core cavity. The surfactant cetyltrimethylammonium bromide (CTAB, 3.2 g) was dissolved in MilliQ H_2O (100 mL) at 70 °C. The polystyrene particles (17.5 g) were diluted with 500 mL MilliQ H_2O, 200 mL of ethanol and basified with 7.5 g of NH_3. The CTAB solution was added to the polystyrene dispersion and allowed to equilibrate for 45 min. Tetraethyl orthosilicate (TEOS, 5.4 g) was added drop-wise to the solution, which was subsequently allowed to react for 1 day. To collect the particles, the solution was centrifuged at 8000 rpm for 1 h. The resulting material was calcined using the following temperature profile: 25 to 250 °C at a rate of 5 °C.min^{-1}, held at 250 °C for 2 h, 250 to 550 °C at a rate of 2 °C.min^{-1}, held at 550 °C for 5 h.

Quantum Rattle synthesis

All glassware were pre-washed in aqua regia (1:3 HNO_3:HCl) and then saturated potassium hudroxide (KOH) in ethanol before any synthesis.

Chloro(triphenylphosphine) gold (I) salt (222.6 mg) and hollow mesoporous silica shells (100 mg) were suspended in chloroform (25 mL) and left to incubate on a rotary plate overnight (>

12 h) at room temperature. The next day, 1-octanethiol (156.2 µL) was added to the gold-silica suspension and left to mix for 20 min. A solution of borane *tert*-butylamine complex (391.4 mg) was then prepared in chloroform (15 mL) and added to the gold-silica-thiol solution while mixing in a round bottom flask. The reaction vessel was then equipped with a condensation column and transferred to a pre-heated 55 °C oil bath. The solution was left to react for 1 h and then cooled to room temperature, followed by purification of the resulting quantum rattles. Diethyl ether (250 mL) was added to the reaction mixture and QR were left to precipitate from the solution overnight at 4 °C. The supernatant was removed and QR were washed and centrifuged 3 times at 1500 rpm for 8 min in diethyl ether (50 mL) and twice at 6500 rpm for 20 min in a mixture of ethanol (0.5 mL) and chloroform (10 mL) then left to dry at room temperature.

Drug loading experiments

Briefly, various quantities of doxorubicin were added to dispersed QR or hollow silica (HS) (0.5 mg, 5 $mg.mL^{-1}$), and they were left to rotate overnight. The next day, the particles were washed to remove unbound doxorubicin, and the quantity of doxorubicin associated with QR was determined by measuring the fluorescence of the supernatant and derived from a calibration curve. %LE = [Entrapped Drug/nanoparticles weight] × 100 and corresponds to the drug content in QR; %EE = [(Drug added - Free unentrapped drug)/Drug added] × 100 and corresponds to the percentage of drug successfully entrapped in QR.

Drug release experiments

Quantum rattles (5 mg) were resuspended in Milli-Q H_2O (25 $mg.mL^{-1}$) by ultrasonication (Sonics Vibra Cell, VCX500), at a power of 125 W. QR was pelleted, the supernatant was removed, and 200 µL of 10 mM doxorubicin solution in Milli-Q H_2O were added to the pellet, which was resuspended by vortexing. QR suspension was rotated overnight, protected from light. The unencapsulated doxorubicin was removed by washing QR 5 times in Milli-Q H_2O (centrifugation at 10000 rpm for 5 min). After the final wash, QR was resuspended in 400 µL 0.5× PBS buffer and the sample was split into two aliquots. QR suspension was incubated at room temperature, or 50 °C. For each time point QR was pelleted, the supernatant was collected and its fluorescence was measured on a plate reader (SpectraMax M5 Microplate Readers, Molecular Devices) (λ_{ex} = 470 nm, λ_{em} = 590 nm), as well as its absorbance at 485 nm. The fraction of encapsulated doxorubicin was derived from a calibration curve.

Removal of ionic surfactant in Liquid Phase

The method used for removal of cetyl trimethylammonium bromide (CTAB) was adapted from Cui *et al* (2012).[9] Non-calcined silica nanoparticles (50 mg) were suspended in ethanol (10 mL) containing 10 % HCl (37 % w/w) in a round bottom flask. The suspension was refluxed at 80 °C for 17 h. It was then allowed to cool to room temperature, and the particles were washed 3 times in MilliQ H_2O, then 3 times in EtOH. The extraction and washing steps were repeated twice.

Cell culture

Human cervical cancer HeLa cells were used in this study. The cells were cultured in Dulbecco's modified Eagle medium (DMEM, Invitrogen) supplemented with 10 % (v/v) FBS (Invitrogen) and 1 % (v/v) Antibiotic-Antimycotic (Invitrogen). The cells were maintained in an incubator at a temperature of 37 °C, regulated with 5 % CO_2, 95 % air, and a saturated humidity. The media was replaced every second day, and the cells were passaged using Trypsin EDTA (0.05 % (w/w), Invitrogen) upon reaching 80 % confluence.

Preparation of QR solutions for *in vitro* studies

QR (or HS) at various concentrations in 1× PBS were prepared prior to use. A solution of dispersed QR (or HS) in MilliQ H_2O (1 mL, 1 mg.mL^{-1}) was centrifuged at 1500 rcf for 20 min. The supernatant was removed and 472 µL of 1× PBS (Invitrogen) were added, resulting in a final concentration of 2.12 mg.mL^{-1} equivalent to 10^{12} QR.mL^{-1} (or 1.90 mg.mL^{-1} equivalent to 10^{12} HS.mL^{-1}). Lower concentrations (10^7-10^{11} particles.mL^{-1}) were obtained by series of dilution. The resulting solutions were sterilized under UV light for a minimum of 1 h and up to 2 h.

Cell viability assay

The cytotoxicity of QR and HS against HeLa cells was evaluated by an MTS assay (CellTiter 96® AQueous One Solution Cell Proliferation Assay, Promega). HeLa cells were seeded at a density of 2.10^4 cells in a 24 well plate. After 24 h incubation, the cells were exposed to a series of doses of QR or HS for 24 h at 37 °C. After the incubation, the cells were washed twice with 1× PBS buffer and then 100 µL of MTS reagent in 500 µL of DMEM-no phenol red (Invitrogen) were added into each well. After 2 h at 37 °C, the absorbance at 490 nm was recorded using a plate reader (SpectraMax M5 Microplate Readers, Molecular Devices).

The statistical analysis was performed using MatLab R2012a (MathWorks). A one-way ANOVA combined with a Tukey-Kramer Multiple comparisons test was used for analysing the significance of differences between cell viability at different particles:cell ratio. These

differences were deemed significant if the probability of the results occurring by random was less than 1 % ($p < 0.01$).

Surface functionalization of quantum rattles

Dispersion of quantum rattles:

Quantum rattles (1 $mg.mL^{-1}$) were dispersed in milliQ H_2O or ethanol using ultrasonication (Sonics Vibra Cell, VCX500), at a power of 125 W. The dispersion of QR was assessed by dynamic light scattering (DLS).

Methoxy poly(ethylene glycol)-silane (mPEG-silane):

A solution of QR in MilliQ H_2O (500 µL, 1 $mg.mL^{-1}$) was centrifuged at 1500 rcf for 20 min. The supernatant was removed and QR were resuspended in ethanol. mPEG-silane (MW 5000, Laysan Bio) was added to the solution and left to react for 1.5 h at room temperature. QR were then washed 3 times in MilliQ H_2O to remove the excess mPEG-silane.

(3-Aminopropyl)triethoxysilane (APTES):

In ethanol: QR, dispersed in ethanol by ultrasonication (500 µL, 1 $mg.mL^{-1}$), were mixed with APTES (2 % (w/v), 10.5 µL) for 3.5 h at room temperature. QR were washed three times in EtOH.

In water: QR dispersed in milliQ H_2O by ultrasonication (200 µL, 1 $mg.mL^{-1}$) were mixed with APTES (2 % (v/v), 2 µL) for 15 min at room temperature. QR were washed three times in milliQ H_2O

Particle Morphology

TEM and HAADF-STEM images of the various materials were recorded on a JEOL 2010 TEM equipped with a Gatan camera and an energy dispersive X-ray spectroscopy detector (Oxford Instrument). The electronic microscope was operated with an acceleration voltage of 200 kV. The TEM samples were prepared by dropping 5 µL of a dispersion of the nanoparticles in EtOH (or otherwise specified) onto mesh copper grids and subsequently dried at room temperature.

Dynamic Light Scattering (DLS)

Zeta potential and size distribution measurements were performed using a Zetasizer Nano ZS (Malvern). In all DLS measurements, the scattering angle was fixed at 173°.

References

1. M. Hembury, C. Chiappini, S. Bertazzo, T. L. Kalber, G. L. Drisko, O. Ogunlade, S. Walker-Samuel, K. S. Krishna, C. Jumeaux, P. Beard, C. S. S. R. Kumar, A. E. Porter, M. F. Lythgoe, C. Boissière, C. Sanchez, M. M. Stevens. *Proc. Natl. Acad. Sci. U. S. A.*, 2015, **112**, 1959–1964.

2. H. Blas, M. Save, P. Pasetto, C. Boissière, C. Sanchez, B. Charleux. *Langmuir*, 2008, **24**, 13132–13137.

3. J. W. Vanderhoff. *J. Polym. Sci. Polym. Symp.*, 1985, **72**, 161–198.

4. P. Branton, P. Hall, K. Sing, H. Reichert, F. Schüth, K. K. Unger. *J. Chem. Soc. Faraday Trans.*, 1994, **90**, 2965–2967.

5. H. Qian, M. Zhu, Z. Wu, R. Jin. *Acc. Chem. Res.*, 2012, **45**, 1470–1479.

6. M. T. Hembury. Gold-Silica Quantum Rattles for Cancer Therapy and Diagnosis, 2012.

7. J. Goworek, A. Kierys, W. Gac, A. Borówka, R. Kusak. *J. Therm. Anal. Calorim.*, 2009, **96**, 375–382.

8. A. M. Alkilany, P. K. Nagaria, C. R. Hexel, T. J. Shaw, C. J. Murphy, M. D. Wyatt. *Small*, 2009, **5**, 701–708.

9. J. Cui, Y. Yan, Y. Wang, F. Caruso. *Adv. Funct. Mater.*, 2012, **22**, 4718–4723.

10. Q. He, Z. Zhang, Y. Gao, J. Shi, Y. Li. *Small*, 2009, **5**, 2722–2729.

11. T. Taniguchi, T. Kashiwakura, T. Inada, Y. Kunisada, M. Kasuya, M. Kohri, T. Nakahira. *J. Colloid Interface Sci.*, 2010, **347**, 62–68.

12. N. Mandzy, E. Grulke, T. Druffel. *Powder Technol.*, 2005, **160**, 121–126.

13. P. Bihari, M. Vippola, S. Schultes, M. Praetner, A. G. Khandoga, C. a Reichel, C. Coester, T. Tuomi, M. Rehberg, F. Krombach. *Part. Fibre Toxicol.*, 2008, **5**, 14.

14. C. Graf, Q. Gao, I. Schütz, C. Noufele, W. Ruan, U. Posselt, E. Korotianskiy, D. Nordmeyer, F. Rancan, S. Hadam, A. Vogt, J. Lademann, V. Haucke, E. Rühl. *Langmuir*, 2012, 7598–7613.

15. Q. He, J. Zhang, J. Shi, Z. Zhu, L. Zhang, W. Bu. *Biomaterials*, 2010, **31**, 1085–1092.

16. J. Jokerst, T. Lobovkina, R. Zare, S. Gambhir. *Nanomedicine*, 2011, **6**, 715–728.

17. M. Hu, J. Chen, Z.-Y. Li, L. Au, G. V Hartland, X. Li, M. Marquez, Y. Xia. *Chem. Soc. Rev.*, 2006,

35, 1084–1094.

Appendix 2

Authorizations

The following authorisations were obtained to reuse published work:

Hembury M, Chiappini C, Bertazzo S, Kalber TL, Drisko GL, Ogunlade O, Walker-Samuel S, Krishna KS, **Jumeaux C**, Beard P, Kumar CS, Porter AE, Lythgoe MF, Boissière C, Sanchez C, Stevens MM. Gold-Silica Quantum Rattles for Multimodal Imaging and Therapy. *Proc Natl Acad Sci USA* **2015**, 112 (7), 1959-1964

"PNAS authors need not obtain permission for the following cases: (1) to use their original figures or tables in their future works; (2) to make copies of their papers for their own personal use, including classroom use, or for the personal use of colleagues, provided those copies are not for sale and are not distributed in a systematic way; (3) to include their papers as part of their dissertations; or (4) to use all or part of their articles in printed compilations of their own works. Citation of the original source must be included and copies must include the applicable copyright notice of the original report."

Jumeaux C, Chapman R, Chandrawati R, Stevens MM. Synthesis and self-assembly of temperature-responsive copolymers based on *N*-vinylpyrrolidone and triethylene glycol methacrylate. *Polym. Chem.*, **2015**, 6, 4116-4122.

Author reusing their own work published by the Royal Society of Chemistry:

You do not need to request permission to reuse your own figures, diagrams, etc, that were originally published in a Royal Society of Chemistry publication. However, permission should be requested for use of the whole article or chapter except if reusing it in a thesis. If you are including an article or book chapter published by us in your thesis please ensure that your co-authors are aware of this.

Reuse of material that was published originally by the Royal Society of Chemistry must be accompanied by the appropriate acknowledgement of the publication. The form of the acknowledgement is dependent on the journal in which it was published originally, as detailed in 'Acknowledgements'.

All cases of republication/reproduction must be accompanied by an acknowledgement of first publication of the work by the Royal Society of Chemistry, the wording of which depends on the journal in which the article was published originally. The acknowledgement should also include a hyperlink to the article on the Royal Society of Chemistry website.

The author also has some rights concerning the deposition of the whole article.

Authors contributing to our publications (journal articles, book or book chapters) do not need to formally request permission to reproduce material contained in another Royal Society of Chemistry publication. However, permission should be requested for use of a whole article or chapter. For all cases of reproduction the correct acknowledgement of the reproduced material should be given. The form of the acknowledgement is dependent on the journal in which it was published originally, as detailed in the 'Acknowledgements' section.

This Agreement between Coline Jumeaux ("You") and Nature Publishing Group ("Nature Publishing Group") consists of your license details and the terms and conditions provided by Nature Publishing Group and Copyright Clearance Center.

License Number	3931291220822
License date	Aug 17, 2016
Licensed Content Publisher	Nature Publishing Group
Licensed Content Publication	Nature Reviews Molecular Cell Biology
Licensed Content Title	Mechanisms of membrane fusion: disparate players and common principles
Licensed Content Author	Sascha Martens and Harvey T. McMahon
Licensed Content Date	Jul 1, 2008
Licensed Content Volume Number	9
Licensed Content Issue Number	7
Type of Use	reuse in a dissertation / thesis
Requestor type	academic/educational
Format	electronic
Portion	figures/tables/illustrations
Number of figures/tables/illustrations	1
High-res required	no
Figures	Figure 4
Author of this NPG article	no
Your reference number	
Title of your thesis / dissertation	Nanomaterials for Biosensing and Cancer Therapy
Expected completion date	Oct 2016
Estimated size (number of pages)	200
Requestor Location	Coline Jumeaux 375 Fulham Palace Road London, SW6 6TA United Kingdom Attn: Coline Jumeaux
Billing Type	Invoice
Billing Address	Coline Jumeaux 375 Fulham Palace Road London, United Kingdom SW6 6TA Attn: Coline Jumeaux
Total	0.00 USD